

INTRODUCTION

OVERVIEW AND MAIN RESULTS

PHYSICS OF THE TOKAMAK PLASMA

QUASI-COHERENT MODES AND THE STATIONARY STATE OF THE EDGE LOCALIZED MODES (F. Spineanu, M. Vlad, D. Nendrean)

INTERPRETATION AND CONTROL OF HELICAL PERTURBATIONS IN TOKAMAKS (C.V. Atanasiu, A. Moraru, D. Dumitru)

ANOMALOUS TRANSPORT IN PLASMA: ROLE OF COLLISIONS, TURBULENCE AND WAVE-PLASMA INTERACTION IN TRANSPORT. APPLICATION TO ITER (I.N. Pometescu, G. Steinbrecher)

ANOMALOUS TRANSPORT IN PLASMA. STOCHASTIC PROCESSES AND TRANSPORT IN TURBULENT PLASMA (M. Negrea, I. Petrisor, D. Constantinescu)

UNDERSTANDING THE $E \times B$ DRIFT NONLINEAR EFFECTS ON TRANSPORT AND STRUCTURE GENERATION IN TURBULENT TOKAMAK PLASMAS (M. Vlad, F. Spineanu, D. Nendrean)

THEORETICAL MODELING OF ERROR FIELDS PENETRATION AND NEOCLASSICAL TOROIDAL VISCOSITY NON-RESONANT MAGNETIC BRAKING EFFECTS IN TOKAMAK PLASMAS (I. G. Miron)

ATOMIC DATA CALCULATION IN SUPPORT OF AMNS ACTIVITY (V.Stancalie, V. Pais, A. Mihailescu, A. Stancalie, O. Budriga)

DEVELOPMENT AND MAINTENANCE OF A MODULE FOR IMPLEMENTING AMNS DATA TO ITM-TF CODES (V.Stancalie, V. Pais, A. Mihailescu, A. Stancalie, O. Budriga)

MAINTAIN AND EXTEND THE ITM PORTAL (V.F. Pais , V. Stancalie, A. Mihailescu, O. Budriga)

PLASMA WALL INTERACTION

SHEATH PROPERTIES AND RELATED PHENOMENA OF THE PLASMA WALL INTERACTION IN MAGNETISED PLASMAS. APPLICATION TO ITER (V. Anita, C. Agheorghiesei, S. Costea, C. Costin, G. Popa, L. Sirghi, M. L. Solomon)

STUDY OF THE THERMAL TREATMENT INFLUENCE IN FORMATION OF THE STABLE BE-C, BE-W AND C-W ALLOYS. TVA GUN ELECTRON BEAM IRRADIATION INFLUENCE (C. P. Lungu, A. Anghel, C. Porosnicu, I. Jepu, A. M. Lungu, P. Chiru, C. Ticos, C. Luculescu)

X-RAY MICRO-TOMOGRAPHY STUDIES ON GRAPHITE AND CFC SAMPLES FOR POROSITY NETWORK CHARACTERIZATION (I.Tiseanu, T. Craciunescu, C. Dobrea, A. Sima)

X-RAY MICROBEAM ABSORPTION/FLUORESCENCE METHOD AS A NON-INVASIVE SOLUTION FOR INVESTIGATION OF THE EROSION OF W (I.Tiseanu, T. Craciunescu, C. Dobrea, A. Sima)

REMOVAL OF CODEPOSITED MATERIALS FROM GAPS WITH A PLASMA TORCH (G. Dinescu, T. Acsente, C. Stancu, E.R. Ionita)

CONTROLLED LABORATORY MODELS OF CODEPOSITED LAYERS FOR FUEL REMOVAL (T. Acsente, E. C. Stancu, G. Dinescu)

FUSION MATERIALS DEVELOPMENT

TRANSMISSION AND BACKSCATTERING MÖSSBAUER SPECTROSCOPY STUDIES OF THE SHORT RANGE ORDER, STRUCTURE AND MAGNETIC PROPERTIES IN α -Fe AND BINARY Fe-Cr MODEL-ALLOY. (WP10-MAT-REMEV) (L. Diamandescu)

FUNCTIONAL GRADIENT W-STEEL MATERIALS BY UNCONVENTIONAL CO-SINTERING ROUTES (A. Galatanu, I. Enculescu, A.D. Jianu)

MICROANALYSIS OF ODS AND FIBRES REINFORCED MATERIALS, IN VARIOUS FABRICATION STAGES (C. Sarbu)

IN-SITU TEM OBSERVATION OF THE DYNAMICS OF SCREW & EDGE DISLOCATIONS AND HE BUBBLES IN α -FE AND BINARY FE-CR MODEL-ALLOYS SUBJECTED TO ION IRRADIATION VERSUS TEMPERATURE (V.S.Teodorescu, C. Ghica, L.C.Nistor, A.V.Maraloiu)

PARTICIPATION AT JET ENHANCEMENT AND EXPERIMENTAL PROGRAM

*MANUFACTURING AND TESTING OF W-COATED CFC TILES FOR
INSTALLATION IN JET FOR THE ITER-LIKE WALL PROJECT (C. Ruset,
E. Grigore, I. Munteanu, N. Budica, D. Nendrean)*

*PRODUCTION OF BERYLLIUM COATINGS FOR INCONEL CLADDING
TILES FOR THE ITER-LIKE WALL PROJECT (C. P. Lungu, I. Mustata, V.
Zaroschi, I. Jepu, C. Porosnicu, A. Anghel, A. M. Lungu, P. Chiru)*

*PRODUCTION OF BERYLLIUM COATINGS FOR BERYLLIUM TILE
MARKERS FOR THE ITER-LIKE WALL PROJECT (C. P. Lungu, I. Mustata,
V. Zaroschi, I. Jepu, C. Porosnicu, A. Anghel, A. M. Lungu, P. Chiru)*

*UPGRADE OF GAMMA-RAY CAMERAS: NEUTRON ATTENUATORS (M.
Curuia, M. Anghel, T. Craciunescu, M. Gherendi, S. Soare, V. Zoita)*

*TANDEM COLLIMATORS FOR GAMMA RAY SPECTROMETER (S. Soare,
M. Curuia, T. Craciunescu, V. Zoita)*

GAMMA RAY SPECTROMETRY (S. Olariu, A. Olariu, D. Dudu)

*OPTIC FLOW METHODS FOR IMAGE PROCESSING OF THE DATA
FROM THE VIDEO CAMERA KL-8 AT JET (T. Craciunescu, I. Tiseanu, V.
Zoita)*

*TRITIUM DEPTH PROFILE MEASUREMENTS OF JET DIVERTOR TILES
BY AMS (C. Stan Sion, M. Enachescu, M. Dogaru)*

COLLECTIVE TRAINING OF YOUNG ENGINEERS AND SCIENTISTS

*RESEARCH ACTIVITY IN ICIT RAMNICU VALCEA IN THE FRAME OF
“TRI-TOFFY” EFDA NETWORK TRAINING (I.Spiridon, S. Brad, G. Ana,
M. Vijulie, A. Lazar)*

INTRODUCTION

The Controlled Thermonuclear Fusion in magnetically confined plasma (tokamak geometry) is probably the most important objective in the contemporary research in physics. It aims to create a source of energy which is : clean (no long term radioactive residuals), safe (no possibility of nuclear accident) and sustainable (generically the source is the water). Such an objective can only be realized by a wide and well-structured effort of many countries in the world, acting to create a synergy by a coordinated participation. In Europe the fusion research is organized by the direct involvement of the European Commission and is based on Agreements that represent fundamental documents: The Contract of Association of the Member States (and Switzerland) to EURATOM, the European Fusion Development Agreement (EFDA), the JET (Joint European Torus) Implementing Agreement, the Staff Mobility Agreement. These instruments have created in Europe a strongly correlated, effectively integrated, research activity in the field of fusion plasma.

An essential milestone in the research in fusion is the construction of the International Thermonuclear Experimental Reactor (ITER) which is expected to demonstrate the possibility to control the plasma in the regime dominated by the fusion reactions, with an effective generation of power representing a factor of ten times the input.

Created in 1999, the Association EURATOM – MEdC Romania coordinates at the national level the activities of many groups of research, from national institutes and universities, in the fusion research. In 2010 the Association has continued the work in various areas of expertise that has been identified as useful for the integrated European fusion research, with effective results.

Overview of activity in 2010 of the Association EURATOM – MEdC Romania

Summary of the principal directions

The year 2010 has been marked by a still increasing importance of the changes related to ITER: physics of ITER and construction of ITER have both influenced the works in the Associations.

The EFDA Work Plan has reflected the need for supporting the physics of ITER by investigations of basic plasma processes, scenarios, material physics for Plasma Facing Components, diagnostics. The Romanian Association has responded by taking part in the European collaborations that have been set up for studying these problems.

It has been actively pursued the involvement in the investigation of physical processes that are not considered, at this moment as being completely understood and, consequently, not completely under control in view of their importance for the ITER functional regimes.

The physics of Transport in plasma has been a major field of activity with several subjects being included, from the part of our Association, in the Task Agreement of the corresponding Topical

Group. The physics of particle transport, in particular impurity, Rotation of plasma, the L to H transition are few examples.

The Edge Localised Modes has been studied on the basis of an original explanation which has been developed in our Association. The filamentation, the generation of channels consisting of vorticity, density and current, leading to destabilization and loss of the High Confinement have been inserted in a unique model based on breaking of the sheared layer at the edge of plasma.

The structure of the magnetic field, using hamiltonian approach, continued with orientation to applications related to suppression of ELMs by stochasticisation close to the separatrix.

The investigation of MHD processes, which in our Association is strongly correlated with numerical modeling, has focused on Resistive Wall Modes. A branch of this work is related to the stability of helical perturbations.

The integration of the European effort in numerical modeling of tokamak plasma has been a part of the Work Plan with particular emphasis on (1) harmonization and unification of numerical codes (2) new physics projects to be examined via numerical simulations and (3) training for a unified system of computer simulations. The Association has been present with several participants at the Code Camps organized by the ITM Task Force.

The year 2010 has been essential for the finalization of the two large scale Contracts 5.1b in which our Association has been involved since 2006. The coating with Tungsten of some of the most exposed tiles of the first wall and of the divertor at JET has been successfully accomplished, according to schedules and quality requirements of the contract. In parallel, the coating with Beryllium of part of the tiles of the first wall has also been successfully finished, with approval of the final report. These two activities represent a major contribution of our Association to the project ITER-like wall at JET. The work carried out on the two major contracts will be followed in next years by participation at the experiments related to the ITER-Like Wall at JET.

Erosion and migration of materials of the first wall have also been studied, with our participation mainly consisting of production of samples using previously developed technologies (Tungsten, Beryllium), followed by analysis carried out in collaborating Associations.

Several tasks were performed also in the frame of the Plasma Wall Interaction Workprogramme:

- An instrument and associated measuring methods, based on combined X-ray tomography and fluorescence have been developed and qualified for investigation of the erosion of W coatings on carbon materials substrates and also for the CFC porosity structure analysis.

- Improved cleaning efficiency of co-deposited layers was obtained by upgrading the atmospheric pressure plasma torch for operations the work with reactive gases (oxygen, air, ammonia, hydrogen or their mixtures).
- A novel developed plasma deposition method (sequential deposition) was developed for obtaining mixed layers of hydrogenated carbon with metal inclusions to be used as laboratory models for tokamak co-deposited layers in fuel removal studies.

The field of Materials has, for the first time, been included in the Work Plan of our Association, on the basis of an exclusive support from the National Authority. At least one of the subjects, welding of Tungsten components on CFC, will be continued as a useful technological Task for future devices.

The work related to diagnostics was mainly dedicated to JET tasks.

It has been continued the improvement of the gamma-ray diagnostics at JET with our Association being involved in the development and construction of the neutron attenuators for the Gamma-Ray Camera and of the Tandem Collimators System. This subject will have to receive a careful consideration, especially in view of its near-future final phase. The tandem collimator, where our Association has the responsibility of leading the Project has continued with substantial allocation of resources. Both these subjects represent a participation of the MEdC Association to the Enhancement Project II at JET.

The work on the Gamma Ray Spectroscopy project was focused on the assessment of the response of the LaBr₃ detector to very high counting rates. The assessment was based on experiments performed at the Tandem and Cyclotron accelerators of the National Institute of Physics and Nuclear Engineering, Magurele. The work on this project has been ended with approval of the final report and with prospects for a future activity in a related subject.

High sensitivity accelerator mass spectrometry analysis were performed for determining the tritium depth profile concentrations in divertor tiles from JET (samples from campaigns 1998-2004, 1998-2007 and 2004-2007).

An optical flow procedure for the JET fast visible camera image processing was developed and implemented. The method is able to cope with several different plasma physical phenomena (pellet injection, plasma filaments and MARFEs) and to provide useful information for modelling.

Characterisation of Pilot-PSI plasma beam was achieved by electrical methods (electrostatic analysers) and plasma diagnostic in the Scrape-off Layer (SOL) of COMPASS tokamak by electrical probes. Two different numerical codes (2D PIC-MCC and 2D fluid model) were developed for the simulation of linear magnetized plasma devices.

The Goal Oriented Training TRI-TOFFY has continued for the second year. The trainee has carried out work according to the programme established by the network of GOT, at KIT, supported under the Mobility agreement.

Research reflected in the Contracts with the main partners in 2010

The basic documents establish a structure of collaboration based on Contracts which have as partners on one side the Associations and on the other side:

- The European Commission, Directorate General Research DG J Energy (EURATOM) (later DG K Energy)
- European Fusion Development Agreement (EFDA), through the Close Support Units Garching and Culham
- JET (Joint European Torus) through EFDA Close Support Unit (CSU) Culham

In 2010 the participation of the Romanian EURATOM Association has been realized through **19 Contracts**, covering the following thematic areas:

- Turbulence and Transport processes in tokamak plasma: 1 contract covering 8 objectives (which are separate contractual commitments)
- Magneto Hydro Dynamics (MHD): 1 contract covering 2 objectives (separate contractual commitments)
- Integrated Tokamak Modelling (ITM): 1 contract covering 4 objectives and 2 objectives with additional support EFDA Art. 8.2a
- Plasma Wall Interaction (PWI): 1 contract covering 9 objectives plus 4 with additional support EFDA Art. 8.2a
- Materials: 3 contracts (OSDFS, WWALLOY, REMEV) covering 4 objectives
- JET Notifications: 4 contracts each covering one objective
- EFDA Fellowship: 1 contract covering 1 objective
- JET ITER-Like Wall Project: 2 Contracts of the type EFDA 5.1b
- Order of Enhancement Project at JET: 5 contracts, corresponding to the objectives of the JET Notifications

In summary there have been **38 contractual objectives of Task Agreements, with the Comission, EFDA and EFDA-JET**, with the following distribution :

- 27 with the European Fusion Development Agreement
- 4 with JET (Joint European Torus)

- 7 with the European Commission DG J

6 contractual objectives have received Additional Support according to EFDA Art. 8.2a.

Conforming to the administrative concept underlying the functioning of the Romanian EURATOM Association, the Task Agreements with the European partners, mentioned above, have led to the signature of **36 internal contracts** between the Institute of Atomic Physics and seven research institution from Romania.

The main collaborations within the system of EURATOM Associations

Every Task Agreement is actually realized by a collaboration of several Associations. In time, the nature of expertise developed by the research groups from Romania has led to creation of recurrent scientific contacts and common works with a number of Associations.

- Universite Libre de Bruxelles
 - Physics of transport in plasmas.
 - Participation to a common project of fluid simulation at High Performance Computer for Fusion Physics.
- IPP Garching
 - MHD processes and Resistive Wall Modes.
 - Analysis of coated samples for studies of material migration.
- FOM Nederlands
 - Diagnostics of edge plasma and development of Langmuir probes.
- Commissariat a l'Energie Atomique
 - Development of the cleaning method by Plasma Torch.
 - Participation to the development of the computer code Gysella.
- Karlsruhe Institute of Technology
 - Common work on tritium technology (extended to a project for Fusion for Energy).
 - Training of a young Romanian engineer in the area of Tritium technology.
- Institute of Plasma Microfusion (Poland Association)
 - Experimental validation of neutron attenuators for the JET Gamma-Ray Camera.
- Association EURATOM-CCFE/JOC, Culham Science Centre, Abingdon, UK and Association EURATOM-CRPP-EPFL, Lausanne, Switzerland

- Development of the neutron attenuators for the JET Gamma-Ray Camera and Tandem Collimators.
- EURATOM-MHST, Jozef Stefan Institute, Ljubljana, Slovenia
 - MCNP evaluation of Neutron Attenuators for the Gamma-Ray Camera.
- Consorzio RFX, Associazione EURATOM-ENEA per la Fusione, Padova, Italy
 - Development of methods for plasma diagnostic based on video camera data at JET.

**List of the Task Agreements of the Association
EURATOM – MEdC Romania in 2010**

BASELINE SUPPORT				
Nr.	Internal code	Code Task Agreement	Support Baseline / Priority Support (ppy)	Specific Objective
1	BS_1	WP10-MHD-03-03-xx-02/MEdC WP10-ITM-IMP12-ACT9-T1-01/MEdC	Baseline	Interpretation and control of helical perturbation in tokamaks
2	BS_2	WP10-TRA-01-04--xx-01/MEdC	Baseline	Equilibrium flows and threshold conditions for accessing high confinement regimes and understanding of the nonlinear dynamics of low
3	BS_3A	WP10-TRA-03-01-xx-01/MEdC WP10-TRA-03-03-xx-01/MEdC WP10-TRA-05-01-xx-01/MEdC WP10-TRA-01-05-xx-01/MEdC WP10-ITM-IMP5-ACT4-T1-01/MEdC	Baseline Priority ITM (0.5)	Anomalous transport in plasmas. Role of collisions, turbulence and wave-plasma interaction in transport. Application to ITER. Model for Edge Plasma Turbulence
4	BS_3B	WP10-TRA-05-01--xx-01/MEdC	Baseline	Anomalous transport in plasmas. Stochastic processes and transport in turbulent plasmas
5	BS_4A	WP10-ITM-ISIP-ACT3-T1-01/MEdC WP10-ITM-ISIP-ACT10-T1-01/MEdC	Priority ITM (0.4) Priority ITM (0.8)	ITM-Portal
6	BS_4B	WP10-ITM-AMNS-ACT2-T1-01/MEdC WP10-ITM-AMNS-ACT3-T1--01/MEdC	Baseline Priority ITM (0.3)	ITM-AMNS
7	BS_13	WP10-MHD-03-03-xx-01/MEdC	Baseline	Theoretical modeling of the resistive wall modes feedback control considering neoclassical toroidal viscosity and error field penetration
8	BS_6	WP10-PWI-04-04-01/MEdC/BS	Baseline	Sheath properties and related phenomena of the plasma wall interaction in magnetised plasmas. Application to ITER.
9	BS_14	WP10-TRA-01-02-xx-01/MEdC WP10-TRA-05-01-xx-01/MEdC	Baseline	Understanding of the ExB drift nonlinear effects on transport and structure generation in turbulent tokamak plasmas
10	BS_18_A	WP10-PWI-06-01-01/MEdC/BS WP10-PWI-06-01-01/MEdC/PS	Baseline Priority	Study of the thermal treatment influence in formation of the stable Be-C, Be-W and C-W alloys . TVA gun electron beam irradiation influence. (BS-PS)

11	BS_18_B	WP10-PWI-06-02-01/MEdC/BS WP10-PWI-06-02-01/MEdC/PS	Baseline Priority	Study of the ternary system formation Be-C-W using thermionic vacuum arc method; Influence of hydrogen/deuterium inclusion into the prepared films on the retention process. D-
12	BS_19_A	WP10-PWI-02-04-01/MEdC/BS	Baseline	Codeposited material removal with a plasma torch. Removal of codeposited materials from gaps with plasma torch.
13	BS_19_B	WP10-PWI-02-04-02/MEdC/BS	Baseline	Laboratory models for the codeposited layers
14	BS_19_C	WP10-PWI-02-04003/MEdC/BS	Baseline	Production of controlled laboratory codeposited layers for fuel removal studies
15	BS_20_A	WP10-PWI-01-02-01/MEdC WP10-PWI-01-02-02/MEdC/PS	Baseline Priority	X-ray micro-tomography studies on graphite and CFC samples for porosity network characterization (BS-PS)
16	BS_20_B	WP10-PWI-05-02-01/MEdC WP10-PWI-05-02-02/MEdC/PS	Baseline Priority	X-ray micro-beam absorption/fluorescence techniques for erosion and deposition of wall materials (BS-PS)
17	BS_M_1	WP10-MAT-REMEV-01-01/MEdC/BS	Baseline	Transmission and backscattering Mössbauer Spectroscopy studies of the short range order, structure and magnetic properties in α -Fe and binary Fe-Cr model-alloys WP10-MAT-REMEV
18	BS_M_2	WP10-MAT-ODSFS-01-01/MEdC/BS	Baseline	Microstructure characterization of ODS ferritic steels (ODSFS) by TEM, X-EDS, EELS and APT, WP10-MAT-ODSFS-01
19	BS_M_3	WP10-MAT-WWALLOY-01-01/MEdC/BS	Baseline	Functional gradient W-Eurofer steel materials by unconventional co-sintering routes WP10-MAT-WWALLOY-01
20	BS_M_4	WP10-MAT-REMEV-06-01/MEdC/BS	Baseline	In-situ TEM observation of dynamics of screw & edge dislocations and He bubbles in α -Fe and binary Fe-Cr model-alloys subjected to ion irradiation versus temperature
21	BS_SC	Task Superconductors	Baseline	Electrical, magnetic and mechanical characterisation of Re123 superconducting cables and tapes
22	BS_9	JET Diagnostics	Baseline	Optic flow methods for image processing of the data from the video camera KL7 at JET

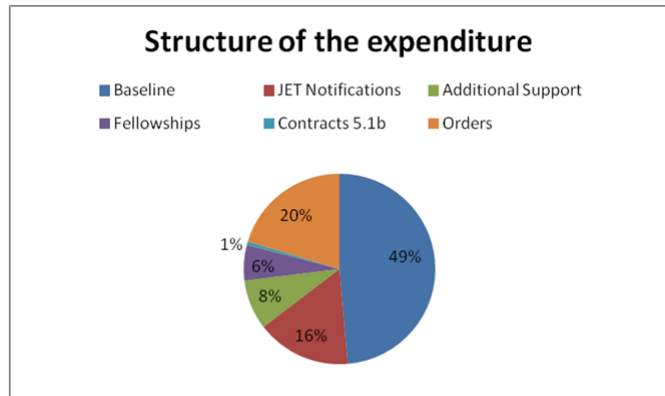
JET NOTIFICATIONS				
Nr.	Internal code	Code Task Agreement	Support Baseline / Priority Support (ppy)	Specific Objective
23	BS_8	JW6-TA-EP2-GRS-05	JET Notification	Gamma Ray Spectrometry Upgrade (GRS)
24	BS_15	JW9-TA-EP2-TCS-01	JET Notification	KM6T Tandem Collimator
25	BS_7	JW6-TA-EP2-GRC-04	JET Notification	Upgrade of the JET KN3 Gamma-Ray Cameras Diagnostics
26	BS_12	WP10-PWI-01-01-01/MEdC	Baseline	Providing W coated CFC samples for fuel retention measurements
27	BS_17	JW9-FT-3.50 JW9-NFT-MEC-16	JET Notification	AMS high sensitivity Tritium depth-profile (JW10-FT-3.60) measurements in PFC samples

TRAINING				
Nr.	Internal code	Code Task Agreement	Support Baseline / Priority Support (ppy)	Specific Objective
28	AS_8	WP08-GOT-TRI-TOFFY	Priority GOT	Task Agreement WP08-GOT-TRI-TOFFY
EFDA Article 5.1 B contracts (running Technology contracts)				
Nr.	Internal code	Code Task Agreement	Support Baseline / Priority Support (ppy)	Specific Objective
29	TT12_5.1b	JW6-TA-EP2-ILC-05	Priority 5.1b	ITER-like Wall Project at JET: Optimisation and manufacturing of 10 µm W-coatings for the CFC tiles to be installed in JET.
30	TT19_5.1b	JW6-TA-EP2-ILB-03	Priority 5.1b	JW6-TA-EP2-ILB-02 Production of Beryllium Coatings for Inconel Cladding and Beryllium tile Markers for the ITER-like Wall project.
EFDA JET Order Art. 6.3				
Nr.	Internal code	Code Task Agreement	Support Baseline / Priority Support (ppy)	Specific Objective
31	F8_O	JW7-OEP-MEC-11		Gamma Ray Spectrometry Upgrade (GRS)
32	TT12_O	JW6-OEP-MEC-06B		ITER-like Wall Project at JET: Optimisation and manufacturing of 10 micron W
33	BS_15_O	JW9-OEP-MEC-15		Tandem Collimators Order
34	BS_7_O	JW6-OEP-MEC-13A		Gamma ray cameras neutron attenuators Order missions + procurement
35	Z_CSU	Secondment Agreement 1699		Secondment Agreement to CSU Culham
36	TT19_O	JW6-OEP-MEC-09C		JW6-TA-EP2-ILB-02 Production of Beryllium Coatings for Inconel Cladding and Beryllium tile Markers for the ITER-like Wall project.

Structure of financing and of expenditure

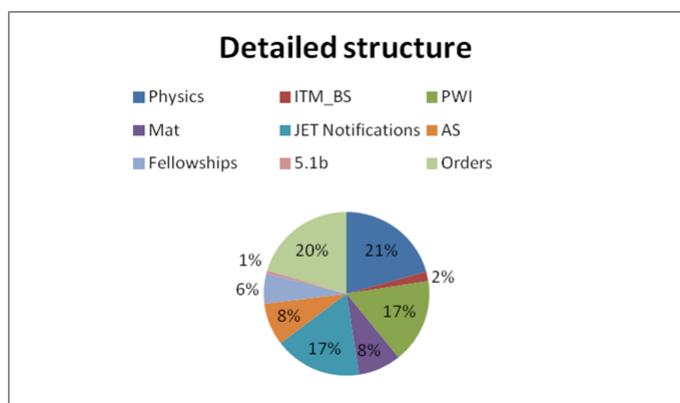
The category of expenditures (all figures are in Euro)

Baseline	645933
JET Notifications	212476
Additional Support	111673
Fellowships	79715
Contracts 5.1b	7895
Orders	270317



Detailed structure of the directions of expenditures (AS = Additional Support EFDA 8.2; PWI = Plasma Wall Interaction; Mat = Materials; ITM = Integrated Tokamak Modeling; BS = Baseline; 5.1b = Contracts 5.1b).

Physics	273668
ITM_BS	24951
PWI	222404
Mat	111031
JET Notifications	226355
AS	111673
Fellowships	79715
5.1b	7895
Orders	270317



The contribution of the Commission to the Baseline has been of 92,400 euro representing 11% of the Baseline budget.

The Romanian research institutions that have participated to the activities of the Association EURATOM – MEdC Romania in 2010

1. National Institute of Laser, Plasma and Radiation Physics, Bucharest
2. National Institute of Cryogeny and Isotope Technology, Ramnicu-Valcea
3. National Institute of Physics and Nuclear Engineering, Bucharest
4. National Institute of the Physics of Materials, Bucharest
5. University “A.I. Cuza”, Iassy
6. University of Craiova
7. Technical University of Cluj-Napoca

The 2010 Work Programme of the Association has involved 140 persons from these institutions, to various degrees of implication. The effective participation is translated into approximately 30 ppy (professional per year)

Staff mobility actions

- **58 Staff Assignment to different Associations and to JET.** The equivalent expenditure for these actions is approximately 95,000 euro, below the approved ceiling. In 2010 it has been noticed a substantial increase in the type of actions related with reporting meetings, project board meetings, kick-off meetings. These are of short duration and the list of approved meetings has been carefully observed.

Public presentations and/or dissemination

- Two presentations of fusion research have been made, having as target scientific public: the Institute of Physics of Materials and Institute of Atomic Physics
- The meeting “Association Day” has been held jointly with the “15th International Conference on Plasma Physics and Applications”, 1 – 5 July, Iassy,
- TV presentation focused on Fusion research (Cristian Lungu and Florin Spineanu, January 2010)
- Printed versions of the Annual Reports 2008 and 2009, widely disseminated
- Realization and distribution of a CD-ROM containing the Annual Reports 2002 – 2009 plus other information on the Association

The WEB page of the Association (<http://www.ifa-mg.ro/EURATOM>) consists of more than 1,6 Gigabytes of information necessary to the communication with the 7 participating institutions (four national institutes and three universities).

PHYSICS OF THE TOKAMAK PLASMA

QUASI-COHERENT MODES AND THE STATIONARY STATE OF THE EDGE LOCALIZED MODES

F. Spineanu, M. Vlad, D. Nendrea

National Institute of Laser, Plasma and Radiation Physics, Bucharest

Overview

We have shown previously that in some regimes of the H-mode the layer consisting of strong concentration of the density, vorticity and current density evolves to break-up of into quasi-singular structures (filaments). This evolution is purely growing in an axisymmetric geometry and is governed by an universal instability of the same type as the Chaplygin gas with anomalous polytropic. The break-up of the current layer and formation of filaments take place on very short time scales, governed by the Alfvén speed in the direction of the layer (transversal on \mathbf{B}).

We show now that the parallel dynamics is inhibited by the same mechanism which damps the poloidal rotation in tokamak, the *magnetic pumping*. The fast increase of the current and of the flow velocity along the magnetic field lines during the filamentation is accompanied by radial currents (localised to the filaments) due to curvature drifts which, in a collisional plasma, absorb energy from the flow on a time scale of the inverse ion-ion collision frequency. As in the usual neoclassical damping the effect is nonuniform along the line and is effectively equivalent to a force acting against the increase of the flow in the filaments. This may generate oscillatory instead of purely growing states. We propose this model as an explanation of the oscillatory regimes preceding the ELM events.

Detailed results

1 Methods

The H-mode is by necessity the stationary regime of the tokamak working as a reactor, due to the lower rate of loss of the energy contained in plasma. This H-mode is characterised by the presence of a layer of poloidally rotating plasma. The layer is close to the plasma edge, at the last closed magnetic surface. For very general reasons, the layer of strongly sheared poloidal rotation must be accompanied by a strong concentration of current density. This is due to the fact that coincidence of vorticity and current density maxima is a state of lower energy for the plasma. In addition, there are local reasons: the gradients of the density and temperature in the "pedestal " necessitate a current density that can ensure the equilibrium relation $\mathbf{j} \times \mathbf{B} = \nabla p$.

The values that have been determined experimentally are high and cannot be justified by reasons related to the neoclassical component (bootstrap, See DIII-D experiments of Burrell).

In the first part of this work, reported previously, it has been shown that the plasma evolves to the break-up of the layer with strong concentration of the density, vorticity and current density into quasi-singular structures (filaments). This evolution is purely growing in an axisymmetric geometry and is governed by an universal instability of the same type as the Chaplygin gas with anomalous polytropic. The break-up of the current layer and formation of filaments takes place on very short time scales, governed by the Alfvén speed in the direction of the layer (transversal on \mathbf{B}). This is a fast transient process which in axisymmetry is only limited by the generation of the singular filaments. The parallel dynamics is arbitrary, as long as the condition $v_z^{elect} \ll v_{th}^{elect}$ is fulfilled.

However the parallel dynamics is inhibited by the same mechanism which damps the poloidal rotation in tokamak, the *magnetic pumping*. The fast increase of the current and of the flow velocity along the magnetic field lines during the filamentation is accompanied by radial currents (localised to the filaments) due to curvature drifts which, in a collisional plasma, absorb energy from the flow on a time scale of the inverse ion-ion collision frequency. As in the usual neoclassical damping the effect is nonuniform along the line and is effectively equivalent to a force acting against the increase of the flow in the filaments. This may generate oscillatory instead of purely growing states. The effect of thermal channeling due to filamentation contributes to the reduction of the efficiency of the damping mechanism and the regime can again be purely growing but saturates the filaments to a finite amplitude.

The precursors to the ELM event are due to the fact that the nonlinear tearing of the current sheet (coinciding with the vorticity layer) is not purely growing but also has an oscillatory part.

The basic fact in the ion-pressure driven instabilities in tokamak is that the parallel dynamics results from a balance where the electron collisions are essential. This represents the condition that must be invoked in the Hasegawa-Wakatani theory of drift-wave turbulence. When the temperature is high the collisionality is low and one expects that the parallel balance is not satisfactorily described as a dissipative mechanism. Frequently it is invoked the parallel Landau damping but the efficiency of this pseudo-dissipation model is problematic for short time scales as the ones that are implied in the Edge Localised Modes.

We propose to consider the transitory process of increase of the parallel current induced by the centrally advected vorticity in a Kelvin-Helmholtz event as constrained by the poloidal viscosity of neoclassical origin. This mechanism, the usual reason for the decay of poloidal rotation in plasma, is efficient due to the different drifts of electrons and ions in the radial direction, leading to currents that are subjected to resistive dissipation. We propose this mechanism as a source of force opposing the gradient of the parallel current. This will allow to balance in an

efficient way the parallel dynamics and will give correct evaluation of the growth rates of the Edge Localised Modes.

2. Results and discussion

The variables are ω (vorticity) and J_{\parallel} . These are the equations:

$$\frac{d\omega_{\parallel}}{dt} = \frac{B^2}{\rho} \nabla_{\parallel} \left(\frac{j_{\parallel}}{B} \right) - \frac{2\mathbf{B} \cdot (\nabla p \times \nabla B)}{\rho B^2} + \frac{\mu}{\rho} \nabla^2 \omega_{\parallel}$$

$$\frac{\partial j_{\parallel}}{\partial t} = \frac{1}{\mu_0} \nabla_{\parallel} (B \omega_{\parallel}) + \frac{\eta}{\mu_0} \nabla^2 j_{\parallel}$$

From these equations one derives a local relationship between the parallel current and the vorticity oriented along the magnetic field lines, which is precisely the case of the filaments. For a highly conducting plasma one gets for a local perturbation

$$j_{\parallel} = - \frac{k_{\parallel} B}{|k_{\parallel} B|} \left(\frac{\rho}{\mu_0} \right)^{1/2} \omega_{\parallel}$$

We note that the nature of the equation obeyed by the vorticity seems to permit an oscillatory behaviour of this quantity. However this should be combined with propagation of perturbations along the poloidal direction, where the spatial modulations should follow the initial periodic formation of the seeds of filaments, from Kelvin-Helmholtz events.

The opposition encountered by an increasing filament of current and vorticity is due to the magnetic pumping. This is because the formation of the filament implies the increase of the parallel current in some particular (periodically disposed) points on the rotation H -mode layer and this increase is equivalent to pushing the plasma along the magnetic field line. The filamentation due to drop-on-ceil instability should be purely growing, while the increase of the flow along the line is a transient process. Plasma is suddenly pushed along the line due to the concentration of the density in the vortex and it has to traverse regions of different magnetic field. It is then subject to the magnetic pumping and the effect is a force that acts as a damping of the motion. This leads to a dynamic balance of the two opposite tendencies:

- 1) increase of parallel velocity of plasma associated with the concentration of density during filamentation and vortex formation
- 2) damping of the parallel motion due to the magnetic pumping effect. The decay of the poloidal rotation in a low beta plasma is related to the motion of the plasma through the spatially-periodic magnetic field of the tokamak. This is the dissipative process of magnetic pumping and its effect is realized via the ion viscosity.

It is considered that at the initial moment a radial electric field exists in plasma. There is a poloidal rotation of plasma due to the interaction of this field with the confining magnetic field.

Moving through this periodic magnetic field the drifts of the particles will create a radial electric current. This is because the drifts of the electrons and the ions are different in magnitude.

The drift kinetic equation is solved for the neoclassical distribution function in the first order in the neoclassical small parameter, δ . The radial current is obtained from the velocity space integral of the particle radial drift, weighted by the first order distribution function.

The electrons and ions moving along a magnetic line experience different deviations induced by the gradient of B and by the curvature (guiding centre drifts). The charge separation is a current with nonvanishing radial component and symmetric periodic amplitude along the line. This current (transversal on the line) in an ideal plasma is simply oscillatory, following the regions of low or high B . The collisionality, even small, opposes a resistivity to this current density and induces an irreversible loss of energy, leading in time to the damping of the poloidal flow component, the one that is confronted with the variation of B .

The current density induced by the drift separation

$$j_D = en(v_{Di} - v_{De})$$

leads to a loss of energy $\Delta \mathbf{E} \sim \eta_{\perp} \langle j_D^2 \rangle t$ averaged over the excursion of the particles that explore the low- B and the high- B regions along the line in the time t . The average loss of energy per unit of time $\partial(\Delta \mathbf{E})/\partial t$ is noted ε and its time integral is bounded from above by the total poloidal energy of the flow. An estimation is

$$j_D \sim en \frac{1}{\Omega_i} (\mu_i \nabla B + v_{\parallel i}^2 (\hat{n} \cdot \nabla) \hat{n}) - en \frac{1}{\Omega_e} (\mu_e \nabla B + v_{\parallel e}^2 (\hat{n} \cdot \nabla) \hat{n})$$

We can neglect the ion field-curvature term due to smaller $v_{\parallel i}$ and the electron ∇B drift

$$j_D \sim en \frac{\mu_i \nabla B}{\Omega_i} - en v_{\parallel e}^2 \frac{1}{\Omega_e R}$$

from which we get an estimation of the power loss

$$\varepsilon \sim e^2 n^2 \eta_{\perp} \left(\frac{1}{\Omega_i} \langle \mu_i \nabla B \rangle - v_{\parallel e}^2 \frac{1}{\Omega_e R} \right)^2$$

and of the maximal variation of the electron parallel velocity

$$v_{\parallel e} \sim \sqrt{\Omega_e R} \left| \frac{\varepsilon^{1/2}}{en \eta_{\perp}^{1/2}} - \frac{1}{\Omega_i} \langle \mu_i \nabla B \rangle \right|^{1/2}$$

The effect on the variation of the vorticity by stretching during filamentation is

$$\frac{d\omega_{\square}}{dt} = \frac{B^2}{\rho} \nabla_{\square} \left(\frac{j_{\square}}{B} \right)$$

Taking $\omega_{\square} \sim v/d$ where v is in the layer (poloidal) and d is the width of the layer,

$$\frac{\partial v}{\partial t} \Big|^{damping} = \frac{dB}{ne\rho} \frac{\partial}{\partial z} \sqrt{\Omega_e R} \left| \frac{\varepsilon^{1/2}}{en\eta_{\perp}^{1/2}} - \frac{1}{\Omega_i} \langle \mu_i \nabla B \rangle \right|^{1/2}$$

This new term must be added to the equation for the velocity v in the layer, and acts like a force opposing the concentration of current density in a filament.

$$\frac{\partial v}{\partial t} + v \frac{\partial v}{\partial x} = -\frac{e}{m_i c} \left(V_z^{(0)} + \frac{e}{m_e c} A \right) \frac{\partial A}{\partial x} - \frac{\partial v}{\partial t} \Big|^{damping}$$

The most important effect is the inhibition of the Chaplygin (drop-on-ceil) instability.

3. Conclusion

The parallel dynamics during the transient filamentation of the current and vorticity sheet at the tokamak edge is the result of a balance between the increased flow along the line and the damping of the motion *magnetic pumping*. This provides the basis for an explanation of the oscillatory precursors of the ELMs: before the filamentation becomes purely growing, the damping from magnetic pumping compensates periodically the increase in the parallel current and the flow due to the vorticity concentration.

INTERPRETATION AND CONTROL OF HELICAL PERTURBATIONS IN TOKAMAKS

C.V. Atanasiu¹, A. Moraru², D. Dumitru¹

¹*National Institute for Lasers, Plasma and Radiation Physics, Bucharest, Romania*

²*University Politehnica of Bucharest, Romania*

Overview

During the period January-December 2010, the theoretical and modelling research activity of the “*Mathematical Modelling for Fusion Plasmas Group*” of the National Institute for Lasers, Plasma and Radiation Physics (NILPRP), Magurele - Bucharest, Romania has been focalized on two directions:

1. Resistive wall modes stabilization, by investigating the *Rotational stabilization of the RWM by coupling to a dissipative rational surface*, with the objective to advance the physics understanding of RWMs stability, including the dependence on plasma rotation, wall/plasma distance, and active feedback control.

2. Evaluation of flow stabilization effects on ITER equilibrium states with the objective to extend the generic linear static equilibrium solutions applied to realistic ASDEX Upgrade equilibria, to ITER equilibria (ITER shaping, poloidal beta, poloidal current, safety factor on axis, internal inductance) with sheared flow parallel to the magnetic field with Alfvén Mach numbers on the order of 0.01 and to investigate the potential stabilizing effect of the flow by applying a sufficient condition for linear stability of equilibria with parallel flow.

Publications

- [1] C.V. Atanasiu, A. Moraru, L.E. Zakharov, *Special aspects of magnetohydrodynamic equilibrium calculation in diverted tokamak configurations*, Rev. Roum. Sci. Techn. – Électrotechn. et Énerg., **54**, 2, (2011).
- [2] J. Adamek, C. Angioni, G. Antar, C.V. Atanasiu, et al., *Axially Symmetric Divertor Experiment (ASDEX) Upgrade Team*, Review of Scientific Instruments, **81**, 3, 033507 (2010).
- [3] C.V. Atanasiu, A. Moraru, L.E. Zakharov, *MHD modelling in diverted tokamak configurations*, The 7th International Symposium on ATEE, May 12-14, 2011, Bucharest, Romania.

Detailed results

1. Resistive wall modes stabilization: Rotational stabilization of the RWM by coupling to a dissipative rational surface

Up to now, we have used the Fitzpatrick seminal model [1] to describe different dissipation mechanisms, like anomalous plasma viscosity, charge-exchange with cold neutrals, neoclassical

flow-damping, sound-wave damping, etc. Unfortunately the results obtained with this model do not correspond to experimentally realistic timescales and plasma rotation values ($O(1\%) \Omega_A$) even it offers some useful information on plasma rotation influence on mode growth rate.

Considering the standard large-aspect ratio, low β , circular cross-section tokamak plasma [2, 3], we have started the developing of an analytical model with a resonant resistive-visco-inertial layer inside of the plasma (Finn [4], Gimblett and Ham [5, 6]). This internal layer could correspond to a tearing or internal kink mode.

To provide the physics within the resonant layer, we have used the known layer theory of Porcelli [8] to analyze the non-ideal effects inside the resonant layer and have included resistivity and viscosity on the growth rate of the resonant layer. Thus, the cylindrical plasma, with a single resonant surface ($q(r_s)=m/n$), is considered ideal outside the resonant layer but with resistivity and viscosity at the rational surface r_s . The perturbed poloidal flux function $\psi(r)$, sufficiently far from r_s is described by the equation [7, 9]

$$\frac{1}{r} \frac{d}{dr} \left(r \frac{d\psi}{dr} \right) - \frac{m^2}{r^2} \psi - \frac{mj'}{rF} \psi = 0, \quad F = \frac{B_\theta}{r} (m - nq), \quad (1.1)$$

where $' \equiv d/dr$, j is the equilibrium current density, and B_θ is the unperturbed poloidal magnetic field. This equation has been drawn from the equation given in Ref. [7] for the toroidal case, by considering a vanishing plasma pressure gradient and zero diamagnetic current. The perturbed quantities have to be in the frame of the standard assumptions in single-mode neoclassical theory where the magnetic field is expressed in second order approximation of the aspect ratio and as safety profile the well known Wesson profile [10] has been used. Even if really, the ideal external kink modes are driven by plasma pressure gradients, in this model, for sake of simplicity, these modes will be considered driven by current gradients. The slow plasma rotation also limits the Alfvén continuum damping effect. Therefore, it is expected that these current driven modes can be reasonably well described and studied by ideal MHD theory, as long as the realistic plasma geometry and equilibrium profiles are taken into account [11]) The solution of this equation is matched at the resonant surface and at the resistive wall $r=r_w$. Following Bondesson [9], we defined two solutions of this equation: $\psi_0(r)$, the solution with no wall and $\psi_\infty(r)$ the solution with a perfectly conducting wall of radius r_w . The linear combination of these two solutions gives the solution to the RWM problem

$$\psi = a\psi_0 + b\psi_\infty, \quad a = \text{const}, \quad b = \text{const}. \quad (1.2)$$

with the boundary condition at r_w [9]

$$\Delta'_w = \frac{[\psi']_{r_w}}{\psi(r_w)} = \gamma\tau_w, \quad \text{with } [\psi'] = \psi'(r_{w+}) - \psi'(r_{w-}) \text{ and } \psi_0(r_w) = 1, \psi_\infty'(r_{w+}) = -\frac{1}{r_w} \quad (1.3)$$

where γ is the growth rate of the mode and $\tau_w = r_w w \mu_0 \sigma_w$ is the wall time with the wall thickness $w \ll r_s$ and $\tau_w \gg \tau_A$.

Knowing that the outer solutions of the magnetic vector potential are continuous across the resonant layer, but present a jump in their first derivatives (the tangential magnetic field), one can use the well known ‘‘Delta prime’’ definition

$$\Delta'_s = \frac{[\psi']_{r_s}}{\psi(r_s)} = \frac{[\psi_0']_{r_s} + \gamma\tau_w [\psi_\infty']_{r_s}}{\psi_0(r_s) + \gamma\tau_w \psi_\infty(r_s)}, \quad (1.4)$$

and applying Newcomb theory [12], it results that the kink mode is unstable.

Eq. (1.1) is used outside the resonant layer and its solutions couple the kink mode to the resonant layer. For the resonant layer Porcelli's model [8] has been used; he has analyzed the effects of resistivity, momentum and viscosity on the growth rate of the resonant layer. Considering a slab geometry around the resonance layer (such simplification is acceptable for the cylindrical geometry we considered), and the Fourier transformed displacement $\xi(k)$ one obtains the solution inside the layer

$$\Delta'_{layer}(\gamma) \square - \frac{r_s}{(r-r_s)^2} \frac{\xi(r)}{\xi'(r)} \Big|_{r \rightarrow r_s} \quad (1.5)$$

We have to match the outer solution (Eq. (1.4)) with the layer solution (Eq. (1.5))

$$\Delta'_{layer}(\gamma) = \Delta'_s(\gamma) \quad (1.6)$$

In function of different plasma parameters, the response of the layer can be of the following types (after Porcelli [8]): 1) tearing or reconnection: when the resistivity is much greater than inertia and viscosity; 2) ideal: when inertia is much greater than viscosity and resistivity; 3) visco-resistive: when viscosity and resistivity are much greater than inertia; 4) visco-ideal: when inertia and viscosity are much greater than resistivity.

From the matching of the outer and inner solution the dispersion relation is obtained. Plasma rotation can be introduced by considering stationary plasma with a rotating wall [13].

Conclusions and general perspectives

1. for the moment, the obtained results are not very conclusive on determining which of the above mentioned dissipation mechanisms is absolutely necessary for RWM stabilization and even if this could be done effectively. We have to continue our investigation by refining the inner solutions of Eq. (1.3). At the same time, alternative approaches have to be.
2. we believe that the following problems are open: - what physics determines the critical rotation rate needed to stabilize the mode, - whether some form of plasma dissipation (e.g., absorption of sound waves, viscosity) is always required for stabilization, - what the optimum properties of the conducting shell are for achieving stabilization at low plasma rotation rates, - the stabilization of RWM in ITER, where it is probably not possible to maintain a very fast plasma rotation is still an open problem.
3. according to the excellent review paper [14], the stabilization effect that has been demonstrated experimentally has not been found to be robust. This is mainly because near the beta limit, the tokamak can also develop other instabilities. These instabilities can excite the RWM. To turn the stabilization effects found up to now into robust, reproducible tools for the

everyday operation of the tokamak should be the next area of research on the RWM for the tokamak.

4. although analytical results (ours included) indicate that RWMs stabilization is possible; little can be done more analytically - the main part has to be numerical.

2. Evaluation of flow stabilization effects on ITER equilibrium states.

We have started with the generic linear analytic solution to the Grad-Shafranov equation [15] applied to realistic ASDEX Upgrade equilibria, where we have considered a current density parametrisation with four degrees of freedom. Thus, an independent choice of the plasma current I_p , the poloidal beta β_p , the internal inductance li , and the safety factor q , at the boundary or at the magnetic axis can be made. We have extended this equilibrium to stationary equilibrium with incompressible flow parallel to the magnetic field, with Alfvén Mach numbers on the order of 0.01. As in the static case, the solution is expressed in terms of confluent hypergeometric functions because the pertinent generalized Grad-Shafranov equation [16] can be transformed to a form identical to the usual Grad-Shafranov equation and therefore static analytic solutions can be smoothly extended to the parallel flow regime. We then examined the particular physically interesting set of equilibria with current density vanishing on the boundary for which the solution is put in a simpler form in terms of Whittaker functions. To make a first evaluation of the possible effects of flow on stability we applied a sufficient condition for linear stability [17] to toroidal configurations of this kind with a rectangular cross-section and ITER-like aspect ratio and elongation. It turns out that unlike to nonlinear equilibria in plane geometry [18, 19], the flow does not have a stabilizing effect in the sense that the aforementioned stability condition is not satisfied. This result confirms a previous conjecture [18, 19] that equilibrium nonlinearity may activate flow stabilization and this should be further examined in connection with possible stabilizing effects of flow for ITER-like equilibria.

The MHD equilibrium states of axisymmetric magnetized plasma with incompressible flows parallel to the magnetic field are governed by the generalized Grad-Shafranov equation which in dimensionless form reads [16, 17]

$$(1 - M^2)\Delta^*\Psi - \frac{1}{2}(M^2)'|\nabla\Psi|^2 + \frac{1}{2}\left(\frac{X^2}{1 - M^2}\right)' + R^2P_s' = 0 \quad (2.1)$$

along with the Bernoulli relation for the pressure

$$P = P_s(\Psi) - \rho \frac{v^2}{2} \quad (2.2)$$

Here, (z, R, φ) are normalized cylindrical coordinates. The quantities are normalized with respect to the geometric center of the configuration, as follows

$$\bar{R} = R/R_0, \quad \bar{z} = z/R_0, \quad \bar{u} = u/(B_0 R_0^2), \quad \bar{\rho} = \rho/\rho_0, \quad \bar{P} = P/(B_0^2/\mu_0), \\ \bar{B} = \bar{B}/B_0, \quad \bar{j} = \bar{j}/(B_0/(\mu_0 R_0)), \quad \bar{v} = \bar{v}/v_{A0}, \quad v_{A0} = B_0/\sqrt{\mu_0 \rho_0}.$$

and, for simplicity the tilde was dropped. z corresponds to the axis of symmetry; the function $\Psi(R, z)$ labels the magnetic surfaces; $M(\Psi)$ is the Mach function of the poloidal velocity with respect to the poloidal-magnetic-field Alfvén velocity; $X(\Psi)$ relates to the toroidal magnetic field; for vanishing flow the surface function $P_s(\Psi)$ coincides with the pressure; v is the modulus of the parallel velocity ($v^2 = M^2 B^2$); $\Delta^* = R^2 \nabla \cdot (\nabla/R^2)$, and the prime denotes a derivative with respect to Ψ . Eq. (2.1) can be simplified by the transformation

$$u(\Psi) = \int_0^\Psi [1 - M^2(g)]^{1/2} dg, \quad (2.3)$$

which reduces (2.1) to

$$\Delta^* u + \frac{1}{2} \frac{d}{du} \left(\frac{X^2}{1 - M^2} \right) + R^2 \frac{dP_s}{du} = 0 \quad (2.4)$$

Note that (2.4) is free of a quadratic term as $|\text{grad}u|^2$ is identical in form with the (quasistatic) Grad-Shafranov equation. Thus, for each choice of the free surface functions $X^2/(1 - M^2)$ and P_s , (2.4) is fully determined and can be solved when the boundary condition for u is given. Note that any solution is valid for arbitrary Mach functions $M(u)$ and densities $\rho(u)$. The transformation (2.3) does not affect the magnetic surfaces, it just relabels them. Also, once a solution of (2.4) is found, the equilibrium can be completely constructed in the u -space; in particular, the magnetic field, velocity, current density, and pressure can be determined by::

$$\vec{B} = \frac{X}{1 - M^2} \nabla \phi + \frac{1}{\sqrt{1 - M^2}} \nabla \phi \times \nabla u, \quad (2.5) \quad \vec{v} = \frac{M}{\sqrt{\rho}} \vec{B}, \quad (M = \pm \sqrt{M^2}), \quad (2.6)$$

$$\vec{j} = \frac{1}{\sqrt{1 - M^2}} \left[\Delta^* u + \frac{1}{2(1 - M^2)} \frac{dM^2}{du} |\nabla u|^2 \right] \nabla \phi + \frac{d}{du} \left(\frac{X}{1 - M^2} \right) \nabla \phi \times \nabla u \quad (2.7)$$

$$P = P_s(u) - \frac{1}{2} M^2 B^2. \quad (2.8)$$

The condition states that a general steady state of a plasma of constant density and incompressible flow parallel to \mathbf{B} is linearly stable to small three-dimensional perturbations if the flow is sub-Alfvénic ($M^2 < 1$) and $A \geq 0$ [17]. With \mathbf{B} and \mathbf{j} given by (2.5) and (2.7), in the u -space for axisymmetric equilibria, A assumes the form

$$\begin{aligned} A &= A_1 + A_2 + A_3 + A_4, \quad A_1 = -(\vec{j} \times \nabla u)^2, \\ A_2 &= (\vec{j} \times \nabla u) \cdot (\nabla u \cdot \nabla) \vec{B}, \quad A_3 = -\frac{1}{2} \frac{dM^2}{du} (1 - M^2)^{-1} |\nabla u|^2 \nabla u \cdot \frac{\nabla B^2}{2}, \\ A_4 &= -\frac{1}{2} \frac{dM^2}{du} (1 - M^2)^{-3/2} |\nabla u|^4 g, \quad g = (1 - M^2)^{-1/2} \left(\frac{dP_s}{du} - \frac{dM^2}{du} \frac{B^2}{2} \right), \end{aligned} \quad (2.9)$$

Conclusions and general perspectives

1. On the basis of the derived analytic solution, the construction of configurations with a lower x -point and complementary ITER confinement figures of merit is under way (in a similar way with the solution of static equilibrium in diverted tokamak configurations) in accordance with the planned objectives. The conjecture that equilibrium nonlinearity may activate flow

stabilization will be further examined in connection with possible stabilizing effects of flow for ITER-like equilibria.

2. Even if analytical solutions can be found for linear Grad-Shafranov equations only (i.e., for parabolic plasma current density distributions), such type of results are useful for both, finding new aspects and benchmark for numerical codes.

Acknowledgement

The reported work includes contributions from the following people outside the EUATOM-MEdC Association: S. Günter, K. Lackner, E. Strumberger, P. Merkel and D. Koster (Max-Planck-Institut für Plasmaphysik EURATOM Association, Garching, Germany), D. Kalupin (EFDA-CSU, Garching, Germany) and G.N. Throumoulopoulos (Association EURATOM-Hellenic Republic, University of Ioannina, Greece).

References

- [1] R. Fitzpatrick, *Phys. Plasmas* **9**, 3459 (2002).
- [2] C.V. Atanasiu, I.G. Miron, "*An analytical model for resistive wall modes stabilization*", 11th European Fusion Theory Conference, 26-28 September 2005, Aix-en-Provence, France.
- [3] C.V. Atanasiu, I.G. Miron, "*A model for resistive wall mode control*", EPS30 (P5.157), Rome, Italy, 19-23 June 2006.
- [4] J.M. Finn, *Phys. Plasmas* **2**, 198 (1995).
- [5] C. G. Gimblett, R. J. Hastie, *Phys. Plasmas*, **7**, 258 (2000).
- [6] C. J. Ham, C. G. Gimblett, R. J. Hastie, *Plasma Phys. Control. Fusion*, **51**, 115010 (2009).
- [7] C. V. Atanasiu, S. Günter, K. Lackner, A. Moraru, L. E. Zakharov, A. A. Subbotin, *Phys. Plasmas* **11**, 5580 (2004).
- [8] F. Porcelli, *Phys. Fluids* **30**, 1734 (1987).
- [9] A. Bondeson, H.X. Xie, *Phys. Fluids* **B1**, 2081 (1989).
- [10] J.A. Wesson, *Tokamaks*, (Oxford University Press, Oxford, UK, 2004).
- [11] Y.Q. Liu, M.S. Chu, Y. In, M. Okabayashi, *Phys. Plasmas* **17**, 072510 (2010).
- [12] W.A. Newcomb, *Ann. Phys.* **10**, 232 (1960).
- [13] C.V. Atanasiu, A. Moraru, L.E. Zakharov, "*Influence of a nonuniform resistive wall on the external kink modes in a tokamak*", ITM General Meeting, 13-15 September 2010, Lisbon, Portugal
- [14] M.S. Chu, M. Okabayashi, *Plasma Phys. Control. Fusion*, **52**, 123001 (2010).
- [15] C. V. Atanasiu, S. Günter, K. Lackner, I.G. Miron, *Phys. Plasmas* **11**, 3510 (2004).
- [16] H. Tasso, G. N. Throumoulopoulos, *Phys. Plasmas* **5**, 2378 (1998).
- [17] G. N. Throumoulopoulos, H. Tasso, *Phys. Plasmas* **14**, 122104 (2007).
- [18] G. N. Throumoulopoulos, H. Tasso, G. Poulipoulis, *J. Phys. A: Math. Theor.* **42**, 335501 (2009).
- [19] G. N. Throumoulopoulos, H. Tasso, *Phys. Plasmas* **17**, 122104 (2010).

*ANOMALOUS TRANSPORT IN PLASMA: ROLE OF COLLISIONS,
TURBULENCE AND WAVE-PLASMA INTERACTION IN TRANSPORT.
APPLICATION TO ITER*

I.N. Pometescu, G. Steinbrecher

Universitatea din Craiova, Facultatea de Fizica, Craiova

Overview

The main research topics for this year have been organized in the following milestones with theoretical and experimental relevance:

1. Study of the turbulent structures and intermittency by stochastic differential equations
2. Stochastic reduced models of different plasma regimes and description of the transition in term of global parameters
3. Numerical experiments with low dimensional kinetic models of the impurity transport
4. Development of an advanced 3D ion Fokker-Planck solver for ions.
5. Impact of central electron heating on both electron and ion temperatures, and on particle and impurity densities.

In the first topic, the previously elaborated methods for study the linear stochastic differential equations with parametric noise was applied to the study of the stochastic stability of the linearized Hasegawa-Mima equations. Instability thresholds depending on the wave vector were established and studied.

In the second topic the possibility to explain at least qualitatively the simultaneous occurrence of intermittency in the L-H transitions was studied. A new class of stochastic models was proposed and its singularity structure was explored.

In the third topic the test particle transport was studied by using the statistical properties of the random electric field extracted from numerical simulations. New data processing method was elaborated.

In the fourth topic new stochastic integration methods were elaborated, for the numerical simulation of the radio frequency heating by ion cyclotron resonance, by accelerated orbit-following Monte-Carlo method.

In the fifth topic was elaborate a model to evaluate the diffusion coefficient of electrons at random transition between two temperature profiles in magnetized plasma due to electron heating. Also, in the same topic, the influence of the radio-frequency heating on the impurities transport was studied through comparative analysis of two discharges in JET.

Publications

- [1] G. Steinbrecher, X. Garbet, B. Weyssow, *Large time behaviour in random multiplicative processes*, ArXiv: 1007.0952v1 [math. PR], (2010).
- [2] G. Steinbrecher, B. Weyssow, *New representation and generation algorithm for fractional Brownian motion*, Roumanian Journal of Physics, 55,1120-1130, (2010).
- [3] N. Pometescu, B. Weyssow, “4th International Workshop & Summer School on Plasma Physics”, July 5-10, 2010, Kiten, Bulgaria
- [4] N. Pometescu, *Power density absorption profile in tokamak plasma with ICRH*, Rom. Journ. Phys., Vol. 55, Nos. 9-10, P. 1041-1048, Bucharest, 2010
- [5] N. Pometescu, *Diffusion coefficient and convective velocity profiles of Ni-impurity in JET plasmas with ICRH*, poster session at “Theory of Fusion Plasmas, Joint Varenna-Lausanne International Workshop”, Varenna, Italy, August 30 – September 3, 2010 ; *J. Phys.: Conf. Ser.* 260 , 012016

Detailed results

1 Statistical properties of edge turbulent transport. Turbulent structures and intermittency.

Study of the turbulent structures and intermittency by stochastic differential equations

Methods

In the previous works from Refs. [1, 2, 3] a new methodology for the study of the noise –driven intermittency was elaborated. In the Ref. [1], for the study of the intermittent events in the plasma boundary, by using the mathematical results from the ref. [4], the class of the reduced models studied in the refs. [5, 6] were generalized adapted. Explicit results were obtained in the study of the wave destabilization in Ref. [1]. The methods from Refs [1-6], for the study of the stability under parametric stochastic perturbations of the physical systems described by non - linear differential equations, was used in the study of the equations of the density gradient drift waves. The problem studied was the stability under parametric random perturbations of the drift waves. In the Hasegawa-Mima model of the density gradient drift waves, a random term was added to the constant driving density gradient. The random density gradient term was modelled by a spatial and temporal white noise. The physical origin of this stochastic fluctuation of the density gradient is related to the turbulence that originates from the plasma core. As a result a system of classical stochastic differential equation of the Ito type was obtained.

Results

By the methods from Refs [1-3] from these stochastic evolution equations a set of deterministic linear differential equations were obtained for fixed time spatial correlation function of the electrostatic potential. The results are the following: In analogy to the stochastic Klein-Gordon equation, also in the framework of stochastic Hasegawa-Mima equation there exists a threshold for the noise intensity, depending on the wave vector, for the random density fluctuation

intensity, such that the modes with non-zero wave vector remains stable below this threshold. This threshold decreases with $|k|$. The mode with $k=0$ is always destabilized by arbitrary weak perturbation. This stability pattern is a candidate for the explanation of the long-range spatial correlations of the electric field.

Conclusions

Linearized stochastic model for the turbulent structures in the edge plasma was elaborated. The study of the models of the edge plasma turbulence is important in the elaboration of a strategy of the large-scale numerical simulations.

2. Statistical properties of edge turbulent transport. Physics of L-H transition

Stochastic reduced models of different plasma regimes and description of the transition in term of global parameters

Methods

New class of reduced stochastic models for the simulation of transitions in stochastic dynamical systems, transitions that can be identified with L-H transitions, was elaborated. The main part of the model consists of a noise driven stochastic model, whose aspects were studied in the Refs. [3, 5, 6]. The main aspect in this class of models is related to the fact that the mean values of the moments of the output of random dynamical system (or, in functional analytic terms, the L_p norms [6]) depends in a very sensitive way on the intensity of the driving multiplicative noise as well as on its correlation times.

Results

The heavy tail exponent of the models is related to that exponent p of the L_p spaces whose norm is finite. An important parameter of the model is the critical exponent p_{crit} , that is identical to the heavy tail exponent of the model. The analytic dependence on the parameters of the model was derived. The L-H transition take place exactly when the critical exponent crosses the value $p_{\text{crit}} = 1$, that is related to the occurrence of the exotic Banach spaces [6]. The $p_{\text{crit}} > 1$ corresponds to the L mode and the $p_{\text{crit}} < 1$ to the H mode. Observe that in the $p_{\text{crit}} < 1$ case the model exhibits also an increased intermittency. In this case the hysteresis is related to generation of driving multiplicative noise, produced by the complex fractal structure, stickiness of the magnetic island chains. This class of models is a stochastic generalization of the models from refs. [7, 8]. Numerical method for generation of the noise with long-range correlations was elaborated [9].

Conclusions

Reduced model of the L-H transitions based on new aspects of the random processes was elaborated. The role of the exotic Banach spaces in stochastic models was studied. These models are useful in the optimal choice of the input parameters in the numerical simulation of the large tokamaks.

3. Particle and impurity transport in standard and advanced tokamak scenarios

Numerical experiments with low dimensional kinetic models of the impurity transport

Methods

In the previous stages, the statistical properties of the electrostatic field, generated with the low dimensional kinetic codes, were studied. C++ code was written that generate random electric field, by using results from Refs. [5, 6, 9]. The particle transport induced by a random electrostatic field, generated by this algorithm, with prescribed statistical properties, extracted from numerical first principle low dimensional gyrokinetic simulations, was studied by numerical methods. Models, where long range temporal correlations are simplified to frozen turbulence, were studied by the methods of ergodic theory in ref. [10].

Results

The statistical post processing of the results of the particle transport simulations was performed by a new class of stable numerical processing method, elaborated on the basis of the results from ref. [11]. In the framework of this new class of numerical filtering methods, it is possible to extract information on the whole spectrum of anomalous diffusion exponents, when the mean square displacement of the random test particle is represented as

$$\left\langle |\mathbf{R}_\omega(t)|^2 \right\rangle_\omega = \int_0^2 t^\alpha d\rho(\alpha) \quad ,$$

where $d\rho(\alpha)$ is a probability measure and the averaging is performed over an ensemble of random trajectories. In the work [5] we proved that in the cases when we have no apriori information, the reconstruction of the spectrum of all of the diffusion exponents, given by the nonnegative measure, is an ill posed, unstable problem. The results of this analysis on simulated data show that the spectrum is continuous. The spectrum of the exponents, specified by the measure $d\rho(\alpha)$ was studied. The dependence of on the test particle mass was studied. In the frozen turbulence limit exact results were derived.

Conclusions

New class of statistical post processing method for the study of the anomalous particle transport were elaborated. The study of simplified models of the particle transport is important in the optimisation of the large tokamaks, in the study of the exhaust of helium.

4. Simulation of ICRF heating

Development of an advanced 3D ion Fokker-Planck solver for ions.

The stochastic differential equation (SDE) used for Monte-Carlo (MC) solution of the Fokker-Planck equation that models the RF interaction in an ideal axial symmetric tokamak configuration be reduced to the particular form [12-14]: $dx = \sigma(x)\sigma'(x)dt + \sigma(x)d\omega(t)$ where $\sigma(x)^2/2 = D(x) = \text{diffusion coefficient}$; Up to a constant, $x(t)$ is the magnetic momentum and $d\omega(t)$ is a standard Brownian motion. The first, main problems are related to the singularity of

derivative of $\sigma(x)$ near $x=0$, according to the analysis from [14]. The second question is the possibility to elaborate a special class stochastic Runge-Kutta method that solves the above equation without computing numerically the derivative, as well as exact preservation of the conservation laws.

Methods

These problems were solved in the following manner. First, the non-smooth character of the terms of the Eq. (1) near $x=0$ was solved by approximating the diffusion coefficient in this range by a local approximation and by the elaboration of an exact solution to this approximate equation near singularity. By using exact solution of the local linear approximation of $\sigma(x)$ in the domains far away the singularity, the problem of avoiding the direct computation of the derivative was solved. Convergence results from the work [15] were used for the foundation of our algorithm. The use of the exact solution to the approximate equation solved also the problem of the preservation of the conservation laws, encoded in the specific form of Eq. (1).

Results

In this stage several combinations of versions of integrators were elaborated in the form of FORTRAN 90 code, tested on soluble simplified models on the Gateway and were uploaded to the GFORGE. In the domains far away the singularity two adaptive methods were elaborated. In the domain near the singularity three methods were elaborated and tested. We also elaborated and tested optimised subroutines for random number generators, by using results from Ref. [16].

Conclusions

Efficient numerical integration method for the study of the ICRH, that accelerates the numerical integration in the cold plasma regime was elaborated and tested. Further optimisations will be related to programming.

5. Impact of central electron heating on both electron and ion temperatures, and on particle and impurity densities.

5a: Diffusion coefficient of electrons at random transition between two temperature profiles in magnetized plasma due to electron heating.

Methods

Using Langevin equations for the guiding center motion of the charged particles on analyze the transport along and perpendicular to the main magnetic field. The model includes collisions and therefore a thermal velocity which we relate to the plasma temperature evolution through a stochastic process and a magnetic field represented as another stochastic process which is independent of the thermal velocity [17].

Results

The combined effect of collisions and magnetic fluctuation in the zero order guiding centre approximation leads to particle sub-diffusion in the perpendicular direction. We look for effects given by transition between the two temperature states and the radial variation of the running diffusion coefficients is analyzed for transition between the two temperature profiles, with a difference between the two temperatures, according to experiment, about 1 keV. The analytic expression obtained for the running diffusion coefficient revealed that the running diffusion coefficient is less sensible to the difference between the two temperatures in the central region than the difference between temperatures in the plasma edge region.

Conclusions

These characteristics are in agreement with experimental observation. For example, in pellet fuelling of Ohmic and Lower Hybrid - driven discharges in Tore Supra [18], the experimental results show for electrons in the central region a temporal evolution of the central electron temperature oscillating between Ohmic discharge temperature and the discharge with Lower Hybrid power induced temperature.

5b. Study of the dispersion equation for multi-species plasma with ITG turbulence in the presence of the radio-frequency heating

Methods

The influence of the radio-frequency heating on the impurities transport was studied through comparative analysis of two discharges in JET: the reference discharge #69808 without RF power and discharge #68383 with the maximum ICRF power of 8.3 MW applied to electrons in Hydrogen Minority Heating scheme. The theoretical model is contained in equation for the impurity density perturbation due to ITG/TE modes in plasmas with radio-frequency heating, obtained in [19] by using multi-fluid Weiland model with trace impurity approximation.

Results and discussion

To find the eigenfrequency modes for ITG instability is a difficult task in general case because of complexity of the dispersion equation. The simplification adopted was to neglect the contribution from trapped electrons, that restrict the study to the inner region of plasma ($0 < r/a < 0.6$). Also, the ion (Hydrogen) temperature profile was assumed the same with Ni-impurity temperature profile. From the dispersion equation result in this case four eigenvalues. For the most unstable mode were evaluated the diffusivity, convective velocity and normalized impurity density peaking factor for Ni-impurity. The growth rate of this eigenmode and the diffusivity of Ni-impurity in the presence of RF heating becomes smaller than in the case without RF heating. The presence of RF heating reduce nearly to zero the magnitude of the convective velocity in the region with $0 < r/a < 0.3$. Hence, in the central region of the plasma the transport due to ITG instability is practically suppressed. But for $r/a > 0.4$ the convective velocity is greater than diffusivity. The density peaking factor in the shot with RF heating is almost two times greater than the density peaking factor in the shot without RF heating [10, 20, 21].

Conclusion

The study of influence of the radio-frequency heating on the impurities transport was done by neglecting the trapped electrons. The work will continue by taking into account the effects of trapped electrons. Also, the conclusions are based here on the multi-fluid model with trace impurity approximation. Application of other theoretical model and comparative study is scheduled.

Acknowledgement

The reported work includes contributions from the following people outside the EURATOM-MEdC Association: Xavier Garbet, CEA-Cadarache, Boris Weyssow, ULB, Remy Dumont, CEA-Cadarache.

References

- [1] G. Steinbrecher, X. Garbet, International Workshop on “Hamiltonian Approaches to ITER Physics”, CIRM, Marseille, 2-6 November 2009.
- [2] V. N. Kuzovkov, W. von Niessen, *Physica A* 369 (2006) 251-265.
- [3] X. Garbet, G. Steinbrecher, Solvay Workshop - A Tribute to Radu Balescu, Brussels, 6-8 March 2008.
- [4] Steinbrecher, W. T. Shaw, *European Journal of Applied Mathematics*, 19, 87, (2008).
- [5] Steinbrecher G, Weyssow B, *Physical Review Letters* 92, 125003 (2004).
- [6] G. Steinbrecher, X. Garbet. B. Weyssow, arXiv:1007.0952v1 [math.PR], (2010)
- [7] D. A. Gates et al, *Nucl. Fusion* 37, (1997), 1593-1606.
- [8] R. J. Buttery et al, *Nucl. Fusion* 43, (2003) 69-83.
- [9] G. Steinbrecher, B. Weyssow, *Roumanian Journal of Physics*, 55, 1120-1130, (2010).
- [10] G Steinbrecher and N Pometescu, Association Day, Iasi, July 2, 2010
- [11] G. Steinbrecher, R. Scorei, V. Cimpoiasu, I. Petrisor, *Journal of Magnetic Resonance*, 146, 321-334 (2000).
- [12] L.-G. Ericsson, M. Schneider, *Physics of Plasmas* 12, 072524, (2005).
- [13] Q. Muhtar, T. Hellsten, T. Johnsson, *IEEE Transactions on Plasma Science* 38, 2185-2189 (2010).
- [14] G. Steinbrecher, R. J. Dumont, ITM General Meeting 2010, Lisbon
- [15] Omid S. Fard, *International Journal of Computational and Applied Mathematics*, 2, 101-113 (2007).
- [16] L. Devroye, *Non-Uniform Random variate Generation*, Springer, 1986.
- [17] N. Pometescu, B. Weyssow, “4th International Workshop & Summer School on Plasma Physics”, July 5-10, 2010, Kiten, Bulgaria
- [18] A Geraud, J Bucalossi et al., *Journal of Nuclear Materials* 337-339, (2005) 485-489
- [19] H Nordman, R Singh, T Fülöp, L-G Eriksson and all, *Phys. Plasmas* 15, 042316 (2008)
- [20] N. Pometescu, *Rom. Journ. Phys.*, Vol. 55, Nos. 9-10, P. 1041-1048, Bucharest, 2010
- [21] N. Pometescu, “Theory of Fusion Plasmas, Joint Varenna-Lausanne International Workshop”, Varenna, Italy, August 30 – September 3, 2010 ; *J. Phys.: Conf. Ser.* 260 , 012016.

ANOMALOUS TRANSPORT IN PLASMA. STOCHASTIC PROCESSES AND TRANSPORT IN TURBULENT PLASMA

M. Negrea, I. Petrisor, D. Constantinescu
University of Craiova

Overview

The main research topics for this year have been organized in three milestones with theoretical and experimental relevance:

1. Simulations of MHD turbulence (TG-T, ULB). Study of turbulent zonal flow including test particle and field line transport. Stochastic magnetic field line diffusion and particle diffusion in MHD.
2. Study of anomalous transport (TG-T, WP10-TRA-05-03, ULB, Association Euratom-Hellenic Republic). Stochastic modelling with application to the edge turbulent transport. Calculus of the diffusion coefficients for test particles in the edge region of tokamak plasma using the decorrelation trajectory method and numerical simulation. Study of the fractional diffusion equation with a coupling between position and momentum space; methods to solve this equation analytically and/or numerically in order to study the radial transport.
3. Studies of the sawtooth oscillations based on the relaxation oscillation theory and on mapping models (TG-T, WP10-TRA-05-03, Association Euratom-France, Association Euratom-University of Latvia, Euratom-Association, D-85748 Garching, Germany).

The test particle diffusion in an electromagnetic stochastic field was studied in the framework of the decorrelation trajectory method (DCT) and using the numerical method [1, 2, 4, 7]. The comparison of the results obtained by these two methods might then allow us to confirm the DCT approach results. These results are important for “Validation of physics-based transport models” and “Plasma edge characterization and modelling”, objectives for ITER.

We have also studied some features of the anomalous transport using mathematical models which involve the fractional calculus: the effect of the electric field, which could be responsible for the anomalous diffusion, was introduced (through a fractional Riesz derivative, which incorporates in the model non-local spatial effects) in the transport model in position and velocity space. Various features of the anomalous transport (Levy flights in space and in velocity, existence of up-hill and down-hill transport), which are not exhibited by the classical transport theory, were pointed out through numerical simulations. Our analysis proves that the fractional transport models could be an interesting alternative for explaining some characteristics of some transport phenomena experimentally observed in tokamaks.

In order to point out some mechanisms susceptible to govern the sawtooth oscillations in tokamaks we considered two different approaches: a discrete model (based on the Hamiltonian

description and the mapping technique) was used in order to reconstruct the evolution of the magnetic field during the saw tooth instability and a low-dimensional continuous model was used for the description of quasi-periodic plasma perturbations.

The pure magnetic approach (the discrete model), based on the theoretical analysis on the onset of the (1,1) internal MHD mode into the nonlinear regime, justifies the use of the magnetic stochasticity hypothesis in order to explain the sawtooth crash and analyses the complete and incomplete nature of the reconnection in two magnetic configurations specific to Tore-Supra and ASDEX-Upgrade [3,5].

The low-dimensional continuous model describes the evolution of the displacement of the magnetic field lines and of the pressure gradient during some periodic nonlinear perturbations of the plasma (sawteeth, ELMs, FIR-NTMs, etc.). It depends on three parameters: the normalized power input into the system, the dissipation, the ratio of the normal heat diffusion and the heat diffusion due to perturbations. In the present study we analyzed the bifurcations that appear in the parameters' space. It was proved that, in spite of its simple nature, our model points out various leads to numerous predictions which agree well with experimental behavior of ELMs [6].

Publications

- [1] C.C. Lalescu, D. Carati, M. Negrea, I. Petrisor, *Virtual particle transport in turbulent MHD Kolmogorov flow*, to be presented to the Conference "Particles in turbulence", 16-18 March 2011, Potsdam (Germany).
- [2] M. Negrea, I. Petrisor, Dana Constantinescu, *Aspects of the diffusion of electrons and ions in tokamak plasma*, Rom. Journ. Phys., Vol. 55, Nos. 9–10, P. 1013-1024, Bucharest, 2010.
- [3] D. Constantinescu, M. Negrea, I. Petrisor, *The study of the sawtooth oscillations in tokamaks using mapping models*, Rom. Journ. Phys., Vol. 55, Nos. 9–10, P. 951–960, Bucharest, 2010.
- [4] M. Negrea, I. Petrisor, H. Isliker, A. Vogiannou, L. Vlahos, Dana Constantinescu, C. C. Lalescu, *On the diffusion of impurities in tokamak plasma*, submitted to Rom. Journ. Phys.
- [5] D. Constantinescu, Marie-Christine Firpo, M. Negrea, I. Petrisor, C. C. Lalescu, *Study of the magnetic reconnection during the sawtooth instability*, submitted to Rom. Journ. Phys.
- [6] D. Constantinescu, O. Dumbrajs, V. Igochine, K. Lackner, R. Meyer-Spasche, H. Zohm and ASDEX Upgrade team, *A low-dimensional model system for quasi-periodic plasma perturbations* submitted to Physics of Plasmas.
- [7] M. Negrea, I. Petrisor, H. Isliker, A. Vogiannou, L. Vlahos and B. Weyssow, *Ion and impurity transport in turbulent, anisotropic magnetic fields*, submitted to Plasma Physics and Controlled Fusion.

Detailed results

- 1. Simulations of MHD turbulence (TG-T, ULB). Study of turbulent zonal flow including test particle and field line transport. Stochastic magnetic field line diffusion and particle diffusion in MHD.**

The work is related to building of the electromagnetic fluctuations, and both the electric and the magnetic fields are obtained through the numerical resolution of the MHD equations derived from first principles. In order to obtain the diffusion coefficients we used the specific incompressible MHD equations for the Kolmogorov flow. The Kolmogorov force, which is usually oriented on the x-direction, depends on the y-coordinate: $\mathbf{f} = (A_f \sin(k_f y), 0, 0)$. The MHD velocity and the magnetic fields are taken to be divergence free. We have started to study simultaneously the first order guiding centre equation and the Lorentz force system specific to ions impurities, $\alpha (\mathbf{e} + \mathbf{v} \times \mathbf{b})$. A friction force, $\chi (\mathbf{u} - \mathbf{v})$ depending on the difference between the test particle velocity and the MHD velocity, which mimics the collisions between the tracers and the velocity MHD field, was taken into account. We have made some longer MHD Kolmogorov flow simulations with Kolmogorov parameters $A_f = 1$, $k_f = 1$ and different values of the z-component of the average homogeneous magnetic field b_{0z} . For a preliminary test, in order to study the particle behaviour, the simulation with a magnetic field on the toroidal axis $b_{0z} = 0.9$ was chosen. The Reynolds number is considered about 250 and the following five different cases for the particles are analyzed: Three different types of “charged particles” given by the coefficients (α, χ) , i.e.: $(\alpha, \chi) = \{(2, 1), (2, 10), (2, 100)\}$. Two types of first guiding centre approximation with $v_{\text{parallel}} = \{1, 10\}$.

For specific parameters that impose the relative velocity we have obtained the mean square displacements in realistic cases specific to ITER, the average kinetic energy for the fluid (averaged over the periodic box) and the average kinetic energy for the three types of charged particles. One first observation is that the transport along the y direction can be super-diffusive for the physical particles. As expected, because there is an external magnetic field along the z axis, both guiding centre approximations and magnetic field lines show ballistic/super-diffusive regimes on this direction. It is also expected that for very large numbers of particles, and large enough χ the average kinetic energy of the test particles will match that of the fluid. More particles and longer integration times are needed for a better conclusion. The work, which is in progress, has been done in collaboration with Dr. D. Carati and Dr. C. Lalescu from ULB.

2. Study of anomalous transport (TG-T, WP10-TRA-05-03, ULB, Association of Hellenic Republic). Stochastic modelling with application to the edge turbulent transport. Calculus of the diffusion coefficients for test particles in the edge region of tokamak plasma using the decorrelation trajectory method and numerical simulation.

We analyzed the influence of the magnetic Kubo number, the drift Kubo number and the stochastic anisotropy on the diffusion of ions when the stochastic magnetic drifts are taken into account. We have shown that the stochastic drifts provide a decorrelation mechanism of the particles from the magnetic lines. A subdiffusive behaviour of the particle mean square displacement is not possible and the particles diffuse even in the absence of the perpendicular collisional diffusion.

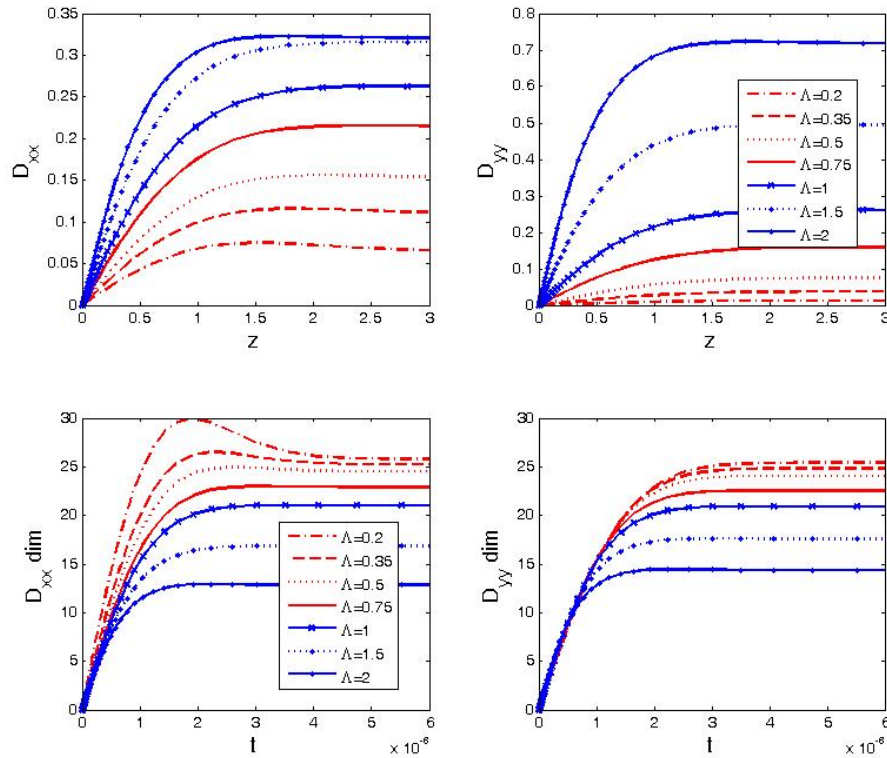


Figure 1. DCT running diffusion coefficients for Be^{4+} for different values of the anisotropy parameter and for $K_m=0.5$, $K_{dr}=0.2$; the two plots on top represent the dimensionless coefficients and the two plots on bottom the dimensional ones.

We have obtained deterministic decorrelation trajectories for fixed values of the magnetic Kubo number K_m and the drift Kubo number K_{dr} and different values of the anisotropy parameter Λ in order to see their influence on the shape of the trajectory. An increased value of the anisotropy parameter leads to oscillations around the starting point in a given subensemble. The trapping effect is more pronounced, the larger Λ and K_m are. As an application, we considered impurities in ITER-like conditions, i.e. we assumed an ion temperature $T_i = 8.1$ KeV and a background magnetic field $B_0 = 5.3$ T. The ions we considered are He^{2+} and the impurities Be^{4+} , Ne^{10+} and W^{74+} , as they are relevant for tokamak devices of the ITER type. In parallel to the DCT method, we numerically generated stochastic magnetic field environments and tracked the impurities with test-particle simulations. The resulting diffusion coefficients are presented and compared with those obtained by the DCT method. We intend to analyze in a future paper using toroidal geometry and the Lorentz force, the transport coefficients and to compare them with those from the present study.

3. Study of the fractional diffusion equation with a coupling between position and momentum space; methods to solve this equation analytically and/or numerically in order to study the radial transport.

The transport models in position and velocity space were formulated in terms of the probability for a particle to be situated in the position “x” and to have the velocity “v” at the moment “t”. The velocity was introduced in the transport models in order to incorporate the

strong background magnetic field (through the usual Vlasov equation), to include the collisions (which modify mainly the speed of the particles, so we introduce a diffusion term) and the effect of the electric field which could be responsible for the anomalous diffusion (through a fractional Riesz derivative).

We obtained the analytical form for the solutions of the fractional transport equation with constant coefficients (which is efficient only in some particular cases, due to its extremely complicated form) and we provided an algorithm for obtaining the numerical solution. The code can be applied for symmetric and asymmetric Riesz derivatives of any order (for physically relevant models the order is between 0 and 2). The results obtained using this code are in agreement with the analytical ones.

The influence of the parameters involved in equations, mainly of the order of the fractional derivatives, was systematically studied in the fractional transport model without collisions, including fractional α -Riesz derivative in space and δ -Riesz derivative in velocity. It was shown that the solution exhibits Levy flights of order α in space and of order δ in velocity, so the transport is anomalous both in space and velocity. In the fractional diffusion model we studied the influence of the symmetry/asymmetry of the Riesz derivative. We observed that pulse initial conditions exhibit a ballistic drift to the right or to the left (depending on the asymmetry of the derivative) reminiscent of the rapid propagation phenomena in perturbative plasma experiments.

4. Studies of the sawtooth oscillations based on the relaxation oscillation theory and on mapping models.

In order to analyse the evolution of the pressure gradient displacement and of the magnetic field lines during some periodic nonlinear perturbations of the plasma (sawteeth, ELMs, FIR-NTMs, etc.) we proposed minimal possible model based on two equations for: the first being responsible for the relaxation dynamics and the second for the drive [8]. It presents the interplay of drive and relaxation dynamics, which represent “typical” situations in fusion plasma when the slow profile dynamics can lead to fast instabilities after a certain threshold of the profile gradient is archived and, at the same time, instabilities relax profile gradients. The model contains two equations: the first being responsible for the instability dynamics (MHD force balance) and the second for the energy conservation. Slight modification of the first equation makes it possible to model also the pellet injection. Three parameters are involved in the system: h = the normalized power input into the system, δ = dissipation, η = (normal heat diffusion) / (heat diffusion due to perturbations). The value of h can be estimated rather accurately from the experimentally measured gradient of the pressure profile and from several basic well known quantities. The system goes over into the ELM/sawtooth regimes only for $h > 1$ which agrees with experimental observations. The main dynamical bifurcations were analysed and various types of evolution were pointed out during the simulations.

The dynamics of such systems is rather complex, depending on the parameters' values. The main dynamical zones are presented in Figure 2, for a fixed value of h , namely $h = 1.5$. Each zone is formed by pairs of parameters (δ, η) which generate systems with different dynamical properties.

The system exhibits damped oscillations if (δ, η) is in zone I. If (δ, η) is in zone II the dynamics of the system is dominated by simple periodic oscillations, while double periodic oscillations are observed when (δ, η) is in zone III.

The chaotic dynamics is observed when (δ, η) is in zone IV because a strange attractor appears in the phase space. Periodic orbits of sawtooth type appear when (δ, η) is in zone V. We can conclude that depending on the values of (δ, η) , very different plasma behavior can be obtained for one and the same heating power.

The model can be generalized to include external perturbations, for example, the pellet injection to influence ELMs or the electron cyclotron current drive to influence sawteeth.

4. Conclusion

For specific parameters that impose the relative velocity we have obtained the mean square displacements in realistic cases specific to ITER, the average kinetic energy for the fluid (averaged over the periodic box) and the average kinetic energy for the three types of charged particles. We have shown that the stochastic drifts provide a decorrelation mechanism of the particles from the magnetic lines. A subdiffusive behaviour of the particle mean square displacement is not possible and the particles diffuse even in the absence of the perpendicular collisional diffusion. We obtained the analytical form for the solutions of the fractional transport equation with constant coefficients (which are efficient only in some particular cases, due to their extremely complicated form) and we provided an algorithm for obtaining the numerical solution. We have concluded that depending on the values of specific parameters, very different plasma behavior can be obtained for one and the same heating power. The model can be generalized to include external perturbations, for example, the pellet injection to influence ELMs or the electron cyclotron current drive to influence sawteeth.

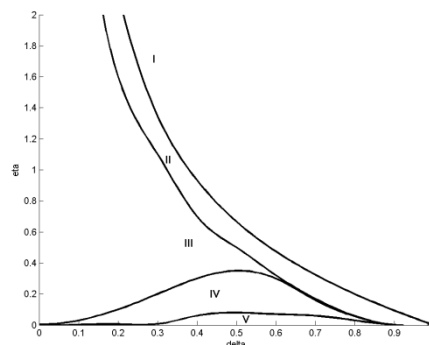


Figure 2. Dynamical zones of oscillations in the (δ, η) plane for $h = 1.5$

Acknowledgement

The reported work includes contributions from the following people outside the EURATOM-MEdC Association: Heinz Isliker, Anastasios Vogiannou, Loukas Vlahos (EURATOM - Hellenic Republic Association, Greece), Daniele Carati (EURATOM – Belgium State Association), Marie-Christine Firpo (Laboratoire de Physique et Technologie des Plasmas, Ecole Polytechnique, France), O. Dumbrajs (Association Euratom-UL Latvia), V. Igochine, K. Lackner, R. Meyer-Spasche, H. Zohm (Association Euratom-IPP, Germany).

References

- [1] M. Negrea, I. Petrisor and D. Constantinescu, *Aspects of the diffusion of electrons and ions in tokamak plasma*, 10th International Balkan Workshop on Applied Physics, Constanta 2009.
- [2] M. Negrea, I. Petrisor, B. Weyssow and H. Isliker, *Aspects related to the magnetic field lines diffusion in tokamak plasma*, invited lecture at 8th School of Fusion Physics & Technology, 6 – 11 April 2009, Volos, Greece.
- [3] M. Negrea, I. Petrisor and B. Weyssow, *Zonal Flow Generation in Weak Electrostatic Turbulence*, invited lecture at 8th School of Fusion Physics & Technology, 6 – 11 April 2009, Volos, Greece.
- [4] H. Isliker, A. Vogiannou, L. Vlahos, M. Negrea, I. Petrisor and B. Weyssow, *Test-particle simulations of ion drift in stochastic magnetic fields*, poster session at 36th EPS Conference on Plasma Physics, June 29 - July 3, 2009, Sofia, Bulgaria.
- [5] M. Negrea, I. Petrisor, D. Constantinescu, H. Isliker, A. Vogiannou and L. Vlahos, *Aspects of the Diffusion of Ions in Tokamak Plasma*, poster session at 13th European Fusion Theory Conference, October 12 -15, 2009, Riga (Latvia).
- [6] M. Negrea, I. Petrisor and D. Constantinescu, *Aspects of the Diffusion of Ions in Tokamak Plasma*, presented at International workshop on “Transport in Fusion Plasma”, University of Craiova, November 9-10, 2009.
- [7] I. Petrisor, M. Negrea and D. Constantinescu, *The zonal flow in anisotropic weak turbulence*, presented at International workshop on “Transport in Fusion Plasma”, University of Craiova, November 9-10, 2009.
- [8] D. Constantinescu, O. Dumbrajs, V. Igochine, K. Lackner, R. Meyer-Spasche, H. Zohm and ASDEX Upgrade team, *A low-dimensional model system for quasi-periodic plasma perturbations*, submitted to Physics of Plasmas.

UNDERSTANDING THE $E \times B$ DRIFT NONLINEAR EFFECTS ON TRANSPORT AND STRUCTURE GENERATION IN TURBULENT TOKAMAK PLASMAS

M. Vlad, F. Spineanu, D. Nendrea

National Institute of Laser, Plasma and Radiation Physics, Magurele

Overview

1. Zonal flow generation and particle trapping in the structure of the turbulent potential

We have shown that a strong connection between the stochastic trapping of the trajectories (eddy motion) and the evolution of the drift type turbulence exists in the strongly nonlinear regime.

Test modes on turbulent plasmas have been studied taking into account the process of ion trajectory trapping in the structure of the background potential. The case of drift turbulence was considered, and the frequency ω and the growth rate γ were determined as functions of the statistical properties of the background turbulence. The main characteristics of the evolution of the turbulence were deduced from γ and ω .

We have shown that trajectory trapping has a strong and complex influence on the evolution of the turbulence. Trapping determines the increase of potential cell and the decrease of the spectrum width, which correspond to the generation of quasi-coherent structures. The reversed effect appears later in the evolution. Ion trapping combined with the motion of the potential with the average diamagnetic velocity determines ion flows: the moving potential advects the trapped ions while the free ions move in the opposite direction. These “zonal” ion flows destroy first the large potential structures and eventually produces the damping of all drift modes. In the same time, the fluctuations of the diamagnetic velocity and the ion flows determine the growth of zonal flows modes.

Thus, in this perspective, there is no causality connection between the damping of the drift turbulence and the zonal flow modes. Both processes are produced by ion trapping in the moving potential, which determines ion flows. The drift turbulence does not saturate but has an intermittent evolution.

2. Density evolution of impurities and particles in turbulent tokamak plasmas

A new mechanism of impurity accumulation/loss was found in 2009. It is a nonlinear effect determined by the ratchet pinch velocity in toroidal geometry due to the poloidal motion of the impurity ions induced by the motion along magnetic lines and by the flows generated by the

moving potential. This poloidal motion determines a time oscillation of the peaking factor. The latter is defined as the ratio of the radial pinch velocity multiplied by plasma radius and the diffusion coefficient. The time oscillation is determined by the variation of the confining magnetic field on the magnetic surface.

The work scheduled for 2010 concern the improvement of the model and the development of a numerical code based. We have modified the model by introducing the toroidal geometry. We have developed a code for determining the macroscopic trajectories of the impurity ions, taking into account the toroidal geometry, the parallel motion and the turbulence. Impurity density is obtained from these “macroscopic” trajectory simulation by a Monte Carlo method.

Publications

- [1] M. Vlad, F. Spineanu, „*Nonlinear effects in the diffusion of charged particles in 3-dimensional stochastic magnetic fields*”, ISRSSP 2010, August 25-27, Sofia, invited paper.
- [2] M. Vlad, F. Spineanu, „*Nonlinear evolution of drift turbulence: inverse cascade, zonal flows, intermittency*”, XVth International Conference on Plasma Physics and Applications, 1-4 July, Iasi, invited paper.

Detailed results

1. Zonal flow generation and particle trapping in the structure of the turbulent potential

The aim of this work is to understand the nonlinear evolution of the drift turbulence on the basis of test modes on turbulent plasmas. A Lagrangian approach of the type of Dupree [1] is developed using the results we have obtained in the last decade on the statistics of test particle trajectories. A new understanding of important aspects of the physics of drift type turbulence in the non-linear phase is obtained. The main role in the processes of inverse cascade, zonal flows and intermittency is shown to be played by ion trapping.

1.1 Test modes on turbulent plasmas

We consider the drift instability in slab geometry with constant magnetic field. We start from the basic gyrokinetic equations for the distribution of electrons and ions. The solution for the potential in the zero Larmor radius limit is $\phi(x,z,t) = \phi_0(x - V_*t, z)$, where ϕ_0 is the initial condition and $V_* = T \partial_x [\ln(n_0)] / eB$ is the diamagnetic velocity produced by the gradient of the average density $n_0(x)$. This shows that the potential is not changed but displaced with the diamagnetic velocity. The finite Larmor radius effects combined with the non-adiabatic response of the electrons destabilizes the drift waves. The frequency ω and the growth rate γ of the modes are:

$$\omega = k_y V_{*eff}, V_{*eff} = V_* \frac{\Gamma_0}{2 - \Gamma_0}$$

$$\gamma = \frac{\sqrt{\pi} k_y^2 (V_* - V_{*eff}) V_{*eff}}{|k_z| v_{Te} (2 - \Gamma_0)}$$
(1)

where $\Gamma_0 = \exp(-b) I_0(b)$, $b = k_\perp^2 \rho_L^2 / 2$ and ρ_L is the ion Larmor radius. The wave number components are k_i , $i=x,y,z$ and $k_\perp = \sqrt{k_x^2 + k_y^2}$. These are the characteristics of the linear (universal) drift instability on quiescent plasmas.

We consider a turbulent plasma with given statistical characteristics of the stochastic potential and we study linear test modes. The growth rates and the frequencies of the test modes are determined as functions of the statistical characteristics of the background turbulence with potential $\phi(x,t)$. A wave type perturbation of the potential $\delta\phi(x,z,t) = \phi_{k\omega} \exp(ik_x x + ik_z z - i\omega t)$ is introduced. It is small ($\delta\phi \ll \phi$) and thus it has a negligible influence on particle trajectories. The solutions for the perturbations of electron and ion densities are obtained using the characteristics method as integrals along particle trajectories in the background potential of the source terms determined by the density gradient. The characteristics are the trajectories obtained by integrating the equation of motion backwards in time with the condition at time t .

The background turbulence produces two modifications in the response. One consists in the stochastic $E \times B$ drift that appears in the trajectories and the other is the fluctuation of the diamagnetic velocity due to the fluctuations of the density δn in the background turbulence. Both effects are important for ions while the response of the electrons is approximately the same as in quiescent plasma. The dispersion relation (quasi-neutrality condition) of a mode with frequency ω and wave number k is obtained and solved. The frequency and the growth rate of the test modes are both modified.

$$\omega = k_y V_{*eff}, V_{*eff} = V_* \frac{\Gamma_0 \mathfrak{S}}{2 - \Gamma_0 \mathfrak{S}} + n V_*$$

$$\gamma = \frac{\sqrt{\pi} k_y^2 (V_* - V_{*eff}) (V_{*eff} - n V_*)}{|k_z| v_{Te} (2 - \Gamma_0 \mathfrak{S})} - k_i^2 D_i \frac{2 - \Gamma_0 \mathfrak{S} n_{tr}}{2 - \Gamma_0 \mathfrak{S}}$$
(2)

where n_{tr} is the fraction of trapped ions, $n_{tr} / (1 - n_{tr})$ and the factor $\mathfrak{S} = \exp(-k_i^2 S_i^2 / 2)$ is determined by the size S_i of the quasi-coherent structures generated by trapping.

1.2 Turbulence evolution

The growth rate and the frequency of the drift modes give an image of the turbulence evolution starting from a weak initial perturbation with very broad wave number spectrum [4]. We show

that a sequence of processes appear at different stages as transitory effects and that the drift turbulence has an oscillatory (intermittent) evolution.

1.2.1. Ion diffusion and damping of large k modes

The development of the turbulence (mode superposition) at very small amplitude determines ion diffusion that is reflected in the second term of the growth rate (2). This is the well known result of Dupree [1] which shows that a stabilizing contribution is produced by the ion diffusion in the background turbulence, which leads to the damping of the large k modes. Here there this term is modified due to ion trapping, by the factors \mathfrak{I}, n_{tr} , which are not negligible in the strong turbulence domain but they do not change the nature of this process.

1.2.2. Trajectory structures and large scale correlations (inverse cascade)

The increase of the turbulence amplitude V above V_{*eff} determines ion trapping or eddying. As we have shown, this strongly influences the statistics of trajectories [2]. The distribution of the trajectories is not more Gaussian due to trapped trajectories that form quasi-coherent structures. A narrow peak and long tails appear in the distribution of the displacements. The peak, which remains unchanged as time increases, corresponds to the quasi-coherent structures. Its width measures the average size of the structures, S_i . The latter increases with the increase of the turbulence amplitude. At this stage the trapping is weak in the sense that the fraction of trapped trajectories $n_{tr} \ll 1$ and n can be neglected in the result of the dispersion equation (2). The effects of trapping appear through the factor \mathfrak{I} produced by the quasi-coherent structures. This process leads to the modification of the effective diamagnetic velocity while the growth rate equation is not modified. The decrease of the effective diamagnetic velocity produces the displacement of the position of the maximum of γ toward small k , of the order $1/S_i$. The size of the unstable k range decreases and the maximum growth rate decreases.

Thus, ion trapping determines the increase of the correlation length of the potential and the decrease of the average frequency. Turbulence evolution becomes slower and leads to ordered states (narrower spectra with maximum at smaller k).

1.2.3. Ion flows and turbulence damping

The evolution of the potential determines the increase of the fraction n of trapped ions. This produces another effect on the test modes. The motion of the potential with the average diamagnetic velocity V_{*eff} determines an average flux of the trapped particles $n_{tr} V_{*eff}$. As the $E \times B$ drift has zero divergence, the probability of the Lagrangian velocity is time invariant, i. e. it is the same with the probability of the Eulerian velocity. The average Eulerian velocity is zero and thus the flux of the trapped ions that move with the potential has to be compensated by a flux of the free particles. These particles have an average motion in the opposite direction with a velocity V_{fr} such that $n_{tr} V_{*eff} + n_{fr} V_{fr} = 0$. The velocity on structures method that we have recently developed shows that the probability of the displacements splits in two components

that move in opposite direction. Thus, opposite (zonal) ion flows are generated by the moving potential in the presence of trapping. They modify both the effective diamagnetic velocity and the growth rate through the terms dependent on n . As seen in Eq. [2], n determines the decrease of the maximum of γ . The effective diamagnetic velocity increases for all values of k and becomes larger than V_* first for small k . This determines the damping of these modes. As n increases modes with larger k are damped and, for $n=1$ all the modes are damped.

1.2.4. Generation of zonal flow modes

The fluctuations of the density produced by the background turbulence determine an additional term in the growth rate. This term is essentially a tensor $R_{ij}k_i k_j$ with a more complicated expression that was not included in Eq. (2). The component R_{11} is very interesting because it generates modes with $k_2=0$ and $\omega=0$. These are static oscillations in the direction of the average density gradient, which are known as zonal flow modes and have been intensely studied in the last decade in connection with internal transport barriers (see [3] and the references therein). We have found that R_{11} depends on n and is essentially determined by the anisotropy that is generated by the difference in the average velocity of the trapped ions V_{*eff} and the average velocity of the free ions $V_{fr}=-nV_{*eff}$. R_{11} increases when the ion flows become important up to a positive maximum and then it decreases to zero. When $n=1$, the ion flows are symmetrical and R_{11} vanishes.

1.3 Conclusions

In conclusion, a different physical perspective on the nonlinear evolution of drift turbulence is obtained. The main role is played by the trapping of the ions in the stochastic potential that moves with the diamagnetic velocity. The structures of trapped ions determine the evolution of the turbulence toward large wave lengths (inverse cascade). They also determine a slower increase of the amplitude of the potential fluctuations and the evolution to more ordered states. The influence of the ion flows produced by the moving potential appears later in the evolution of the turbulence. The ion flows determine the damping of the small k modes, the decay of the growth rate and eventually the damping of the drift modes with any k . The ion flows also determine transitory zonal flow modes (with $k_y=0$ and $\omega=0$) in connection with the fluctuation of the diamagnetic velocity due to the background turbulence.

Thus, in this perspective, there is no causality connection between the damping of the drift turbulence and the zonal flow modes. Both processes are produced by ion trapping in the moving potential, which determines ion flows. The drift turbulence does not saturate but has an intermittent evolution.

2. Density evolution of impurities and particles in turbulent tokamak plasmas

2.1 Macroscopic effects of the ratchet pinch

Impurity transport in magnetically confined plasma is one of the important problems in fusion research. This process is not completely understood and it represents a very active research field.

We have found a new type of pinch, *the ratchet pinch*, which is presented in a series of papers [5-7]. It appears in turbulent plasmas due to the gradient of the confining magnetic field as an average velocity directed parallel or anti-parallel to ∇B , depending on the characteristics of the turbulence. We have shown that the pinch effect is dominant compared to the diffusive transport in the nonlinear stage of the turbulence characterized by trajectory trapping.

The ratchet pinch effect can be amplified through the large scale ion motion. The parallel motion of the ions determines a decorrelation time $\tau_{II,i}$ that is the largest characteristic time in the ordering of the drift turbulence. Consequently, it should have a negligible effect in the transport of the ions. However, due to the toroidal geometry of the tokamak magnetic configuration, an indirect effect is shown to appear, which is mass-charge dependent. The parallel motion brings periodically the particles from the low to the high magnetic field side of the magnetic surface. The effects of the parallel motion are coupled to a different periodic poloidal motion, which appears in the nonlinear stage of the drift turbulence. The trapped ions are advected by the moving potential with the effective diamagnetic velocity while the free ones move in the opposite direction. These ion flows compensate such that the total flux is zero.

Scale separation between the fundamental diffusion process and the ion “macroscopic” trajectory permitted to introduce a two step averaging procedure. The turbulent advection was first averaged taking into account trajectory trapping in the structure of the stochastic potential (eddy motion). It was shown that the complex nonlinear process can be described by determining separately the transport characteristics of the trapped and free ions. The decorrelation trajectory method was adapted for the calculations in this module. Realistic models for plasma turbulence were developed. The model includes space anisotropy and potential motion with the diamagnetic velocity. In the second step, the macroscopic ion trajectories are determined and averaged using the (local) transport coefficients obtained at small scale.

2.2 Monte Carlo model and code for impurity density

The code determines the average effect of the turbulence on the space-time scale of the macroscopic trajectories. It contains a part for determining the transport coefficients at small scale and a Monte Carlo simulation of the macroscopic trajectories.

The transport model includes a moving potential with the poloidal velocity V_{*eff} . The potential has Gaussian distribution and given Eulerian correlation. Finite correlation lengths along magnetic field lines are included. The Eulerian correlation is modelled starting from given spectra of the wave numbers in the poloidal, radial and toroidal directions. This permits to include in the model different correlation length on the three directions (space anisotropy) and dominant waves. The Eulerian correlation can be small scale (with Gaussian shape) or large scale (with slow space decrease, of algebraic type). The connection of this module for the average effect of the turbulence to the equation of the macroscopic trajectories implies conceptual modification of the decorrelation trajectory method. It is not necessary to determine the diffusion coefficient and the pinch velocity, but rather the mean square displacement and the average displacement during the macroscopic time step. Only in the case of scale separation these quantities are expressed in terms of diffusion coefficients and pinch velocity. Moreover, the trapping in the structure of the stochastic potential is fully taken into account by averaging separately on the trapped and free trajectories.

The configuration of the magnetic field influences the macroscopic trajectories both directly and through the parametric dependence of the turbulence effects on the confining magnetic configuration.

2.3 Conclusions

In conclusion, we have realized the computer code that is necessary for the quantitative analysis of the strength of the new mechanism that produces impurity loss/accumulation. It is a nonlinear affect that appears due to the poloidal motion of the impurity ions. The latter has two components: motion along magnetic lines in toroidal geometry and ion poloidal flows induced by the drift turbulence. Depending on the ratio of the two components, impurities can be accumulated or lost.

References

- [1] Dupree T. H., Phys. Fluids 15 (1972) 334.
- [2] M. Vlad, F. Spineanu, Physical Review E 70 (2004) 056304(14).
- [3] Diamond P. H., Itoh S.-I., Itoh K., Hahm T. S., Plasma Phys. Control. Fusion 47 (2005) R35.
- [4] M. Vlad, F. Spineanu, Plasma and Fusion Research 4 (2009) 053-1:8.
- [5] M. Vlad, F. Spineanu and S. Benkadda, Phys. Rev. Lett. 96, 085001 (2006).
- [6] M. Vlad, F. Spineanu and S. Benkadda, Phys. Plasmas 15 (2008) 032306 (9pp).
- [7] M. Vlad, F. Spineanu and S. Benkadda, Plasma Phys. Control. Fusion 50 (2008) 065007.

***THEORETICAL MODELING OF ERROR FIELDS PENETRATION AND
NEOCLASSICAL TOROIDAL VISCOSITY NON-RESONANT MAGNETIC
BRAKING EFFECTS IN TOKAMAK PLASMAS***

I. G. Miron

National Institute of Laser, Plasma and Radiation Physics, Bucharest

Overview

The aim of the above objectives of the present project is to derive an axisymmetric 2-dimensional analytic model capable to illustrate the involved physical phenomena. As a first step, a 2-dimensional, analytic resistive wall mode (RWM) dispersion relation has been obtained. As a second step, a dynamic theoretical model that proves the phenomena of global tokamak plasma deceleration and neoclassical toroidal viscosity (NTV) braking of the plasma toroidal rotation has been built.

A 2-dimensional model provides a more realistic description of the phenomena involved by taking into account realistic plasma shape parameters like the Shafranov shift, toroidicity, ellipticity and triangularity that cannot be considered within a cylindrical model description. Flux (natural) coordinates will be used into calculus. The calculated metric coefficients will be functions of the above mentioned parameters. The angular dependence of the equilibrium magnetic field together with the irregular plasma shapes are responsible for neoclassical effects that finally give rise to the mechanism of toroidal momentum dissipation and NTV global braking due to the non-resonant error fields destabilizing effect.

Detailed results

1 Determination of a general RWM dispersion relation for 2-D axisymmetric geometry in the presence of neoclassical viscosity and non-resonant error fields

The ultimate task of this objective is to provide an explicit analytic dispersion relation of the RWM. The objective is structured as: i) equilibrium description, ii) obtaining the 2-D perturbed MHD equations, iii) solving the Laplace equation in vacuum, in 2-D geometry, iv) obtaining the 2-D perturbed feedback equations, v) obtaining the 2-D perturbed "jump" equations across the plasma boundary, vi) deriving the general 2-D RWM dispersion relation. All the above steps have been achieved. Finally we have obtained the following compact polynomial form in the RWM growth rate (γ_0) that provides the axisymmetric 2-dimensional dispersion relation of the RWM we are interested in:

$$\sum_{k=0}^{6L} \gamma_0^k \sum_{\substack{l_1, \dots, l_{2L}=1 \\ \text{distinct}}}^{2L} \text{sgn}(l_1, \dots, l_{2L}) \sum_{\substack{\alpha_1, \dots, \alpha_{2L}=0 \\ \alpha_1 + \dots + \alpha_{2L} = k}}^4 \prod_{s=1}^{2L} \Gamma_{s\alpha_s}^{l_s} = 0 \quad (1)$$

The index ordering transformation is presented in [1]. We have analytically derived $\Gamma_{s\alpha_s}^{l_s}$:

$$\begin{aligned} \Gamma_{s\alpha_s}^{l_s} = & Q_{s\alpha_s}^{l_s} H(L-l_s)H(L-s) + \tilde{Q}_{s\alpha_s}^{l_s} H(l_s-L-1)H(L-s) \\ & + F_{s\alpha_s}^{l_s} H(L-l_s)H(s-L-1)H(2-\alpha_s) + \tilde{F}_{s\alpha_s}^{l_s} H(l_s-L-1)H(s-L-1)H(2-\alpha_s) \end{aligned} \quad (2)$$

H is the Heaviside unit step function. $L = (m_2 - m_1 + 1)(n_2 - n_1 + 1)$ where the (m, n) mode spans $m = m_1, \dots, m_2$ and $n = n_1, \dots, n_2$. $Q_{s\alpha_s}^{l_s}$ and $\tilde{Q}_{s\alpha_s}^{l_s}$ are *explicitly derived* coefficients as functions of all the plasma boundary parameters taken into account: ρ_a (plasma mass density), η_a (ion viscosity coefficient), ν (plasma flow damping due to charge exchange with neutrals), c_{sa} (plasma sound speed), q_a (safety factor), s_a (magnetic shear), Δ_a , E_a , T_a , Δ'_a , E'_a , T'_a (Shafranov shift, ellipticity, triangularity and their radial derivatives). The particular disposal of the resistive wall (HBT-EP tokamak type) from [1] is used. $F_{s\alpha_s}^{l_s}$ and $\tilde{F}_{s\alpha_s}^{l_s}$ are *explicitly derived* coefficients as functions of all the feedback parameters taken into account: r_w , r_f , r_d (resistive wall, radial feedback coils and radial detector coils "radial" flux coordinates), R (feedback coils resistance), δ_f (feedback coils thickness), $\delta\theta_f$, $\delta\varphi_f$ (feedback coils poloidal and toroidal leg angular extents), $\Delta\theta_f$, $\Delta\varphi_f$ (feedback coils poloidal and toroidal angular extents), G_p , G_d (proportional and derivative amplification factors), $\Delta\theta_d$, $\Delta\varphi_d$ (detector coils poloidal and toroidal angular extents), δ_{w1} , δ_{w2} (aluminium and stainless steel wall thicknesses), $\Delta\varphi_{w2}$ (stainless steel wall toroidal angular extent), N (the common number of aluminium and stainless steel wall segments), $\{\theta_p\}_{p=1, \dots, M}$ (the randomly disposed poloidal angles where the feedback coils and detectors are centered), $\Delta_{w,f,d}$, $\Delta'_{w,f,d}$, $E_{w,f,d}$, $E'_{w,f,d}$, $T_{w,f,d}$, $T'_{w,f,d}$. The obtained relation (1) is a 2-D *compact analytic* multimode RWM dispersion relation able to provide in a simple manner (root solving) the growth rate of the RWM which indicates the RWM stability. The optimal conditions for the RWM stabilization can be found as functions of all the above plasma and feedback parameters. Mode coupling has been taken into account. An axisymmetric 2-dimensional approach of the magnetic surfaces structure has been considered. A realistic shape and disposal of the passive and active feedback systems have been used.

This work was presented at the "EURATOM-MEdC Association Day" Meeting, July 2nd, 2010, held in Iasi, Romania (http://www.ifa-mg.ro/euratom/program_ad2010.php).

2 a) Derivation of the evolution equations for the plasma angular motion at the level of the plasma boundary and inner non-ideal MHD layers (that develop at the corresponding

inner rational surfaces) to prove global plasma deceleration and NTV braking of the plasma rotation;

b) Electromagnetic and NTV torques calculation for shapes of the flux surfaces structure that include toroidicity, ellipticity, triangularity. The influence of the above parameters in finding the optimal less destabilizing error field spectrum will be calculated.

The term *global* refers to the locations of all the non-ideal, inertial layers that develop around every magnetic surface inside the plasma. The RWM dispersion relation obtained within the frame of the first objective will still be used with a well-thought substitution of the RWM's growth rate by the time derivative due to the dynamic treatment of the involved phenomena.

The derived toroidal component of the 2-dimensional dynamic equation of every non-ideal, inertial layer (IL) inside the plasma is (after IL volume integration):

$$\frac{d\Omega_\varphi}{dt} + \frac{\eta_2}{\rho r_s^2 d_s^2} (\Omega_\varphi - \Omega_{\varphi 0}) = \frac{1}{8\pi^2 R_0^3 \rho_m r_s^2 d_s} T_{\varphi EM} \quad (3)$$

Ω_φ is the toroidal angular velocity of the IL, r_s the "radial" flux coordinate of the corresponding magnetic surface and $d_s = \delta_s / r_s$, where δ_s is the "radial" half-width of the layer. The second term in the left hand corresponds to the perturbed NTV torque with η_2 the perpendicular viscous coefficient [2]. $\Omega_{\varphi 0}$ is the unperturbed IL toroidal angular velocity. $T_{\varphi EM}$ is the perturbed electromagnetic torque that corresponds to the coupling of the perturbation modes due to the error field action as the marginal stability of the perturbations is approached.

The objectives are structured as: i) finding a 2-D explicit expression for the perturbed electromagnetic torque, ii) obtaining the 2-D dynamic perturbed MHD equations, iii) obtaining the 2-D dynamic perturbed feedback equations, iv) obtaining the 2-D dynamic perturbed "jump" equations across the IL, v) finding the perturbed magnetic flux functions as solutions of the algebraic inhomogeneous 2-D complete system of the dynamic perturbed equations, vi) solving the 2-D dynamic equation of the IL. The above steps have been fulfilled. We have obtained the following expression for the perturbed electromagnetic torque:

$$T_{\varphi EM} = -(4\pi^2 / \mu_0 R_0 r_s q_s^2) \sum_m \alpha_s^m (m - n q_s) \sum_{j=-3, j \neq 0}^3 [(m+j)(m+j-nq_s) / j] \text{Re} (\phi_{ts}^{mn} \phi_{ts}^{m+jn*}) \times \left\{ [r_s / R_0 + a\varepsilon (r \Lambda_{js}')'] \delta_{|j|1} - (2a\varepsilon / r_s) [(j^2 - 1) \Lambda_{js} - r_s (1 - r_s q_s' / q_s) \Lambda_{js}'] (1 - \delta_{|j|1}) + \mathcal{G}(\varepsilon^2) \right\} \quad (4)$$

The index s refers to the flux coordinate r_s where the IL is positioned at. $\phi_{ts}^{mn} \equiv [d\phi^{mn} / dt]_{r_s}$, where $-\phi_{ts}^{mn}$ is the (m, n) Fourier component of the perturbed scalar electric potential at $r = r_s$. $\Lambda_{js} \equiv \Delta_s \delta_{|j|1} + E_s \delta_{|j|2} + T_s \delta_{|j|3}$ ($j=1,2,3$ and δ Kronecker delta). Δ_s , E_s and T_s correspond to q_s magnetic surface. α_s^m refers to the jump expression of the (m, n) perturbed flux across the IL. * denotes the complex conjugate of a number. The above expression clearly shows the mode

coupling prevalence in explaining the influence of the perturbed electromagnetic torque on the plasma stability. In $\mathcal{G}(\varepsilon)$ approximation, $j \neq 0$ from the above expression indicates that single mode theory (i.e. *resonant* error field) is unable to explain the involved phenomena. The resonant component influence has $\mathcal{G}(\varepsilon^2)$ magnitude, thus the adjacent mode coupling prevails. From the derived dynamic MHD, feedback and "jump" perturbed equations we were able to find ϕ_{ts}^{mn} and insert it into the perturbed electromagnetic torque expression (4). Finally we have obtained the following quasi-analytic solution of the 2-D dynamic equation of the IL:

$$\Omega_{\varphi}(t) = \Omega_{\varphi 0} \left[1 + \exp\left(-\eta_2 t / \rho_m r_s^2 d_s^2\right) \right] + \frac{d_s}{4\mu_0 r_s R_0^4 q_s^2} \sum_m \alpha_s^m \sum_{j,k=0}^{7L-L_0} \frac{e_{jk}^{mn} + e_{kj}^{mn*}}{\eta_2 + \rho_s r_s^2 d_s^2 (\sigma_j + \sigma_k^*)} \exp[(\sigma_j + \sigma_k^*)t] \quad (5)$$

$\{\sigma_i\}_{i=0,\dots,7L-L_0}$ and e_{jk}^{mn} are explicitly derived coefficients of plasma and feedback parameters. It can be clearly seen that all the error field poloidal modes couple with the IL corresponding poloidal mode within this multimode model description. On the other hand, a non-resonant error field couples with all the poloidal modes whose magnetic surfaces the inertial layers develop at. The intrinsic toroidal mode coupling effects are contained within the $\{\sigma_i\}_{i=0,\dots,7L-L_0}$ terms and they are due to the feedback system toroidal resistive inhomogeneity. Within the single mode theory, only a $\mathcal{G}(\varepsilon^2)$ term would remain in the second right hand term of (5) and the $\mathcal{G}(\varepsilon)$ term would disappear as well as the main and global error field destabilizing effect.

3. Results and discussion

The data used to plot the $\Omega_{\varphi}(t)$ dependencies is characteristic for the HBT-EP tokamak plasma.

The main achievement of the 2-dimensional model we have presented has been accomplished.

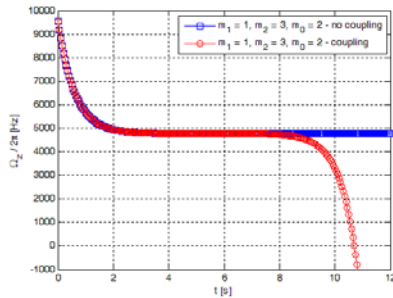


Figure 1

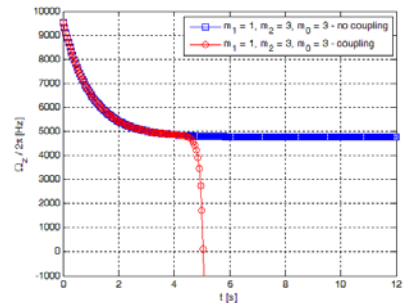


Figure 2

Figs. 1 and 2 clearly illustrate the deceleration and braking of the plasma rotation at the level of the inertial layers we have considered. Fig. 1 shows the (2,1) internal mode behavior, whereas Fig. 2 corresponds to the boundary marginal (3,1) mode. The (1,1) or (2,1) modes have the same dependency type. The influence of the error field mode coupling is obvious compared to the no-coupling case. In fact, the coupling of the modes is responsible for the increase of the

NTV torque influence that finally brakes the plasma rotation. Fig. 3 shows the dynamic dependence of $\Omega_\phi(t)$ as the plasma boundary ellipticity varies, $E_a = 2R_0[Z|_{\omega=\pi/2} - (R-R_0)|_{\omega=\pi}]/[Z|_{\omega=\pi/2} + (R-R_0)|_{\omega=\pi}]^2$. (R, ω, Z) are the orthogonal cylindrical coordinates and ω is the poloidal geometrical angle related to θ by the expression:

$$\omega = \theta - (r/R_0)\sin\theta - a\varepsilon[\Delta'\sin\theta + (E/r - E')/2\sin 2\theta + (2T/r - T')/3\sin 3\theta] + \mathcal{O}(\varepsilon^2) \quad (6)$$

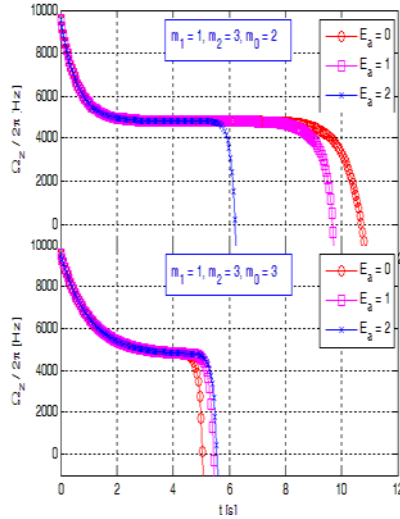


Figure 3

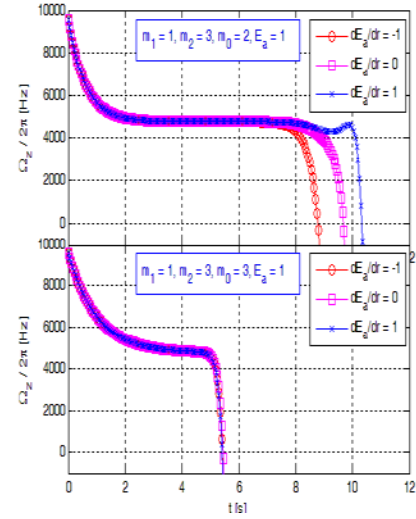


Figure 4

For internal plasma modes (2,1) or (1,1) the ideal configuration for less destabilization corresponds to $E_a = 0$, i.e. the cylindrical form for the plasma column. On the contrary, for the more unstable external kink mode (3,1), the $E_a > 0$ condition provides less destabilization. However, for $E_a > 0$ (condition required by other stability considerations, beyond the present study) the less destabilizing configuration implies $dE_a/dr > 0$ (Fig. 4) for all the internal modes. The increased ellipticity of the magnetic surfaces as their "radial" coordinate grows provides less instability. Consequently, the combined effect of ellipticity and its radial derivative assumes that the optimal error field spectrum involves the prevalence of higher internal mode amplitudes compared to the external kink (or RWM) mode amplitude. A lower (3,1) mode amplitude minimizes the coupling with its adjacent internal modes and the result is a slower deceleration of the corresponding IL. Figs. 5 and 6 show the IL toroidal angular velocity $\Omega_\phi(t)$ dynamic dependencies for different plasma boundary triangularities $T_a = (R_0/Z|_{\omega=\pi/2})[(R-R_0)|_{\omega=\pi}/Z|_{\omega=\pi/2} + 1]$ and dT_a/dr , respectively. The less destabilizing configuration corresponds to $T_a \geq 0$ for internal modes and $T_a > 0$ for the (3,1) mode. Unlike the ellipticity case, the $dT_a/dr < 0$ condition is less destabilizing for all the modes. Again, under the $T_a > 0$ and $dT_a/dr < 0$ conditions, the optimal error field spectrum assumes a lower (3,1) mode amplitude condition to be fulfilled.

All the above analysis for every mode of instability provides the parametric data in order to find the optimum non-resonant error field spectrum for the less destabilizing configuration.

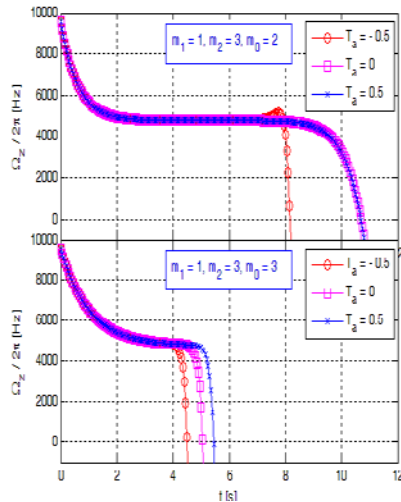


Figure 5

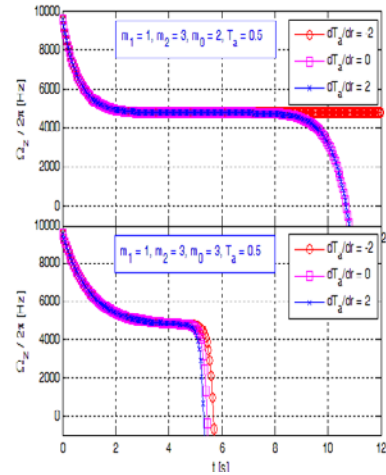


Figure 6

4. Conclusions

An axisymmetric 2-D model for the RWM stabilization has been built within the large aspect ratio approximation, the thin resistive shell condition and the assumption that the resistive shell and the active feedback coils are disposed on magnetic surfaces. A compact dispersion relation of the RWM, (1), has been obtained. No complicated numerical codes are needed.

An axisymmetric 2-D theoretical model has been built to prove the global plasma deceleration and NTV braking of the plasma rotation. A quasi-analytic expression for any inertial layer toroidal angular rotation has been provided. A multimode treatment has been considered. Within the large aspect ratio assumption, it has been demonstrated that the error field modes coupling effect prevails and the single mode theory is unable to provide realistic results. The influence of toroidicity, ellipticity and triangularity parameters in finding the less destabilizing configuration has been showed.

Whereas the fluid (MHD) model provides an expected theoretical description of the phenomena, the particle model provides a more reliable, quantitative description. Therefore, not only the electromagnetic torque term is responsible for the perturbed magnetic flux nonlinear effects, but also the NTV torque term, in the frame of the kinetic model. The next milestones to be achieved should consider the particle, kinetic model for the NTV term and the toroidal moment equation and the solving of the IL toroidal equation of motion for different collisionality regimes.

References

- [1] I.G. Miron, Plasma Phys. Control. Fusion 50 (2008) 095003.
- [2] S.I. Braginskii, Rev. Plasma Phys. 1 (1965) 205.

ATOMIC DATA CALCULATION IN SUPPORT OF AMNS ACTIVITY

V.Stancalie, V. Pais, A. Mihailescu, A. Stancalie, O. Budriga

National Institute for Laser, Plasma and Radiation Physics, Bucharest

Overview

The aim of the project is to contribute to atomic data calculation in support of the AMNS activity, and to further development, and maintenance of a module for implementing AMNS data to ITM-TF codes (WP10-ITM-AMNS-ACT2, WP10-ITM-AMNS-ACT2). The present work refers to the calculation of atomic data for plasma spectroscopy (for ADAS). These data have to be implemented, in a given standardized data format, into the ITM data base. All codes in the ITM, which require atomic data, will draw it from ADAS via common mechanism. In the case of atomic data, the ADAS database can provide, virtually, all the data needed by the ITM-TF.

Carbon ions and atoms are released from the walls into the edge plasma by a number of processes (physical sputtering, chemical erosion, radiation enhanced and thermal sublimation). Such impurities have a detrimental effect on plasma heating. A detailed knowledge of carbon transport properties is required, which can be obtained through spectroscopic monitoring. To deduce relevant physical quantities from the measurements requires accurate cross section data.

Electron collisions with Fe, Ni and Co elements and their ions are important in hot plasmas with low electron density, i.e. in stellar objects or in tokamaks, since the collisional rate of de-excitation for metastable levels may be lower than the decay rate by magnetic dipole or electric quadrupole transitions, which become observable. These ‘forbidden’ lines are the only transitions of the multicharged ions in the visible or near ultraviolet spectral regions in which ion temperatures can be derived from line profile measurements.

The project aims to obtain accurate atomic data for C atoms, and for Co IV ion, using the R-matrix theory and codes. The atomic excitation lying in the continuum part of atomic spectra is theoretically studied. Particularly, the main issue addressed here, is the situation when the single-particle states are strongly coupled to more complicated configurations, mainly two-particle-one-hole states, giving rise to the spreading width of the resonances. These processes are difficult to study, both experimentally and theoretically, because, their formation, and decay, is time dependent processes. We have considered two approaches that offer a partial solution to these problems. The first, of these, is the single-photon reaction approach. The high-lying single-particle states, in one-photon transfer reaction, manifest themselves as broad ‘resonance’-like structures superimposed on a large continuum. It has been very successful in describing atomic structure properties, as well as photo-ionization, and electron-impact excitation processes, especially in the near-threshold resonance regime [1, 2]. The second is the R-matrix

approach for electron-scattering process. This method has been, previously, used to calculate atomic data, and generalized oscillator strength, for Li-like Al ions [3, 4].

Results of a series of calculations, intended specifically to explore the role of single-particle-one-hole (1p-1h), and two-particle-one-hole (2p-1h) resonances in scattering process, in the vicinity of selected thresholds of atomic carbon, and Co IV ion, have been obtained [5-7]. Large scale atomic data, as: energy levels, transition probabilities, and line strengths, has been provided. The R-matrix method was used to calculate cross sections, and collision strengths, for low energy inelastic scattering of electrons by these atomic systems. Of particular interest, here, is the formation of 2p-1h intermediate resonant states in which the dominant configuration has two electrons in 'excited' orbitals leaving one electron 'missing' from the initial-state orbitals. The role of configuration interactions allowing for distortion of the initial- state and excited-state orbitals due to electron correlation effects has been explored. Some evidence of resonance structures at low energies have been observed [8].

Publications

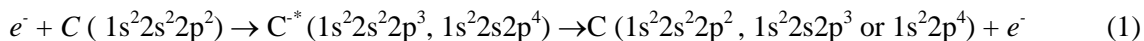
- [1] V.Stancalie, V. Pais, A. Mihailescu, O.Budriga, A. Oprea, *Recent progress in the theoretical investigation of laser-atom, laser-plasma interactions*, Romanian Rep. Phys. 62(2010)528.
- [2] V.Stancalie, A. Oprea, *Single and two-particle-one hole resonance structure in the low-energy inelastisc scattering of electrons by atomic systems*, 37th Conference on Plasma Physics, 21st -25th June 2010, Dublin, Ireland.
- [3] V. Stancalie, *Forbidden transitions in excitation by electron impact in Co³⁺: an R-matrix approach*, Physica Scr. 83(2011)025301.

Detailed results

1 Methods

1.1 Single and two-particle-one-hole resonance structure in the low energy inelastic scattering of electrons by atomic carbon

The process under consideration is:



Three separate calculations have been performed: calculation (A) where the intermediate states in the equation (1) are not included; calculation (B) where intermediate states are introduced by including, explicitly, in the (N+1)-electron collision wavefunction configurations $2s^2 2p^3$ and $2s 2p^4$; and calculation (C) which extend the calculation B with additional twelve states of C derived from the configurations $1s^2 2s 2p^3$ and $1s^2 2p^4$. Finally, theoretical excitation energies and linestrengths have been provided for atomic carbon.

The above first two calculations for carbon atom, which do not include the $2s 2p^3$ and $2p^4$ configuration, explore the importance of including configuration interaction wavefunctions in

the target-state expansion and in the (N+1)-electron quadratically integrable function expansion. In the first calculation, we represent the target states by the single $1s^22s^22p^2$ configuration and thus include only the (N+1)-electron quadratically integrable function expansion (1). In the second calculation, we also include the $2s2p^3$ and $2p^4$ configurations in the target state representation, and the intermediate states in (N+1)-electron configurations in expansion (1), for completeness. The third and larger calculation will show the effect on the collision strengths of including the 12 additional terms with the configuration $1s^22s2p^3$ and $1s^22p^4$. To perform electron collision calculation we use the RMATXII code for the internal region, and FARM for the external region. The excitation cross sections and collision strengths are provided for low electron collision energy in order to illustrate the presence of real two-particle one-hole resonance states.

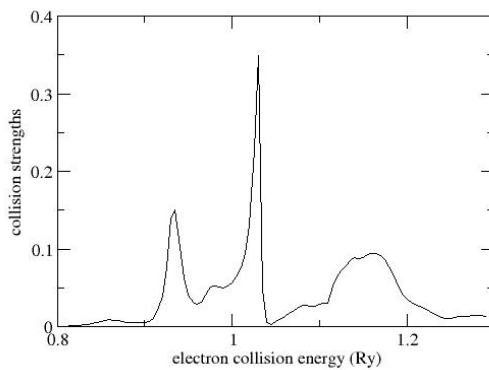


Figure 1 - Collision strengths for excitation from the $1s^22s^22p^2$ 1D ground term to the $1s^22s2p^3$ $^3D^0$ state in carbon (calculation A)

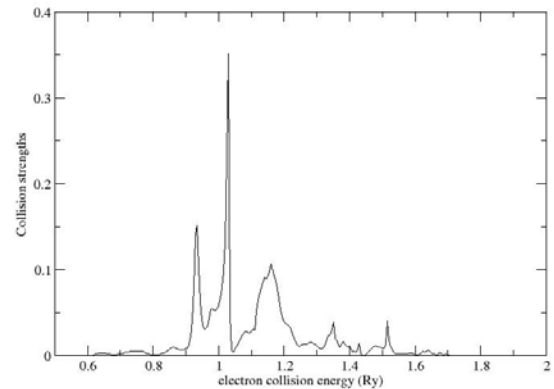
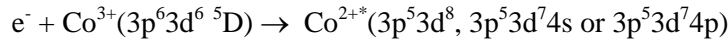
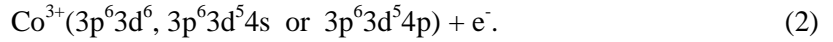


Figure 2 - Collision strengths for excitation from the $1s^22s^22p^2$ 1D ground term to the $1s^22s2p^3$ $^3D^0$ state in carbon (calculation B, where intermediate states are introduced by including, explicitly, in the (N+1)-electron collision wave function configurations $2s^22p^3$ and $2s2p^4$)

1.2 Two-particle-one-hole resonance structure in the low energy inelastic scattering of electrons by Co^{3+} ion

The Co IV ion is isoelectronic with Fe III ion. Due to higher nuclear charge number the low energy spectrum is simpler. In particular, for Co IV ion, $1s^22s^22p^63s^23p^63d^6$ 5D ground configuration, the energies of the $3d^54p$ terms are lying between $3d^6$ and $3d^54s$ states but overlapping both. We therefore decided to carry out a first calculation (Calculation A) in which 136 LS terms of just the three configurations $3d^6$, $3d^54s$ and $3d^54p$ were included in the R -matrix expansion. We have considered the following excitation ways:



$$\downarrow$$


The second calculation, Calculation B, retains also 136 LS terms arising from the three configurations above (Calculation A) augmented with $3p^4 3d^8$, $3p^4 3d^7 4s$ and $3p^4 3d^7 4p$ in the target state expansion and the configurations $3p^5 3d^8$, $3p^4 3d^9$, $3p^5 3d^8$, $3p^4 3d^9, 3p^4 3d^8 4s$ and $3p^6 3d^5 4s^2$ in the $(N+1)$ -electron quadratically integrable function expansion. In order to have a consistent set of wave functions for the N and $(N+1)$ –electron wave functions, the $(N+1)$ electron configuration data have been obtaining by adding one electron to the N electron configurations in all possible ways. Hence, we can include these $(N+1)$ -electron configurations in the collision wave function by including the CI wave functions with configuration $3p^5 3d^7$ in the basis set used in the CI expansion of the N -electron target states. These first two calculations explored the importance of including configuration interaction wave functions in the target-state expansion and in the $(N+1)$ -electron quadratically integrable function expansion. The third and largest calculation, Calculation C, shows the effect on the collision strengths of including additional 48 levels with electronic configuration $3p^5 3d^7$. In this calculation the target states were represented by nine configurations $3d^6$, $3d^5 4s$, $3d^5 4p$, $3p^4 3d^8$, $3p^4 3d^7 4s$ and $3p^4 3d^7 4p$, $3p^5 3d^7$, $3d^4 4s^2$ and $3d^4 4s 4p$, and correspondingly the $(N+1)$ -electron configurations $3p^6 3d^7$, $3p^6 3d^6 4s$, $3p^6 3d^6 4p$, $3p^6 3d^6 4s^2$, $3p^6 3d^5 4s 4p$, $3p^6 3d^5 4p^2$, $3p^5 3d^8$, $3p^4 3d^9$, $3p^4 3d^8 4p$, $3p^4 3d^7 4s 4p$, $3p^5 3d^7 4p$, $3p^4 3d^7 4p^2$, $3p^5 3d^6 4s^2$, $3p^5 3d^6 4s 4p$ and $3p^5 3d^6 4p^2$. Thus comparison of Calculation B with Calculation A will show the presence of any resonance structure due to intermediate Co III resonance states in equation (2), while further comparison with calculation C will illustrate the effect on such features of the inclusion of the specific target states with which these resonances are associated.

3. Results and discussion

In Figs. 3 and 4 we show a plot of collision strengths against incident electron energy as obtained from the Calculation A and the Calculation B, respectively, for the transition from the ground state $3d^6$ ($^5D^e$) to the first excited state $3d^6$ ($^3P^e$), for the $^4F^e$ symmetry, in Co IV ion. This symmetry has been selected as it provides the largest contribution to the total collision strength for this transition. The Rydberg series of resonances converging to thresholds below approximately 3 Ryd are not strongly affected by the inclusion of the additional configurations. From parity consideration, the enhancement of the Rydberg resonance structure in the region of 3 Ryd–4 Ryd is due to the inclusion of the $3p^5 3d^7 4p$ configuration in the expansion of the $(N+1)$ -electron collision wavefunction. At higher energies, very distinctive resonances appear in the second calculation between 4.3 and 4.8 Ryd which are absent from the first calculation.

Our analysis shows that these are real two particle-one hole physical resonances arising from the intermediate $(N+1)$ -electron states.

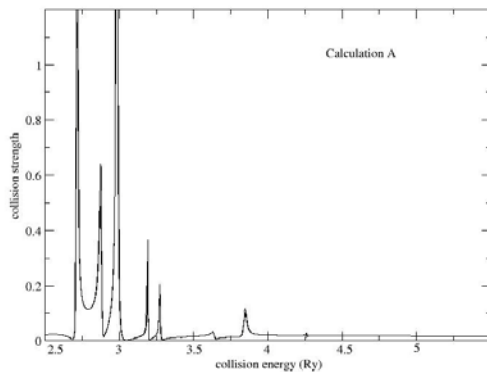


Figure 3- Collision strength for the ${}^5D^e - {}^3P^e$ transition of Co^{3+} . The curve corresponds to the first calculation: Calculation A. In this first calculation the only $3d^6$, $3d^54s$ and $3d^54p$ target states are included into the R-matrix expansion.

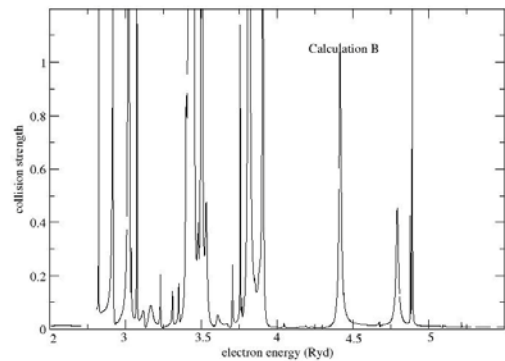


Figure 4 - Collision strength for the ${}^5D^e - {}^3P^e$ transition of Co^{3+} . The curve corresponds to the second calculation: Calculation B. In this calculation six target state configurations $3d^6$, $3d^54s$, $3d^54p$, $3p^43d^8$, $3p^43d^74s$ and $3p^43d^74p$ are included into the R-matrix expansion.

In Fig. 3 we present graph of the collision strengths against incident electron energy for the third calculation and the same transition plotted in Figs. 1 and 2. This figure shows new Rydberg series of resonances associated with $3p^53d^7$ states. It is found that the inclusion of additional the 48 states associated with $3p^53d^7$ state yields to additional resonance structures while the resonance structure observed in Fig. 2 is moved down in energy, very slightly.

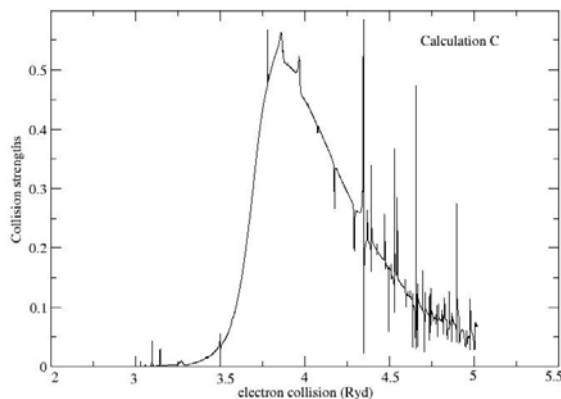


Figure 3 - Collision strength for the $5De - 3Pe$ transition of Co^{3+} . The curve corresponds to the third calculation: Calculation C. In this calculation nine target state configurations $3d6$, $3d54s$, $3d54p$, $3p43d8$, $3p43d74s$, $3p43d74p$, $3p53d7$, $3d44s2$ and $3d44s4p$ are included into the R-matrix expansion.

4. Conclusion

The current state of plasma modeling requires data for the excitation of highly excited levels of the target ion/atom. Such calculations are extremely difficult to perform, as a large number of target excited states have to be included. Moreover the energy range in which the atomic data are required necessitates a calculation over very many partial waves, including a large number of continuum orbitals representing the scattered electron. In the reported work here, the R-matrix computer packages have been used to calculate cross sections and collision strengths for important transitions to the $n = 3$ and $n = 4$ levels of carbon. A full set of cross sections are

available from the authors for transitions between all the levels included in the three calculations. Some resonance structure can be seen at lower energies, but a detailed study requires more accurate target wave functions than those used here. A new calculation adapted to such a study is planned.

Separately, the presence of two-particle one-hole resonances in low energy domains of electron collision with Fe-peak element Co IV, has been put into evidence. We have carried out the first detailed calculations of electron-impact excitation of forbidden transitions amongst states with $3d^6$, $3d^54s$ and $3d^54p$ configurations in this ion. We have explored the effect of including configuration interaction wave functions both in the target states expansion and in the $(N + 1)$ -electron quadratically integrable functions expansion. The target states have been represented by elaborate configuration interactions in an attempt to account for electron correlation effects where it is essential to include the $3p^2 \rightarrow 3d^2$ core excitation in both the target and scattering wave functions. We found that this gives rise to very distinctive two-particle one hole resonances at higher energies.

DEVELOPMENT AND MAINTENANCE OF A MODULE FOR IMPLEMENTING AMNS DATA TO ITM-TF CODES

V.Stancalie, V. Pais, A. Mihailescu, A. Stancalie, O. Budriga

National Institute for Laser, Plasma and Radiation Physics, Bucharest

Overview

The aim of the project is to develop and maintain a module for implementing AMNS data to ITM-TF codes. All codes in the ITM, which require atomic data, will draw it from ADAS via a common mechanism. In the case of atomic data, the ADAS database can provide, virtually, all the data needed by the ITM-TF.

AMNS data are needed in several of the ITM modelling projects, but especially in IMP#3 and IMP#5. A consistent approach, taking into account the specific requirements of the ITM while maintaining the work aligned with other European efforts in this area, is therefore required.

A significant amount of atomic data (not always easily accessible) is needed. It will take a significant amount of time and effort before the bulk part of the needed data can be made available in the ITM-TF. The short term needs can be summarised as follows : Rate coefficients (as a function of n and T) for: ionization, recombination, charge-exchange, nuclear reaction rates, cooling rates, ionization potential, energy per nuclear reaction + fraction of it going to electron and ion components (this is to a large part a question for IMP#5). The elements needed are: High priority: H, D, T, He, C; Since the ADAS database is very well established and contains data essential to several ITM-TF codes, it will be used as a pilot project to import atomic data to the ITM-TF data repository.

The work on providing the AMNS data includes recommendation of the best data to be used/stamp of approval. Highly useful data is residing in data bases not readily accessible to the general user (e.g. in private data bases). With the access to such data, we have supplied, when appropriate, relevant data to the ITM-TF database. This includes suggesting recommendation for the best data to be used.

To aid to data delivery, a module for the ITM codes have been written. This module makes use of the existing atomic data for carbon. In 2010 the ITM data structure Atomic data was finalised; a module taking Carbon data from the AMNS database and write them to the and ITM AMNS database via the data structure was developed (more elements are in the pipeline); and a first version modules for reading AMNS data from the ITM database and deliver them to ITM codes were written.

Publications

- [1] B. Guillerminet, F. Iannone, F. Imbeaux, G. Manduchi, A. Maslennikov, V. Pais, P. Strand., „Gateway: New high performance computing facility for EFDA task force on integrated Tokamak modelling” Fusion Engineering and Design 85(2010) pp. 410-414.

Detailed results

A survey of the needs for AMNS data was carried out among the members of IMP#3 and IMP#5. It should be emphasised that the survey does not present an exhaustive list of data needed. In particular, it is likely that items will be added as the ITM-TF develops and gradually extends the scope of its modelling. All codes in the ITM, which require atomic data, will draw it from ADAS via common mechanism. In the case of Atomic data, the ADAS database can provide virtually all the data needed by the ITM-TF. As member of ADAS consortium, our work contribute to the development of ADAS databases.

In fusion research, carbon composite materials are often used in the walls of the confinement chamber devices as the tokamak at JET. Carbon ions and atoms are released from the walls into the edge plasma by a number of processes (physical sputtering, chemical erosion, radiation enhanced and thermal sublimation). Such impurities have a detrimental effect on plasma heating, and must be rapidly removed. A detailed knowledge of carbon transport properties is thus required, which can be obtained through spectroscopic monitoring. To deduce relevant quantities from the measurements requires accurate cross section data. The purpose was to provide the ITM-TF as a whole with up-to-date Atomic, Molecular, Nuclear and Surface (AMNS) data. Delivery of the data to codes is made by ITM developed standardized modules, where traceability (including provenance) of data is ensured.

Standardised module delivering AMNS data in a standardised form to ITM codes have been developed in Fortran90. They are now able to take data from an ITM database via the AMNS CPO. The existing modules are written in F90 and work on a C++ wrapper has started. This work will be completed in 2011, including documentation. Developed module need to be updated as more AMNS data are put into the ITM database. Extension to other programming languages supported by the ITM are also envisaged.

MAINTAIN AND EXTEND THE ITM PORTAL

V.F. Pais , V. Stancalie, A. Mihailescu, O. Budriga

National Institute for Laser, Plasma and Radiation Physics

Overview

The longer term goal of the ITM-TF is to provide the European fusion community with a validated suite of simulation tools for ITER exploitation and to provide the basis for a complete simulation environment for fusion plasmas generally available for use also for modelling on current devices and in support of theory and modelling in general. IMPs have dual responsibilities in that they should continue to develop and manifest the physics foundations for Integrated Modelling in standalone packages targeting the code platform environment while they are also supporting the integration efforts towards scenario modelling tools.

The ITM Portal acts as an interface between users and the various tools available on the ITM Gateway. Various problems arising from the usage of the ITM Portal were dealt with in the context of the ISIP-ACT10 task. Furthermore, a closer look to the ACL (Access Control List) mechanism of Gforge was required in order to make it easier for the users to work with.

Detailed results

The ITM Portal acts as an interface between users and the various tools available on the ITM Gateway.

Various problems arising from the usage of the ITM Portal were dealt with in the context of the ISIP-ACT10 task. Some of the solutions were posted as Wiki entries in the Portal Wiki system.

During this period the problem of synchronizing external software repositories with the content stored in ITM Gforge was solved using custom designed scripts that periodically bring remote content into the local software repositories on the ITM Gateway.

Updates were performed on the text editors in use by the ITM Portal related tools. The updates included a new equation editor installed in the form of a plugin for the FCKEditor inside Gforge. This allows equations to be inserted in wiki/forum/bug tracker posts.

In order to facilitate the interaction with the support team (WP10-ITM-ISIP-ACT1), links to the General Support group were added in various places, including the front page of Gforge.

Project IMP1 and IMP2 have been merged, including their user groups, resulting a new user group called IMP12. Therefore, new access control lists (ACLs) were needed to allow access to users belonging to this new user group.

As a result of the continuous development of the content stored inside the Portal, the machines hosting this content started to move slowly. Therefore a rollback performance test was performed, resulting the need to migrate all the existing files to a new content management system. After a series of discussions it was decided to start with a test machine having the Joomla content management system. The speed of this new machine was much better compared to the one of the old system, thus the migration of content started.

Nevertheless, there were some problems regarding the integration of the single sign-on mechanism, Shibboleth, with this new machine. This was due mainly to the fact that Joomla is not aware of user groups, and thus the ACLs defined at group level needs to be transformed into ACLs at user level. This is still an ongoing work.

At this time all the ITM related content, accessible through the ITM Portal, is served using the new Joomla machine for content management.

The overall usage of the ITM Portal has increased constantly since its creation, thus requiring new techniques for data handling.

The current integration with Joomla is trying to achieve this by using the Joomla content management system only for information organisation and ACL management while allowing an highly optimised version of the Apache web server to serve content directly from the high speed filesystem available in the ITM Gateway.

A closer look to the ACL (Access Control List) mechanism of Gforge was required in order to make it easier for the users to work with.

In order to demonstrate setting ACLs under GForge a new project called “Test GForge ACLs”(with repository “gforge_acl”) was created. This project started with the default settings associated with any new ITM software project (created after 28 January 2009).

Furthermore, a new user called “testsvn” was created and given ITM membership rights similar to those of regular ITM users.

Notes:

- In order to be able to manipulate the access rights of a particular user he/she must become a member of the project (it is not possible to change the rights for a user who is not a member of a project)
- Groups are not part of GForge. The “itm_members” pseudo-group is just a trick that can be translated as “every itm member becomes a restricted, hidden, member of the project”. Therefore it is somewhat equivalent to manually adding each user to the project, the only difference being that these users are not actually visible and only “itm_members” virtual user is shown.

- When ACLs are modified it take a maximum of 30 minutes (typically 15) in order to become effective.

The following test use cases were considered:

1) Add write permission for a user who already has read permission as member of a group

Since “testsvn” is member of itm_members group, it already has read access to the repository. However, it does not have write access to any directory.

In order to give write permissions to “testsvn” the user must first join the project. When the project admin approves the request, he can make the “testsvn” user member of “Software Developer” role, thus giving it write access to the repository, without the need to further define additional ACLs.

2) Limit access to a subdirectory to single users and/or subgroups

For the purpose of this test, it is assumed that the “testsvn” user is not a member of the project, but is still a member of the “itm_members” pseudo-group (like it was the case prior to the changes indicated at 2.1. above).

In order to limit read access for “itm_members” to the “/tags” subdirectory, two new ACLs are required:

a) For directory “/” itm_members is set to “no access”

b) For directory “/tags” itm_members is set to “read”

At this point, user “testsvn” can checkout from http://gforge.efda-itm.eu/svn/gforge_acl/tags and read everything under this directory, but the user is unable to checkout from /trunk or any other directories that are not under /tags. This applies for every member of itm_members that is not a member of the project.

In order to give write access to user “testsvn” to the repository/parts of the repository, the user must first join the project and approved as a “Software developer”. Afterwards, for each defined ACL, the project admin must click on “Edit permissions” and “Submit”. This confirms adding the new user to the defined set of ACLs. Of course, read or write access can be given to the user. By default, the user will have write access.

3) Cancel read access for a single user to a specific directory

In order to cancel the read access for a particular user, the corresponding ACL must be set to “no access”. This will simply remove the user from the ACL and thus it must be used with care since the user may be member of another top-level ACL that would give him read/write access. Also, the user must be member of the project in order to manipulate his ACLs. Warning: Since all users are members of itm_members, it is not possible to define something like “All itm_members have read access to /tags, however testsvn does not”. In order to do this, it is necessary to manually add each user to the project, except “testsvn”, thus manually doing what

the “itm_members” pseudo-group did. Of course, in this case the “itm_members” must be removed from the project members.

Since a certain user can appear twice (or more) into an ACL, due to its membership to various groups, it became clear that a certain order must be applied. Otherwise, it is uncertain what permissions a particular user will have when the ACL is formed by combining various user groups.

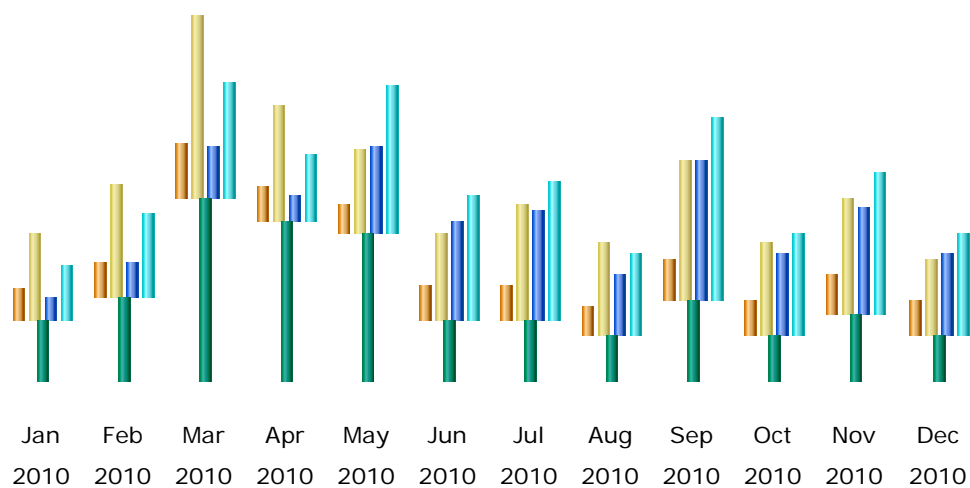
This was achieved by writing and applying a patch on the file used to generate the actual ACL from inside Gforge.

Tables 1 and 2 offer a view on the overall traffic on Portal and Gforge machines.

The Portal and Gforge usage has considerably increased since the first months of the year. This will most likely require in the future new techniques for storing and offering access to the data. Combined with complex ACLs inside Gforge, this requires a lot of computing power since the ACLs must be verified and enforced on each file accessed from SVN.

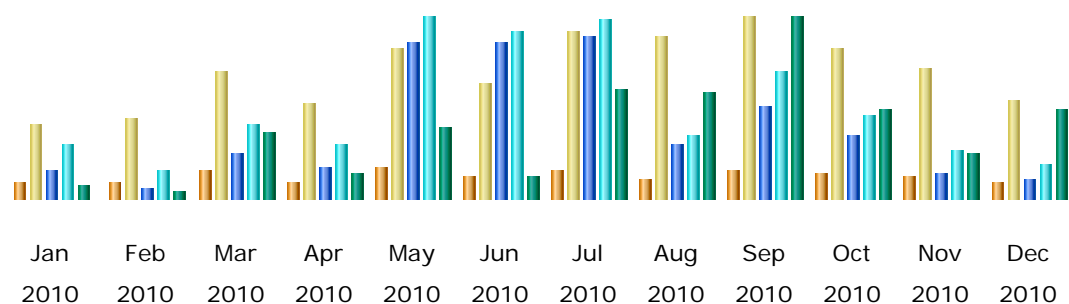
A Catalog Querying Tool was developed and installed on the Portal machine in order to give web access to the Catalog Database. Currently there is no data stored in the database but its structure is available inside a MySQL database.

The web interface allows for searching through the database tables and to paginate results. Details will be available for each data entry. In order to allow easy integration of this tool with other, more complex tools, a web service interface was used for actually accessing the data. Therefore, the graphical interface is decoupled from the data access mechanism. The graphical interface is represented by a set of PHP pages displaying the data, while the query mechanism is represented by a web service based interface, that directly communicates with the MySQL engine.



Month	Unique visitors	Number of visits	Pages	Hits	Bandwidth
Jan 2010	178	468	8654	22851	275.37 MB
Feb 2010	197	634	13582	34242	389.20 MB
Mar 2010	292	1002	20866	48314	850.67 MB
Apr 2010	199	637	10476	28058	753.21 MB
May 2010	166	467	36025	61641	697.60 MB
Jun 2010	187	470	41667	51452	287.69 MB
Jul 2010	195	635	45528	58112	279.26 MB
Aug 2010	149	515	25302	33634	212.06 MB
Sep 2010	228	778	57847	75040	386.61 MB
Oct 2010	196	512	32640	42396	225.44 MB
Nov 2010	214	642	44546	58827	317.10 MB
Dec 2010	183	420	33415	41859	211.68 MB
Total	2384	7180	370548	556426	4.77 GB

Table 1 - ITM Portal usage report for the period Jan-Dec 2010



Month	Unique visitors	Number of visits	Pages	Hits	Bandwidth
Jan 2010	54	225	13976	29658	2.65 GB
Feb 2010	51	236	5852	14356	1.68 GB
Mar 2010	84	379	24520	40233	14.42 GB
Apr 2010	48	286	16063	28230	5.56 GB
May 2010	96	453	82663	95508	15.54 GB
Jun 2010	67	345	81925	89226	5.26 GB
Jul 2010	86	503	85433	95038	24.37 GB
Aug 2010	60	489	29588	33131	23.70 GB
Sep 2010	85	541	49711	67527	39.75 GB
Oct 2010	76	452	33283	44119	19.78 GB
Nov 2010	61	393	13297	25904	10.35 GB
Dec 2010	54	294	10040	17841	19.81 GB
Total	822	4596	446351	580771	182.87 GB

Table 2 - ITM Gforge usage report for the period Jan-Dec 2010

PLASMA WALL INTERACTION

SHEATH PROPERTIES AND RELATED PHENOMENA OF THE PLASMA WALL INTERACTION IN MAGNETISED PLASMAS. APPLICATION TO ITER

V. Anita, C. Agheorghiesei, S. Costea, C. Costin, G. Popa, L. Sirghi, M. L. Solomon

“Alexandru Ioan Cuza” University of Iași, Romania

Overview

Electrical plasma diagnostics were performed for Pilot-PSI linear machine using 61 plane probes inserted in the middle of target, under the EFDA PWI Task Force (WP10-PWI-04-04/BS). A series of 2D recordings of floating potential and grounded probes electrical currents depending on the magnetic field induction (0.4 to 1.6 T) and discharge current intensity (80-140 A) were performed. Using a 3-grid electrostatic analyzer was able to obtain the energy distribution function of ions. These energy distribution functions recorded have shown thermal energy of ions around 1 eV.

Electrical diagnostic measurements have been carried out in COMPASS tokamak (IPP Prague), using an array of 39 Langmuir probes embedded in the divertor. Temporal evolutions of the floating potential and ion saturation currents were measured. Current-voltage characteristics of the probe were also recorded in order to estimate the electrons temperature. A new divertor probe array was designed to serve for toroidal correlation measurements.

Two numerical codes (2D both) based on the fluid model and on the PIC-MCC technique (PLUIAC), were used for the simulation of the plasma column of Pilot-PSI.

Publications

- [1] M. L. Solomon, V. Anita, C. Costin, I. Mihaila, L. Sirghi, G. Popa, M. J. van de Pol, R. S. Al, G. J. van Rooij, J. Rapp, “2D distributions of current and floating potential at the target surface in Pilot-PSI”, 37th European Physical Society (EPS) Conference on Plasma Physics, 21-25 June 2010, Dublin, Ireland (poster presentation)
- [2] M. L. Solomon, V. Anita, C. Costin, I. Mihaila, L. Sirghi, G. Popa, M. J. van de Pol, G. J. van Rooij, J. Rapp, “Current and floating potential distributions measured by a multi-probe system at the end plate surface in Pilot-PSI”, 15th International Conference on Plasma Physics and Applications (CPPA), Iasi, Romania, 1-4 July 2010 (poster presentation P6-07)
- [3] M. L. Solomon, V. Anita, C. Costin, I. Mihaila, G. Popa, H. J. van der Meiden, R. S. Al, M. van de Pol, G. J. van Rooij, J. Rapp, “Multi-channel analyzer investigations of ion flux at the target surface in Pilot-PSI”, *Contrib. Plasma Phys.* 50(9), 898-902 (2010)

Detailed results

1. Methods

Characterisation of Pilot-PSI plasma beam by electrical methods (electrostatic analysers).

A multiple plane probe system installed in the centre of Pilot-PSI target (at FOM, The Netherlands) was used mainly for two types of measurements: i) plasma current drawn by the grounded collectors and ii) floating potential of the collectors. The measurements were performed for different experimental conditions: H gas flow of 3 slm, magnetic field strength $B = 0.4, 0.8$ and 1.2 T and different plasma-source currents $I_S = 80, 100, 120$ and 140 A.

Plasma diagnostic in the Scrape-off Layer of COMPASS tokamak by electrical probes.

Two sets of plasma diagnostics, based on probes, are already installed on COMPASS tokamak (at IPP Prague, Czech Republic): the Langmuir probe array embedded in the divertor tiles and the midplane reciprocating probe.

Theory and modelling: Development of a 2D PIC-MCC model for linear magnetised plasma devices; development of a 2D fluid model for simulation of Pilot-PSI device.

The PIC-MCC code was adjusted to study plasma parameters in front of a solid surface, with direct application to Pilot-PSI target. The combined fluid models for charged particles (electrons and positive ions) and neutrals, written for Ar and H, were applied for modelling of the plasma column produced in Pilot-PSI.

2. Results and discussion

Multi-probe system – current measurements at the target.

Our experiments were correlated with temperature measurements on the surface of the target by using a non contact method (infrared camera). These measurements revealed a very high increase of the target surface temperature in the centre and a sharp decrease on the edge of the target. The surface temperature is influenced by both the plasma source current and the applied magnetic field strength. The measured values varied between 320 °C (at 80 A and 0.4 T) and 2500 °C (at 140 A and 1.2 T). These measurements indicate very difficult conditions for electrical diagnosis devices in Pilot-PSI.

The currents flowing through a compact copper target (grounded) were measured with a digital oscilloscope as the voltage drop on a resistor. In the case of $B = 0.4$ and 0.8 T the registered target current was maximum at the plasma-source current of 120 A. In the case of 1.2 and 1.6 T the target current increased continuously with the increase of the plasma-source current (*e.g.* from 5.11×10^4 A/m² at 80 A to 7.08×10^4 A/m² at 140 A, for $B = 1.2$ T).

The 61 plane probe system (0.63mm^2 single electrode area) was used to measure the radial variation of the current density on the target. The probes were protected by a carbon plate

of 38 mm in diameter, in contact with high density plasma. Fig. 1 shows the variation of the probe current density with the radial position from the centre of the plasma beam, having the discharge current intensity I_S and the applied magnetic field B as parameters (grounded probes). The results revealed a very non uniform current density distribution on the target surface.

An example of 2D distribution of the current intensity measured for a magnetic field strength of 0.8 T is plotted in Fig. 2. The negative values of the measured currents are related to the electron dominated current received by the grounded collectors. The 2D distributions showed a good cylindrical symmetry and a strong radial gradient of the current could be noticed in all cases. The maximum of the current distribution is recorded almost in the centre of the target. The increase of the magnetic field creates a better plasma confinement, reflected in a strong amplification of the measured electric current intensity and steep radial gradients. The maximum values of the measured currents intensity were ~ 2.4 A at 0.4 T and ~ 4.8 A at 0.8 T, in the centre of the plasma column. The multi-plane probe system worked well up to 1.2 T but the central probe was melted at 1.6 T as a consequence of the high current density determined by the confinement of the plasma beam at this high magnetic field.

Multi-probe system – floating potential measurements at the target.

An example of 2D floating potential distribution measured for a magnetic field strength of 0.8 T is plotted in Fig. 3. A good cylindrical symmetry is also noticed on the 2D floating potential distributions. The measured floating potential ranges between ~ 0 V at the side of the beam and -70 V at 0.4 T up to ~ -165 V at 0.8 T in the centre of the plasma column. An increase of the total discharge current was observed to decrease the floating potential at the target.

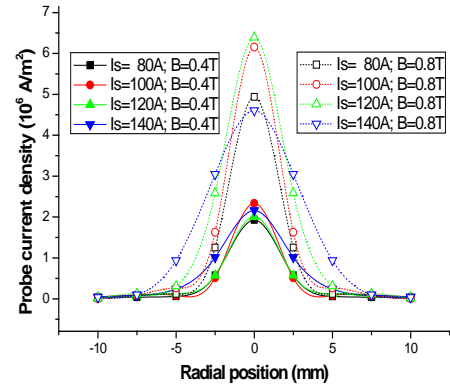


Figure 1 – Radial variation of the probe current (with I_S and B – parameters)

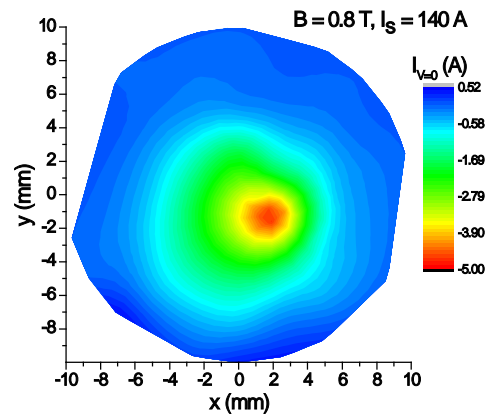


Figure 2 – 2D distribution of the current intensity for $I_S = 140$ A and $B = 0.8$ T

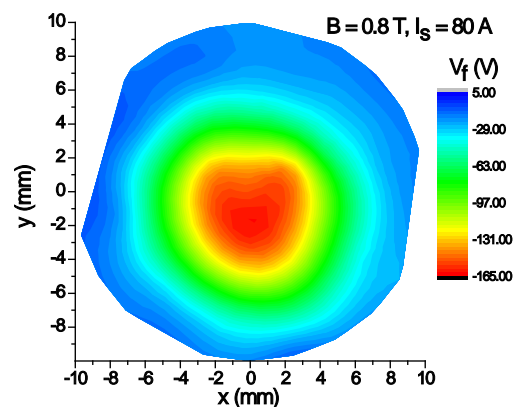


Figure 3 – 2D distribution of the floating potential for $I_S = 80$ A and $B = 0.8$ T

The magnetic field dependence is explained by a decreasing cross field conductivity. Both floating potential and current intensity followed the time evolution of the magnetic field during its switching-on/off. To determine the electron temperature and density in the plasma column, Thomson scattering measurements were made by FOM researchers simultaneously with the electrical measurements.

Cross-correlation signal analysis.

In signal processing, cross-correlation is a measure of similarity of two waveforms as a function of a time-lag applied to one of them. If the cross-correlation signal has a well defined peak it means that the two functions are similar and the time-lag value corresponding to the peak indicates the delay between the two functions. In the case of the cross-correlation of a signal with itself (called auto-correlation), there will always be a peak at a lag of zero. This analysis technique was applied to study the time correlation between the current intensity signals measured by different collectors of the analyzer. The main purpose of this analysis was to study the rotation of the magnetized plasma column. The tungsten probes were arranged on four concentric circles of different radii (2.5, 5, 7.5 and 10 mm). We chose a reference collector on the 3rd circle and we calculated the cross-correlation between the signals measured on that collector and six other collectors of the same circle (3 successive collectors before and 3 after). It was noticed that all 6 signals are correlated with the reference one and the delay between each two neighbour signals is 1 μ s. This confirms that the plasma column rotates and the distance between two adjacent collectors from the third circle is covered in 1 μ s.

The corresponding rotation velocity at the radial position of 7.5 mm is about 2.6 km/s. It has to be mentioned that the data acquisition frequency was 1 MHz meaning that the time delay between 2 consecutive acquired data on the same channel was 1 μ s. This places the result of the cross-correlation analysis at the limit of the time resolution, reflected in an imprecision of the calculated plasma rotation velocity of about 50%. The rotation of the plasma column could also be observed representing successive (1 μ s delay) 2D current intensity distributions.

Measurements with 3-grid electrostatic analyzer.

An ion energy electrostatic analyzer with 3 grids has been manufactured and also mounted in the centre of Pilot-PSI target. The stainless steel grids and the collector (disks of 10 mm in diameter) were mounted in a stainless steel Faraday cup. The active area of the analyzer was limited to a circular opening of 0.5 mm in diameter of a carbon diaphragm mounted in front of the grids. A biasing circuit and data acquisition system for analyzer I-V characteristics was built based on a source measuring unit (SMU) mounted on the XPI device of National Instruments. The SMU was controlled by home-made LabView software.

The electrostatic analyzer was biased with respect to the ground. The potential of the hydrogen plasma column during the confinement in the magnetic field was negative, between -10 V and -40 V as function of the magnetic field intensity and discharge current intensity. We

have successfully acquired I-V characteristics of the analyser which indicate that the thermal ion energies are spread into less than 1eV. The electrostatic analyzer was used only at $B = 0.4$ T and it was melted by plasma at a discharge current of 120 A. The main problem of this device was the overheating, which led to the melting of the grids. Further design research has to be made in order to improve the analyzer.

Measurements of the I-V characteristics of the Langmuir probes embedded in the divertor tiles of COMPASS tokamak.

The divertor Langmuir probe array consists of 39 probes disposed in poloidal direction with spatial resolution of 5 mm. The acquisition system allowed the simultaneous use of maximum 5 probes. These probes were used to directly measure the floating potential V_{fl} , the ion saturation current I_{sat} (probe bias in this case was -100 V with respect to the ground) or they were used in sweeping mode (+/-100 V at 1 KHz) in which case electron temperature could also be estimated. Measurements were performed either with all 5 probes in High Field Side / Low Field Side of the divertor or with the 5 probes spread along the array. Measured ion saturation current was in the range of tens mA and electron temperature of 10-20 eV was obtained from the ion part of the I-V characteristics. Both negative and positive values of the floating potential (of the order of tens V) were registered either on different shots or during the same shot. The existing divertor probe array allows correlation measurements in poloidal direction. In order to investigate the possible correlation of plasma parameters in toroidal direction a second probe array is necessary in the divertor region.

Design of the probe array for correlation measurements on the COMPASS tokamak.

The head of a second probe array was designed. It will be installed from the bottom of the vessel, in the high field side region of the divertor. The head will be made of carbon, sustaining about 20 cylindrical probes (tungsten wire) disposed in poloidal direction with 2.5 mm spatial resolution. The probe head will be shaped following the profile of the actual divertor probe array. The new probe array will cover the same poloidal region as the first 8 Langmuir probes of the actual array. In order to insert the second array inside COMPASS we will use an existing probe manipulator available from CASTOR tokamak.

Development of a 2D PIC-MCC model for linear magnetised plasma devices.

The plasma-source was simulated as electrons and positive ions (Ar^+) entering in the simulation space through a loading aperture of 1cm in diameter, carrying a fraction f of the measured plasma-source-current. This fraction is a scaling factor for the simulation code. In Fig. 4 are compared two current-voltage characteristics of Pilot-PSI target, an experimental one and the second obtained from simulation.

The simulation reproduces the experimental results when the scaling factor f is $1/2$, meaning that in the case of a plasma-source current of 90 A, only half of this current is carried by the plasma column at 10 cm in front of the target. The numerical simulations were performed on 2CPU (4 cores) linux computing machine using POSIX multithreads parallel code. Part of the simulation code was adapted from Berkley's Plasma Simulation Group XOOPIC [1].

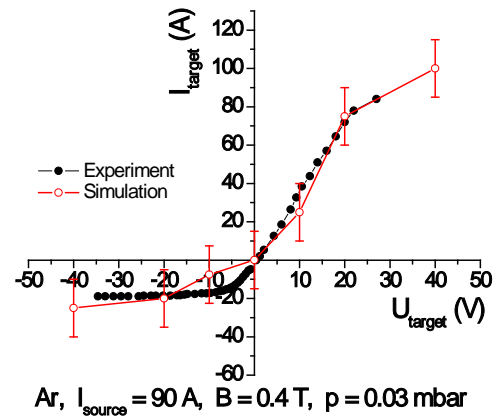


Figure 4 – Experimental and numerical simulation of the target I-V characteristic in Pilot-PSI

Development of a 2D fluid model for the simulation of Pilot-PSI device.

Radial and axial distributions of plasma parameters, such as plasma potential, charged particle densities and fluxes could be obtained. The major inconvenient of this approach is its limitation with respect to plasma density. The code can deal with maximum plasma density of the order of 10^{11} cm^{-3} which is at least two orders of magnitude lower than in Pilot-PSI. A higher plasma density requires at the same time the use of a space grid with very small cells (linear dimension of the order of the Debye length, which for a plasma density of 10^{11} cm^{-3} and electron temperature of 1 eV is $\sim 20 \mu\text{m}$) and very small time steps ($< 10^{-13} \text{ s}$, imposed by the CFL stability criterion [2] and by the Maxwell time characterising the electric field relaxation [3]). Working with such parameters would lead to the necessity of huge computer resources and extremely long computing time, which overtakes our facilities.

3. Conclusion

In 2010 plasma diagnostic experiments were focuses on two specific objectives: (i) characterisation of Pilot-PSI plasma beam by electrical methods (electrostatic analysers) and (ii) plasma diagnostic in the Scrape-off Layer (SOL) of COMPASS tokamak by electrical probes.

Two different numerical codes were developed and used in order two complete the specific objectives for theory and modelling: a 2D PIC-MCC model and a 2D fluid model for the simulation of linear magnetised plasma devices.

Acknowledgement

C. Agheorghiesei would like to thank to Berkley's Plasma Simulation Group for allowing him to use the XOOPIC code as starting point for developing his own PIC-MCC simulation code.

References

- [1] J. P. Verboncoeur, A. B. Langdon and N.T. Gladd, *Comp. Phys. Comm.* 87, (1995) 199-211.
- [2] R. Courant, K.O. Friedrichs and H. Lewy, *IBM Journal* 11 (March 1967) 215.
- [3] M.S. Barnes, T.J. Colter and M.E. Elta, *J. Appl. Phys.* 61 (1987) 81.

STUDY OF THE THERMAL TREATMENT INFLUENCE IN FORMATION OF THE STABLE BE-C, BE-W AND C-W ALLOYS. TVA GUN ELECTRON BEAM IRRADIATION INFLUENCE

C. P. Lungu, A. Anghel, C. Porosnicu, I. Jepu, A. M. Lungu, P. Chiru, C. Ticos, C. Luculescu

National Institute for Laser, Plasma and Radiation Physics, Bucharest

Overview

Since the operation conditions for the nuclear fuel removal in a fusion power plant like ITER involves wall baking at higher temperatures of the plasma facing components - i.e. 515 K for the first wall and 623 K for the divertor area - it is important to know how this thermal treatment procedures will affect the materials' properties. It was observed that by heating at 623 K, the carbon from the graphite substrate diffuses into the deposited beryllium film forming a mixed layer of Be, BeO and Be₂C at the interface, while the oxygen present at the Be-C interface diffuses to the surface of the film. Comparing the results obtained by Nuclear Reaction Analysis we observed that the deuterium implanted after annealing was retained in deeper layers in the case of thermally treated samples due to the structural changes induced in the films by the Be/C mixed layer formation and the effects of the oxygen diffusion into the thermal treated films.

Publications

- [1] Cristian P. Lungu, *TVA gun electron beam irradiation influence on mixed films prepared using TVA method*, Report on task agreement WP10-PWI-06-01-02/MEdC/PS at TF-PWI annual Meeting, 3-5 Nov 2010, Vienna, Austria
- [2] A. Anghel, C. Porosnicu, C. P. Lungu, K. Sugiyama, C. Krieger, J. Roth, *Influence of Thermal Treatment on Beryllium/Carbon Formation and Fuel Retention*, Journal of Nuclear Materials, In Press, Corrected Proof, Available online 6 February 2011, [doi:10.1016/j.jnucmat.2011.01.131](https://doi.org/10.1016/j.jnucmat.2011.01.131).
- [3] K. Sugiyama, J. Roth, A. Anghel, C. Porosnicu, M. Baldwin, R. Doerner, K. Krieger, C.P. Lungu, *Consequences of Deuterium Retention and Release from Be-containing Mixed Materials for ITER Tritium Inventory Control*, Journal of Nuclear Materials In Press, Corrected Proof, Available online 8 October 2010 [doi:10.1016/j.jnucmat.2010.09.043](https://doi.org/10.1016/j.jnucmat.2010.09.043).

Detailed results

1 Methods

1.1 Introduction

In magnetic confinement fusion devices, plasma facing components are subject to heat and particle fluxes that strike the first wall either continuously or in bursts. The effect on the wall

surface is usually tolerable in present facilities but in future fusion power reactors the power load will be much higher and the duration of the plasma discharges much longer. The potential scale of the damage to the first wall challenges fusion research and technology, particularly for the development of the divertor. Even when most of the power of the plasma is exhausted in volumetric processes, some plasma facing components will have to withstand peak temperatures of more than 1300 K, despite being actively cooled.

On the other hand, it was established that baking the inner walls of the chamber at 515 K and 623 K for the divertor area is a solution for the nuclear fuel removal from the plasma facing components [1-3].

It is important to expand the knowledge how the thermal treatments and the heat loads will influence the materials which will be used as plasma facing components (Be, W, C) and their compounds. In this report, the influence of thermal treatment on Be-C mixed material formation and deuterium retention under controlled laboratory conditions is studied.

1.2 Sample preparation

The beryllium films were deposited on mirror polished fine grain graphite substrates using the thermionic vacuum arc (TVA) technology developed by the research group.

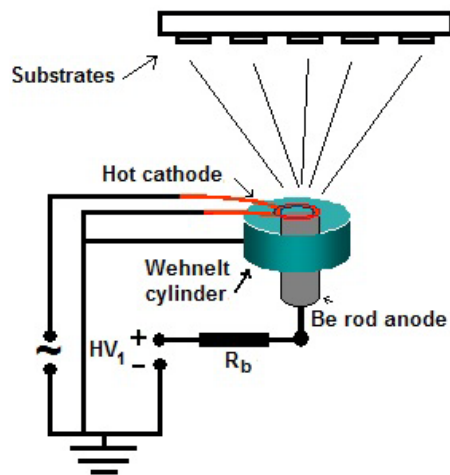


Figure 1 – Schematic representation of the thermionic vacuum arc (TVA) deposition method

The TVA technique involves preparation of thin films from the pure vapors of the metal to be deposited without using any buffer gas [4-5]. The TVA principle scheme is presented in Fig. 1, as well as in the previous published papers [4-5].

1.3 Thermal treatment, deuterium ion implantation and retention analysis

After the deposition, the composition of each sample was analyzed by Rutherford Backscattering Spectrometry (RBS) using a 2.6 MeV $^4\text{He}^+$ ion beam in the Tandem Accelerator available at IPP – Garching, Germany [6], confirmed by X-ray Photoelectron Spectroscopy – XPS, [7] and then annealed at 623 K in high vacuum conditions, at around 10^{-5} Pa, using the

thermal desorption spectroscopy (TDS) setup in IPP-Garching. The temperature ramp rate was $\approx 0.25 \text{ K}\cdot\text{s}^{-1}$ from room temperature to 635 K. Counting that the mixing of beryllium and carbon in the interface area it is a time dependent process, the samples were kept at this temperature for different time scales, 30, 60 and 90 minutes respectively. Other samples were annealed up to the temperature of 1000 K. After annealing, the composition depth profiles of the samples were determined by RBS (using the SIMNRA code) and XPS depth profile measurements.

Deuterium ion implantation into thermally treated samples was performed in the High Current Ion Source at IPP-Garching. The energy of the D ion beam was 600 eV D_3^+ , meaning 200 eV/D. The implantation fluences were up to $\sim 2 \times 10^{23} \text{ D}\cdot\text{m}^{-2}$. This value corresponds to the expected fluence to the ITER first wall after 400 s discharge with the flux of $\sim 3 \times 10^{19} \text{ D}\cdot\text{m}^{-2}\cdot\text{s}^{-1}$. The incident angle was normal to the target surface, and the implantation temperature was set as room temperature.

After the implantation, the deuterium retained profiles were determined using the $\text{D}({}^3\text{He}, \text{p}){}^4\text{He}$ nuclear reaction before the TDS measurements.

2. Results and discussion

Figure 2 shows a typical depth profile of the as-deposited beryllium films on graphite substrates using the TVA technique. It can be seen that the only impurity found in the film was the oxygen, below 5 at %, present as BeO as the XPS measurements revealed. An increase in the oxide amount was observed at the films surface, due to atmosphere exposure of the samples after the deposition, but also at the Be-C interface, due to the residual oxygen content present in the chamber in the beginning of the deposition process.

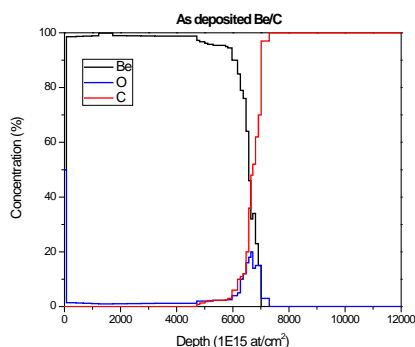


Figure 2 – Elemental composition depth profile of an as deposited Be film obtained by RBS.

Figure 3 shows the RBS elemental depth profiles obtained for the samples thermally treated in high vacuum at 623 K during 30, 60 and 90 min respectively. As it can be seen, even the annealing of the samples for only 30 minutes induces changes at the interface, where a mixture of Be, Be_2C and C was found. It is known that at the chosen temperature of 623 K, beryllium carbide (Be_2C) formation starts, in agreement with [8]. Also, it was observed that the oxygen coming from the graphite substrate migrates into the Be film leading to the formation of a

thicker beryllium oxide layer at the interface. Increasing the annealing time to 90 minutes, the mixed material layers present at the interface becomes thicker as well as the oxide.

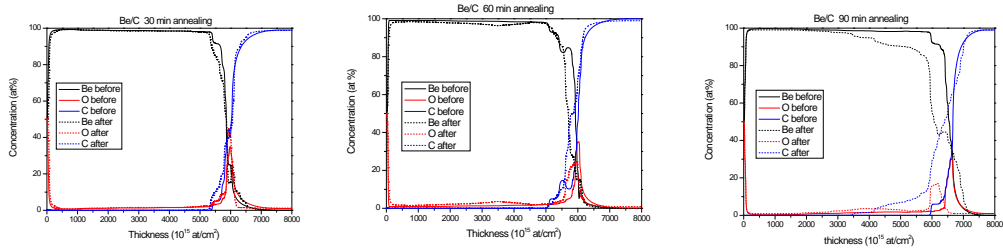


Figure 3 – Elemental composition depth profiles of Be films annealed at 623 K for 30, 60 and 90 min time scales obtained by RBS.

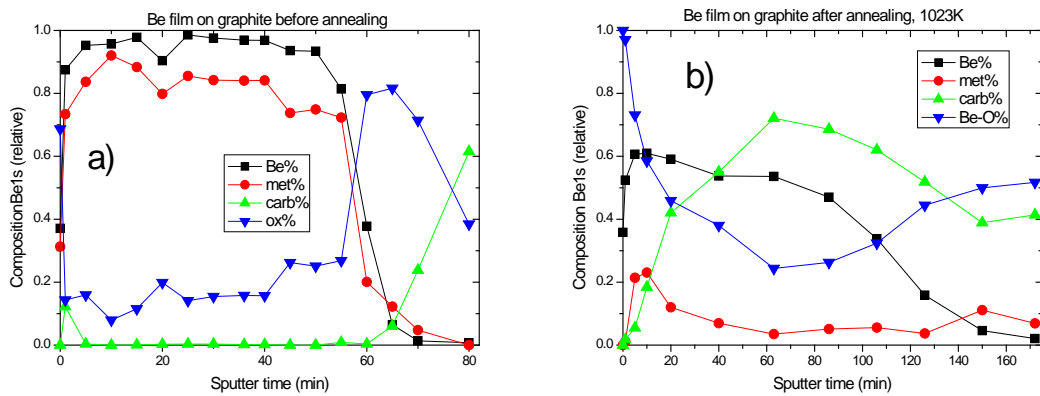


Figure 4 – XPS depth profiles of Be films on graphite before (a) and after (b) annealing at 1023 K

After annealing the samples at ~ 1023 K it was found out that the entire Be film became a mixture of metallic Be, BeO and Be₂C. In Fig. 4, the XPS depth profile shows, for comparison, the distribution of chemical states of Be in the film before and after annealing to 1023 K. These results are in good agreement with the RBS measurements performed.

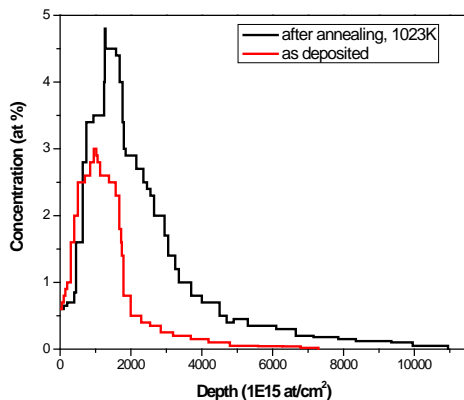


Figure 5 – Deuterium depth profiles before and after thermal treatment at 1023 K.

No significant differences were observed in deuterium retention between the samples annealed at 623 K due to the thickness of the Be films of $\cong 500$ nm, which was larger than the deuterium implantation range of about 200 nm. The smaller differences observed, meaning a decrease in the total amount of deuterium retained in the film while increasing the annealing time, are attributed to the surface oxide layer which acts like a barrier.

A significant change in the retention behavior was observed for the samples annealed at 1023 K. For explanation, Fig. 5 shows the deuterium depth profiles obtained by NRA measurements before and after the thermal treatment. For that sample a fluence of 5×10^{18} D·cm⁻² was used for implantation and the NRA measurements revealed that for the as-deposited sample a total amount of $2,9 \times 10^{16}$ D·cm² was retained while for the annealed sample the deuterium amount increased to 1×10^{17} D·cm². Also, in the case of thermally treated sample, the distribution of the deuterium in the film changes by means that the implantation depth becomes higher compared to that of the pure beryllium film. This behavior is related not only to the Be-C mixed material formation but also to the increase in the BeO concentration in the near surface area.

Further investigations regarding the deuterium retention as well as the desorption behavior of films thinner than D ions implantation depth range (≈ 100 nm) are ongoing in order to obtain information about the influence of mixed material formation by thermal treatment at 623 K.

3. Conclusion

The influence of thermal treatment at 623 and 1023 K of beryllium films deposited on graphite by TVA method by means of changes induced at the interface as well as the deuterium retention was investigated.

It was found out that by annealing the samples at 623 K a mixed material layer appears at the interface. The thickness of this mixed layer increases while increasing the annealing time. Also an increase of the beryllium oxide amount present in the film was observed while the annealing time increases. This behavior is caused by the migration toward the Be film of the oxygen present in the graphite substrate and the large affinity between beryllium and oxygen. The XPS measurements confirmed that the mixed layer consists of pure Be, BeO and Be₂C. By deuterium retention measurements only small changes caused by the surface beryllium oxide layer were observed.

By thermal treatment of the samples at 1023 K the mixed material layer extends to the whole film, changing the retention behavior. The total deuterium amount retained in the annealed films increases with an order of magnitude for the same implantation fluence.

Acknowledgement

The reported work includes contributions from the following people outside the EUATOM-MEdC Association: K. Sugiyama, J. Roth, K. Krieger (Max-Planck-Institut für Plasmaphysik, *IPP-EURATOM Association*, Garching, Germany).

References

- [1] R A Pitts, A Kukushkin, A Loarte, A Martin, M Merola, C E Kessel, V Komarov and M Shimada, *Phys. Scr. T138* (2009) 014001.
- [2] T Tanabe, N Bekris, P Coad, C.H Skinner, M Glugla, N Miya, *J. Nucl. Mater.*, 313-316 (2003) 478.
- [3] N. Bekris, C. H. Skinner, U. Berndt, C. A. Gentile, M. Glugla, A. Erbe, W. Pilz, *J. Nucl. Mater* 329-333 (2004) 814.
- [4] C. P. Lungu, I. Mustata, V. Zaroschi, A. M. Lungu, A. Anghel, P. Chiru, M. Rubel, P. Coad G. F. Matthews and JET-EFDA contributors, *Phys. Scr. T128* (2007) 157.
- [5] A. Anghel, I. Mustata, C. Porosnicu, C. P. Lungu, *J. Nucl. Mater.* 385 (2009) 242.
- [6] J. Roth, D. S. Walsh, W. R. Wampler, and M. Mayer, *Nuclear Instruments and Methods in Physics Research Section B: Beam Interactions with Materials and Atoms*, 136-138, (1998), 689.
- [7] K. Schmid, A. Wiltner, Ch. Linsmeier, *Nuclear Instruments and Methods in Physics Research Section B: Beam Interactions with Materials and Atoms*, 219-220, (2004), 947.
- [8] F. Kost, Ch. Linsmeier, M. Oberkofler, M. Reinelt, M. Balden, A. Herrmann, S. Lindig, *J.Nucl. Mater.* 390-391 (2009) 975.

X-RAY MICRO-TOMOGRAPHY STUDIES ON GRAPHITE AND CFC SAMPLES FOR POROSITY NETWORK CHARACTERIZATION

I. Tiseanu, T. Craciunescu, C. Dobrea, A. Sima

National Institute for Laser, Plasma and Radiation Physics, Bucharest-Magurele

Overview

Quantitative characterization of the porosity structure of the carbon reinforced carbon fibre (CFC) materials is carried out by high resolution cone-beam X-ray micro-tomography (CB μ CT). It is shown that CB μ CT provides useful information pertaining to the in-depth fuel migration into carbon tiles function of the CFC material structure. The investigated materials comprised two types of non-irradiated CFC samples (former ITER reference CFC NB31 and JET CFC DMS780) and a series of CFC N11 samples in the frame of the Deuterium Inventory in Tore Supra (DITS) *post-mortem* analysis. A procedure for the quantitative evaluation of the CFC sample porosity factor has been introduced and tested. Useful information about the pores connectivity and also about the metal impregnation inside the CFC macroscopic pores penetration of metallic structures along fibre interspaces, in case of heat sink region of the TS DITS CFC, can be retrieved. The method can be used for the quality control monitoring of the new CFC ITER reference materials.

Publications

- [1] Tiseanu, E. Tsitrone, A. Kreter, T. Craciunescu, T. Loarer, B. Pégourié, T. Dittmar, X-Ray Micro-Tomography Studies on Carbon Based Composite Materials for Porosity Network Characterization, Fus. Eng. Des. (in print), DOI: [10.1016/j.fusengdes.2011.04.079](https://doi.org/10.1016/j.fusengdes.2011.04.079).

Detailed results

1. Introduction and Objectives

The carbon reinforced carbon fibre (CFC) monoblocks of the ITER divertor vertical target must sustain high heat fluxes of 10 MW/m² during 400 s (normal operation) and up to 20MW/m² during 10 s (off-normal event). CFCs have a unique combination of high conductivity, low Z and resistance to damage induced by the high heat loads. Given the demanding environmental requirements of the ITER divertor, specially developed CFCs are needed as plasma facing components (PFC) materials.

The problem of fuel (tritium) retention in a carbon material is a major concern due to its radioactivity and inventory constraints within the ITER installation. So far, most data on fuel retention were obtained in all-carbon machines, so that comparison with carbon free machines

(all-W ASDEX Upgrade, future ITER like Wall in JET) needs to be performed for better prediction in ITER conditions. Scaling of the retention rate as function of plasma/ machine parameters (injection rate, incident flux/fluence, PFC materials, PFC temperature) is only poorly characterized. Albeit the main retention mechanisms have been identified (such as the co-deposition with C and/or Be, bulk diffusion and trapping in CFC and W) their relative contributions in ITER conditions are still uncertain being subject of active research, from laboratory experiments, modeling as well as integrated tokamak experiments [1,2]. According to earlier investigations, the retention in the material bulk was considered to be less critical than the retention in co-deposited layers. Even if the DITS experiment showed that bulk retention concerns only ~10% of the total permanent retention in Tore Supra [3,4], techniques are envisaged to remove the deposits from removed areas (and thus recover the fuel stored in these deposits), when it will be definitely impossible to recover the fuel trapped in the bulk of the CFC constituting the PFCs. This bulk retention was demonstrated to be due to a-C:H layers deposited in the pores of the CFC ([5]~10-15% of voids due to porosity for the CFC N11).

It is expected that an accurate 3D porosity description of the CFC materials would provide an essential input for the quantization of the fuel retention in the material bulk. Here, the problem of the quantitative characterization of the porosity structure of CFC materials is addressed by means of high resolution X-ray micro-tomography (XCT) The non-invasive inspection was pursued on samples with or without refractory/marker metal coating, on non-irradiated or on *post-mortem* samples. The main challenge is posed by the required micron range of the spatial resolution for rather macroscopic samples.

2. Experiments and Results

2.1 Experimental setup

Most experiments were carried out at our newly upgraded X-ray tomography facility [6]. X-ray fluorescence analysis for the determination of samples composition was performed with our newly developed instrument *Tomo-Analytic* [7]. The instrument combines a 3D X-Ray microtomograph with a microbeam fluorescence system. The microbeam fluorescence component is a configurable elemental composition mapping tool, including optical X-ray beam collimation.

2.2 CT optimization

We have measured three types of CFC samples: former ITER reference CFC NB31, JET CFC DMS780 and a series of CFC N11 samples in the frame of the DITS post-mortem analysis. For reference a porosity free fine-grain graphite EK98 sample was also scanned.

Moderate resolution measurements of CFC samples at voxel resolution of approximately 7 μm , with an estimated minimum detectable feature of ~7-10 μm , were devoted to the optimization of the X-ray source and detection parameters.

Once the optimum parameters have been determined, high resolution measurements (~ 2.5 $\mu\text{m}/\text{voxel}$) were performed by the proprietary, recently developed, “offset tomography” (Off-CT) technique. Using multiple scans of the investigated object, Off-CT is able to almost double the magnification factor and therefore doubling the space resolution for a given detector size. While the maximum resolution of 2.5 $\mu\text{m}/\text{voxel}$, on a relatively large sample ($5 \times 5 \times 5$ mm^3), is a remarkable performance, the images noise might be a perturbation factor for the accurate porosity factor evaluation. In order to reduce the image noise two steps were considered: 1) reduction of reconstruction artefacts like “ring artefacts” [8] and “beam hardening artefacts” [9] and 2) upgrade the irradiation head of our X-ray tube with a high power diamond target for improved photon statistics. The diamond target allows for a ten-fold increase in the thermal conductivity as compared to the conventional transmission targets. As a result, high energy electron beams can be kept in focus to maintain the small focal spot size required for high image resolution. Using a JIMA mask, the test pattern of 2 μm can be clearly resolved even for a target power up to 20 Watts. As part of the optimization experiments, we have also installed a low contrast X-ray target which consists on a thin molybdenum layer on a beryllium window. This configuration has been used for the scanning of relatively small and X-ray transparent samples currently provided within the DITS project.

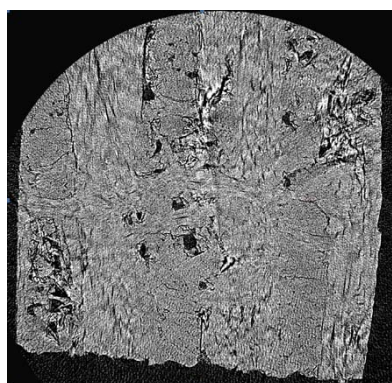


Figure 1 - Tomographic cross-section at 2.5 $\mu\text{m}/\text{voxel}$ for NB31 CFC sample. The tomographic reconstruction was obtained using the Off-CT scanning technique.

A set of up to 1440 radiographies at equidistant angles have been used for the high resolution fully 3D tomography. Fig. 1 shows a representative tomographic image with voxel resolution of 2.5 μm of CFC of type NB31.

2.3 Porosity determination method

To determine the main CFC network porosity characteristics the 3D reconstructed volumes were further processed. For the quantitative analysis of the porosity structure in terms of total void fraction, network connectivity, wall thicknesses we used the powerful 3-D visualization and measurement software: VGStudioMax, Volume Graphics GmbH, Heidelberg, Germany, www.volumegraphics.com. The critical step in the data post-processing consist in finding an optimal choice for the threshold level, in order to create a correct border between CFC and porous regions (Fig. 2).

The porosity factor calculation procedure was applied for three types of CFC samples relevant for the fusion technology. The porosity factor values (Table 1) are in good agreement with the manufacturer nominal specifications. It can be remarked that the N11 porosity factor measured in the frame of the Deuterium Inventory in Tore Supra DITS *post-mortem* analysis is significantly higher than the one of the new, more advanced NB31 and DMS780 and the recently developed NB41CFC materials. An effort has been made to obtain very high resolution radiographies for the NB41CFC sample. Fig. 3 shows two images obtained at 1.66 micron/pixel and even at 0.63 micron/pixel. At 1.66 microns/pixel one can see very well the pitch fiber structure while at 0.63 microns/pixel one can distinguish individual carbon fibers.

Table 1 – The porosity factor for three CFC samples

Material	NB31	DMS780	N11	NB41
Porosity factor (%)	8.1	9.4	10.5÷12	6.4

It is remarkable the improvement of the porosity factor associated with the most advanced NB41 CFC material. One should note that the currently available DITS N11 CFC samples have a relatively small volume ($2 \times 2 \times 6 \text{ mm}^3$). These samples result from the cutting of CFC N11 Tore Supra tiles ($20 \times 20 \times 6 \text{ mm}^3$) in three slices of 2 mm each. The sample whose upper surface was in contact with the plasma is labeled "top", the one the closest to the Cu heat sink is the "bottom" sample." This might explain the rather large uncertainty of the porosity factors. We also plan to scan N11 samples with statistically significant volumes.

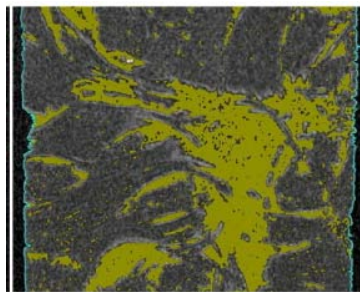
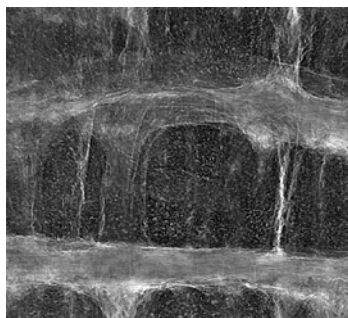
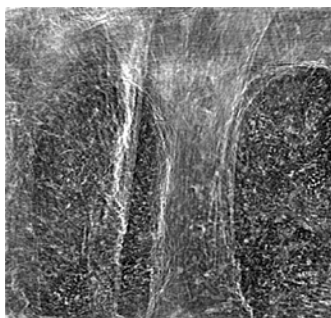


Figure 2 – Cross-section through the tomographic reconstruction of a DITS "top" sample after image thresholding for porosity factor calculation. Scanning parameters: HV=80 kV, I=150 μ A, target: Mo, focus spot size: <math><1.5 \mu\text{m}</math>, voxel resolution: 2.75 $\mu\text{m}</math>, cross-section width: 2 mm.$

Certainly, our current 3D micro-tomography reconstructions for the relatively large samples ($5 \times 5 \times 5 \text{ mm}^3$) of NB31 and DMS780 CFC could be considered a good basis for the characterization of the initial porosity of the new CFC ITER reference material NB41.



1.66 μm / pixel



0.63 μm / pixel

Figure 3 – High resolution digital radiography on NB41 CFC sample . At 1.66 microns/pixel one can see the pitch fiber structure. At 0.63 microns/pixel one can distinguish individual carbon fibers.

2.4 Tomography on CFC samples with metallic insertions (coatings)

Besides the evaluation of the porosity factor, tomographic reconstructions provided additional useful information concerning the morphology of the CFC samples. For example the penetration of metallic structures (Cu, Ti) along fibre interspaces can be revealed. The presence of Cu and Ti is due to the way the fingers of the TPL are built: the Cu heat sink and CFC tiles are joined using "Active metal Casting" [9]. Fig. 4 illustrate the investigation of the Cu heat sink region for DITS CFC samples.

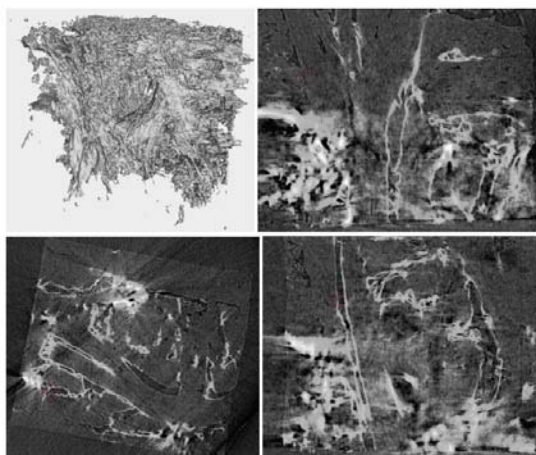


Figure 4 – Tomographic analysis of the Cu heat sink region of DITS “bottom” sample: 3D reconstructed volume (top-left), longitudinal (top-right), transversal (bottom-left) and sagittal (bottom-right) cross-section. Bright regions correspond to metallic structures present in the gaps between the main fibres. Scanning parameters: HV=90 kV, I=200 μ A, target: Mo, focus spot size: <1.5 μ m, voxel resolution: 2.75 μ m, cross-section width: 2 mm.

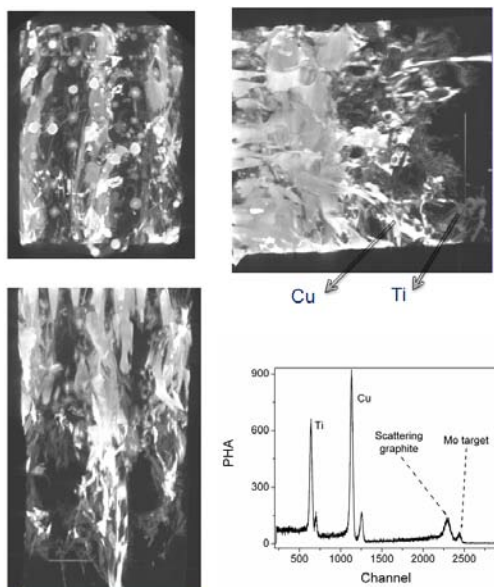


Figure 5 – Image fusion of axial (top-left), transversal (top-right) and sagittal (bottom-left) tomographic cross-sections. Bright regions correspond to Cu and gray regions correspond to Ti. X-ray fluorescence spectrum confirms the presence of Ti and Cu along the main fibres interspaces.

Despite the wide range of the X-ray attenuation coefficients displayed by this region which induces strong artefacts the tomographic analysis reveals a strong connectivity of the pores along the main fibre direction. It can be also observed that the pores are coated by a thin Ti layer and the metallic structures advance along main fibre direction interspaces up to 3 mm. To obtain an enhanced visualization of this phenomenon, additional image post-processing was performed. The image fusion obtained by summing the transversal, longitudinal and sagittal cross-section is presented in Fig. 5. The identification of the material composition was certified by the X-ray fluorescence analysis (see again Fig. 5).

3. Conclusion

High resolution cone beam micro-tomography was optimized for the analysis of CFC samples. An important result was the determination of the dependence of the porosity evaluation accuracy on the space resolution and the amount of tomography images noise. Following the optimization of both the measurement and reconstruction processes a spatial voxel resolution of 2.5 μm has been obtained. A procedure for the quantitative evaluation of the sample porosity factor has been introduced and tested. This procedure has been utilized on all CFC materials relevant for the fusion technology. It is proved that the tomographic analysis provides useful information about the pores connectivity and, in case of heat sink region of the DITS CFC PFC, the penetration of metallic structures along fibre interspaces. For the first time we have analyzed by 3D tomography the DMS780 CFC coated by tungsten realized within the ITER-like wall project The characterization of the initial porosity of the new CFC ITER reference material NB41 has been obtained.

Acknowledgement

This work, supported by the European Communities under the contract of Association between EURATOM and MEdC, CEA, FZJ, was carried out under the framework of the European Fusion Development Agreement. The views and opinions expressed herein do not necessarily reflect those of the European Commission.

References

- [1] A. Kreter, et al., Journal of Physics: Conference Series **100** 062024 (2008).
- [2] A.T. Peacock, et al., Phys. Scr. **T128** 23 (2007).
- [3] B. Pégourié et al. JNM **390-391** 550 (2009).
- [4] E. Tsitrone et al. NF **49** 075011 (2009).****
- [5] P. Pelicon et al. "Deuterium mapping with micro-NRA using high energy focused He-3 beam for fuel retention studies in the walls of fusion reactors", to be published.
- [6] I. Tiseanu, et al., , Fus. Eng. Des. (in print), DOI: 10.1016/j.fusengdes.2011.04.079.
- [7] *Tomo-Analytic*, a combined 3D X-Ray micro-tomograph and micro-beam fluorescence system, (<http://tomography.inflpr.ro>).
- [8] J. Sijbers et al., Phys. Med. Biol. **49** N247 (2004).
- [9] I.Tiseanu, et al., Fusion Eng. Des. 75–79 1055 (2005).

X-RAY MICROBEAM ABSORPTION/FLUORESCENCE METHOD AS A NON- INVASIVE SOLUTION FOR INVESTIGATION OF THE EROSION OF W

I. Tiseanu, T. Craciunescu, C. Dobrea, A. Sima

National Institute for Laser, Plasma and Radiation Physics, Bucharest-Magurele

Overview

Tungsten erosion, its subsequent transport and redeposition are of great interest, because a full tungsten divertor is foreseen to be used during the deuterium–tritium operational phase of ITER. The erosion of tungsten and carbon marker layers was extensively studied in the outer divertor of ASDEX Upgrade (AUG), and work is currently in progress to completely replace the existing JET CFC tiles with tungsten-coated tiles within the JET ITER-like wall project. The need for fast and non-destructive method which allows the quantitative determination of the thickness of a tungsten coating on a carbon material on large areas led us to evaluate a combined absorption/fluorescence X-ray (XRTF) technique. The method can provide fast analysis, high spatial resolution and a material selective detection of deposited layers and inclusions. It was applied on W coated fine grain graphite (FGG) tiles from AUG's divertor. It is proved that the method is able to provide information about the uniformity of the tungsten coating on a graphite or CFC substrate whilst the technique can be used to determine the thickness of the tungsten and other marker materials coatings. It represents a unique instrument for the post-mortem analysis of the coatings.

Publications

- [1] I. Tiseanu, M. Mayer, T. Craciunescu, A. Hakola, S. Koivuranta, J. Likonen, C., C. Dobrea, *X-ray microbeam transmission/fluorescence method for non-destructive characterization of tungsten coated carbon material*, Surface & Coatings Technology, [doi:10.1016/j.surfcoat.2011.03.049](https://doi.org/10.1016/j.surfcoat.2011.03.049)

Detailed results

1. Introduction

Tungsten erosion, subsequent tungsten transport, and redeposition are of great interest, because a full tungsten divertor is foreseen to be used during the deuterium-tritium operational phase of ITER. The erosion of tungsten and carbon marker layers was extensively studied in the outer divertor of ASDEX Upgrade, and work is currently in progress to completely replace the existing JET CFC tiles with tungsten-coated tiles within the JET ITER-like wall project.

Global erosion, redeposition and transport of first-wall materials have been extensively studied in ASDEX Upgrade during the last seven years, using post-mortem surface analysis of tiles [1].

Specially prepared divertor or limiter tiles are used, which contain thin marker stripes for erosion/deposition measurements and are analyzed before and after exposure. Also regular tiles were analysed after exposure. Long-term samples are installed at the vessel walls or in remote areas without direct plasma contact. All samples are typically exposed during one discharge campaign, and they provide information about the campaign-integrated net material erosion/deposition pattern.

Due to the time consuming measurements and data evaluation, this technique allows to measure only a limited number of data points, typically along one line in poloidal direction. The need for a fast and nondestructive method, which allows the quantitative determination of the thickness of a tungsten coating on a carbon material on large areas, led us to evaluate a combined transmission/fluorescence X-ray (XRTF) technique. It is proved that this technique allows a good spatial resolution (several 10 μm), and it is fast enough to allow measurements for thousands of data points. Consequently 2-D erosion pattern on a whole divertor tile may be retrieved.

2. Methods

The method for erosion analysis was implemented using the Tomo-Analytic system (Fig. 1), which we developed especially for fusion materials analysis [2]. Tomo-Analytic is a combined X-ray fluorescence (XRF) and cone-beam tomography (3D-CT) system for the noninvasive 3-D morphology and composition mapping. The 3D-CT component is configured to take several hundred highly resolved (48 μm) radiographic views of the object in order to build a 3-D model of its internal structure. 2-D slices through this volume can be viewed as images, or the 3-D volume may be rendered, sliced, and measured directly. For the NDT inspection of miniaturized samples the microtomography analysis is guaranteed for feature recognition better than 15 μm .

The key element of the XRF component is polycapillary lens which provides a focal spot size in a range from few tens to a few hundreds of micrometers. A significant increase of X-ray intensity (up to three orders of magnitudes) is also obtained [3]. This guaranties higher detection sensitivity and shorter measurement time. The main limitation consists in the possibility to investigate relatively thin samples. The implementation of a confocal geometry realized with the attachment of a polycapillary conic collimator to the X-ray detector would further allow the extension of capabilities of the instrument towards fluorescence tomography (3-D composition mapping).

The XRF component can be used in three different procedures for the determination of the coating thickness:

XRF1) the coating X-ray fluorescence peak intensities are converted to elemental concentrations and/or film thicknesses.

- XRF2) the X-ray fluorescence radiation emitted by the substrate is attenuated by the coating material; a correlation can be derived between the secondary emissions and the coating thickness.
- XRF3) the coating thickness is determined from the correlation with the attenuation of the X-ray back-scattered radiation by a substrate with low effective atomic number. This procedure has the advantage to be more suitable to carry reference free thickness measurements.

3. Experiments and Results

ASDEX Upgrade fine grain graphite tiles were coated with tungsten of typical thicknesses ($0 \div 1.5 \mu\text{m}$). The coating uniformity analysis is performed using the X-ray transmission XRT and the X-ray fluorescence mapping by procedures XRF1 and XRF3.

A typical result of the XRT analysis is presented in Fig. 1. The X-ray transmission map can be used for the determination of the absolute value of the thickness of the W coating layer in terms of atoms/cm². Tungsten mass attenuation coefficients were generated with the XCOM program [6].

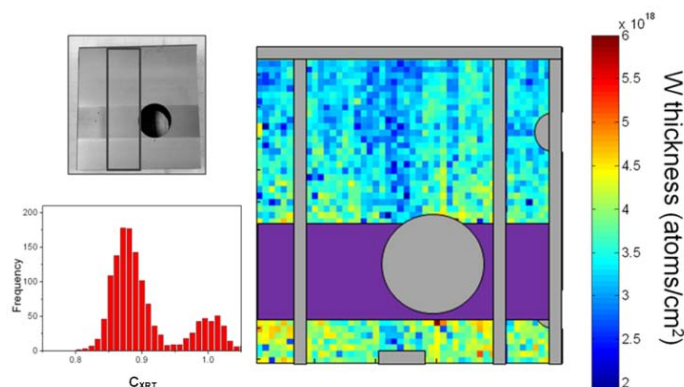


Figure 1 - W thickness determination by XRT. The sample (left) is presented together with the transmission map (right).

In order to compensate the influence of the graphite substrate, a non-coated reference sample must be used. A calibration curve relating the X-ray transmission factor and the graphite thickness is obtained. As the real tiles contain several cutting up profiles, the CAD model of the tile must be also taken into account. The X-ray transmission ensures fast and high resolution analysis. The images presented in Fig. 1 are obtained for a scanning time of approximately two hours on a 70×70 pixels matrix. For each image pixel one has averaged the transmission values over an area of 1.0 mm^2 in order to reduce the effect of the coating/substrate roughness.

Fig. 2 shows the X-ray fluorescence X-ray spectra of the ASDEX Upgrade W/Ni coated marker tiles. The peak intensities of the tungsten characteristics lines L_α (8.40 keV) and L_β (9.67 keV) are very sensitive to the coating thickness. Hence the XRF1 procedure is recommended for relatively fast coating uniformity mapping in relative units. However this technique is limited to W layers not thicker than $\sim 4 \mu\text{m}$ due to the high self-attenuation of the low energy of the W characteristic lines. When the coating process makes use of an intermediate layer (for example a Mo may be used as an interface layer between C substrate and the W coating layer [5]) the

XRF2 technique can be used to determine the thickness of the coating layer. Thus, we can measure thicker W layers due to the higher energy of the Mo X-ray line ($K_{\alpha}=17.48$ keV).

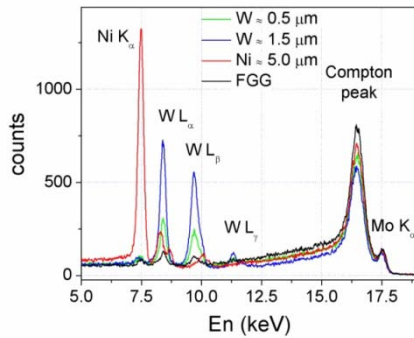


Figure 2 – X-ray fluorescence spectra in case of a W ($0 \div 1.5$ μm) and Ni (~ 5 μm) coated fine grain graphite sample.

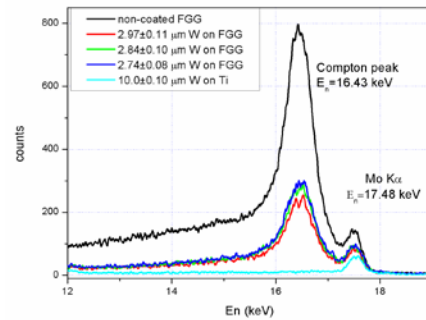


Figure 3 – Compton and elastic scattering intensities as function of tungsten coating thickness in case of microbeam back-scattering method (XRF3).

The Compton peak intensities are also very sensitive to the coating thickness values (Figs. 2 and 3) and therefore the mapping of the coating thickness in absolute values is possible within the XRF3 procedure without using thickness standards. Using a Mo target X-ray source it is possible to measure W layer thicknesses up to 6-7 μm .

In case of tungsten coated CFC materials one has to take into account the influence of the substrate morphology. Fig. 4 shows the radiography of a NB31 ITER like reference CFC material and a microbeam backscattering profile. One can see a clear radiological contrast between the pitch-fibres (brighter parallel structures) and the pan-fibres composed of tiny fibres (needling) distributed somewhat randomly and going perpendicularly to the main pitch-fibre direction. The line profile shown in the right panel displays variations of the back-scattering intensity of up to 20%, which should be compensated for in the XRF3 procedure.

A 2-D map obtained using the combined XRF1/XRF3 techniques is presented in Fig. 5. In the pseudo-colour map red/blue corresponds to high/low intensities, respectively.

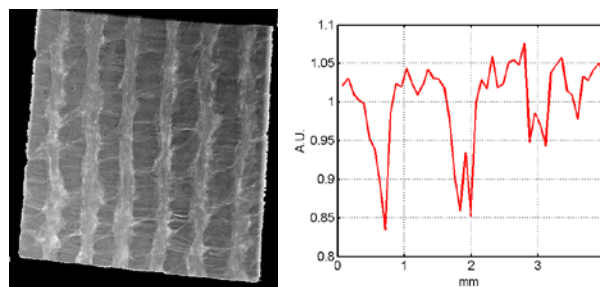


Figure 4 – High resolution radiography of NB31 ITER like CFC (left) correlated with the microbeam backscattering profile (right).

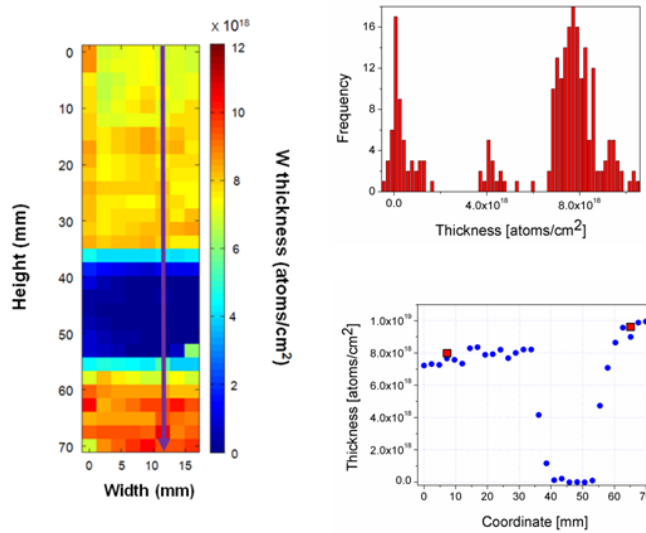


Figure 5 – Post-mortem analysis of a W coated fine grain graphite divertor tile: photo of the analyzed sample (left) showing the region of interest and pseudo-color map for W, Compton and elastic scattering.

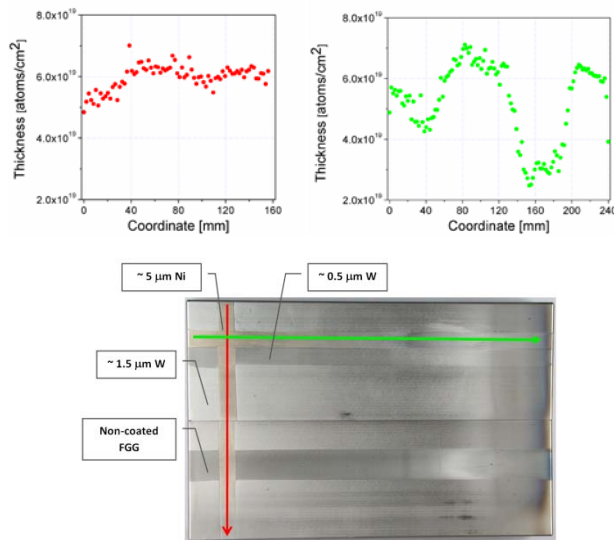


Figure 6 – The erosion profiles along poloidal (green) and toroidal (red) directions as measured by the XRF3 technique applied to the corresponding Ni stripes.

Line profiles of the W/Ni coatings were measured with the purpose to assess the erosion/redeposition in the all-tungsten divertor of ASDEX Upgrade (Fig. 6). The Ni/W thickness absolute values could be derived and they are in good agreement with the measurements carried out in [1]. Fig. 6 shows the erosion profiles along the poloidal and toroidal directions as measured by the XRF3 technique applied to the corresponding Ni stripes. In all measurements it is possible to detect redeposition of Ni/W on non-coated graphite stripes.

4. Conclusion

An instrument and associated measuring methods have been developed and qualified as a non-invasive solution for investigation of the erosion of W coatings on carbon materials substrates. The Tomo-Analytic instrument is a combined X-ray fluorescence (XRF) and cone-beam tomography (3D-CT) system for the non-invasive 3-D morphology and composition mapping.

The XRT component ensures fast and high resolution analysis of large areas of carbon materials coated with tungsten. However, the transmission method requires calibration in order to remove the influence of the fine graphite layer.

The main advantages of the XRF module are: i) high thickness resolution and material selectivity and ii) it permits calibration-free methods for the determination of the thickness of the coating layer. However the time needed for the XRF inspection of the sample is considerably larger in comparison to the XRT method. Therefore if a fine spatial resolution is required, the XRT method represents an appropriate alternative. The combined use of X-ray transmission and X-ray fluorescence methods represent a unique instrument for the post-mortem analysis of large area coatings. It can provide fast analysis, high spatial resolution and detection of deposited layers and intrusions. The combined method was successfully applied on W coated fine grain graphite tiles from the all-tungsten divertor of ASDEX Upgrade.

5. Acknowledgments

This work, supported by the European Communities under the contract of Association between EURATOM and MEdC, IPP and Tekes was carried out under the framework of the European Fusion Development Agreement. The views and opinions expressed herein do not necessarily reflect those of the European Commission.

References

- [1] M. Mayer, et al. *J. Nucl. Mater.* 390-391 (2009) 538.
- [2] I. Tiseanu, et al., Proc.of Fachtagung Prozessnahe Röntgenanalytik, PRORA 2009, Berlin, Germany, 2009.
- [3] B. Beckhoff et al., *Handbook of Practical X-Ray Fluorescence Analysis*, Springer,2006, XXIV, ISBN: 978-3-540-28603-5, pp 89-190
- [4] M.J. Berger, et al., XCOM: Photon Cross Section Database. Web Version 1.2. Available from: <http://physics.nist.gov/xcom>, National Institute of Standards and Technology, Gaithersburg: MD 20899, USA; August 1999.
- [5] C. Ruset, et al., *Physica Scripta*, T128, 171-174 (2007).

REMOVAL OF CODEPOSITED MATERIALS FROM GAPS WITH A PLASMA TORCH

G. Dinescu, T. Acsente, C. Stancu, E.R. Ionita

National Institute for Laser, Plasma and Radiation Physics, Bucharest

Overview

The long term material codeposition on walls of Tokamaks is associated with tritium retention issues, which become prominent in plasma facing components (PFCs) with gap structures. The removal of co-deposited carbon layers by a plasma torch operating with reactive gases at atmospheric pressure was approached in the context of EFDA Plasma Wall Interaction activities. Removal of codeposited layers by the plasma torch at atmospheric pressure is based on scanning of the surface with a small size plasma source, and this technique is promising in respect with “in situ” cleaning of walls. In previous experiments plasma torch operation in argon and nitrogen and its use for cleaning were studied. The cleaning experiments were successful on flat surfaces and also inside gaps (of 0.5-1.5 mm wide). The present contribution focuses on the investigation of torch operation with reactive gases and gas mixtures (using oxygen, air, argon/ammonia, argon/hydrogen and argon/oxygen) and its efficiency in removal of carbon and, in addition, of mixed codeposited layers from flat and castellated surfaces.

Publications

- [1] E.R. Ionita, C. Stancu, T. Acsente, B.Mitu, G. Dinescu, C. Grisolia, *Plasma torch cleaning of carbon layers from deep gaps at atmospheric pressure*, 26 th Symposium on Fusion Technology (SOFT 2010), Porto, Portugal, 27 September – 1 October, 2010.
- [2] C. Stancu, M. Teodorescu, A.C. Galca, G. Dinescu, *Carbon layers cleaning from inside of narrow gaps by a RF glow discharge*, Surface and Coatings Technology, In Press, Corrected Proof, Available online 29 March 2011, ISSN 0257-8972, DOI: 10.1016/j.surfcoat.2011.03.090.

Detailed results

1 Methods

Previous studies performed on removal of a-C:H layers from the inside of gaps using atmospheric pressure plasma torch proved the efficiency of this cleaning method. For improving the cleaning operations, the work with reactive gases was foreseen. It was thought that possible higher removal rates could be obtained by using reactive gases like oxygen, air, ammonia, hydrogen or their mixtures. But working with reactive gases could have also led to shortage of the device lifetime and limited domains of operation. For testing and researching the operation domains of the plasma torch, several aspects were taken into consideration, like: electrodes oxidation, difficult matching due to the wider range of plasma impedance in various gases, and the instability of operation. Thus, part of the research and upgrade of the plasma source had to

include new materials resistant to oxidation, cooling of the electrodes, research on matching, firmer connections, high quality cables, research on operation domains, and discharge stability in various gases.

The experiments of carbon removal were realized by scanning of flat graphite surfaces with the plasma torch at atmospheric pressure working in different pure gases (argon, nitrogen) and mixtures (argon/ammonia, argon/oxygen, argon/hydrogen, nitrogen/hydrogen, and nitrogen/oxygen). A computer controlled x-y translation table assisted the scanning procedure. The study was focused on the influence on the removal rate of the gas nature, the torch-surface distance, RF power, mass flow rates and the number of scans. The assessment of the cleaning efficiency of carbon from flat surfaces was performed with profilometry measurements. The removal rates of carbon were calculated from the removal profiles.

Cleaning experiments of mixed layers on flat and castellated surfaces were performed in nitrogen and nitrogen/oxygen mixture with different number of scans. The castellated surfaces are delimited by two aluminium cubes; silicon surfaces coated with the a-C:H/W mixed layers were mounted on inside the faces of cubes. For these experiments the parameters were chosen, considering the optimum results obtained in the carbon removal experiments.

Assessment of the mixed layers removal from flat surfaces and for in gap cleaning was performed by AFM and EDX measurements.

2. Results and discussion

2.1 Characteristics of the atmospheric pressure plasma torch operated in reactive gases.

The work performed for modification of the atmospheric pressure plasma in order to be operated with reactive gases had included changes of the RF electrode materials and manufacturing. The brass was replaced thoroughly with stainless steel material for RF electrode. The diameter of the active RF electrode was increased from 8 mm to 10 mm. The gas admission was changed from the inside of the an RF electrode, to the outside making available more space for cooling. The direct connection of the RF cable was also modified, avoiding the use of the RF- 7/16 connector. Also, changes were performed to the internal electrode cooling system. The Polyethylene Terephthalate (PET) tubes were replaced with Fluorinated Ethylene Propylene (FEP) tubes (resistant to temperature, shriveling and plying). The water volume in RF electrode was increased from 2.3 cm³ to 3.4 cm³, while the water inlet and outlet's inner diameter were also increased from 1 mm to 1.8 mm. By performing such modifications the water flow rate increased from 0.6 to 1.5 liter/ min, thus enabling a much efficient cooling, beneficial for the device lifetime.

The final result made the atmospheric pressure plasma torch much more robust, more compact and flexible and easier to be integrated on a robotic arm. Also the changes of the materials made it more resistant on corrosion.

For the torch's operation in reactive gases, most of the work involved the establishing of the possible values for the power (P), gas flow rate values (F), and gas flow rate ratios, for stable and reliable operation. The criteria used in the determination of the operation domains included the volume extension of the plasma jet (the expansion had to be visible outside the interelectrode space), the stability of operation (without spots and arcing), and without excessive heating (the returning cooling water should be still cold, with no visible reddish of the nozzle).

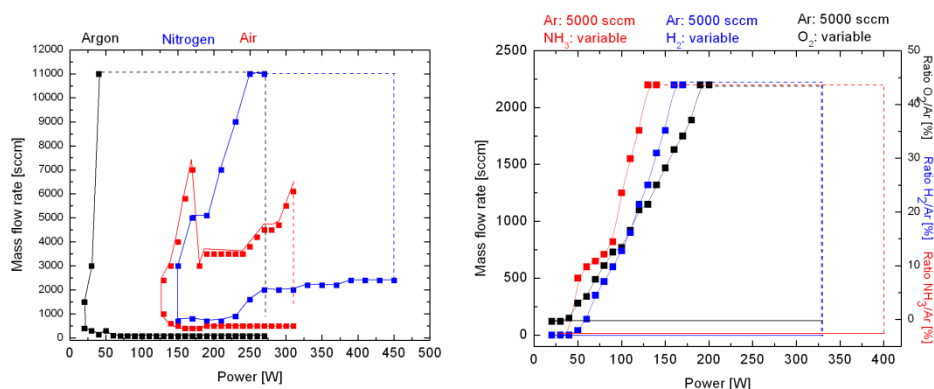


Figure 1 – Operation domains of the atmospheric pressure plasma torch in pure gases (left) and in gases mixtures (right). The vertical dotted lines represent the limit of excessive heating of the nozzle while the horizontal ones represent the limit of the mass flow rate of the gas mixed with nitrogen.

The fulfillment of the criteria was studied by using variable power and flow rates; the jet appearance was studied by imaging techniques, and the cleaning ability was demonstrated through a cleaning example. The operation domains in pure gases were established (Figure 1, left side). From the graphic it was concluded that the operation in nitrogen and air require more power and that the domain in air is restricted to a smaller area. For the optimum operation of the plasma source in nitrogen, air and argon, power and mass flow rate values from the central region of the domains should be used. For the operation domains in gas mixtures (Figure 1, right side) it was observed that the operation in Ar/O₂ requires more power, while the operation in Ar/NH₃ is more facile.

Of the encountered problems it's worth mentioned that in pure O₂ or large O₂ content (over 10%) and air the long time operation was not possible. The nozzle does not resist for long periods of time in oxygen and perhaps it should be changed with Hafnium material. Also the insulator (quartz) is eroded in time, and a replaceable material is difficult to identify.

2.2 Cleaning of carbon layers

The experiments of carbon removal were realized by scanning of flat graphite surfaces with the plasma torch at atmospheric pressure working in different gases (nitrogen, argon) and

mixtures (argon/ammonia, argon/oxygen, argon/hydrogen, nitrogen/hydrogen, and nitrogen/oxygen). Figure 2 a shows the image of the flat graphite sample during cleaning experiments while Figure 2 b,c shows images of a graphitic surface before and after scanning along parallel lines, with nitrogen plasma (RF power = 300W, N₂ mass flow rate = 3000 sccm, distance = 5 mm, scanning speed = 5 mm/sec) for an increased number of scans.

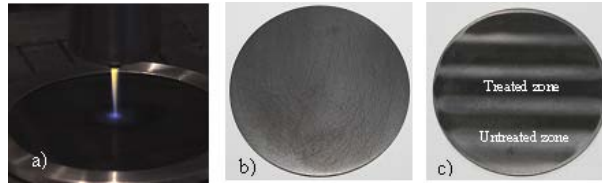


Figure 2: - (a) Image of the graphite sample during scanning (a), before (b,) and after (c) cleaning experiments.

Considering the cleaning experiments with pure gases, usage of Ar as feeding gas was inefficient; the effect on the surface was too low to obtain measurable profiles. Contrary, carbon removal rates were calculated from obtained profiles in nitrogen. Figure 3 presents the removal rates of carbon by plasmas generated at different N₂ flows and different RF powers, after five scans, for two distances between the plasma torch and the graphite surface (5mm, respective 10mm).

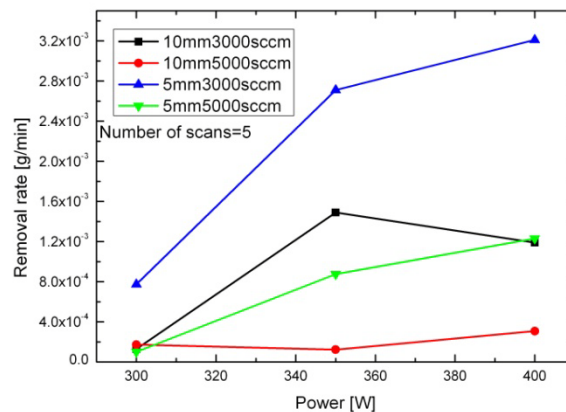


Figure 3: - Carbon removal rates after different N₂ flows and different RF powers.

It can be observed that the optimum parameters for nitrogen plasma cleaning are obtained for a distance of 5mm between plasma torch nozzle and substrate, 400W applied RF power and 3000sccm N₂ mass flow rate. These experimental parameters were considered in the experiments of cleaning with nitrogen mixed with the reactive gases previously mentioned.

As regarding cleaning experiments in argon/ammonia, argon/oxygen, argon/hydrogen, and nitrogen/hydrogen mixtures, the deepness of the erosion profiles were very low and did not allowed the determination of the removal rate. Much better results are obtained in nitrogen/oxygen mixture. Figure 4 presents the dependence of the removal rate upon the added O₂ mass flow rate. It is seen that an optimum value of 10% O₂ in the nitrogen leads to the highest removal rate of about 10⁻² g/min.

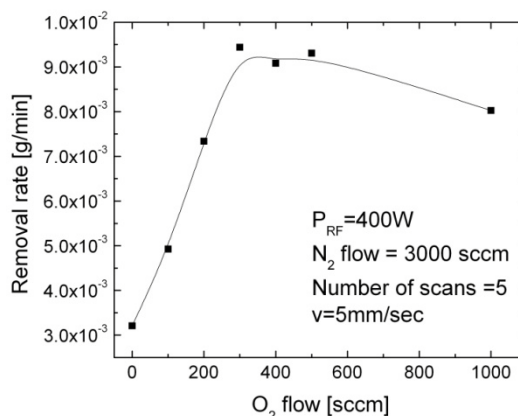


Figure 4: - Carbon removal rates afterscanning with different O₂ flows.

2.2 Cleaning of carbon/metal mixed layers

Cleaning experiments of mixed layers (a-C:H/W, a-C:H/Al) on flat and castellated surfaces were performed in nitrogen and nitrogen/oxygen mixture, with different number of scans. The experimental parameters were chosen considering the optimum results obtained in the carbon removal process: 400W applied RF power, 5mm between plasma torch nozzle and substrate, 5mm/s scanning speed, 4000 sccm nitrogen mass flow rate.

Removal experiments from flat surfaces, performed on 650nm thick a-C:H/W layers deposited on silicon, in nitrogen and nitrogen/oxygen mixture, show the apparent cleaning of the surface after only one scan (by visual inspection). AFM investigation of treated flat mixed layers (5 microns, a-C:H/W) with the plasma torch working in nitrogen showed an increase in the treated sample roughness while the number of scans increases, indicating the material removal. EDX investigations performed on a-C:H/Al mixed layers (Figure 5) show a stronger reduction of the C component due to plasma treatment comparative to the Al one. Modifications of EDAX signal correspond to an increase of Al (at %) /C (at %) ratio from 0.14 (for untreated probe) to 0.39 (for 10 plasma scans). This leads to the conclusion that plasma treatment removes mainly the C from the co-deposited layer.

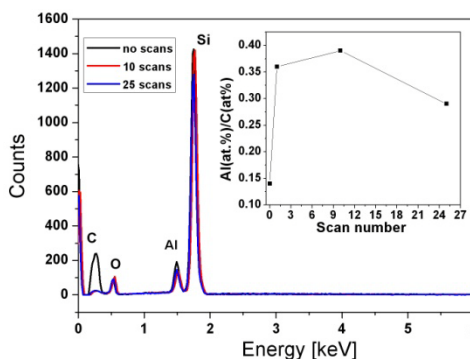


Figure 5: - EDX investigations of a sample coated with a-C:H/Al mixed layer.

The cleaning experiments performed on castellated surfaces covered with a-C:H/W mixed layers showed that the cleaning goes deep inside gaps up to 20 mm, is faster at the top margin of the gaps, and it is very effective on its bottom.

4. Conclusion

For improving the cleaning efficiency of codeposited layers, the atmospheric pressure plasma torch was upgraded for operations the work with reactive gases (oxygen, air, ammonia, hydrogen or their mixtures). For testing and establishing the operation domains of the plasma torch, several aspects were taken into consideration, like the electrodes oxidation, the wide range of plasma impedance with various gases, and the instability of operation. As it has been proved, the torch operates optimally in Ar, N₂, Ar/NH₃, Ar/H₂ gases; problems of the long term discharge operation with oxygen containing gases still remain.

Cleaning experiments on flat graphite samples and on flat and castellated surfaces covered with mixed layers were performed. On flat graphite samples, the best cleaning results are in nitrogen and nitrogen/oxygen. Removal rates increase with the number of scans. In nitrogen/oxygen mixed gases, with 3000 sccm nitrogen mass flow rate, the removal rate increases with the oxygen mass flow rate, and reaches an optimum of around 10⁻² g/min at 3000 sccm; after this value the removal rate decreases again. On flat mixed layers scanned with the plasma torch, the roughness increases with the number of scans. EDX investigation showed that during cleaning procedure, the carbonic matrix is preferentially removed with respect to the metallic component contained in the codeposited layer.

Considering the possibility to work in both neutral and reactive gases and the ability in removal of the mixed layers from the flat surfaces and from the gaps, we conclude that the atmospheric pressure plasma torch is a versatile and feasible device for cleaning applications inside the Tokamak reactor, as example for mirrors.

Acknowledgement

The reported work includes the activities performed in the framework of the WP10-PWI-02-04-01/MEdC/BS EURATOM-MEdC contract.

CONTROLLED LABORATORY MODELS OF CODEPOSITED LAYERS FOR FUEL REMOVAL

T. Acsente, E. C. Stancu, G. Dinescu

National Institute for Laser, Plasma and Radiation Physics, Bucharest

Overview

The investigation and cleaning of material codeposited on Tokamaks walls and plasma facing components (PFC) are important for safe operation of fusion machines. The present contribution presents the realization of mixed layers of hydrogenated carbon with metal inclusions (a-C:H/W, a-C:H/Al, Al being used as a Be substitute), to be used as laboratory models for tokamak codeposited layers. The mixed layers were produced by a novel developed plasma deposition method (sequential deposition). Stable a-C:H/W mixed layers with well predefined composition and up to five microns thickness were produced and supplied for fuel removal experiments using different approaches (atmospheric pressure plasma jets, laser ablation, discharges). Interaction of codeposited layers at contact with atmospheric air was investigated by controlled exposure of a-C:H/Al mixed layers to air and its components.

Publications

- [1] T. Acsente, E.R. Ionita, D. Colceag, A. Moldovan, C. Luculescu, R. Birjega, G. Dinescu, *Properties of composite a-C:H/metal layers deposited by combined RF PECVD/magnetron sputtering techniques*, Thin Solid Films, 519-12(2011)4054-4058.
- [2] T. Acsente, E.R. Ionita, C. Stancu, M.D. Ionita, G. Dinescu, C. Grisolia, *OES monitoring of sequential deposition of C/W layers by PECVD/magnetron sputtering techniques*, Surface and Coatings Technology, In Press, Corrected Proof, Available online 29 March 2011, ISSN 0257-8972, DOI: 10.1016/j.surfcoat.2011.03.085.
- [3] T. Acsente, E. R. Ionita, C. Stancu, G. Dinescu, *Laboratory made codeposited layers for fuel removal studies*, 26 th Symposium on Fusion Technology (SOFT 2010), Porto, Portugal, 27 September – 1 October, 2010 (poster presentation).

Detailed results

1 Methods

Mixed layers of a-C:H/Metal (matrix of hydrogenated amorphous carbon with incorporated metal particles, as laboratory models for the co-deposited layers, were synthesised using a novel plasma deposition method, namely sequential deposition [1]. It consists in cyclic (sequential) exposure, for predefined time intervals, of a substrate (W, silicon) to totally independent two

radiofrequency (13.56MHz) plasma deposition sources, working in alternative sequences: magnetron sputtering (MS) in Ar for metal deposition and Plasma Enhanced Chemical Vapor Deposition (PECVD), using a mixture of Ar and C₂H₂ for deposition of hydrogenated amorphous carbon (a-C:H) matrix. A deposition cycle consists in the following steps: metal deposition by MS (lasting for t_M seconds), transport (using a stepper motor) of the substrate in the front of PECVD (performed in t_{TR} seconds), deposition of a-C:H (lasting for t_C seconds), and backward transport of the substrate in the front of MS. While the values of t_M and t_C time durations impose the elemental composition of the deposited layer, the thickness of the deposited mixed layer is controlled by the number of successive deposition cycles N_{CYC} . The substrate is transported between the plasma sources by means of a stepper motor; during the substrate movement the plasma sources are not energized and proper gas composition for the following deposition step (Ar atmosphere for metal deposition and a mixture of C₂H₂/Ar for a-C:H deposition) is prepared. The entire deposition process is computer controlled through an electronic interface (for stepper motor and gas admission control), and a LabVIEW graphical interface for setting the temporal parameters (t_C , t_M , t_{TR} , and N_{CYC}) and the plasma processes parameters (deposition RF powers, deposition gas composition). For evaluating the repeatability of the deposition cycles during deposition of one sample and also of different samples deposited in the same conditions the sequential deposition process is monitored by means of optical emission spectroscopy setup [2].

The metals selected for deposition of laboratory models for codeposited layers are W and Al (as substitute for Be). While the mixed layers of a-C:H/W type are stable, the a-C:H/Al mixed layers presents a fast chemical change at the contact with ambient atmosphere. For this reason, only a-C:H/W mixed layers were selected to be used as laboratory models for assessment of fuel removal experiments.

Comparing with other literature reported plasma deposition methods of carbon/ metal mixed layers (in which the composition and structure of the deposited films can be tailored only by plasma parameters adjustment (discharge power, gas composition or pressure), the sequential deposition method allows tuning of the deposited layer properties and by proper choice of the temporal parameters (mainly the plasma exposure durations, t_C and t_M) while the plasma parameters are kept constant.

The influence of the cycle deposition times t_M and t_C over the structural and compositional properties of the a-C:H/W deposited layers was studied by systematic varying these parameters, while maintaining constant the total effective deposition time during one deposition cycle ($t_w+t_C=13s$, t_w having the following values: 2s, 4s, 6s, 8s and 10s). All the samples were deposited on silicon substrates using a transport time $t_{TR}=5s$ and a number of deposition cycles $N_{CYC}=80$. In the followings, the deposited samples will be denoted with the pair (t_w , t_C) plasma exposure durations. For comparison, there were sequentially deposited two monocomponent reference samples (W_{REF} , containing only W and C_{REF} , containing only a-C:H) using the plasma exposure

durations pair $t_w = 6s$, $t_c = 7s$. During the study, the other process parameters were kept constant: discharge powers $P_c = 80W$, $P_w = 80W$, while the pressures were 2.7Pa (5sccm C_2H_2 mixed with 70sccm Ar) and 2.4Pa (70sccm Ar) during W deposition.

The material morphology, structure and composition of the deposited samples were investigated using specific techniques: atomic force microscopy (AFM), scanning electron microscopy (SEM), energy dispersion X-ray spectroscopy (EDX) and X ray diffraction (XRD).

Physical and chemical modification of the codeposited layers at contact with ambient air was studied using a-C:H/Al mixed layers: after sequential deposition of a 200nm mixed layer on the substrate (glass and silicon), the deposition chamber was filled with interaction gas (air or one of its components: Ar, N_2 , O_2 and H_2O vapors mixed with Ar). During the exposure of the mixed a-C:H/Al mixed layer to gas, there was monitored the optical transmission modification (in the visible spectral range) of the glass deposited sample. The chemical transformation of the a-C:H/Al mixed layers were studied by FTIR (Fourier Transform Infrared Spectroscopy) investigation of a-C:H/Al samples after their interaction with the mentioned gases.

2. Results and discussion

2.1 Properties of a-C:H/W mixed layers

Topography and morphology of a-C:H/W layers

The roughness (RMS) of the mixed a-C:H/W layers is slightly influenced by the ratio of carbon and metal deposition times, (it ranges from 3.4nm to 2.7nm when t_w is increasing from 2s to 10s). It was also observed that mixed samples roughness present a value in between that of carbon reference sample (RMS = 1.4 nm) and tungsten reference sample (RMS = 4.3 nm). Supplementary, the roughness of the a-C:H reference sample (1.4nm) is much smaller compared to that of any mixed a-C:H/W samples (lying in between 2.7nm and 3.4nm). Concluding, the metal incorporation in the a-C:H films increases their roughness. The SEM investigation of an a-C:H/W 4 μ m thick sample revealed a granular aspect of the sample surface, with grain size of about 200nm, with cauliflower type morphology of the grains [1].

Film composition and structure

Figure 1 shows the dependence of the elemental atomic concentration obtained from the EDX investigations, upon the exposure times t_w and t_c for the (2,11), (6,7) and (10,3) a-C:H/W samples. The results prove the possibility of tuning the atomic elemental concentration (reported to the total W and C amount) of the film metallic component in between 10% - 50 at.% by modifying the temporal parameters of the deposition cycle (t_w and t_c).

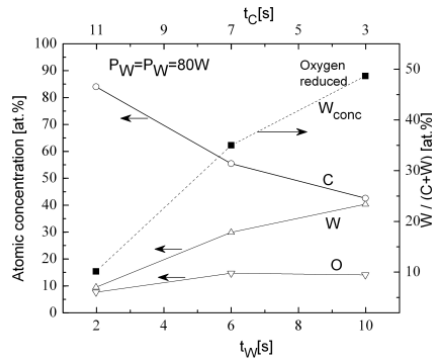


Figure 1 – Dependence of elemental atomic concentration in a-C:H/W layer on (t_w , t_c) values; the full line lines represent the data extracted from EDX measurements while the dotted one does not consider the oxygen present in the film.

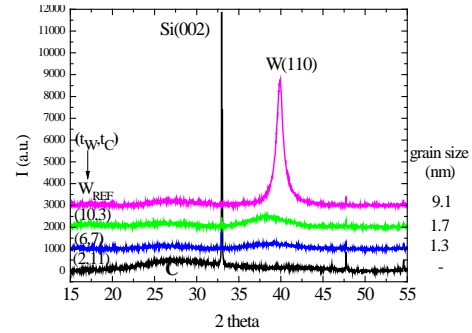


Figure 2 – The XRD diffractograms of the a-C:H/W mixed probes (2,11), (6,7) (10,3) and on the tungsten reference probe.

The XRD diffractograms of the a-C:H/W mixed probes (2,11), (6,7), (10,3) and tungsten reference probe $W_{REF}(6,7)$ were obtained in 2 theta configuration and are presented in Figure 2. The diffraction peaks corresponding to film components and substrate (C and W(110) and Si(002)) are observed.

The diffraction peak corresponding to W(110) is very pronounced and narrow for the tungsten reference sample, while for the mixed samples it decreases and is enlarged. By comparing the diffractogram of mixed samples (10,3), (6,7) and (2,11), one can observe that the height of the peaks is lower for the samples with lower tungsten content whilst the carbon peaks behave oppositely. From the profile of the tungsten peaks the size of the particulates in the film can be estimated by Debye-Scherrer formula. It results that the a-C:H/W layers contains tungsten nanocrystals with sizes in the range 1-2nm. Their dimension is higher for the samples deposited at higher t_w values.

2.2 Transformation of the model codeposited layers induced by gases

Interaction of a-C:H/Al with gases is, in general, followed by delamination of the film from the substrate. The delaminating effect depends on the nature of interaction gas. Such, it can be observed a total delamination of the samples exposed to atmospheric air and to the mixture of Ar and H_2O . In the case of the sample exposed to O_2 , the a-C:H/Al layer is still adherent to the substrate immediately after interaction but it delaminates rapidly (few minutes) after exposure in ambient air. The a-C:H/Al layers which reacted with N_2 are adherent to the substrate for much longer time even after few months exposure in atmospheric air; this suggest a possible post deposition treatment of the a-C:H/Al thin films in view of increasing their stability in atmospheric air.

Figure 3 presents the time variation of optical absorbance $\Delta A(t)$ during the exposure of the a-C:H/ layers deposited on glass substrates to the considered gases, at the monitored wavelength 638nm. It can be observed that Ar do not produce any effect over the a-C:H/Al layer optical

absorbance (the small variation during the chamber filling which is due to the optical system misalignment caused by windows displacements when the pressure changes from low to atmospheric value is negligible). This is not the situation for a-C:H/Al mixed layers interacting with N₂ or O₂; after chamber filling with every of those gases, the optical absorption of the layer decreases constantly. Comparing with the Ar which is an inert gas it results that the change in a-C:H/Al layer absorbance is produced by the chemical interaction between N₂ or O₂ with the mixed layer. Still, the effect of these gases is not so severe like that produced by atmospheric air, which is comparable only with that of the Ar and H₂O vapors mixture.

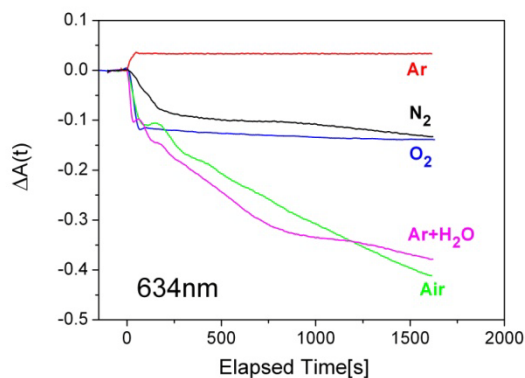


Figure 3 – Variation of a-C:H/Al layers optical absorbance during treatment with ambient air gaseous components.

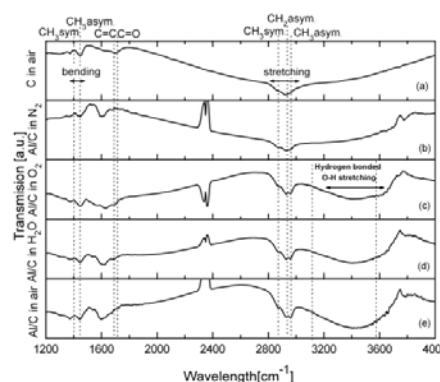


Figure 4 – FTIR spectra of a) a-C:H sample exposed in ambient air, and a-C:H/Al nanocomposite samples exposed to b) nitrogen, c) oxygen, d) water vapors and e) ambient gaseous components.

In Figure 4 are presented the FTIR spectra of the a-C:H reference sample exposed in ambient air, and a-C:H/Al nanocomposite samples exposed in ambient air and N₂, O₂, H₂O vapors. In all the spectra there are present the typical stretching bands of CH₂ and CH₃ in the spectral region 2800 – 3100 cm⁻¹ and the C-H bending bands specific to the methyl group.

In comparison with the reference a-C:H layer (Figure 4a), in the structure of composite a-C:H/Al layer exposed to ambient atmosphere (Figure.4e) there can be remarked the absence of the C=O bond and the presence of an large absorption band around 1600cm⁻¹ wavelength, specific to the conjugated C=C bonds. Supplementary, there can be remarked an extreme large absorption band in the spectral range 3000–3600 cm⁻¹, centered on 3400cm⁻¹, which is associated with an overlapping of the absorption produced by the stretching in the primary and secondary amines NH₃ and NH₂ (3300 – 3400 cm⁻¹) and absorption band produced by OH groups (3200 – 3600 cm⁻¹). This large absorption band is also present in the spectrum of the a-C:H/Al mixed layer exposed to O₂ (Figure.4c); supplementary, in this situation can be observed the enlargement of the absorption band around 1600cm⁻¹, specific to apparition of C=O bonds in the layer structure. The FTIR spectrum of a-C:H/Al layer exposed to a mixture of water vapors and Ar (Figure 5d) presents the same features like the spectrum of a-C:H/Al layer exposed to O₂; the single difference consists in a smaller enlargement of the 1600cm⁻¹ absorption band. The

FTIR spectrum, recorded for the a-C:H/Al layer exposed to N₂ atmosphere (Figure 4b) do not present the 3400 cm⁻¹ absorption band, proving that exposure to N₂ of the mixed layer do not promote apparition of the NH₃ and NH₂ bonds. It results that the 3400cm⁻¹ band (observed in a-C:H/Al samples treated in air, O₂ and Ar+H₂O mixture) originate from the layer oxidation and apparition of OH bonds. Such as, the water vapors and O₂ are responsible for the chemical changes of a-C:H/Al exposed to ambient atmosphere.

4. Conclusion

Mixed a-C:H/W layers with elemental predefined concentrations were deposited as laboratory models for the co-deposited layers in fusion reactors. The deposition was performed by means of a sequential deposition method. Using EDX analysis there were identified the sequential process parameters leading to predefined layer composition by adjusting the substrates exposure times to the plasma sources (t_w for magnetron and t_c for PECVD deposition processes). Using this method there were deposited thick (in range 1-4µm) mixed samples and mono-component layers (pure tungsten and pure hydrogenated carbon) on tungsten and graphite substrates. These samples were submitted for plasma cleaning experiments.

A study of the transformation of the model codeposited layers (a-C:H/Al) induced by atmospheric gases was performed. Results obtained from the optical transmission monitoring and FTIR investigation of the samples of a-C:H/Al (laboratory models for Be containing codeposited layers, Al being used as Be substitute) deposited on glass and Si substrates proved that the fast degradation of these layers during their exposure in open atmosphere are due O₂ and water vapors from the ambient.

Acknowledgement

The reported work includes the activities performed in the framework of the following EURATOM-MEdC contracts: WP10-PWI-02-04-02/MEdC/BS and WP10-PWI-02-04-03/MEdC/BS. The reported work includes contributions from the following people outside the EUATOM-MEdC Association: Christia Grisolia (EURATOM - CEA Association, Cadarache, France).

References

- [1] T. Acsente, E.R. Ionita, D. Colceag, A. Moldovan, C. Luculescu, R. Birjega, G. Dinescu, *Properties of composite a-C:H/metal layers deposited by combined RF PECVD/magnetron sputtering techniques*, Thin Solid Films, 519-12(2011)4054-4058.
- [2] T. Acsente, E.R. Ionita, C. Stancu, M.D. Ionita, G. Dinescu, C. Grisolia, *OES monitoring of sequential deposition of C/W layers by PECVD/magnetron sputtering techniques*, Surface and Coatings Technology, In Press, Corrected Proof, Available online 29 March 2011, ISSN 0257-8972, DOI: 10.1016/j.surfcoat.2011.03.085.

FUSION MATERIALS DEVELOPMENT

**TRANSMISSION AND BACKSCATTERING MÖSSBAUER SPECTROSCOPY STUDIES
OF THE SHORT RANGE ORDER, STRUCTURE AND MAGNETIC PROPERTIES
IN α -Fe AND BINARY Fe-Cr MODEL-ALLOY**

L. Diamandescu

National Institute of Materials Physics, Bucharest, Romania

Overview

Chromium ferritic/martensitic steels are potential candidates for blanket structural materials in future fusion reactors [1]. Their use for this application requires a careful assessment of their mechanical stability under high energy neutron irradiation [2]. Thus, their chemical composition and thermo-mechanical treatments have been optimized over decades of experimental investigations to resist the expected unfriendly conditions [3]. It was established that the magnetic properties and electrical resistivity depends strongly on Cr content of the binary alloys. For fusion reactor steels, the chromium content is around 10 %. Phase stability of the Fe-Cr system is an essential topic, as the formation of chromium-rich ' α ' precipitates triggers hardening and embrittlement of ferritic/martensitic steels under neutron irradiation. The peculiarity of the Fe-Cr system is the existence of a wide miscibility gap in the phase diagram where both Fe and Cr are insoluble at room temperature (RT). The chemical arrangement of the atoms in the alloy can either be *random* or exhibit *clustering* among similar atoms [4], according to the preparation method and further heating treatment.

In the last decade many advanced techniques were applied in order to investigate the relationship structure – physico-chemical properties of Fe-Cr alloys, *inter alia* Mössbauer spectroscopy. This is a versatile technique that can be used to provide information in many areas of science such as Physics, Chemistry, Biology and Metallurgy. It can give very precise information about the structural, magnetic and time-dependent properties of a material.

It was the aim of this project to investigate the short range order, structure and magnetic properties of α -Fe materials and some Fe-Cr based alloys by transmission and backscattering (conversion electron-CEMS and conversion X-ray-CXMS) Mössbauer spectroscopy.

Publications

- [1] Lucian Diamandescu, Serban Constantinescu, Ion Bibicu, Marcel Feder, Doina Tarabasanu-Mihaila, Traian Popescu, *Mössbauer Spectroscopy Investigations on FeCr Based Alloys for Fusion Reactors*, CNF 2010, September 22-23, Iasi, Romania, 2010.
- [2] L. Diamandescu, S. Constantinescu, I. Bibicu, J.B. Correia, M. Feder, D. Tarabasanu-Mihaila, A. Banuta, T. Popescu, *Mössbauer spectroscopy studies of hyperfine magnetic fields and short range order parameter in Y and Ti doped Fe-Cr nanoscaled alloys*, ICAME 2011, 25-30, September, 2011, Kobe, Japan.

Detailed results

1. Methods

Bruker Advance D8 X-ray diffractometer (with Cu-K α radiation) was utilized to record the XRD patterns. Mössbauer spectra have been recorded at room temperature by means of Promeda (Israel) type standard spectrometer with a WissEL (Germany) acquisition interface. A 25 mCi Co/Rh source was used in a velocity range of ± 10 mm/s. Helium liquid temperature Mössbauer investigations have been performed on a SeeCo (USA) close cycle cryostat.

2. Sample preparation

The following α -Fe samples (in powder or foil) were analysed by Mössbauer spectroscopy: α -Fe Merck, α -Fe Riedel de Haen, α -Fe foil enriched in Fe⁵⁷ and α -Fe standard (for velocity calibration in Mössbauer Spectroscopy). Two samples of FeCr like alloys, FeCrY and FeCrTiY (courtesy of Prof. Jose Brito Correia - IST Portugal) were considered for Mössbauer investigations. The FeCr alloys were prepared by ball milling in argon atmosphere, at 400 rot/min for 18 hours, using planetary mill Retsch PM100MA with stainless steel vials. The mean particle dimension of the obtained samples is ~ 10 nm. The target composition was: 85.2%Fe-14.1%Cr-0.3%Y-0.3%Ti. One of the bunches milling charge was constituted by 17.16g of Fe, 2.82 g of Cr and 0.02g of Y; the other was constituted by: 17.05 g of Fe, 2.82 g of Cr, 0.06 Y and 0.07 g of Ti.

3. Results and discussion

Figure 1 shows the Mössbauer spectra of the analysed α -Fe samples. All spectra exhibit a typical six lines magnetic hyperfine pattern characteristic for α -Fe.

The transmission Mössbauer spectra display similar six line patterns characteristic for bcc α -Fe structure. The difference between powders and foils of are given by the intensities of the lines 2 and 5 due to the alignment of the nuclear magnetic moments in the foil samples. For all samples the resulted hyperfine magnetic field at the iron nucleus is close to 33.0 T. The very narrow line widths support the hypothesis of unique position of iron in the cubic α -Fe lattice.

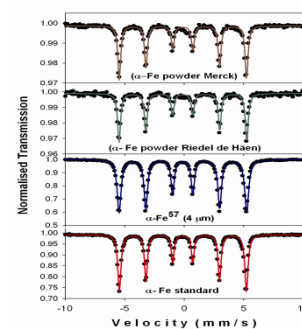


Figure 1 - FeCrY and FeCrTiY obtained by planetary ball milling.

According to the equilibrium Fe-Cr phase diagram the disordered bcc solid solution exists at temperatures above the spinodal decomposition line. The chromium XRD pattern is very similar to that of α -Fe ($a = 2.8660\text{\AA}$) because it crystallizes similarly in a bcc structure (S.G. No. 229) with lattice parameter $a = 2.883\text{\AA}$. The diffraction technique becomes obviously unfavourable when two elemental powders possess nearly identical lattice constants in the same crystallographic structure and result in a homogeneous solid solution. Due to the relevant presence of iron in our samples the Mössbauer spectroscopy was applied in order to obtain more accurate information about the FeCrYTi system under mechanical activation.

As it was shown by structural calculation, in the lattice around Iron atom in FeCr alloys the first and the second metallic surroundings are *cubic* and respectively *octahedral*, containing 8 and respectively 6 neighbours. The third and the fourth metallic shells contain 12 and respectively

24 neighbours, arranged in parallel planes along Z axis. It has been reported that Fe atoms, which possess Cr atoms as the nearest neighbour, exhibit a smaller hyperfine field than that of pure Fe, and its reduction rate per Cr atom is about 3 T [5]. J. Cieślak & S.M. Dubiel [6] found a drop of 3.2 T for each Cr atom in the first coordination sphere and 2.2 T for the second one. The hyperfine magnetic field at the iron nucleus can be approximated by the formula,

$$H(m, n, c) = H(0, 0, c) + m \cdot \Delta H_1 + n \cdot \Delta H_2 \quad (1)$$

where $\Delta H_1 = 3.2$ T and $\Delta H_2 = 2.2$ T.

The contribution of the Cr in third and fourth coordination sphere is too low to give a relevant change in Mössbauer spectra. Consequently we can consider only two first coordination spheres when we account for the effects of Fe substitution by Cr in this alloy. *If the substitution process is random*, the probability to find ‘m’ Cr atoms in first coordination and ‘n’ Cr atoms in the second one, at given chromium concentration ‘c’, is given by combinatorial formula:

$$P(m, n, c) = \binom{8}{m} \binom{6}{n} c^{m+n} (1-c)^{14-m-n} \quad (2)$$

In order to characterise the *situation where there is a deviation from the random distribution* of substitutional element, a new parameter was introduced by Cowley [7]. For a binary XY alloy a “**short range order parameter**” (SRO) or “Cowley parameter” was defined as α_j :

$$\alpha_j = (1 - pY(j))/cY \quad (3)$$

where $pY(j)$ is the probability of finding Y atom as a j^{th} neighbour of an X atom, and ‘cY’ is the fraction of Y atoms in XY alloy.

$\alpha_j = 0$ perfect random distribution

$\alpha_j < 0$ mutual arrangement of atoms is correlated

$\alpha_j > 0$ clustering – shortage (short-range separation).

The following relation exists [8, 9] between the mean hyperfine magnetic field at the Iron nucleus $\langle H \rangle$ at concentration c of substituting element (Cr in our case) and α parameter:

$$\langle H \rangle = (1 + kc) \left[1 + c \sum_{i=1}^N z_i h_i (1 - \alpha_i) \right] \quad (4)$$

$\langle H \rangle$ is the average hyperfine magnetic field: $\langle H \rangle = \sum_{i=1}^N A_i H_i / \sum_{i=1}^N A_i$

where A_i are the Mössbauer normalised areas and N – number of magnetic sublattices.

$z_1 = 8$ and $z_2 = 6$ are the coordination numbers, $h_i = \Delta H_i / \Delta H_{Fe}$ $k =$ field magnification factor.

In the range of chromium concentration ~13-14%, V.V. Ovchinnikov [8, 9] showed that $\alpha_1 = \alpha_2 = \alpha$. Equation 4 becomes:

$$\langle H \rangle = (1 + kc) \left[1 + c(1 - \alpha) \sum_{i=1} z_i h_i \right] \quad (5)$$

Based on equation (5) we calculated SRO parameters using the magnetic field values $\langle H \rangle$ as resulted from the fit with both models (binomial and distribution) using the following values of h_1 and h_2 [10]: $h_1 = -0.082$; $h_2 = -0.074$.

With these considerations in mind, the Mössbauer transmission, CEMS and CXMS spectra reordered at RT or LHT were fitted to obtain information regarding the hyperfine fields and SRO parameters in FeCrY and FeCrYTi nanoscaled alloys obtained by planetary ball milling. The report in December 2010 presented all the spectra together with the fit parameters

and calculated curves or distributions. In the following we shall present some of representative transmission and backscattering Mössbauer spectra together with the final table of results.

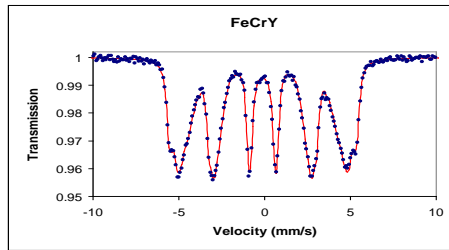


Figure 2 - RT Mössbauer spectrum. H_{hf} distribution fit

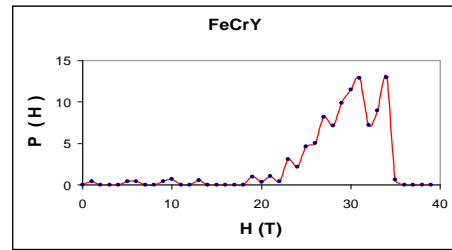


Figure 3 - RT distribution probabilities $P(H)$.

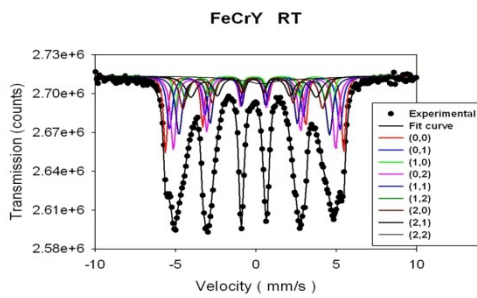


Figure 4 -RT Mössbauer spectrum. Binomial fit.

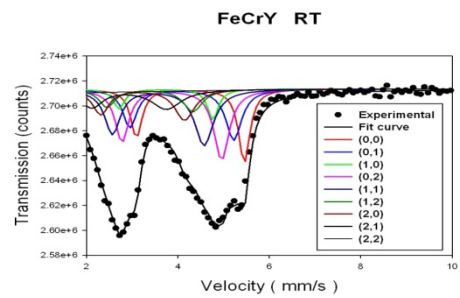


Figure 5 - Fit detail from binomial model.

Figure 6 - RT CEMS. Distribution fit

Figure 7 - Distribution probabilities $P(H)$.

Figure 8. RT CEMS. Binomial fit.

Figure 9. RT CXMS. Binomial fit.

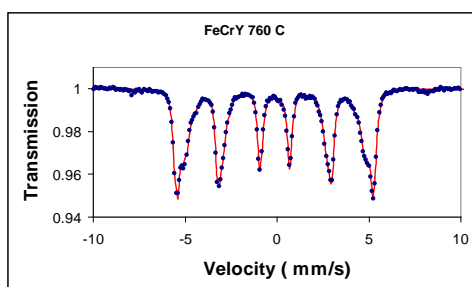


Figure 10 - RT Mössbauer spectrum of treated sample (distribution fit).

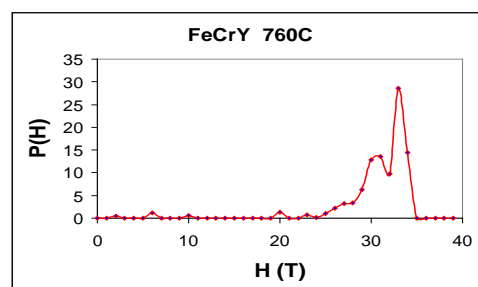


Figure 11 - RT distribution probabilities $P(H)$.

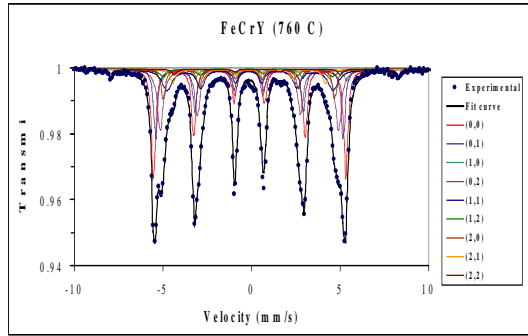


Figure 12 - RT Mössbauer spectrum of the treated samples FeCrY (left) and FeCrTiY (right); binomial fit.

Table 1. $\langle H \rangle$ average hyperfine magnetic field and SRO parameters of the analysed samples.

Sample	H(0,0) (kOe)	$\langle H \rangle$ (kOe)	$\langle H \rangle$ (kOe)	SRO (α)	SRO (α)
		Dist. fit	Binom. fit	Dist. fit	Binom. fit
FeCrY RT	340.1	289.1	289.1	0.05	0.04
FeCrTiY RT	337.3	278.5	278.8	-0.11	-0.11
FeCrY 4K	354.0	295.5	298.4	-0.05	0.00
FeCrTiY 4K	354.0	295.3	298.3	-0.05	-0.01
FeCrY CEMS	337.4	288.0	290.1	0.07	0.11
FeCrTiY CEMS	334.2	275.1	277.9	-0.12	-0.03
FeCrY CXMS	339.3	289.5	295.7	0.07	0.18
FeCrTiY CXMS	339.9	279.9	286.4	-0.12	-0.01
FeCrY 760 °C	336.6	306.3	312.1	0.12	0.29
FeCrTiY 760 °C	337.4	307.1	313.1	0.12	0.30
Errors	± 0.4	± 0.4	± 0.4	± 0.02	± 0.02

4. Conclusion

α -Fe samples in powder or foils as well as some binary Fe-Cr model-alloys obtained by planetary milling have been investigated by means of XRD, transmission and backscattering Mössbauer spectroscopy.

In the case of α -Fe samples, the Mössbauer spectra display similar six line patterns characteristic for bcc α -Fe structure. The difference between powders and foils are given by the intensities of the lines 2 and 5 due to the preferential alignment of the nuclear magnetic moments in the foil samples.

In the case of FeCrY and FeCrTiY nanoscaled alloys (~10 nm), two fitting models were applied in the Mössbauer spectra computing for all recorded data: a hyperfine magnetic fields distribution (Hesse-Rübartsch model) and the binomial model. The theoretical evaluation of hyperfine magnetic fields H (m, n, c), for different numbers (m, n) of chromium atoms in the first and respectively second vicinity of iron, at a given concentration c, is in good agreement with the experimental Mössbauer data. No phase transitions were evidenced between the room temperature and liquid helium temperature. For the FeCrY samples (without thermal treatment)

the SRO values are close to zero, revealing a rather random distribution of Cr atoms in α -Fe structure. In the case of FeCrTiY nanoscaled sample, the SRO parameter becomes negative indicating an increase of Fe-Cr pairs in the system. For thermally treated samples (vacuum \sim 760 °C) the best fit with the experimental data in the binomial model was obtained at a chromium concentration of \sim 9% instead of 14.1% (nominal content in the untreated samples). The values of $\langle H \rangle$, given by the distribution model for the treated samples, support the same chromium concentration value. This finding, together with the positive SRO values, indicates a shortage in Fe-Cr pairs after thermal treatments and a possible chromium clustering process. Due to the very small crystallite size (\sim 10 nm) of the studied samples, the results by CEMS and CXMS measurements are similar with those obtained in transmission geometry.

Based on the present study we can infer that Mössbauer spectroscopy is a very appropriate method to study the magnetic hyperfine interactions and SRO parameter peculiarities in Fe-Cr based alloys, information that can be used to improve the production technology of FeCr materials for fusion reactors.

Acknowledgement. We are grateful to Prof. Jose Brito Correia - IST Portugal for supplying us the nanoscaled alloys. The financial support from the Romanian National Authority for Scientific Research under EURATOM contract FU-07-CT-2007-00064 is greatly acknowledged.

References

- [1] R. L. Klueh, D.R. Harries, High-Chromium Ferritic and Martensitic Steels for Nuclear Applications, ASTM, 2001.
- [2] K. Ehrlich, Fus. Eng Des. 71, 56-57 (2001).
- [3] M. Matijasevic, A. Almazouzi, Journal of Nuclear Materials 377,147–154 (2008).
- [4] S. Dubiel, C. Sauer, W. Zinn, Phys. Rev. B 30, 6285 (1984).
- [5] S. M. Dubiel and J. Zukrowski, J. Magn. Magn. Mater. 23, 214 (1981).
- [6] J. Cieślak, S.M. Dubiel, J. Alloys Comp., 387, 36–43 (2005).
- [7] J.M. Cowley, Phys. Rev. 77, 669-675(1950).
- [8] V.V. Ovchinnikov et al, Fiz. Met. Metalloved., 42, 310 (1976).
- [9] V.V. Ovchinnikov, B.Yu. Goloborodsky, N.V. Gushchina, V.A. Semionkin, E. Wiser, Appl. Phys. A 83, 83–88 (2006).
- [10] G.K. Werthaim, V. Jaccarino, J.H. Wernik, D.N.E. Buchanan, Phys. Rev. Lett.,12, 24 (1964).

FUNCTIONAL GRADIENT W-STEEL MATERIALS BY UNCONVENTIONAL CO-SINTERING ROUTES

A. Galatanu, I. Enculescu, A.D. Jianu

National Institute of Materials Physics, Bucharest

Overview

FGM W-Fe and W-steel (316) cylindrical samples with 10-20 mm diameters and 1-10 mm heights have been sintered at different temperatures and applied pressures. The samples were realized by spark plasma sintering (SPS) or classical sintering starting with mixtures of powders in 1:0, 1:1, 1:2, 1:3 atomic proportions, placed in up to 9 different layers with thickness from 0.1 to 5 mm. SEM and EDX investigations have been performed for all samples, aiming to investigate the influence of layer thickness and compositions as well as the role of different sintering temperatures and pressures in process optimisation. Important results were obtained concerning the effects of different thermal and electrical conductivities of W and Fe in SPS process, the oxygen influence on sintering process and the diffusion of Fe and W in final materials.

Detailed results

1. Sintering of W-Fe FGM

In a first stage FGM W-Fe cylindrical samples with 10-20 mm diameters and 1-10 mm heights have been sintered at different temperatures and applied pressures. The samples were realized by spark plasma sintering (SPS) or classical sintering starting with mixtures of Fe and W powders in 1:0, 1:1, 1:2, 1:3 atomic proportions, placed in up to 7 different layers with thickness from 0.2 to 5 mm. A typical specimen is depicted in Fig 1.

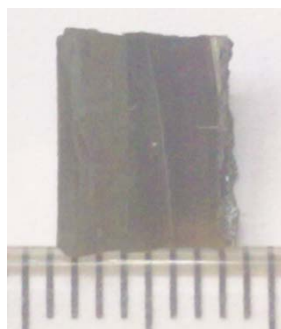


Figure 1 - Typical W-Fe FGM specimen, realized by SPS at 1120 C and 80 MPa in Ar.

Fe spherical powder with grain sizes from 1-4 μm and W powders 0.5-10 μm have been mixed by ball milling at low energy in 1:0, 1:1, 1:2, 1:3 atomic proportions. The different shapes of the

Fe and W grains allowed us to visually monitor the sintering effect in final materials. From this powder mixtures up to 7 different layers have been placed in graphite mold and sintered at 980-1450 C, 0-100 Mpa in Ar or air by SPS. Analysis of SEM and EDX results showed that Fe diffusion in W is higher than W diffusion in Fe. This result can be clearly deduced from the EDX specific metal profiles as shown in figure 2.

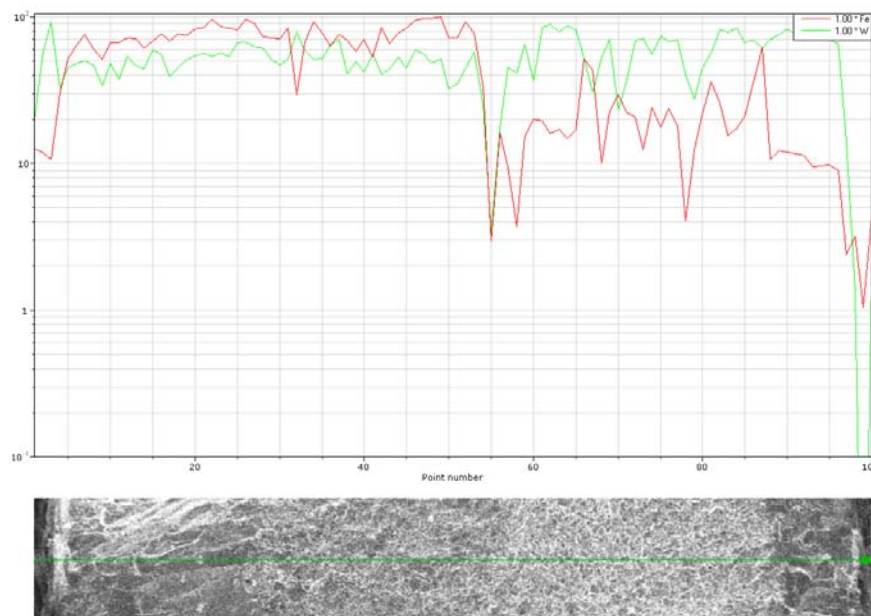


Figure 2 - A 0.5 mm zone at the border of 1:1 FeW to W (each about 0.25 mm) in a sample produced by SPS at 1450 C in Ar at about 50 Mpa. Left zone FeW (Fe = red), note the slight decrease of Fe content. Right zone W, note about 15% Fe content.

The Fe diffusion can be seen in the entire W rich zone, up to the sample edge. A quantitative EDX analysis at this edge confirms presence of Fe and also a higher oxygen content at this edge compared to the Fe rich edge. One should also notice the relatively high C content in the material. This is due to the C migration from the graphite mold. From this results some important improvement for sample preparation have been inferred. We have also noticed the presence of O in the samples and the oxidation effect is important to the strength of the samples. Thus EDX spectra have been recorded in different zones of the samples. A typical result is plotted in figure 3.

The quality of the Fe-W FGMs can be estimated from the sample morphology. Thus SEM pictures have been recorded from different areas in the section of the samples. SEM results for a FGM obtained by SPS at 980 C in Ar, at about 80 MPa, show a sharp change at 100%-75% interface, but a better gradient appears in the sample middle sections. Thus one can draw the conclusion that more layers and thinner toward sample edges are necessary. Concerning the work temperature a lower contraction was recorded, pointing to the necessity of a higher sintering temperature.

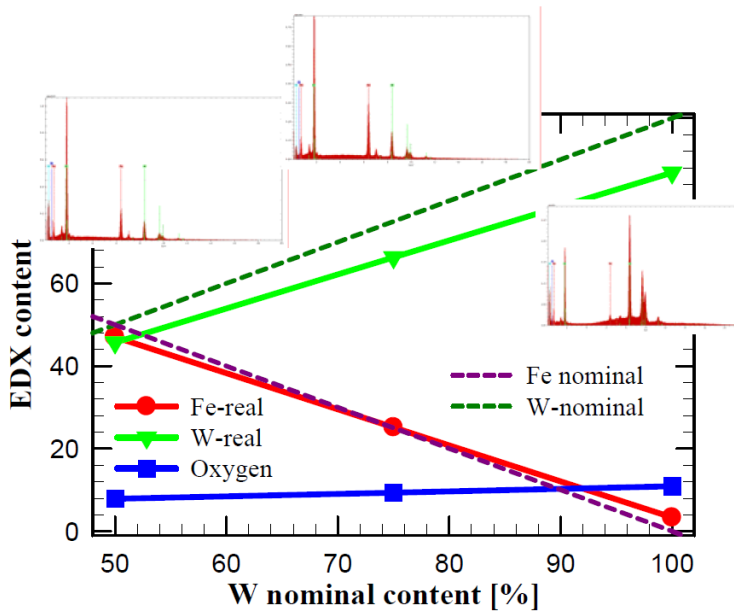


Fig 3. Oxygen content along a Fe-W FGM sample (SPS at 1450 C in Ar, at about 50 MPa powder manipulation in air)

SEM results for a FGM obtained by SPS at 1120 C in Ar, at about 80 Mpa, are show a generally sharp change in the sample morfology. Thus we concluded that more layers are necessary for a proper gradient and also a decrease of layer thickness is needed. Comparisson with other results and the literature brought the conclusion that 1100 C is the lowest temperature possible for effective sintering of powders with μm grain size.

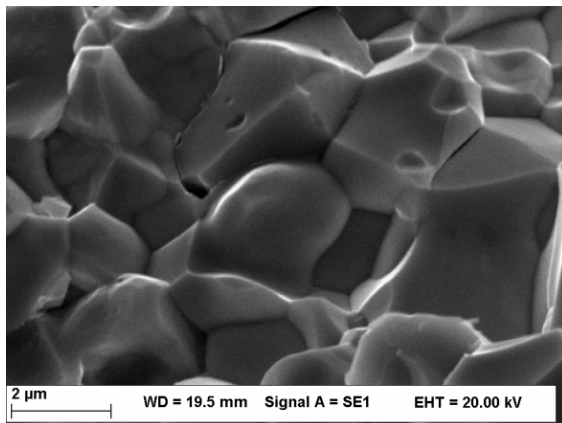


Figure 4 - An almost perfect sintering of the Fe-W mixture obtained by SPS at 1450 C.

SEM results for a FGM obtained by SPS at 1450 C in Ar, at about 50 MPa, are show a partial melting in the Fe rich area. This melting can be explained by the lower thermal and electrical conductivity of the Fe compared to W at high temperature. The former induces a longer time necessary for the dissipation of the accumulated heat while the later produces an enhanced Joule heating of the sample in this area. Thus a decrease of the sintering temperature might be necessary to avoid partial sample melting. On the other hand, as shown in figure 4, a very good sintering was observed in the Fe-W mixture area with a general compaction of the sample toward 100%.

2. Sintering of W-steel FGM

In a second stage we have optimized the process for W and steel. For these FGM we have produced cylindrical samples with 10 mm diameters and 1-8 mm heights. The samples were realized by spark plasma sintering (SPS) starting with mixtures of steel and W powders in various atomic proportions, placed in up to 9 different layers with thickness from 0.1 to 3 mm. The samples have been sintered at temperatures between 1100 and 1300 C with applied pressures between 60 and 80 MPa in Ar. The experiments were carried out aiming to solve 3 main points in the material optimization.

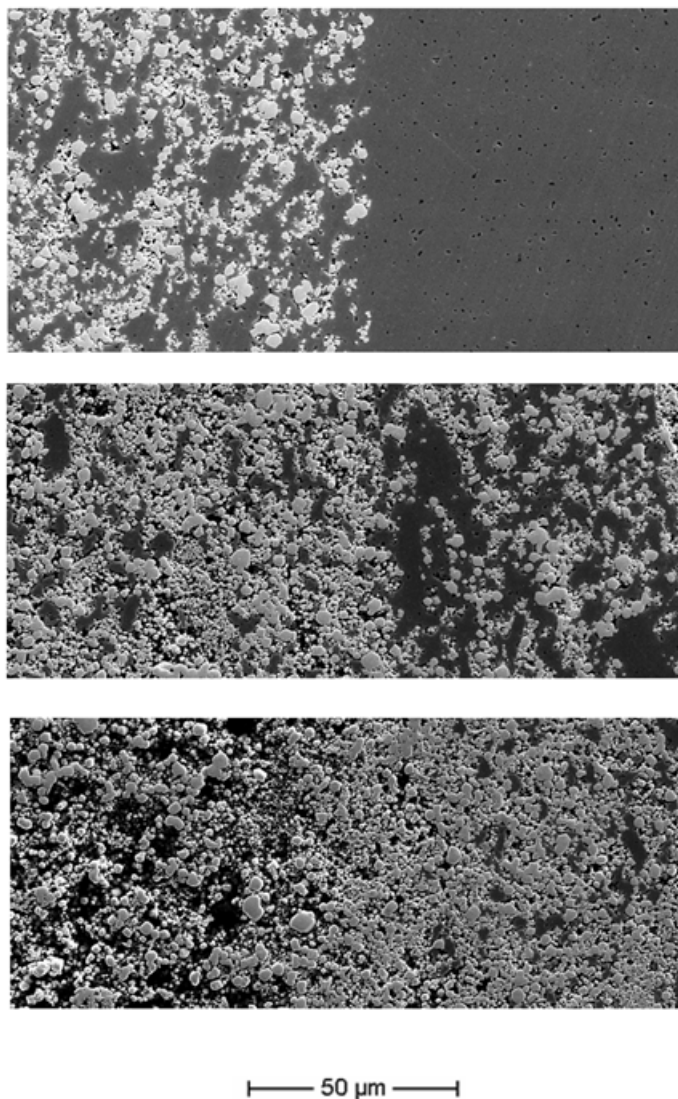


Fig. 5. Comparison of interfaces between layers with different W-steel compositions:

Top W 50% (atomic %) with steel,

Middle: W 75% with W 50%,

Bottom: -.W 70% with W 60%.

The first point of interest is to determine the optimal temperature for sintering the FGM. Since steel and W have different electrical conductivities, the current going along the sample will increase the temperature depending on the layer particular composition, while the process

temperature is determined only at one edge of the sample. Thus it is possible either to melt the steel rich part if there the temperature is higher than expected or to have a poor sintering of the W rich side if there the temperature is lower than expected. We have determined that a process temperature of 1300 C read at the steel rich side of the sample is optimal to achieve a good consolidation in the whole sample without melting the steel.

The second point of interest is related to the porosity of the material. The first tests performed on W-Fe FGM in the first stage have shown that applying the pressure at low temperature and heating the sample afterwards results in a small amount of porosity (about 10%) which decreases when the sintering temperature increases. However, applying pressure during heating further reduces the porosity with final results around 97% densification of the samples.

The third main point of interest in the process optimization concerns the realization of a material to a true compositional and morphological gradient in the final material. This can be achieved by increasing the number of layers while decreasing their thickness and taking into account the different diffusion rates of the constituents. Of course, one should keep in mind that a very high number of layers complicates the preparation procedure, especially at industrial scale. Figure 5 compares the morphology of interfaces between layers with different compositions. According to our experimental results, an optimum might be obtained for 8 mm thick sample with 9 layers with composition W:steel of 10:0, 9:1, 8:2, 7:3, 6:4, 4:6, 2:8, 1:9, 0:10 and almost constant increasing of layer thickness toward steel reach end.

3. Joining steel to steel and W to W plates

We have also tested and obtained concluding proofs concerning the possibility to join steel plates (steel to steel) and W plates (W to W) using the SPS equipment. Using our SPS equipment we have joined several steel and W plates. The procedure implied connecting plates from the same material (standard industrial steel, or W, or ODS-Germany), applying low pressure (less than 20 MPa) and heating at 400 C/min up to a material dependent maximum, then cooling down to about 75% of this temperature and maintaining it for about 5 minutes. These tests are an important step toward future developments since it might be necessary to join FGMs with EFDA designed structural materials at temperatures different (lower) to those required for FGM consolidation.

4 Hot pressing fibrous W

In the frame of EFDA cooperation we have also used our equipments to consolidate W fibers composites realized by the IPP Garching. The composites consisted in W fibers, with a W oxide layer and an outer W layer deposited by CVD. The samples have been slowly heated and then slowly pressed up to about 60 MPa. We have obtained a densification of about 10-15%. Several ways to improve the procedure have been investigated.

5. Conclusions

The investigation of process parameters and preparation routes for W-Fe FGM shows that sintering of samples 10-20 mm diameter, 1-10 mm height with 0.2-5 mm thick layers is possible at 1100-1400 C with moderate pressures. For an apparent morphologic gradient 2-4 thin layers toward each margin composition are necessary. EDX and SEM results show that Fe diffuses more in W than W in Fe. Also we observed that oxygen is more present in W rich layers. Thus we conclude the necessity of powder manipulation in protecting atmosphere. Since both thermal and electrical conductivity of Fe are lower than those of W the temperature must be lower in Fe rich zones. Slightly lower sintering temperatures or an improved design of the molds is important to avoid partial melting of the sample.

The investigation of process parameters and preparation routes for W-steel FGM p lead to process optimization. We have produced cylindrical samples with 10 mm diameter and up to 8 mm height by SPS realized from up to 9 different layers. Optimal temperature, pressure and layers composition have been determined.

We have also tested and obtained concluding proofs concerning the possibility to join plates (steel to steel, ODS to ODS and W to W) using the SPS equipment, as an important step toward future developments of materials for DEMO.

Finally, we also successfully tested the hot press procedures to consolidate W fibers composites realized by the IPP Garching.

The present results will contribute to the development of material science and advanced materials for DEMO. The information and know-how obtained will be a start point for further work concerning property gradient joint between W-Eurofer by unconventional co-sintering.

References

- [1] R.M. German, Z.A. Munir. Metallurgical Transactions A, **7A** (1976) 1873.
- [2] G. Prahbu, A. Chakraborty, B. Sarma, Int Journal of Refractory Metals & Hard Metals; **27** (2009) 545.
- [3] S. Grasso, Y. Sakka, G Maizza, Sci. Technol. Adv. Mater. **10** (2009) 053001.
- [4] Y. Kawakami, F. Tamai, T. Otsu, K. Takashima, M. Otsu, Solid State Phenomena; **127** (2007) 179.
- [5] H. Wang, Z. Zak Fang, Kyu Sup Hwang, H. Zhang, D. Siddle, Int Journal of Refractory Metals & Hard Metals; **28** (2010) 312.

ELECTRICAL, MAGNETIC AND MECHANICAL CHARACTERIZATION OF RE123 SUPERCONDUCTING CABLES AND TAPES

T. Petrisor, L. Ciontea

Technical University Cluj-Napoca

Overview

The discovery of high temperature superconductivity (HTS) opened new perspectives in the area of high field magnets for fusion reactors. Moreover, the intrinsic characteristics of several HTS compounds, such as REBa₂Cu₃O₇ (RE = Y, Nd, Gd), are superior to Nb₃Sn. For example, the upper critical field, B_{C2}, of Nb₃Sn at 4.2 K is 23 T, while the upper critical field, B_{C2}, of YBCO at 77 K is greater than 35 T. Another advantage of using RE123 instead of NbTi or Nb₃Sn is the reduced refrigeration cost. Thus, by increasing the operating temperature from 4 K to 77 K the refrigeration costs are reduced by a factor of 10⁴.

During the last decade great progress has been registered in the field of YBCO based coated conductors fabrication. Thus, using the RABiTS technology, a long superconducting tapes up-to 10³ m with a critical current greater than 1MA/cm² at 77 K and zero magnetic are now available on the market. In order to applied the REBa₂Cu₃O₇ (RE123) superconducting tapes in the field of fusion reactor a fully characterization of the HTS superconducting conductors is necessary. This report presents the structural, morphological and electrical characterization of three superconducting coated conductors architectures: YBCO/CeO₂/NiO/Ni-V, YBCO/CeO₂/Ni-W and YBCO/CeO₂/YSZ/CeO₂/Pd/Ni-W.

Publications

- [4] A. Vannozzi, Gy. Thalmaier, A. Armenio, A. Angrisani, A. Augieri, V. Galluzzi, A. Mancini, A. Rufoloni, T. Petrisor, G. Celentano, *Development and characterization of cube-textured Ni-Cu-Co substrates for YBCO-coated conductors*, Acta Materialia 58-3(2010)910-918.
- [5] V. Galluzzi, A. Augieri, T. Petrisor, L. Ciontea, G. Celentano, A. Mancini, A. Vannozzi, A. Angrisani, A. Rufoloni, *Deposition and characterization of YBCO films with BZO inclusions on single crystal substrate*, Physica C, 470-1(2010)S141-144.

Detailed results

2.1 YBCO/CeO₂/NiO/Ni-V

Details about the surface oxidation epitaxy of the Ni-V substrate have been presented elsewhere [1]. The out-of-plane crystallographic alignment of the epitaxial YBCO/CeO₂/NiO/Ni-V structure, as determined by XRD ω -scans through the (002)Ni-V,

(002)NiO, (002)CeO₂ and (005)YBCO peaks, is shown in Fig.1. The FWHM (Full Width Half Maximum) are 6°, 7°, 5.5°, and 8°, respectively. The in-plane alignment determined by the (113)YBCO, (111)CeO₂, (111)NiO and (111)Ni-V pole figures revealed the presence of a (001)[100] cube texture for the Ni-V substrate. The epitaxial relationship of YBCO/CeO₂/NiO/Ni-V multilayer structure is [100]YBCO//[110]CeO₂/[110]NiO/[100]Ni-V. The highest value obtained for the critical current density at 77K and zero magnetic field was 5.4×10^5 A/cm². This value is lower than that observed for YBCO epitaxially grown on (100) SrTiO₃. The J_c depression is probably correlated with the existence of poor coalescence zones close to the substrate grain boundaries. On the other hand, the presence of a-axis oriented grains, revealed by X-ray, causes high-angle grain boundaries which deteriorate the transport properties of the film. A magnetic field dependence of J_c at T=77K and 65K is shown in Fig. 2. The magnetic field, B, was applied parallel to the c-axis.

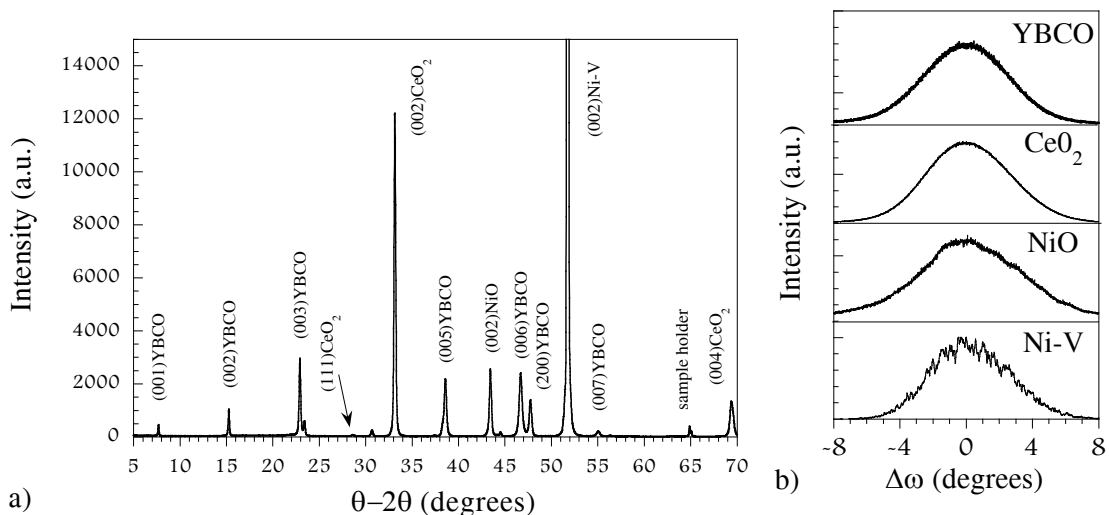


Figure 1 - (a) The X-ray diffraction θ - 2θ pattern of the YBCO/CeO₂/NiO/Ni-V architecture. (b) The ω -scans through the (002)Ni-V, (002)NiO, (002)CeO₂ and (005)YBCO peaks.

These measurements concern a sample with a $T_{cR=0}=87$ K. For comparison the same J_c vs B measurements for a 1 μ m thick YBCO film grown on (001) SrTiO₃ (STO) is also presented. The magnetic field behaviour of the J_c is very similar for both the YBCO film on cube textured Ni-V substrate and the YBCO film on (100) SrTiO₃. The existence of the plateau in the J_c vs B curve in the strong magnetic field (up to 12T) region demonstrates good in-plane and out-of-plane orientations of the YBCO film deposited on the Ni-V substrate. The weak-link behaviour in the limit of low field is more emphasized for the film on Ni-V with respect to the film grown on STO, indicating a greater fraction of weak-linked grains in the YBCO film deposited on Ni-V.

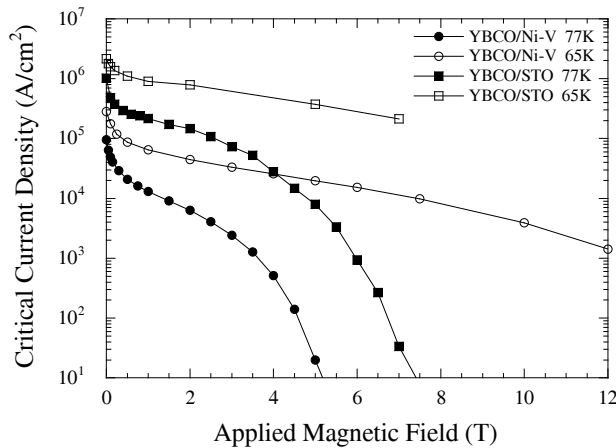


Figure 2 - DC critical current density versus magnetic field measurements at $T=77\text{K}$ and 65K for the YBCO film on $\text{CeO}_2/\text{NiO}/\text{Ni-V}$ and for a YBCO film grown on $(100)\text{SrTiO}_3$.

2.2. YBCO/ CeO_2 /Ni-W

The θ - 2θ scan of the YBCO/ CeO_2 /Ni-W multilayer structure shows that both CeO_2 and YBCO layers exhibit a good c -axis orientation. Nevertheless, the presence of YBCO($h00$) peaks in the XRD spectra indicates that a small fraction of the grains are a -axis oriented. The ω -scans reveal a sharp out-of-plane texture with the FWHM of 5.8° , 5.5° and 5.6° for the (005)YBCO, (200) CeO_2 and (200)Ni-W peaks, respectively.

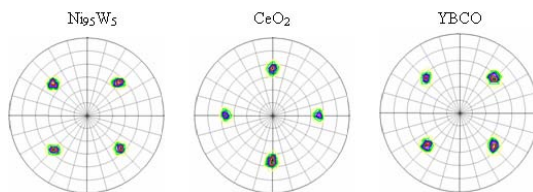


Figure 3 - The Ni-W(111), CeO_2 (111) and YBCO(113) pole figure.

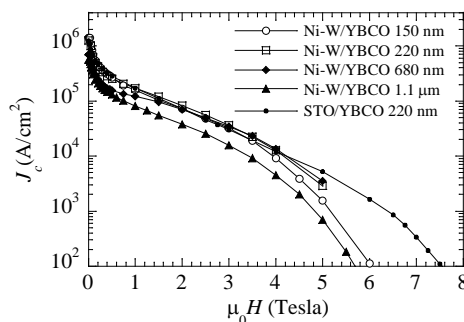


Figure 4 - Critical current density vs. magnetic field for the YBCO film on $\text{CeO}_2/\text{Ni-W}$ and on $(100)\text{SrTiO}_3$.

The FWHM values are very close, indicating a high degree of epitaxy for both CeO_2 and YBCO films. As shown in figure 3, the Ni-W(111), CeO_2 (111) and YBCO(113) pole figures demonstrate that the CeO_2 and YBCO layers are epitaxially grown with a single orientation. The epitaxial relationship of the YBCO/ CeO_2 /Ni-W multilayer structure is $[100]\text{YBCO}/[110]\text{CeO}_2/[100]\text{Ni-W}$. The φ -scans reveal an in-plane texture with the FWHM of 6.6° , 7.2° and 7° for (113)YBCO, (111) CeO_2 and (111)Ni-W, respectively.

The zero resistance critical temperature for the YBCO films is $\approx 88\text{K}$ and the transition width is of about 1 K. The films exhibit a linear behaviour of the normal state resistance with the

R(300)/R(100) ratio of about 2.6, which suggests a high c -axis oriented film. The magnetic field dependence at 77K of the transport critical current density, J_c , for two YBCO films, 0.1 and 0.3 μm thick, grown epitaxially on single crystal substrate and $\text{CeO}_2/\text{Ni-W}$ template, respectively, is shown in figure 4. The highest J_c obtained so far is $\approx 1.2 \times 10^6 \text{ A/cm}^2$. It should be noted that, up to 1 μm thick films, no degradation of the J_c with film thickness was observed.

2.3. YBCO/CeO₂/YSZ/CeO₂/Pd/Ni-W

The details on the deposition and properties of the Pd seed layer are presented elsewhere [2]. Summarizing, the X-ray spectra have revealed that the Pd films are epitaxially grown at temperatures above 200 °C, with the relative intensities ratio $I(002)/(I(111)+I(002))$ ranging from 99.8% to 100%. Above 450 °C, a peak broadening in the high angle tail of the (002)Pd reflection is observable. This feature is related to the Pd-Ni interdiffusion. A sharpening up to about 60% with respect to the Ni-W substrate is reached at higher deposition temperatures. The ϕ -scans analyses on the (111)Pd and (111)Ni peaks reveal that the improvement of the Ni in-plane alignment induced by Pd is limited at about 18-20%.

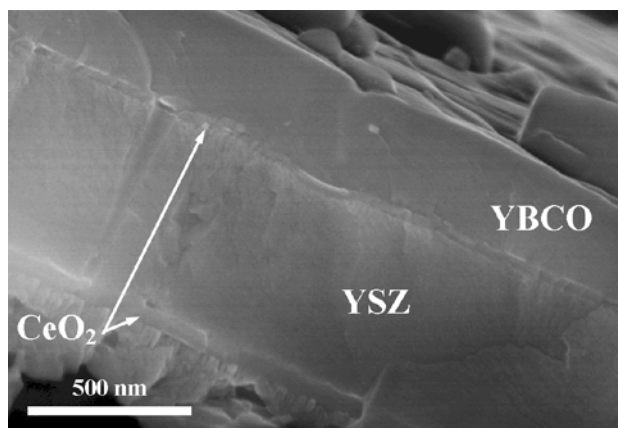


Figure 5 - SEM cross-section of the YBCO film on $\text{CeO}_2/\text{YSZ}/\text{CeO}_2$ deposited on Pd-buffered Ni-W.

YBCO films and the standard $\text{CeO}_2/\text{YSZ}/\text{CeO}_2$ buffer layer structure have been grown on a Pd-buffered Ni-W by PLD [2]. The ω -scans in TD, are reported in table 1 for (005) YBCO, (002) CeO_2 , (002) YSZ and (002) Ni-W. In table 1 the (002) ω -scans for the as deposited Pd film are also reported. As can be seen the FWHM drops from 7.5° of Ni-W to 2.7° of Pd, keeps constant through the oxide buffer layer structure and reaches a value of 2.7° in YBCO. Pole figures analyses reveal a single in-plane orientation with the epitaxy relationship $[100]\text{YBCO} \parallel [110]\text{CeO}_2 \parallel [110]\text{YSZ} \parallel [100]\text{Pd} \parallel [100]\text{Ni-W}$. The FWHM values of the ϕ -scans for the (113)YBCO peak are of about 6°. Morphological analyses reveal that the YBCO films show a smooth and free of cracks surface, together with a good coalescence among the YBCO grains.

Layer	Peak	FWHM
Ni-W	(002)	7.5°
Pd	(002)	2.7°
YSZ	(002)	3.5°
CeO ₂	(002)	3.1°
YBCO	(005)	2.7°

Cross section analysis of fractured samples, figure 5, show that the whole buffer layer architecture and the YBCO film are dense and compact and the interface between each layer is clean and well defined. These results are remarkable, taking into account that, at YBCO deposition temperature, the interdiffusion between Pd and Ni-W is complete.

The zero resistance critical temperature for the YBCO film deposited on CeO₂/YSZ/CeO₂/Pd/Ni-W is about 88.5 K and the transition width is about 2 K. J_c measurements were performed on 2 mm wide as-deposited strip at 77 K and zero magnetic field. The J_c values obtained for some samples are listed on table 2, for YBCO films of two different thicknesses. J_c up to 2.1 MA/cm² is obtained for the 100 nm thick sample. As expected, the sharpening of the orientation distribution results in an improvement of the J_c value.

Table 2 - J_c values

YBCO thickness (nm)	Pd (002) scan FWHM (°)	YBCO (005) scan FWHM (°)	YBCO (113) scan FWHM (°)	J_c (MA/cm ²)
280	8	6.3	6.7	0.75
280	3	3.2	6	1.35
100	3	3.1	6.1	2.1

References

- [1] T. Petrisor, V. Boffa, G. Celentano, L. Ciontea, F. Fabbri, V. Galuzzi, U. Gambardelle, A. Mancini, A. Rufoloni, E. Varesi, *Physica C* 377 (2002) 135-145
- [2] G. Celentano, V. Galluzzi, A. Mancini, A. Rufoloni, A. Vannozzi, A. Augieri, T. Petrisor, L. Ciontea, and U. Gambardella, *Journal of Physics: Conference Series* 43 (2006) 158–161.

MICROANALYSIS OF ODS AND FIBRES REINFORCED MATERIALS, IN VARIOUS FABRICATION STAGES

Corneliu Sârbu

National Institute for R&D of Materials Physics, Bucharest

Overview

We have analysed several kinds of materials by means of an adequate application of microanalysis methods associated with TEM (X-EDS, HRTEM), of XRD and Mössbauer spectroscopy. In the category of ODS type materials were analysed: (1) two mechanically alloyed (MA) powders for sintering as ODSFS; (2) two sintered ODS W-alloys fabricated by PIM (Powder Injection Moulding). A pure PIM sintered W sample was also analysed as a standard material. In the category of Ta-reinforced materials were analysed: (1) a W-Ta sintered alloy made by PIM from mixed powders; (2) one W-composite with Ta-fibers, sintered by SPS (Spark Plasma Sintering).

Publications

- [1] D.T.Blagoeva, J.B.J. Hegeman, M.Jong, J.Opschoor and C.Sarbu, *Development and Characterization of Reference Tungsten / Tungsten-alloys and SiC_f / SiC for DEMO Fusion Applications*, accepted at PFMC-13 (13th Int. Workshop On Plasma-Facing Mater. and Components for Fusion Appl. & 1st Int. Conf. On Fusion Energy Mater. Sci.) Rosenheim, Germany, May 9-13, 2011
- [2] D.T.Blagoeva, J.B.J. Hegeman, M.Jong, J.Opschoor and C.Sarbu, *Development of tungsten alloys for DEMO divertor applications via PIM technology*, accepted for oral presentation at ICFRM-15 (15th Int. Conf. On Fusion Reactor Materials, Oct. 16-22, 2011, Charleston, South Carolina, USA, *Abstract Log Number 15-390*)

Detailed results

1. Methods

The microanalysis methods are standard ones and do not need a detailed description. We used the following TEM microanalysis instruments: (1) a JEOL JEM-200CX-Temscan CTEM microscope equipped with a JEOL-made SEM attachment (allowing the operation of microscope in SE scanning mode and the precise control of the electron-beam position incident on the sample) and with an X-EDS microanalysis attachment model EDS2004 made by IXRF Systems Inc., 15715 Brookford Drive, Houston, Texas, USA; (2) a FEI made HRTEM model Tecnai™ G-2 F-30 S-TWIN, equipped with an EDAX made X-EDS system. We used a Bruker D8 Advance XRD diffractometer in Bragg-Brentano configuration, working with filtered Cu-

K α radiation. We used also a Promeda model Mössbauer spectrometer which allows the acquisition of spectra at RT and liquid nitrogen temperatures of sample.

2. Results and discussion

A. Microanalysis of ODSFS powders alloyed by MA

The MA alloyed powders were prepared by the IST Portuguese Association from initial pure elements powders (Fe: 99% pure, average particles dimension 44 μ m; Cr: 99.95%, particles size < 25 μ m; Y: 99.9%, median particle size 500 μ m; Ti: 99.9%, particle size < 105 μ m), aiming at getting the following two final powder compositions: 85.2wt%Fe-14.1wt%Cr-0.3wt%Y and 85.2wt%Fe-14.1wt%Cr-0.3wt%Y-0.3wt%Ti (based on the process: SS(Fe,Cr,Y,Ti) by MA \rightarrow HT reaction (Fe,Cr)+ Y₂O₃ / TiO₂), to be subsequently used for sintering of ODS nanograined ferritic alloys of Fe-Cr solid solution strengthened with nanoparticles of Y₂O₃, with and without addition of 0.3wt%Ti.

XRD diffractograms have shown that the MA resulted in a b.c.c. Cr-Fe phase which is very similar crystallographically with the ferritic matrix of the 434L steel, with an average particles size (deduced by applying the Scherrer formula to the FWHM of the strongest (110) reflection of the b.c.c. matrix phase) of less than 10nm (approximately 8nm). The particle dimensions distribution was confirmed also by the dark-field CTEM images and by the HRTEM images.

The elemental composition at nano level was determined by X-EDS, the spectra being generated by the micro electron-beams controlled in SEM operation mode (at 40kV and 200kV), either directed on stationary positions on points of a number of individual powder particles or directed to scan nano-sized areas of a number of other individual particles. Surprisingly, the Ti was detected almost everywhere (not only in the samples prepared with initially added Ti powder). Many other impurities were detected almost everywhere in both samples. The presence of Y was detected as randomly present and not in all the individually analysed powder particles. Besides, individual Ytria particles were identified, showing that part of the initial pure Y powder component of the mixture did not enter the b.c.c. Fe-Cr solid solution particles.

The Mössbauer spectroscopy confirmed the b.c.c. Cr-Fe lattice distortion, by comparison with the pure Fe spectrum. The distortion of the pure-Fe spectrum is due to the penetration of Cr in the b.c.c. lattice of Fe. An estimation of the amount of Cr penetrated in the Fe-lattice is of about 15%Cr, showing that the task of getting an appropriate powder to be sintered as ODSFS of 14YWT type (this is one of the EFDA tasks concerning the ODSFS alloys) could be accomplished.

Final conclusions of the microanalysis of ODSFS powders: (a) The Y is not uniformly distributed among the MA alloyed particles. Part of the pure initially added Y is lost, without entering the final MA alloyed powder particles. (b) Ti is present almost overall, even in the

sample which is supposed not to contain this element. (c) Many impurities containing particles were detected. The most frequently observed impurity is Si, but Ca, Mo, Zn, S and Al are also present.

The IST Association ceased to produce any ODSFS materials at mid term of 2010 and we ceased any further microanalysis of that kind of materials.

B. Microanalysis of ODS W-alloys prepared by PIM (Powder Injection Moulding)

A preliminary microanalysis research of two sintered ODS W-alloys was started at the end of 2010, to be continued in 2011. The analysed alloys were (a) W + 1vol%Y₂O₃, (b) W + 5vol%Y₂O₃ and (c) pure-W as a reference material, all these being prepared by NRG Dutch Association by an industrial PIM technology.

(a) Microanalysis of ODS alloy W + 1vol%Y₂O₃

The main results concerning this material:

1). Yttria nanoinclusions were detected in almost all W matrix grains of the sintered material, showing that the task of ODS reinforcing of W matrix was accomplished. Many W matrix grains are containing more than one Yttria nanoinclusion, as indicated by the blue arrows in Figure-1 (which shows a typical aspect of the grain microstructure of the W + 1vol%Y₂O₃ sintered material).

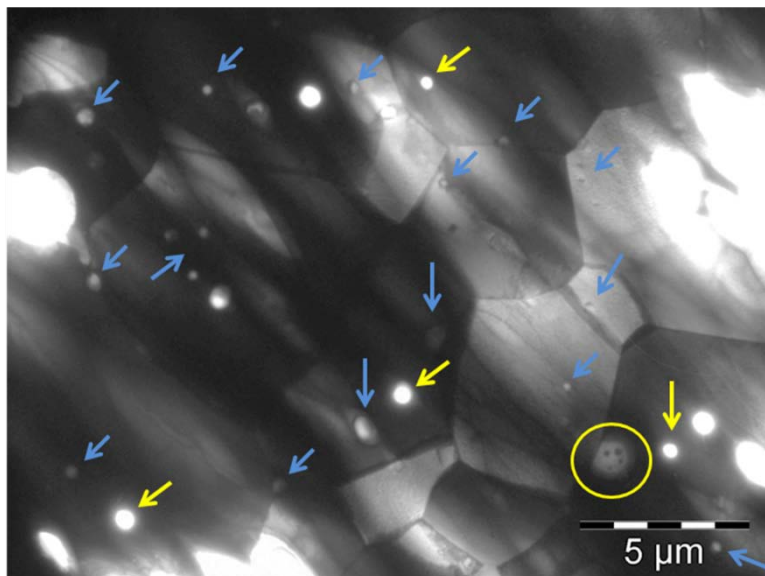


Figure 1 - Matrix grains, pores (indicated by yellow arrows) and Y₂O₃ nano-inclusions (indicated by blue arrows, single or multiple in every matrix grain). The nature of yellow circle marked feature is explained below.

2) We have seldom observed in this material the kind of feature marked by the yellow circle in Figure-1, with an internal structure similar to that shown in detail in Figure-2b. It is located either as shown in Figure-1, i.e. joining two normal W-matrix grains, or as shown in Figure-2a, as an inclusion inside a normal W-matrix grain. The composition of this kind of material structures was determined by X-EDS as being Yttria (appearing in bright contrast in the TEM images from Figures 1, 2a and 2b) which is embedding nano-particles of W (which appears as

dark contrast in the same figures). This microstructure feature was not frequently observed in the ODS W + 1vol% Y_2O_3 alloy.

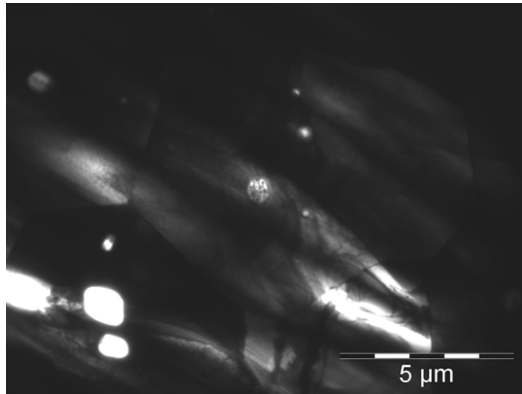


Figure 2.a - A large Y_2O_3 inclusion located inside a W-matrix grain. It contains W nano-inclusions, as determined by X-EDS analysis.

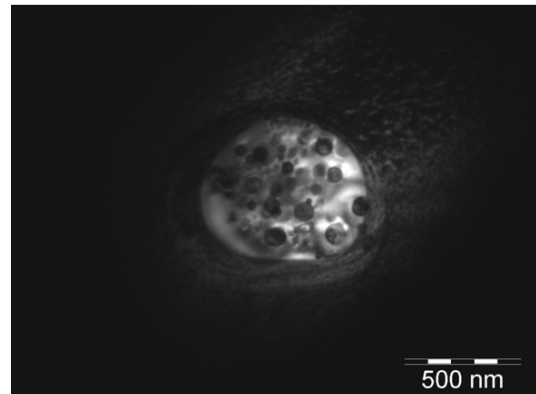


Figure 2.b - The microstructure of an Y_2O_3 large inclusion located inside a W-matrix grain. Similar microstructure has the yellow circle marked feature in Figure-1. The black inclusions contain a large amount of W, according to the X-EDS microanalysis.

(b) Microanalysis of ODS alloy W + 5vol% Y_2O_3

The characteristic grain microstructure of this material is shown in Figure-3, which reveals that the W-matrix grains contain Ytria inclusions (indicated by blue arrows in the image), similar to the W + 1vol% Y_2O_3 ODS alloy. The main difference consists in the presence in the grain microstructure of the W + 5vol% Y_2O_3 ODS alloy of many matrix grains which are large Y_2O_3 particles which are containing nano-inclusions of W inside their volume. This kind of “abnormal” matrix grains is observed much more frequently than in the W + 1vol% Y_2O_3 ODS alloy.

A detailed view of the microstructure of such an “abnormal” matrix grain is shown in Figure-4. X-EDS composition measurements made on several favourably thinned “abnormal” grains have shown that the nano-inclusions appearing as black contrast in Figure-4 contain almost exclusively W and therefore we can admit that, in general, all these “abnormal” matrix grains are made of Y_2O_3 with W nano-inclusions inside it.

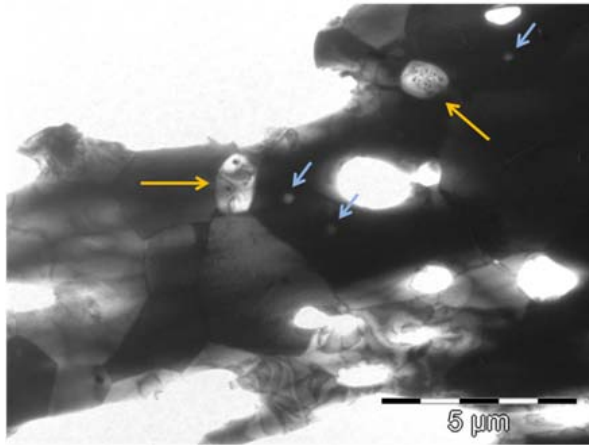


Figure 3 - W-matrix grains, Y_2O_3 inclusions inside W-matrix grains (indicated by blue arrows) and large Y_2O_3 abnormal matrix grains which contain W nano-inclusions.

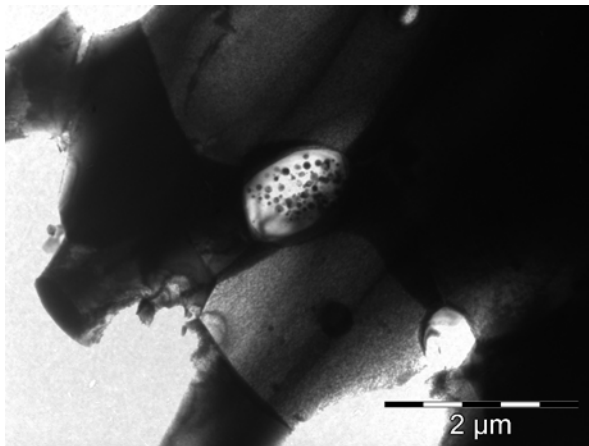


Figure 4 - Detailed structure of an abnormal matrix grain, made of Ytria and containing W nano-inclusions.

The presence of such a significant amount of “abnormal” matrix grains in the ODS W + 5vol% Y_2O_3 could explain the lower thermal conductivity of this alloy, experimentally measured by the producer of the samples and reported to EFDA monitory meetings.

C. Microanalysis of W + Ta(f)10at% composite, prepared by SPS (Spark Plasma Sintering)

The microanalysis of this material was a preliminary one, initiated in 2010 to be followed by a thoroughly conducted research in 2011. The powders for sintering was prepared by MA of W powder and Ta(f) (Ta-fibers). The preliminary X-EDS analysis has shown that as a result of SPS sintering the elements W and Ta are diffusing among different phases (the W matrix and the Ta fibers) in a rather large amount. The existence of those two phases is revealed by the areas of different contrast shown in Figure-5, which is a SEM image at 200kV.

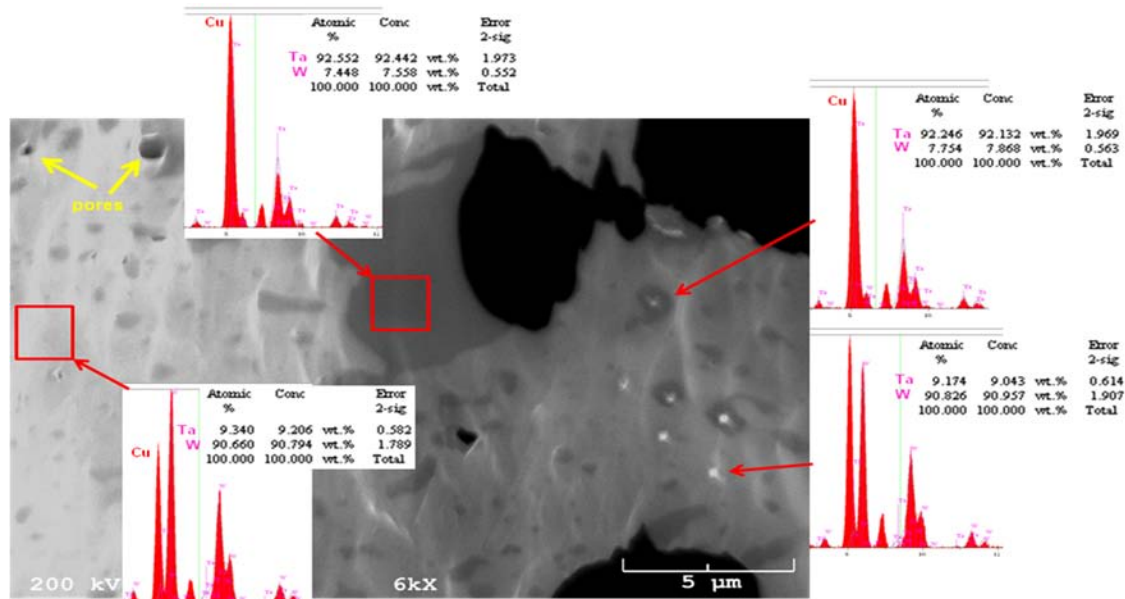


Figure 5 - The existence of two phases is revealed: (a) the brighter-contrast one, which is W-matrix phase containing a large amount of diffused Ta and (b) the darker-contrast one, which is Ta containing a large amount of diffused W. The X-EDS analysis was performed on thin areas of a sample specially thinned for TEM and therefore the quantification based on thin-film approximation is very close to the actual composition. The large amount of interphase diffusion was confirmed also by a more accurate X-EDS analysis performed at the beginning of 2011 by using our new, more performant electron microscope.

4. Conclusion

We have analysed various material samples in as much as they were produced and delivered in due time by our collaborators, which are Associations outside Euratom-MEdC Association. An important result was the revealing of the existence of “abnormal” matrix grains in both W + 1vol%Y₂O₃ ODS alloy and W + 5vol%Y₂O₃ ODS alloy, which is an important indication concerning the cause of the lower thermal conductivity of ODS W + 5vol%Y₂O₃ as compared to that of pure-W reference material produced by the same technology. Our results are evidencing the importance of the composition microanalysis in providing important informations to the materials producers.

Acknowledgement

The reported work includes contributions from the following Associations outside the EUATOM-MEdC Association: NRG-Petten Association and IPS Association, who made the analysed materials.

IN-SITU TEM OBSERVATION OF THE DYNAMICS OF SCREW & EDGE DISLOCATIONS AND HE BUBBLES IN α -FE AND BINARY FE-CR MODEL-ALLOYS SUBJECTED TO ION IRRADIATION VERSUS TEMPERATURE.

V.S.Teodorescu, C. Ghica, L.C.Nistor, A.V.Maraloiu

National Institute for Material Physics, Bucharest

Overview

In situ study of dislocations dynamics in α -Fe and binary Fe-Cr alloys model samples have been performed by (TEM) transmission electron microscope observations. Ribbon samples of Fe and Fe-Cr (9%Cr) alloy have been prepared by melt-spinning method starting from pure materials (99.995% from Alfa Aesar). TEM specimens were prepared by ion milling method. In situ studies were performed by specimen heating in the microscope and the observation of specimen structural transformations in the temperature range RT-500°C. A high density of dislocations has been observed, decorated in majority with gas nano-bubbles. TEM video registrations of dislocation motions have been performed and analyzed. α -Fe ribbons with helium nano-bubbles have been produced by melt-spinning using helium instead of argon as evacuation gas. The TEM observations indicate the presence in these samples of a dislocations and helium nano-bubble nets. The size of the nano-bubbles is dependent on the ribbon production parameters and subsequent annealing temperature. Specimens produced from pure bulk Fe rods were exposed at 10 keV He ion irradiation. The irradiation process induced modifications only at the surface and no bubbles were observed in the specimen volume.

Publications

- [1] V.S.Teodorescu, C. Ghica, L.C.Nistor, A.V.Maraloiu, M. Valeanu, F.Tolea, Helium nano-bubbles in pure Fe ribbons obtained by melt-spinning in He atmosphere, (*in preparation*).

Detailed results

1. Introduction

Due to their low activation property, the high-chromium ferritic-martensitic steels are considered to have the thermal and mechanical properties needed for structural materials to be used in fusion reactors. New structural studies of pure α -Fe and Fe-Cr model alloys are necessary in order to compare the modelling calculations with the experimental data. One old

problem, which is again important, is the gas bubbles formation during irradiation phenomena and dynamics of the irradiation defects. Our goal is to perform experimental in situ TEM studies on samples of pure α -Fe and pure Fe-Cr alloys prepared by melt spinning in NIMP, in the frame of the MAT-REMEV project. These samples showed the presence of gas nano-bubbles and a high density of dislocations, resulted directly from the melt spinning process.

2. Methods

The ribbon samples were produced by melt-spinning at different rotations speeds of the spinning wheel, using pure metals (from Alpha Aesar). The ribbons are extracted in 1atm Ar or He atmosphere, using an evacuation pressure of 1.3 atm. A continuum ribbon is formed in the case of 2000 rot/min. In this case, the surface of the wheel has a radial speed of about 20m/s. The ribbon remained in contact with the Cu wheel for about 4 cm, and left the wheel surface with a speed equal to the radial wheel speed, at a temperature around 700-800 °C, as estimated

The ribbon width is about 1.1 mm. The outer surface of the ribbons is not flat, while the surface at the contact with the wheel is quite flat with a high density of small holes. At this surface, the liquid in contact with the RT copper of the wheel has a cooling rate of about 10^9 - 10^{10} K/s. However, in the ribbon thickness, this cooling rate is lower and is estimated to be around 10^7 K/s at the free surface of the ribbon. Figure 1 shows schematically the data related with the ribbon formation in the melt spinning process and the relation between the ribbon thickness and the wheel speed. About 2 m of ribbon is produced in about 100 ms.

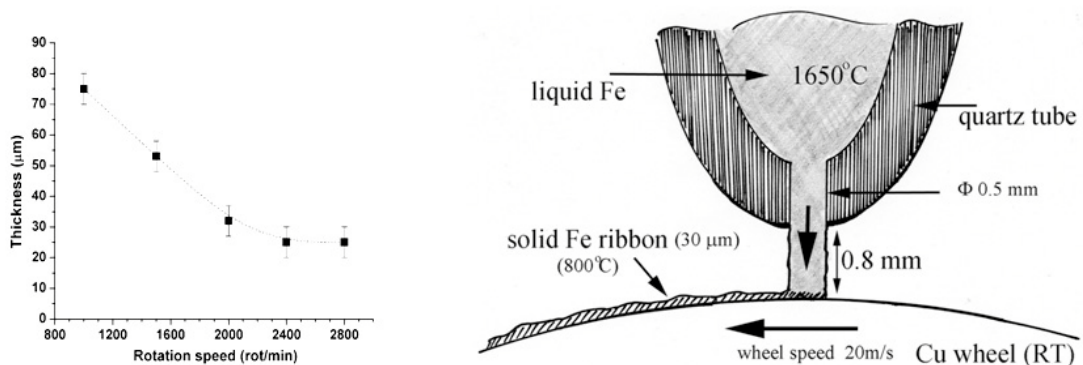


Figure 1 - Schematic showing formation of the ribbon in the melt-spinning process. The thickness of the ribbon is dependent of the wheel speed. Higher the wheel speed, higher the cooling rate of the ribbon.

The TEM observations were performed using the JEOL 200 CX analytical transmission electron microscope provided with a SIS-Olympus Keen View - 20 CCD camera for TEM image recording and processing via the iTEM software platform, an IXRF EDS 2004 system for the chemical composition analysis, a double-tilt specimen holder and a single-tilt heating holder. TEM specimen preparation was performed by ion milling (Gatan PIPS) and electrochemical thinning (Struers).

3. Results and discussion

The morphology of the ribbons is similar regarding the size of the grains and the densities of the defects and subgrainboundaries. In all the examined Fe and Fe-Cr alloy samples, the gas bubbles observed are connected with a network of dislocations, as it can be seen in figure 2. The bubbles are easy to be evidenced by a small underfocus. The majority of the TEM observations were performed in transparent areas with an orientation near to the [100] zone axis. All ribbons showed a weak [100] texture.

The in situ TEM observations were performed by heating the specimens between RT and 500°C. The heating do not lead to any clear modification in the bubbles morphology. Only some moving dislocations were observed during heating. The dislocations dynamics was studied by video recording and frame analysis and is presented in figure 3. By heating at a higher temperature, the oxidation of the specimen is rapid and the TEM observation became not conclusive. Additional heating at 1000°C was performed ex-situ in order to study the changes in the bubble size and morphology.

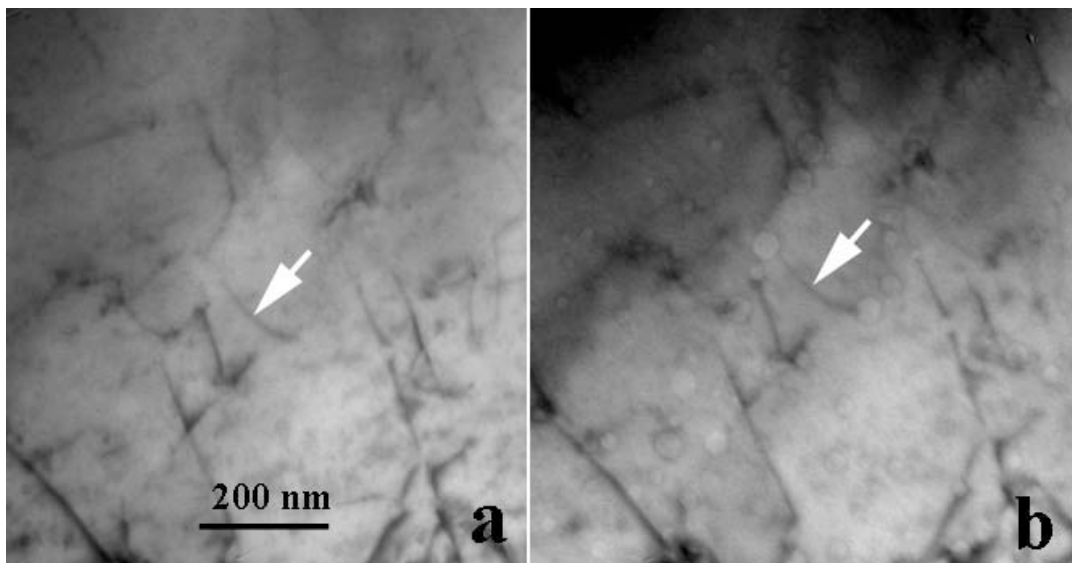


Figure 2 - Dislocation line connecting helium gas nano bubbles: a- TEM image in focus; b- underfocus TEM image: Fresnel contrast at the nano-bubble walls makes them visible

The size of the helium bubbles observed in Fe ribbons depends on the cooling speed-of the ribbon, i.e. of the speed of the spinning wheel. The average size of the bubbles is 14 nm for a 2000 rot/min speed (see figure 4) and grows to 34 nm after ex-situ annealing at 1000 °C. In the ribbon produced with a speed of 1000 rot/min, the average bubble dimension is 52 nm. ~~and~~ After annealing, it grew up to 200 nm, but their density is lower.

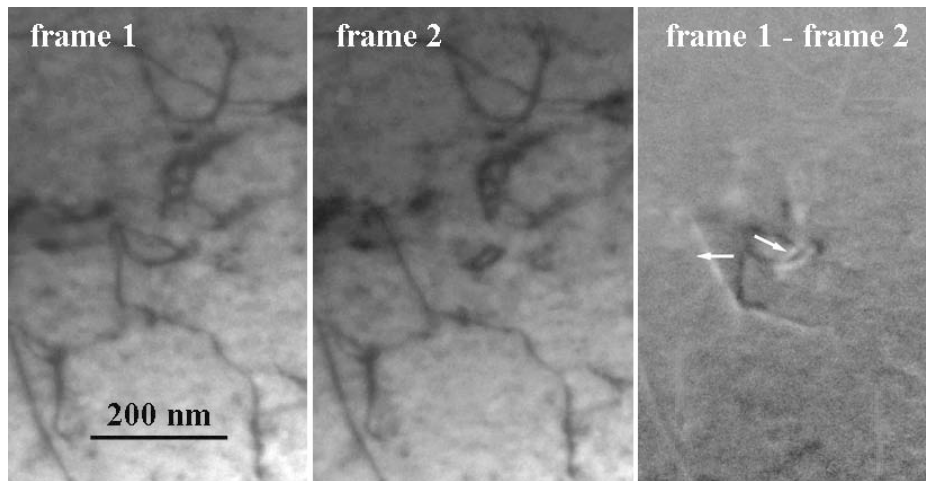


Figure 3 - Dislocations mobility in Fe observed during in-situ heating at 400 °C.

Ribbons prepared at a speed higher than 2500 rot/min do not show bubbles. Only after the ex-situ annealing at 1000°C bubbles with sizes of 100-200 nm can be observed. Our experiments showed that the helium gas is present in all the as prepared iron ribbons, even if the bubbles are not yet nucleated or not visible. The bubbles formation is probably stopped if the cooling speed of the ribbon is high. In all situations, the bubbles are connected with dislocations. It is quite clear that the bubbles nucleation is related to the presence of dislocations. Our in-situ experiments showed also that the moving dislocations are dislocations which are not connected with bubbles. Consequently, the bubbles act as pinning points for dislocations.

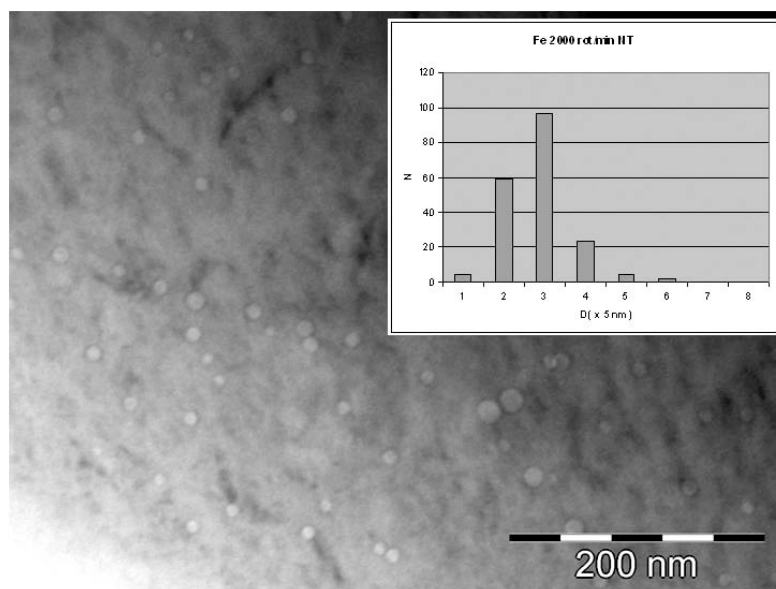


Figure 4 - Spherical He bubbles in the ribbon produced at 2000rot/min. Average size is 14 nm.

The He bubbles became faceted when they reach sizes larger than 50 nm. As the TEM specimen is observed near the [100] zone axis, in the majority of the cases, the shape of the large bubbles became square. The differences in the bubbles size distribution observed in the ion thinning and electropolishing specimens are not pregnant, meaning that the bubbles are not formed during the ion thinning process.

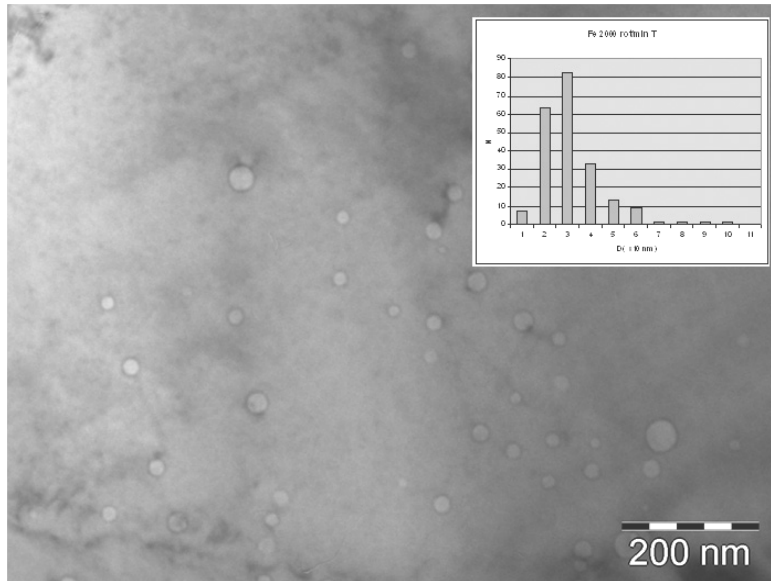


Figure 5 - Spherical bubbles observed in the 2000rot/min sample, after annealing at 1000°C for 5 minutes. The average size is 34 nm. The bubbles remain connected by dislocation lines after annealing.

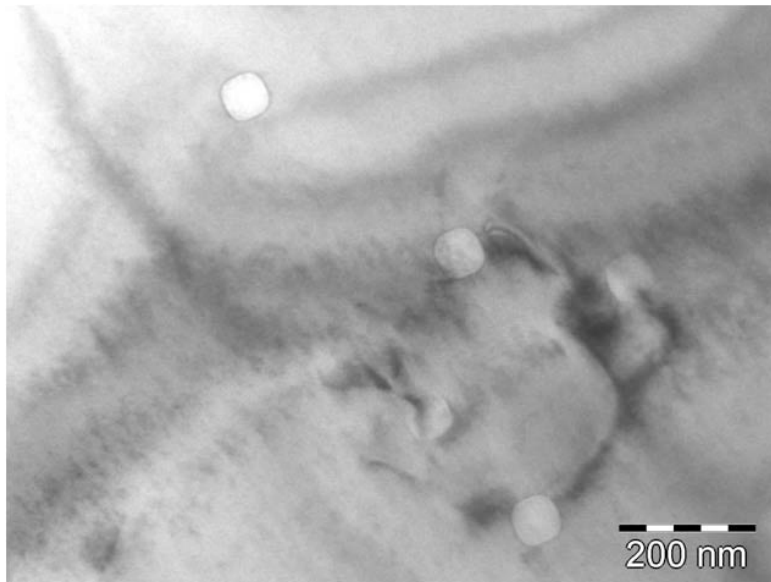


Figure 6 - He bubbles with size between 20 and 120 nm, in the ribbon produced with 1000 rot/min wheel speed. The average size is about 52 nm.

A last experiment was performed by using a modified Gatan Duo Mill apparatus working with helium gas, in order to irradiate a pure iron sample with 10keV helium ions. The total estimated fluence was 10^{16} ions/cm² in about 1000 seconds of irradiation. No bubbles are formed in the sample volume, but the surface of the sample gets a relief, as it can be seen in the AFM image in figure 7.

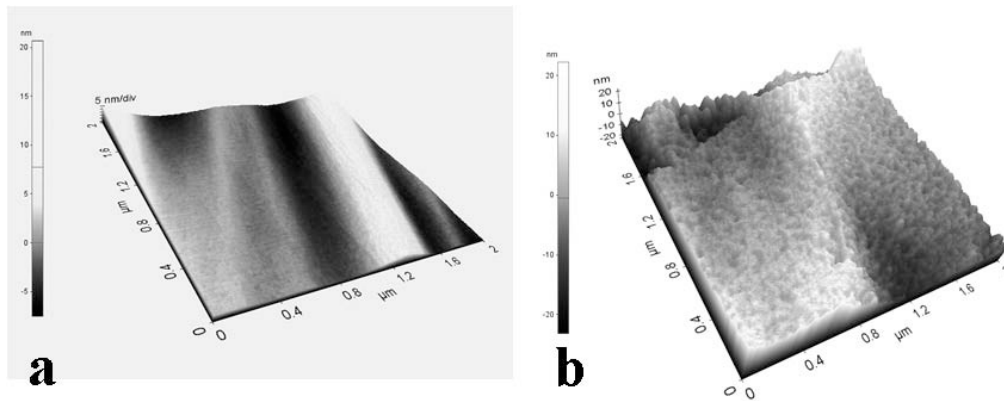


Figure 7. AFM images of the pure iron TEM specimen surface submitted to low energy He ions irradiations. *a*- Surface of the TEM specimen before He irradiation, *b*- Surface of the TEM specimen after He ions irradiation. (10keV , 10^{16} ions/cm^2)

4. Conclusion

Thin Fe and Fe-Cr model alloy ribbons were produced by spin melting method. The TEM specimens were prepared using the ion thinning method (Gatan PIPS) and electropolishing method. The TEM observations were performed at RT and by heating in-situ up to 500°C .

The model Fe and Fe-Cr alloy samples are crystallized with quite large grains and show the presence of a dense network of dislocation and gas nano-bubbles. The size of the bubbles depends of the parameters of the melt-spinning ribbon production, i.e. the size is lower if the cooling rate of the ribbon is higher.

The movement of dislocation segments during heating was observed only in Fe specimens.

The majority of the gas bubbles are interconnected by dislocation lines. These dislocation lines are not mobile during TEM observations or in situ TEM heating observations. The bubbles act as pinning point for the dislocations lines.

The ex-situ annealing at 1000°C was performed in vacuum in order to transform the iron BCC structure into the FCC structure. The BCC \rightarrow FCC transformation does not dramatically modify the network of dislocations and gas bubbles.

TEM and AFM studies were performed on TEM specimens produced from pure bulk Fe rods, which were exposed at 10keV He ion irradiation. The irradiation process induced modifications only on the surface. A surface relief with amplitude of about 10 nm is created by sputtering effects. No nano-bubbles were observed in the specimen volume.

***PARTICIPATION AT JET ENHANCEMENT AND
EXPERIMENTAL PROGRAM***

MANUFACTURING AND TESTING OF W-COATED CFC TILES FOR INSTALLATION IN JET FOR THE ITER-LIKE WALL PROJECT

C. Ruset, E. Grigore, I. Munteanu, N. Budica, D. Nendrean

National Institute for Laser, Plasma and Radiation Physics, Magurele, Bucharest

Overview

Currently, the primary ITER materials choice is a full beryllium main wall with CFC (Carbon Fibre Composite) at the strike points and tungsten at divertor baffles and dome. Since this combination has never been tested in a tokamak, ITER-like Wall project has been launched at JET (Joint European Torus) with the aim to replace the actual CFC first wall with a new one, comprising the same materials choice as it planned for ITER. In the R&D phase of this project (2005-2006) it was demonstrated that W coatings deposited on CFC by Combined Magnetron Sputtering and Ion Implantation (CMSII) technology, which was developed in MEdC Association, exhibited superior thermo-mechanical properties in comparison with other W coatings deposited by conventional PVD and CVD techniques. Consequently, this technology was selected for 10 μm W coating of about 1,000 tiles from the main chamber of tokamak, of different size and dimensions, under industrial conditions. The divertor tiles had to be coated with 200 μm W using Vacuum Plasma Spray technology. Due to the serious technical problems with this technology the strategy concerning the W coating of CFC tiles for JET has been changed. It was accepted that a W coating with a thickness of 20 – 25 μm would be enough for divertor. Under these conditions CMSII technology became a candidate for this job together with Cathodic Vacuum Arc technology. The High Heat Flux (HHF) tests were running in parallel at IPP Garching with GLADIS ion beam facility during the period September 2008 – June 2009. Again, Romanian CMSII new technology proved its superiority. As a result, the task of coating about 800 CFC tiles for divertor was transferred to MEdC Association by extended the existing Art. 6.3 Order to the Task Agreement JW6-TA-EP2-ILC-05.

Since the inner divertor tiles are subjected to deposition and only the outer tiles are subjected to erosion, two coating thickness were applied: 10-15 μm for G3, G4 and HFGC tiles and 20-25 μm for G1, G6, G7, G8 and LBSRP tiles.

Consequently, all CFC tiles for the ITER like Wall project were coated at MEdC.

Publications

- [1] C. Ruset, E. Grigore, H. Maier, R. Neu, H. Greuner, M. Mayer, G. Matthews and JET-EFDA contributors, *Development of W coatings for fusion applications*, 26th Symposium on Fusion

Technology, 27 September - 1 October 2010, Porto, Portugal, Fusion Engineering and Design, (in print for 2011).

- [2] H. Maier, M. Rasinski, E. Grigore, C. Ruset, H. Greuner, B. Böswirth, G.F. Matthews, M. Balden, S. Lindig, JET EFDA contributors, *Performance of W Coatings on CFC with respect to Carbide Formation*, 19th PSI Conference, May 24-28, 2010, San Diego, USA, Journal of Nuclear Materials, 2010 (in press, corrected proof)
- [3] M. Rasinski, H. Maier, C. Ruset, M. Lewadnowska, K. J. Kurzydowski, *Carbide formation in tungsten coatings on CFC substrates*, EMRS 2010, Spring Meeting, 7-11 June 2010, Strasbourg, France.
- [4] An interview concerning the W coating of CFC tiles for the ITER like Wall project at JET was given by Cristian Ruset for JET insight brochure. It is published in the June 2010 issue.

Detailed results

1 Objectives

As it was stated in the previous reports, the main objective of the project was W coating of particular tiles for the main chamber and divertor tiles for the new JET wall. In total there were about 1,800 tiles which had to be coated with layers of 10-15 μm and 20-25 μm .

In 2010 the W coating activity was focused on the main chamber tiles and reserve tiles (both for main chamber and divertor). At the same time, at the technical meeting which occurred at JET on 25.03.2010 it was decided that a new lot of 62 divertor tiles has to be coated as spares. A priority list containing 288 remaining tiles to be W coated with 10-15 μm and 20-25 μm at that moment was issued. Priorities were organized on 6 levels. The final date for the Task Agreement was delayed from September to November 2010.

2. Results and discussion

The priority list induced some difficulties in the W coating production because the jiggling devices had to be changed frequently and this reduced the productivity.

A particular attention was paid to IWGL (Be) tiles which have been coated and sent in USA to be assembled together with the Be tiles. A batch of IWGL (Be) and Shinethrough protection tiles is shown in Fig.1a. The two axes rotation device was used in order to achieve a good uniformity of the coating on two or three sides of the tiles. For the big tiles like G1 and G8 the central rotation jiggling device was used (Fig.1b).

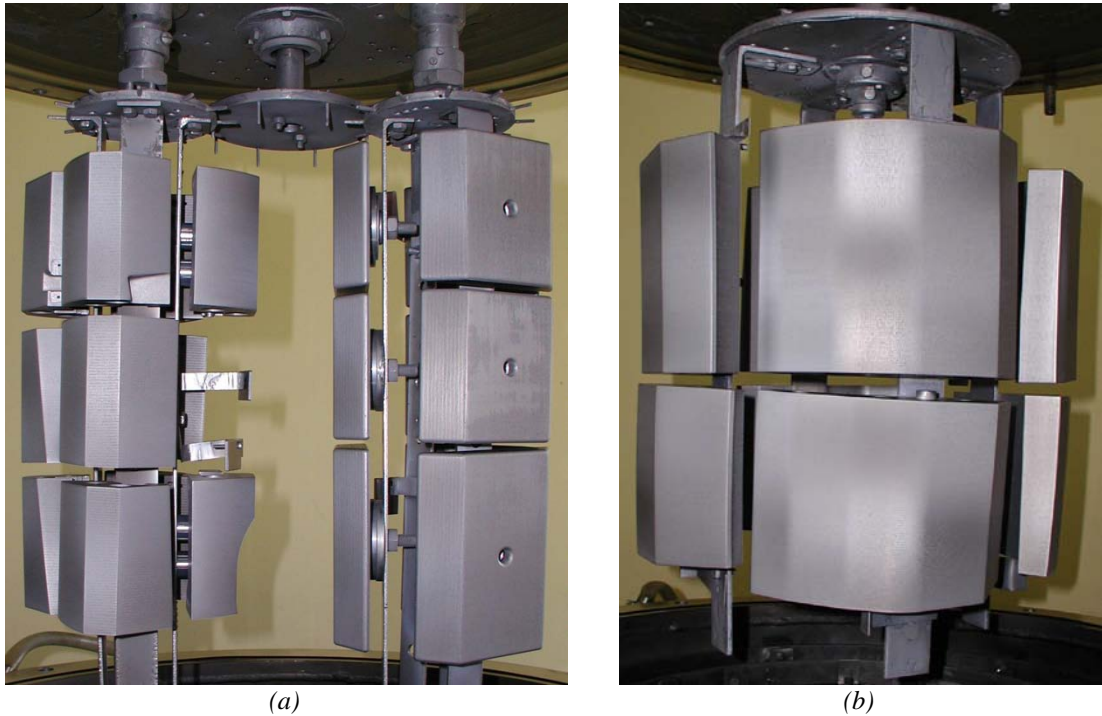


Figure 1- W coated IWGL (Be) and Shinethrough protection tiles (a) and G1, G8 divertor tiles (b)

Another component which required a special attention was the scintillator cup. It had an axial geometry and had to be coated as uniform as possible. This component is shown in Fig.2.

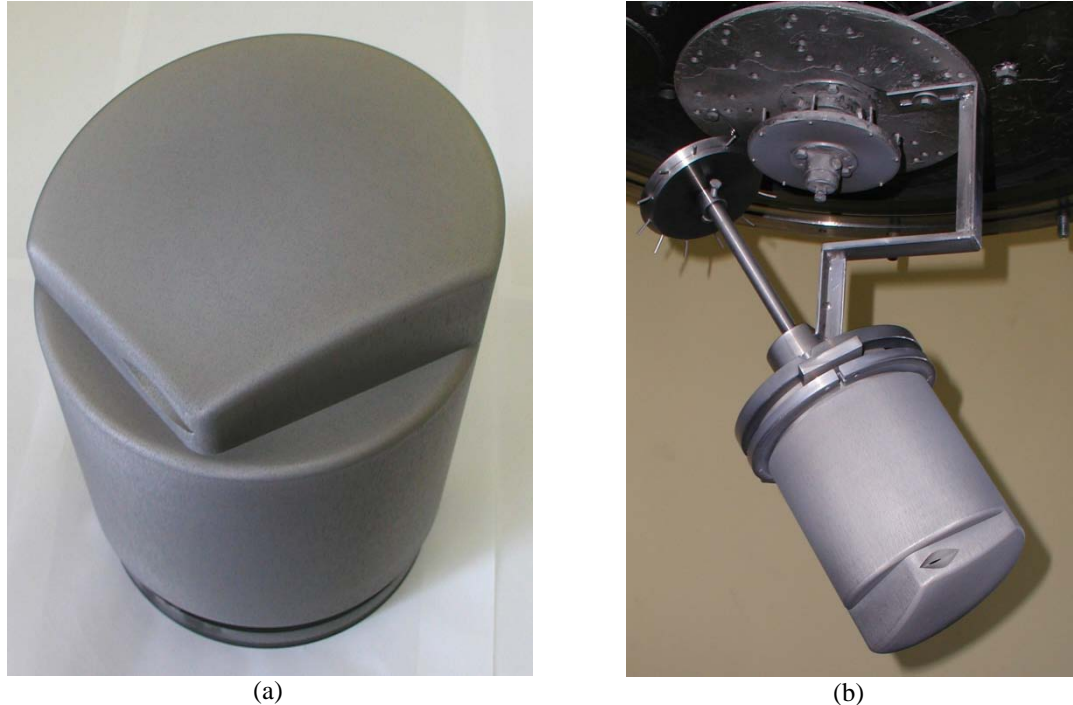


Figure 2 - Scintillator cup coated with 10-16 microns of tungsten (a) and the jigging device for the scintillator cup (b)

A special jigging device with the axis at 35° with respect to the chamber axis was designed and manufactured. Before coating the real CFC scintillator cup, an identical prototype made of fine grain graphite was coated. On this prototype a number of 6 Ti witness samples were positioned in different locations with the aim to check the coating uniformity. After coating, it was found

out that the coating thickness was in the range of 7.7 – 12.5 μm . The real CFC scintillator cup was coated with the same device but the process duration was increased so the final coating thickness to be in the range of 10 – 16 μm . It should be noticed that the CFC for the scintillator cup (A035) was different from DUNLOP CFC used for the other components. The W coating deposited on this material was successfully tested at high heat flux (HHF) in GLADIS at IPP Garching before coating the scintillator cup.

During the reporting period a number of 723 tiles of which 578 for the main chamber and 145 for divertor have been coated and delivered to JET in 7 consignments.

The quality documentation was finalized for these consignments. This documentation included: quality plans, certificates of conformity, inspection release notes, deviation permits, list of tiles versus coating thickness and certificates of cleaning the tiles for each consignment. As annexes to the quality plans the inspection reports and GDOS profiles were issued for each coating run. This documentation was discussed, signed and delivered in a technical meeting at JET which occurred on 8.12.2010.

3. Collaborative actions

- The tungsten coating activity was monitored by weekly meetings between JET and MEdC. Sometimes IPP participates as well. The current status of the production, the priorities in W coating of particular tiles and various problems were discussed in details. - About 10% of the tiles coated in series production were tested at IPP Garching.
- C.Ruset attended the Project Board and the associated technical meeting at JET.

4. By products

The existence of a CMSII industrial coating unit in INFLPR opened new perspectives concerning the development of new technologies for other applications. In this respect a hard coating (2,500-3,000 HV0.05) with a friction coefficient of ~ 0.2 was produced and it is now on tests for automotive applications. This is a nano-composite containing nano-crystallites of WC_{1-x} imbedded into a carbon amorphous matrix (nc- $\text{WC}_{1-x}/\text{a-C}$). Hard WC_{1-x} ensures the wear resistance while carbon is responsible for tribological properties.

5. Conclusions

- 1) „ITER like Wall” project, with a budget of more than 50 M€ is very important for both ITER and JET. It will provide information about the plasma-wall interaction under these particular conditions (Be wall in the main chamber and W at divertor), about the transport of the wall particles through the plasma and about the capability of these materials to sustain the real thermal loads they are subjected at.

- 2) EURATOM MEdC Association has brought a significant contribution to the project by coating with W all the tiles which had to be coated. This means about 1,800 tiles of different shapes and dimensions. This milestone has been successfully accomplished.
- 3) CMSII technology developed in the MEdC Association appears to be not only the best European technology for W coating of carbon based materials (CFC and FFG – Fine Grain Graphite), but the only technology able to produce at the industrial scale relative thick layers (20 – 25 μm) capable to sustain cyclic thermal loads up to 16 MW/m^2 ($T \sim 1,600 \text{ }^\circ\text{C}$) without delamination.
- 4) The project was finished at 31.12.2010. The Final Report was issued and approved.

PRODUCTION OF BERYLLIUM COATINGS FOR INCONEL CLADDING TILES FOR THE ITER-LIKE WALL PROJECT

C. P. Lungu, I. Mustata, V. Zaruschi, I. Jepu, C. Porosnicu, A. Anghel, A. M. Lungu, P. Chiru

National Institute for Laser, Plasma and Radiation Physics, Bucharest

Overview

The project's aim is the coating of about 800 inconel tiles to be used on the first wall of the JET fusion device in Culham, UK. During the 2010 were planned coating activities of 8 μm beryllium thick films on inconel tiles, beryllium coatings on test samples and film thickness characterization. Starting with January 2010, UKAEA sent to the Nuclear Fuel Plant (NFP) – Pitesti the Inconel tiles in few lots. Because during the 2009 were not performed beryllium coatings due to the postponed schedule was necessary, at the beginning of 2010, the re-testing of the deposition systems. New beryllium coatings were performed on test samples, repeating the pre-production coatings. The next step consisted in deposition on real Inconel dump-plates in the presence of specialists from JET (Les Pedrick) and EFDA (Zoita Vasile)

The third step consisted in 8 μm thickness beryllium film deposition using thermal evaporation method on IWGL Cladding, IWC and Dump Plates Inconel tiles.

Were performed thickness tests, adherence tests as well smear tests on the plastic bags used for the coated tiles packing.

The coated tiles were collected by a transport company under the CCFE-Culham management. In total 816 Inconel tiles were coated with beryllium.

Publications

- [1] G. Burcea, F. Dinu, A. Tomescu, L. Pedrick, C. P. Lungu, I. Mustata, V. Zaruschi, and JET-EFDA contributors, *Beryllium coatings on Inconel tiles*, SOFT international Conference, September 2010, Porto, Portugal.

Detailed results

1 Methods

The ITER-like Wall Project, part of the "JET programme in support of ITER", to be implemented on JET included R&D activities to develop a method of depositing Be layers on

an interlayer plus a Be over layer onto Be tiles and characterization of the Be coating purity by surface and structure analysis techniques as well.

The JET main wall will be made of solid Be tiles. In order that the erosion rate of the Be wall to be assessed, it is necessary to be measured erosion of a few microns of beryllium. The “markers” tiles will be distributed in the areas of interest such as Outer Poloidal Limiters (OPL) and Inner Wall Guard Limiters (IWGL).

The “marker” is a Be tile with a stripe of an easily detected heavy metal deposited on it as a thin interlayer, and with a few microns layer of the bulk-like Be on top of that. If the outer layer is eroded at the same rate as the bulk, then the erosion rate can be determined by detecting the distance of the interlayer from the final surface, for erosion of less than the film thickness.

According to the Individual Task Description for the Article 6.3 Order JW6-OEP-MEC-09C the main objectives are the following:

A. To produce Be-coatings on Inconel tiles in accordance with the technical specifications and the JET requirements contained in ILW-EDM-1223-T002

The aims of this task is the manufacturing of Be coatings on inconel samples provided by JET using thermal evaporation method developed at Nuclear Fuel Plant (NFP) in Pitesti

2. Results and discussion

Beryllium coatings on inconel using thermal evaporation in vacuum

The activities for qualification procedure of the thermal evaporation deposition method started in 2008, examining the qualification documents:

1. The qualification plan: Beryllium coatings on Inconel tiles;
2. Quality inspection of Beryllium coatings;
3. Beryllium coatings: technical preparation procedure;
4. Beryllium coatings: Operating procedure;
5. Handling, identification and packing the materials;
6. Beryllium thickness adjustment;
7. Repairing of the inconel tiles coated with Beryllium.

There have been produced Be films coatings on stainless steel test samples and zirconium alloy tiles, material used in serial production at NFP Mioveni-Pitesti. There have been made new adherence tests to ensure the coatings reproducibility. The samples were measured using the MICRODERM device of NFP. The values obtained were between the limit values requested by the project (the thickness of the Be films 7-9 μm).

During 2008, there have been made Be films coatings for method qualification, on inconel tiles and witness samples, sent by UKAEA, Culham, England, respectively: 2 IWGL Tiles, 4 IWC Tiles, 2 DPC Tiles, 100 Inconel witness samples of $6 \times 29.5 \times 1.2 \text{ mm}^3$ and 25 inconel witness samples of $15 \times 20 \times 1.2 \text{ mm}^3$.

The tiles and the witness samples have been placed in the deposition chamber, using for Be films coatings the thermal evaporation method, observing the operating procedure approved by UKAEA.

Figs. 1 shows the photographs of IWGL tiles coated with Be and Fig. 2 shows inconel witness samples after the adherence test.



Figure 1 – Inconel IWGL tiles coated with Be by thermal evaporation in vacuum method

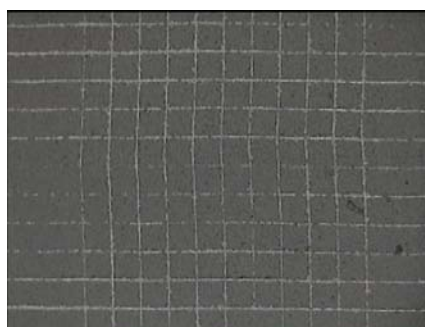


Figure 2 – Inconel witness samples after the adherence test

Thickness measurements (from which resulted that the Be thickness layer was in the range 7-9 microns) and the adherence measurements (from which resulted that the films' adherence is proper) have been made in the presence of UKAEA specialists.

An Inconel sample set coated with Be has been sent to UKAEA for impurities' measurements in the coated layers.

Starting with January 2010, CCFE sent to the Nuclear Fuel Plant (NFP) – Pitesti the Inconel tiles in few lots. The agreed coating schedule was:

Table 1 Be Coating Schedule

Tile System	Latest Arrival Date
IWGL Cladding	8-Feb-2010
IWC	31-Mar-2010
Dump Plates	30-Apr-2010

Because in 2009 were not performed beryllium coatings due to the postponed schedule was necessary, at the beginning of 2010, the re-testing of the deposition systems. New beryllium coatings were performed on test samples, repeating the procedures carried out during the qualification of the evaporation method.

First, were used as substrates, Inconel plates of 5 mm x 10 mm and 15 mm x 20 mm sizes. Thickness was found in the range of 7.09 – 7.97 μm and adherence tests were satisfactory, as shown in Fig. 4. (The documents accompanied the witness samples and the pre-production lot)

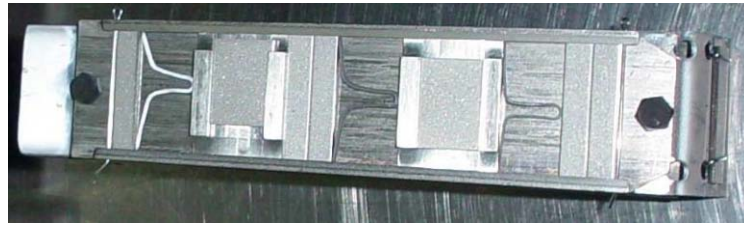


Figure 3 – Photograph of the witness samples mounted on the coating holder.

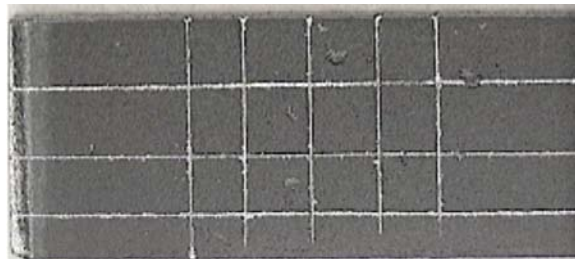


Figure 4 – The adherence test performed on the witness samples.

The next step consisted in deposition on real Inconel dump-plates in the presence of specialists from JET (Les Pedrick) and EFDA (Zoita Vasile)

The third step consisted in 8 μm thickness beryllium film deposition using thermal evaporation method on IWGL Cladding, IWC and Dump Plates Inconel tiles.

The first lot of 48 off IWGL Inconel tiles was collected on March 13.2010



Figure 5 – Adjusting Inconel tiles on the jigging device



Figure 6 – Inconel tiles after beryllium coatings

The updated Be coatings plan was established at 13.05.10:

1. Lot 1 Dump Plate (DP) carrier tiles (196 tiles): 07.05.10
2. Inner Wall Cladding (IWC) tiles (200 tiles): 04.06.10
3. Lot 2 Dump Plate (DP) carrier tiles (196 tiles): 30.06.10
4. Lot 3 Dump Plate (DP) carrier tiles (88 tiles): 30.07.10
4. Lot 3 Dump Plate (DP) carrier tiles (88 tiles): 30.07.10

After be coatings on all Inconel tiles transferred at NFP Pitesti (working in 2 or three shifts in order to reduce the coating period) were performed thickness and adherence tests on the coated tiles and witness samples, respectively. Smear tests were performed on the plastic bags used for the coated tiles packing. Every production lot was accompanied by the following documents:

- a. Packing list for Consignment to JET (Inconel tiles)
- b. Certificate of Conformity for Consignment to JET (Inconel tiles)
- c. INVOICE (not for payment)

The last coated Inconel tiles lot (680 tiles – 10 wooden crates) was collected by a transport company under the CCFE-Culham management. The total number of coated tiles was 816.

4. Conclusion

816 Be-coated Inconel tiles were produced by thermal evaporation at FNP in Mioveni-Pitesti according to the specifications developed during the R&D process and pre-production tests. The tiles were shipped to JET.

The original findings during the project evolution were published in scientific journals [1-2].

Acknowledgement

The reported work includes contributions from the following people outside the EUATOM-MEdC Association: G. Burcea, V. Bailescu, F. Din, A. Tomescu (Nuclear Fuel Plant, Mioveni-Pitesti, Romania), T. Hirai, J. Linke, F. Philips (FZJ EURATOM Association, TEC, Jülich, Germany).

The Romanian research and production groups, greatly acknowledge the contribution of Mark Rubel, Christian Grisolia, Jerome Pamela, Paul Coad, Leslie Pedrick, John Vince, Vasile Zoita, as well as the leaders of the EURATOM MEdC Association Th.Ionescu Bujor and F. Spineanu.

References

- [1] C. P. Lungu, I. Mustata, V. Zaroschi, A. M. Lungu, P. Chiru, A. Anghel, G. Burcea, V. Bailescu, G. Dinuta, F. Din, J OPTOELECTRON ADV M, Vol. 9, No. 4, 2007, 884-886.
- [2] M. Rubel, J.P. Coad, J. Likonen, C.P. Lungu, G.F. Matthews, V. Philipps, E. Wessel and JET-EFDA contributors, Fusion Engineering and Design, Fusion Engineering and Design, Volume 83, Issues 7-9, December 2008, Pages 1072-1076.

PRODUCTION OF BERYLLIUM COATINGS FOR BERYLLIUM TILE MARKERS FOR THE ITER-LIKE WALL PROJECT

C. P. Lungu, I. Mustata, V. Zaroschi, I. Jepu, C. Porosnicu, A. Anghel, A. M. Lungu, P. Chiru

National Institute for Laser, Plasma and Radiation Physics, Bucharest

Overview

The aim of the project represents the coating with 2 μm Ni films followed by coatings of 8 μm Be films on marker tiles made of full beryllium blocks, using the thermionic vacuum arc method (TVA). The marker tiles will be installed on the first wall of the JET device in Culham, UK in order to determine the erosion grade of the wall after the experimental fusion campaigns.

At the beginning of the year 2010 were received a lot of 23 marker tiles in order to be coated. At NILPRP, Elementary Processes in Plasma and Applications group was organized the production flux in order to perform the coatings in the best conditions. The form and the dimensions of the marker tiles were analyzed carefully in order to design and manufacture the jiggling devices to ensure a uniform coating. The Ni and Be coatings were realized during 6 production runs, fulfilling the quality and production documentation. Were performed thickness and adherence measurements on the witness samples deposited in the same deposition runs as the marker tiles. Were carried out the documentations concerning the transfer of beryllium marker tiles and was obtained the needed authorization delivered by the Romanian Authority which control the activities in connection with the use of nuclear materials. The lot of 23 marker tiles was delivered to the JET, Culham and we received the confirmation that the tiles arrived in good conditions. Total number of marker tiles sent to JET: 45.

Publications

- [1] C. P. Lungu, J. Likonen, C. Porosnicu, A. Anghel, I. Jepu, V. Zaroschi, A. M. Lungu, P. Chiru, I. Mustata, *SIMS analyses of beryllium films prepared by TVA method*, SOFT International Conference, September 2010, Porto, Portugal.

Detailed results

1. Marker coatings using thermionic vacuum arc method

Due to the requirement to coat uniformly larger surfaces, a new thermionic vacuum arc (TVA) setup was developed. It uses cylindrical symmetry evaporating TVA guns for both beryllium and nickel, as seen in Fig. 1. The beryllium has been evaporated without a special crucible,

being heated by the TVA electron beam at the upper surface. The bottom part of the anode was cooled by a water cooled stainless steel holder. The evaporation of this kind of anode reduces to zero the contamination of the growing layer.

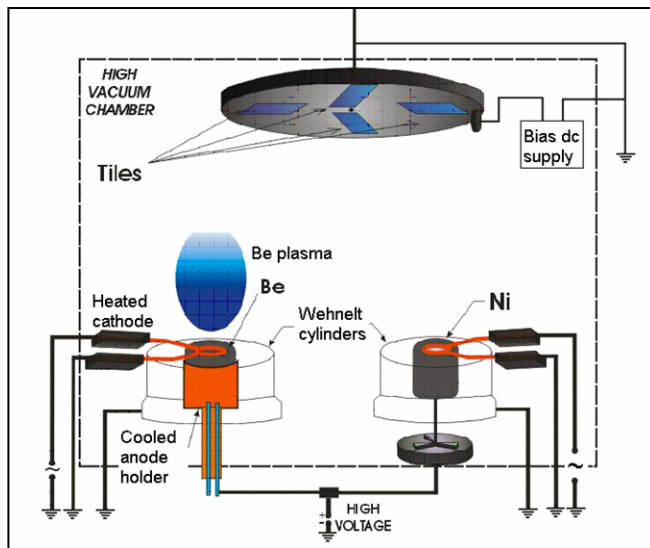


Figure 1 – Berillium and Nickel coating TVA setup

The deposition rates were of 3 - 7 nm/s for Be and 1 - 1.5nm/s for Ni. Nickel was evaporated using a TiB_2 crucible. The ions generated inside the plasma have been accelerated using a bias voltage source having a value of -700V and 10-15 mA current.

The activities for the qualification of the thermionic vacuum arc method in order to produce beryllium heavy metal started in 2008, producing Be/Ni test-samples.

Parallelepiped shaped test samples made of stainless steel were coated with a Ni layer of $2 \pm 0.5 \mu\text{m}$ and then a Be layer of 7-9 μm .

In this purpose there have been adapted the coating equipment resulting in redesigning and manufacturing of the revolving oven for substrates' heating during coating. It was redesigned and manufactured within "Elementary Processes in Plasma and Applications" laboratory. For the revolving system trimming and for markers' efficient coating there has been made a stainless steel plate with clipping devices for simultaneous coatings of 3 "marker" plates of 60mm x 100mm x 30mm, each of them containing 60 stainless steel elements replaceable with Beryllium elements, brought by the JET (Culham) collaborators for TVA deposition method qualification.

3. Results and discussion

Production runs

The parameters used in the sequential deposition of Ni ($2 \pm 0.5 \mu\text{m}$) and Be (6-9 μm) processes were recorded and Technological records, produced for the every run. An example of the coating processes parameters is presented below:

Nickel Coating

- Cathode filament heating: Vac, 50A

- Oven pressure (target $<5 \times 10^{-5}$ torr): start 5.5×10^{-6} torr, end 4.8×10^{-6} torr
- Tile surface temperature: start 253 °C, end 398 °C
- DC discharge Supply: $V_{dc} = +1500V$, $I_{dc} = 1.33A$
- DC bias Supply : $V_{dc} = -700V$, $I_{dc} = 15mA$
- Ni coating time: 40 min
- Thickness reading on QMB: 1.719~2 μm

Beryllium Coating

- Cathode filament heating: V_{ac} , 53.4 A
- Oven pressure (target $<5 \times 10^{-5}$ torr): start 3.8×10^{-6} torr, end 3.6×10^{-6} torr
- Tile surface temperature: start 370 °C, end 380 °C
- DC discharge Supply : $V_{dc} = 1350 V$, $I_{dc} = 870 mA$
- DC bias Supply : $V_{dc} = -700 V$, $I_{dc} = 10 mA$
- Length of time for Be coating time: 40 min
- Thickness reading on QMB: 6.110~7.5 μm (equivalent with 8.1 – 8.5 7.5 μm)

An example of two marker tiles **F70100061** and **F70100107** before and after coatings are shown in Fig. 2 and 3.

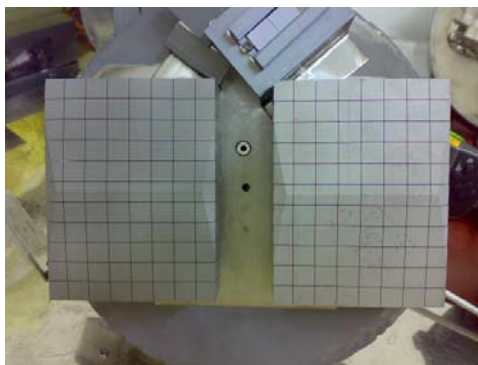


Figure 2 - Photograph of two marker tiles before deposition (IMG_2288)

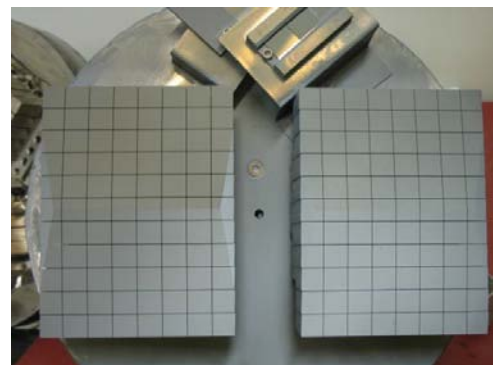


Figure 3- Photograph of of two marker tiles after Ni/Be deposition (IMG_3623)

PRODUCTION-Run 1

This way, the 22 beryllium tiles were coated with 2-3 μm Ni and 7-9 μm Be. The scratch adherence tests inferred the good adhesion of the coated layers. Thickness measurements were performed by JET staff (Paul Coad and Anna Widdowson) using IBA technique. An example of the film thickness distribution along the middle of the marker tile (F70100060) surface is presented in Fig. 4.

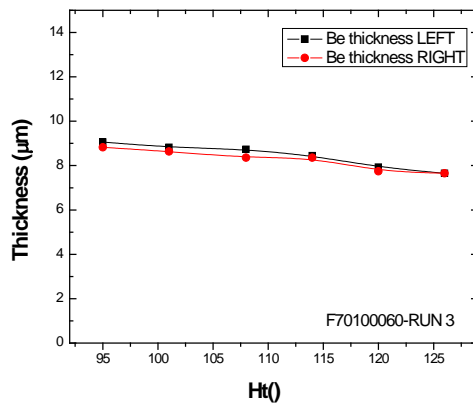


Figure 4 - Thickness measurement of the Be layer of the marker tile F70100060

After the coatings, the marker tiles were double heat sealed, packed in carton crates and put together in a wooden box. The plastic bag surfaces, carton crates and wooden box were smeared in order to characterize the beryllium contamination. After receiving the negative smear tests tiles were sent to JET site by a carrier company managed by JET –CCFE.

In 2010 a lot of 23 beryllium marker tiles were coated with Ni and Be using the same parameters of the thermionic vacuum arc method.

An example of an efficient loading of the heating oven is presented in Fig. 5 and 6. (marker tiles: F70201024/293, F70201026/103, F70201026/335, F70201025/463, F70201025/458, F70201026/082, F70201026/293, F70201024/290)

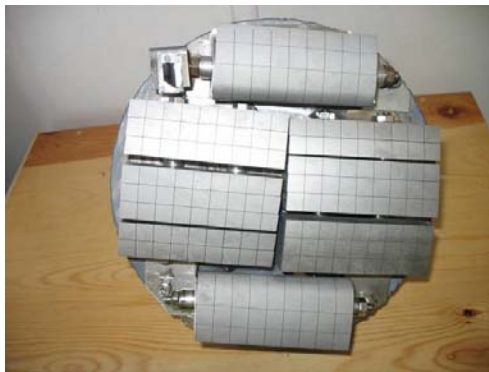


Figure 5- Photograph of two marker tiles before deposition

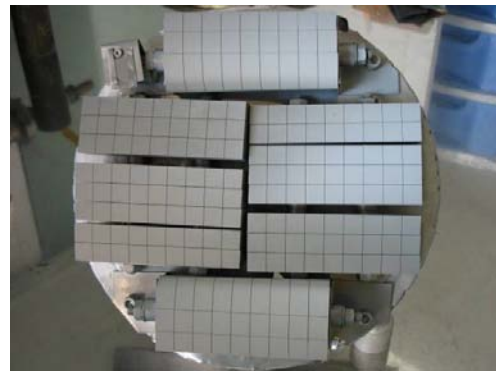


Figure 6- Photograph of two marker tiles after Ni/Be deposition

PRODUCTION-Run 4

After coatings, the tiles were double heat sealed; packed in carton crates and put together in a wooden box. The plastic bag surfaces, carton crates and wooden box were smeared and the smear products (25 mm paper filters) were sent to NFC-Pitesti in order to analyze the Be contamination. The results of the measurements show the Be content under the detection limit ($< 0.1 \mu\text{g}/\text{filter}$). The marker tiles lots were accompanied by the requested documents: Technological records, Packing list for Consignment to JET, Certificate of Conformity for Consignment to JET (marker tiles), Invoices.

4. Conclusion

Thermionic vacuum arc (TVA) method was used to obtain thin film layers of 2-3 μm Ni and 7-9 μm Be for coating on a number of **45 marker tiles** (two lots), as part of the ITER-like fusion reactor wall. By TVA method were evaporated from two different sources nickel and beryllium materials, without opening the vacuum chamber between the two deposition processes. The control of the ion energy and of the electron flux by handling the exterior plasma parameters ensured realization of dense Ni and Be layers, similar to the bulk materials used for the ITER-like Wall beryllium block tiles.

The original findings during the project accomplishment were published in scientific journals and presented at international conferences[1-5].

Acknowledgement

The reported work includes contributions from the following people outside the EURATOM-MEdC Association: T. Hirai, J. Linke, F. Philips (FZJ EURATOM Association, TEC, Jülich, Germany).

The Romanian research and production groups, greatly acknowledge the contribution of Mark Rubel, Christian Grisolia, Jerome Pamela, Paul Coad, Leslie Pedrick, John Vince, Vasile Zoita, as well as the leaders of the EURATOM MEdC Association Th.Ionescu Bujor and F. Spineanu.

References

- [1] C. P. Lungu, I. Mustata, V. Zaroschi, A. M. Lungu, A. Anghel, P. Chiru, M. Rubel, P. Coad G. F. Matthews and JET-EFDA contributors, *Phys. Scr.* T128 (March 2007) 157–161
- [2] C. P. Lungu, I. Mustata, V. Zaroschi, A. M. Lungu, P. Chiru, A. Anghel, G. Burcea, V. Bailescu, G. Dinuta, F. Din, Vol. 9, Iss. 4, 2007, *J Optoelectron Adv M*, Vol. 9, No. 4, 2007, 884-886.
- [3] T. Hirai, J. Linke, M. Rubel, J.P. Coad, J. Likonen, C.P. Lungu, G.F. Matthews, V. Philipps, E. Wessel and JET-EFDA contributors, *Fusion Engineering and Design*, Volume 83, Issues 7-9, December 2008, Pages 1072-1076.
- [4] C. P. Lungu, I. Mustata, A. Anghel, C. Porosnicu, I. Jepu, C. Ticos, A. M. Lungu, M. Ganciu, A. Sobetkii, G Honciuc and P. Chapon, *Frontier of Applied Plasma Technology* (Edited by Osaka University, Japan), Vol.2 July 2009, pp1-6.
- [5] C. P. Lungu, J. Likonen, C. Porosnicu, A. Anghel, I. Jepu, V. Zaroschi, A. M. Lungu, P. Chiru, I. Mustata, SOFT Conference, September 2010, Porto, Portugal

UPGRADE OF GAMMA-RAY CAMERAS: NEUTRON ATTENUATORS

M. Curuia¹, M. Anghel¹, T. Craciunescu², M. Gherendi², S. Soare¹, V. Zoita²

¹ National Institute for Cryogenics and Isotopic Technologies, Rm. Valcea

² National Institute for Laser, Plasma and Radiation Physics, Magurele, Bucharest

Overview

Design solutions based on water neutron attenuators have been developed for the KN3 Gamma-Ray Cameras (the KN3-NA diagnostics upgrade) [1]. All the components of the KN3-NA assembly have been manufactured and in-house tested (mechanical, electrical, pneumatic and hydraulic) on a test stand which was an exact replica of the KN3 horizontal camera neutron attenuator assembly and partially replicated the installation configuration for the KN3 vertical attenuator installation configuration.

The functionality of the neutron KN3 attenuators assembly was tested before delivery to JET. The in-house tests addressed all the functions of the neutron attenuators assembly except for the radiation functions. After in house tests the KN3-NA assembly was delivered to JET and the installation process has been started.

The short version of the Vertical Camera Neutron attenuator casing (VC-NA (S)) is presently installed. This attenuator casing is compatible with 5 bar internal water pressure. The long version of the VC-NA (L) needs to be manufactured again following issues related to the positioning of the internal reinforcement. It is expected that only design modifications will be needed before going into manufacture. For the Horizontal Camera Neutron Attenuator casing (HC-NA), internal reinforcements have to be added, to the present drawings to withstand the latest proposed supplied water pressure (4.5 bars). A new design has been done in February 2011, and then a new TCD-I has been issued. In parallel it was proposed to use the present HC-NA “prototype” to proceed with the installation and tests of the HC-NA system in general and to swap the prototype and the final casing once the latter is available. The manufacture of the new casings for the long version of the VC-NA and the new HC-NA will be done within the present project budget with a redistribution of resources.

Radiation tests on vertical camera neutron attenuator prototype have been done using Plasma Focus Installation PF1000 as neutron source at the IPPLM Euratom Association in Warsaw. The attenuation factor was measured and proved to be in agreement with the attenuation factors considered to be attainable within the project constraints as estimated by neutron transport calculations.

Publications

- [1] M. Curuia, M. Anghel, N. Balshaw, P. Blanchard, T. Craciunescu, T. Edlington, M. Gherendi, V. Kiptily, K. Kneupner, I. Lengar, A. Murari, P. Prior, S. Sanders, M. Scholz, S. Soare, I. Stefanescu, B. Syme, V. Zoita, *Implementation and testing of the JET gamma-ray cameras neutron filters pneumatic system*, Fusion Engineering and Design, [doi:10.1016/j.fusengdes.2011.01.125](https://doi.org/10.1016/j.fusengdes.2011.01.125).

Detailed results

1 Installation at JET of the KN3-NA Assembly

The operation of the neutron KN3 attenuators assembly was tested before delivery to JET. The in-house tests were carried out on a test stand specifically designed for this purpose. The in-house tests addressed all the functions of the neutron attenuators assembly except for the radiation functions.

In July 2010 the KN3-NA Assembly was delivered to JET and the commissioning process has been started. During the commissioning process a careful on site inspection has been carried out when manufacturing errors and serious design flaws has been revealed. An important source for the design errors was the change of water supply system. During the Scheme Design Phase the attenuators were proposed to be filled with static water. Immediately after this solution was changed, due to demineralised water sampling issues, into to pressurized water supply and not all drawings have been updated to the new situation.

The manufacturing errors were generated by high pressure water supply that claims a strong internal and external reinforcement structure that could have a considerable influence over the neutron and gamma ray measurements. All these issues have been discussed during two meetings held at JET with the responsible persons. As results of these meetings, a new solution for attenuators water supply has been identified, meaning the reducing of demineralised water pressure from 5 bars to 4.5 bars (an initial JOC proposal proposal to reduce the water pressure to 0.5 barr was not feasible from technical point of view). Taking into account this new solution for water supply new casings for the horizontal and vertical (long version) attenuators will be redesigned and reconstructed (cost redistribution within the Art. 6.3 Order 13A).

1.1 Horizontal camera neutron attenuator

The Horizontal Camera Neutron Attenuator (HC-NA) casing was initially designed to work with static demineralised water filling. In order to withstand the latest proposed supplied water pressure (4.5 bars) the casing had to be redesigned and internal reinforcements had to be added. A new design has been proposed in February 2011, and a new TCD-I is going to be issued.

1.2 Vertical camera neutron attenuator

The Vertical Camera Neutron Attenuator (VC-NA) short version VC-NA (S) with internal reinforcements, compatible with 5 bars internal pressure has been installed at its location on JET. MCNP calculations in order to evaluate the effects of the internal plates on the gamma-ray field at the position of the gamma-ray detectors (the CsI (Tl) detectors) have been done. The results show that the effects are negligible. The constructed Vertical Camera Neutron Attenuator long version VC-NA (L) has internal plates which intersect the FoV of two gammas – ray detectors, therefore a new casing will be design and manufactured. Due to limited financial resources for NOTIFICATION within Association EURATOM-MEdC, this task will be postponed for the year 2012.

2 Radiation tests on the neutron attenuator prototype

2.1 Methods

Neutron-photon transport calculations have shown that the radiation distribution inside the KN3 neutron attenuators is strongly influenced by the surrounding structures. Thus it would be very difficult (if not impossible) to measure independently the neutron attenuation factors with the attenuators at their final location on JET, using the KN3 detectors. It was therefore proposed to construct an independent setup in order to get experimental information on the neutron field. This setup includes the use of other detectors than those of the KN3 diagnostics. The experiments have to be compared with MCNP calculations. A key point is represented by the attenuation factor. The experiments should prove that the value of the attenuation factor is in agreement with the value estimated to be attainable within the project constraints [4] (see Table 1).

Table 1 – The the attenuation factors estimated to be attainable within the project constraints

Neutron attenuator	Material	Neutron energy	
		2.45 MeV	14.1 MeV
KN3-HC-NA	H ₂ O	10 ²	15
KN3-VC-NA (Long)	H ₂ O	10 ⁴	10 ²
KN3-VC-NA (Short)	H ₂ O	10 ²	15

However due to the specific operations schedule during JET shutdown it was not possible to allow enough time for the experiments. Therefore, the test experiment plan was changed and a new location was proposed at the Institute of Plasma Physics and Laser Microfusion, IPPLM-

Euratom Association Warsaw, Poland. The neutron source is provided by the Plasma-Focus PF1000 device.

In order to measure the transfer function of attenuator, the neutron field was measured using super-heated fluid detectors, SHFD's (also known as "bubble detectors") [3]. Using detectors with different energy thresholds, a bubble detector spectrometer (BDS) is obtained. The BDS covers a broad energy range (0.01 – 20 MeV) and provides six energy thresholds in that range. Therefore the SHFD detectors were used for measuring the neutron fluence and also to determine the neutron energy distribution.

The experiments were performed using the prototype version of the KN3-VC-NA (Short) attenuator. The main goal of the experiments consisted in determining the fast neutron attenuation factor (mean neutron energy about 2.5 MeV).

Preliminary experiments were performed during May 2010 and were dedicated to the characterization of neutron field specific to the PF-1000 device. During extensive experiments neutron spectra were recorded, using the detectors with different energy thresholds (BDS bubble detector spectrometer). The attenuator and detectors were placed on the discharge chamber axis, in the down-stream direction. The experimental results revealed that even without the attenuator, the energy distribution has a strong component in the low energy range ($E < 0.1$ MeV). It was assessed that the main reason for this component were the surrounding structures. The low-energy neutron field would have a strong influence on measurements concerning the attenuation factor. Therefore further experiments were performed during the second half of the year 2010 in order to find an optimum experimental setup and to determine the transfer function of the attenuator.

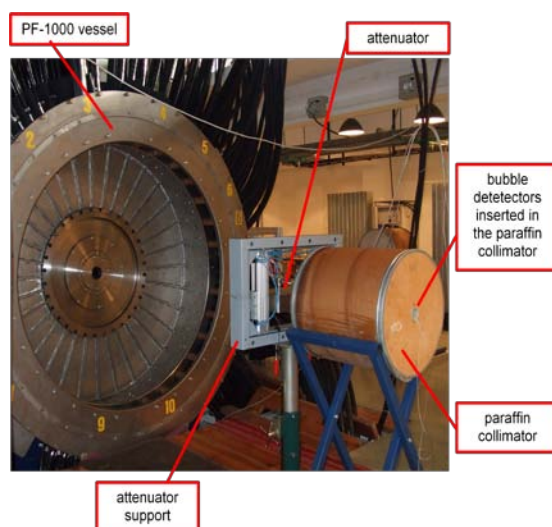


Figure 3 – Experimental configuration

A new measuring location was used: the attenuator and detectors are placed on the discharge chamber axis, in the up-stream direction. The location was chosen in order to minimize the influence of the neutron scattering surrounding structures. Additionally the detectors were placed inside a paraffin collimator in order to provide additional shielding from neutron scattering structures (Fig. 3). This detector-attenuator-source configuration is also a better simulation of the KN3 neutron profile monitor (central channel).

3. Results and discussion

In order to test this configuration neutron spectra were recorded, using detectors with the different energy thresholds (BDS, bubble detector spectrometer).

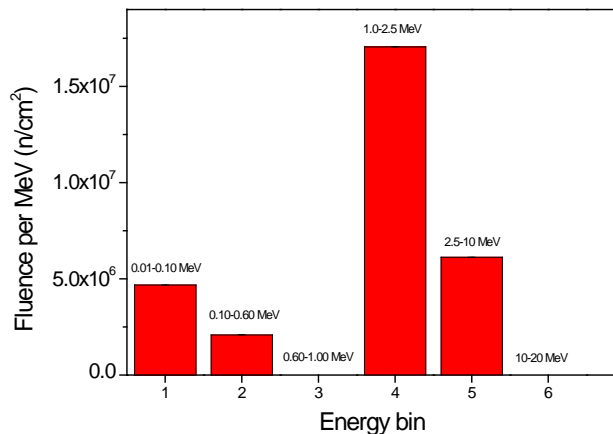


Figure 4 - Neutron energy distribution obtained using an experimental configuration #2 (no attenuator).

The BDS spectrometer for energy distribution recording - energy thresholds/energy bins (MeV) are: (0.01-0.10), (0.10-0.60), (0.60-1.00), (1.00-2.50) and (2.50-10.00). The BDS energy bins used for attenuation factor determination (MeV) are: (1.00-2.50) and (2.50-10.00). It is worth mentioning that for these experiments a new set of spectrometric detectors (BDS), with increased efficiency (especially for the energy thresholds above 1 MeV) were purchased and used.

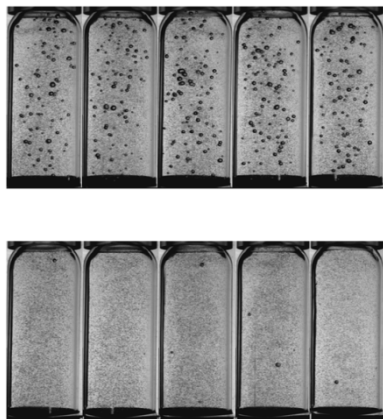


Figure 5 – Representative Detector exposure for attenuation factor determination, BDS (> 1 MeV): detectors after irradiation without attenuator (top) and detectors after irradiation using the attenuator (bottom).

The energy distribution obtained with the new BDS (before introducing the attenuator between the detectors and the neutron source) is illustrated in Fig. 4. The energy distribution was recorded in multiple shots which cumulates a total neutron production of $4.80 \cdot 10^{11}$.

As it can be observed the distribution has a small component in the low energy range ($E < 0.1$ MeV). This component is due to the neutrons moderated by the paraffin collimator and scattered into the detector region.

The attenuation factor was determined by recording the detector response, with and without attenuator, in the energy range above 1 MeV. A representative result is presented in Fig. 5.

The detectors were exposed to multiple shots in order to ensure a good statistics. The total integrated neutron production was $0.81 \cdot 10^{12}$ for the measurements without attenuator and $1.03 \cdot 10^{12}$ for the measurements with attenuator, respectively. The detector responses were normalised both with respect to the neutron production characteristic during their exposure and to their sensitivity. The detector response function was used for detector response deconvolution. The value of the attenuation factor is 110 ± 30 . The evaluated attenuation factor

proved to be in agreement with the attenuation factors considered to be attainable with the short version of the vertical camera neutron attenuator ($\sim 10^2$) [3].

4. Conclusion

The short version of the Vertical Camera Neutron attenuator casing (VC-NA (S)) has been installed on its location at JET. Electro-Pneumatic Cubicle and PLC Cubicle have also been installed and the connection between PLC and CODAS successfully tested. New drawings for HC-NA, compatible with 4.5 bars water pressure have been issued and a new TCD-I has been launched.

Radiation tests for the validation of KN3-NA attenuators were performed. The experiments were performed by using the PF-1000 plasma-focus device at Institute of Plasma and Laser Microfusion IPPLM Warsaw. They used the prototype version of the VC-NA (S) attenuator. After extensive preliminary experiments a measurement arrangement characterized by a negligible scattering background was implemented. Neutron energy distribution measurements confirmed the efficiency of this setup. The attenuation factor was measured and proved to be in agreement with the attenuation factors considered to be attainable within the project constraints as estimated by neutron transport calculations. The results presented here may be considered as the first step in the commissioning procedure for the JET KN3-NA diagnostics upgrade.

Acknowledgement

The reported work includes contributions from the following people outside the EURATOM-MEdC Association: P. Blanchard (EFDA/CSU, Culham Science Centre, Abingdon, UK), N. Balshaw, T. Edlington, V. Kiptily, P. Prior, D. Croft, S. Sanders, G. Kaveney (Association EURATOM-CCFE/JOC, Culham Science Centre, Abingdon, UK), A. Murari (Association EURATOM-ENEA, RFX, Padova, Italy), Marek Scholz, Marian Paduch, Sławomir Jednorog and Rafał Prokopowicz, Association EURATOM-IPPLM (Poland), I. Lengar, Association EURATOM-MHST (Slovenia).

References

- [1] V. Zoita et al., *Fus. Eng. Des.* 84(2009)2052.
- [2] H. Schmidt et al., *Physica Scripta*. Vol. 66, 168, 2002.
- [3] M. Gherendi et al., *J. Optoelectronics Advanced Mat.*, 10 (2008) 2092-2094.
- [4] I. Lengar et al., JET EP2 GRC project report, November 2008.

TANDEM COLLIMATORS FOR GAMMA RAY SPECTROMETER

S. Soare¹, M. Curuia¹, T. Craciunescu², V. Zoita²

¹ National Research and Development Institute for Cryogenics and Isotopic Technologies, Rm Valcea

² National Institute for Laser, Plasma and Radiation Physics, Magurele

Overview

Gamma-ray diagnostics at JET (gamma-ray spectrometry [1] and imaging [2]) have provided some of the most interesting results in experiments such as those of the TTE campaign [3]. The extension of the application of this diagnostics to high power deuterium and, especially, deuterium–tritium discharges is however limited by the present capabilities of these diagnostics. For instance, with the existing diagnostics capabilities the gamma-ray signal is completely overwhelmed by neutron events even in JET discharges using a few MW's of neutral beams. A coherent set of upgrades was therefore considered indispensable to extend the JET gamma-ray diagnostic capabilities and to improve the measurements in order to better support the experimental programme.

The main aim of the KM6T Tandem Collimators for the Tangential Gamma Ray Spectrometer (TCS project) is to provide a proper collimation for the gamma-ray (BGO) detector of the tangential gamma-ray spectrometer, with a well-defined field of view at the plasma end of the diagnostics line-of-sight. The collimation system should at the same time improve the signal-to-background ratio at the detector end of the line-of-sight.

Publications

- [1] S. Soare, N. Balshaw, P. Blanchard, T. Craciunescu, D. Croft, M. Curuia, T. Edlington, V. Kiptily, A. Murari, P. Prior, S. Sanders, B. Syme, V. Zoita, *Tandem Collimators for the JET Tangential Gamma-Ray Spectrometer*, Fus. Eng. Des. 2010 (in print), DOI: [10.1016/j.fusengdes.2010.12.073](https://doi.org/10.1016/j.fusengdes.2010.12.073).

Detailed results

1. KM6T Pre-collimator. Components and Location.

Due to constraints imposed to the design of the collimators system, the clearances between the collimators bore and the KX1 flight tube had to be increased. This led to an increment in the field of view determined by the collimators and thus additional sources of parasitic gamma-rays

will fall into the field of view. To overcome this, a third object was proposed to be inserted into the system (originally designed as a tandem collimator) called TCS pre-collimator.

The TCS pre-collimator is proposed to be installed on the OCT8 vacuum port flange, clamped onto the KX1 flight tube flange, Fig. 1.1. The collimating (for gamma radiation) material will be Pb nuclear grade encased in a steel structure (all welded). Total weight of the pre-collimator is 205kg.

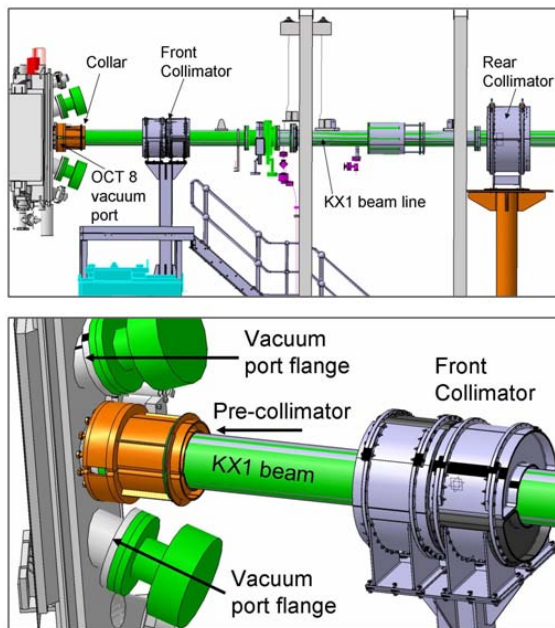


Figure 1 Proposed position of the KM6T pre-collimator

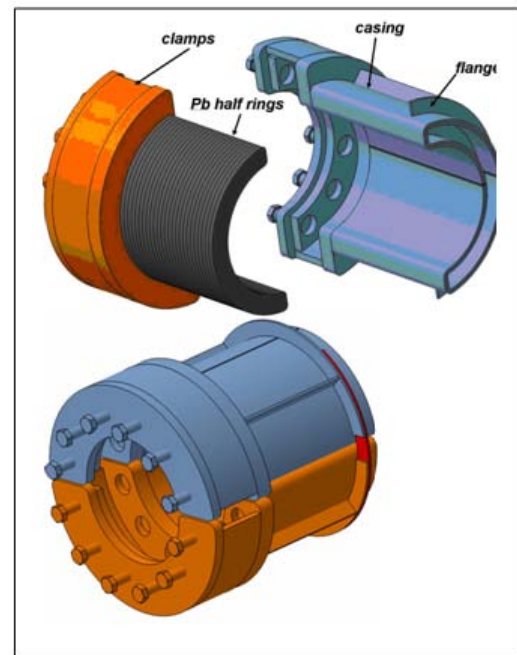


Figure 2 Pre-collimator and its main components

The main components of the pre-collimator are (Fig. 2): i) collimating material: half rings, Pb nuclear grade; ii) two identical casings: SS304, all 5mm sheets but clamping parts are thicker; iii) connectors: M10 screws; ii) two flanges

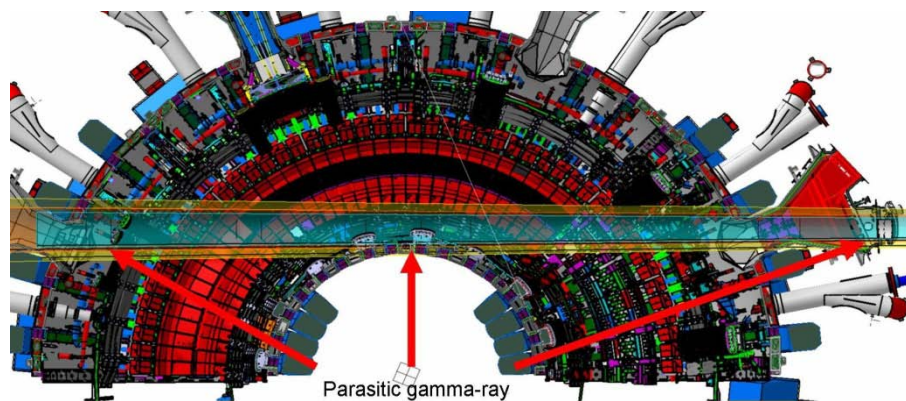


Figure 3 Mid-plane section with the pre-collimator field of view

The field of view determined by the collar is shown in the Fig. 3 as both mid-plane section and scheme with the parasitic gamma-ray sources and fields of view. The benefit that rises from the introduction of the pre-collimator is that the parasitic gamma-ray sources reduced in terms of area and volume, table 1.1, 1.2 and 1.3

Table 1.1 Reduction of area of Be within the fields of view

OCT.	Front Collimator FoV		Pre-collimator FoV		Reduction %	
	LHCD Antenna (m2)	Poloidal Limiter (m2)	LHCD Antenna (m2)	Poloidal Limiter (m2)	LHCD Antenna	Poloidal Limiter
3	0.075	0.077	0.054	0.061	28	20.78

Table 1.3 Reduction of the amount of Cu within the fields of view

OCT	Volume of Cu (Duct Scraper)				Reduction %
	FC (m3)	FoV	Collar (m3)	FoV	

Table 1.2 Reduction of the amount of Be & INCONEL

OCT	Front Collimator FoV		Pre-collimator FoV		Reduction %	
	Be (kg)	INCONEL (kg)	Be (kg)	INCONEL (kg)	kg of Be	kg of INCONEL
1	12.4	7.5	10.9	6.6	12.10	12.00
2	12.12	7.36	10.6	6.4	12.54	13.04
3	7.56	12.88	5.58	9.2	26.19	28.57

The proposed location of the pre-collimator generated concerns about the neutron scattering on the nearby KN1 diagnostics. The influence was evaluated by MCNP calculation and the results are presented in the following section. However the pre-collimator installation in the proposed location was not accepted. The capacity of the vacuum port flange to sustain an additional weight (about 205kg) during the worst case scenario loading was evaluated and it was found that the safety factor will be unacceptably decreased.

A more detailed analysis should go beyond evaluation and should make clear if the pre-collimator clamping on the vacuum port flange is a suitable installation spot.

2. MCNP evaluation

The evaluation was performed by means of Monte Carlo numerical simulations using the MCNP-5 code. A full description of the radiation field at the position of the tandem collimators would involve complex and long duration calculations which are much beyond the possibilities (resources) of the project. Therefore a simplified geometry that uses point (neutron and photon) sources irradiating the collimators within a defined solid angle and detectors placed behind the collimators will be used (Fig. 4).

The neutron was placed at the intersection of the KM6T axis with the (vertical projection of) tokamak magnetic axis. This is at a distance of approximately 4.8 m from the front face of the front collimator. The point neutron source has a Gaussian shape neutron spectrum with the mean energy at $E_0 = 2.45$ MeV and a full width at half maximum (FWHM) of 0.5 MeV.

The gamma-ray source was placed at the intersection of the KX1 axis with a plane perpendicular to the surface of the inner wall guard limiter in Octant 2. The 9 MeV gamma-ray line corresponds to the most intense nickel neutron capture gamma-ray line expected.

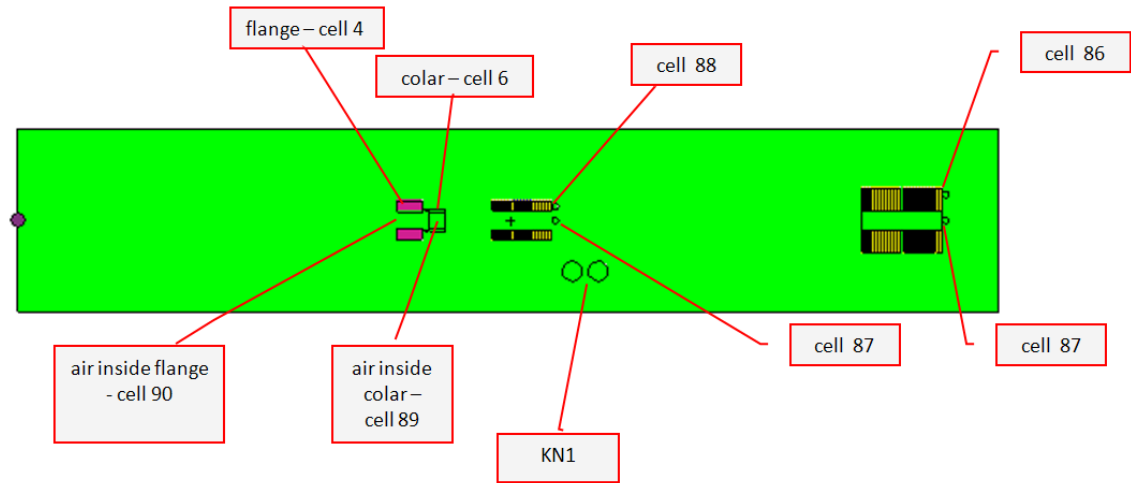


Figure 4 - MCNP model for CONFIG4-NEW (2.5 MeV geometry) evaluation.

In order to reduce the computation time, the propagation space was limited to a reduced solid angle. This conical collimation preferentially biases the emission of particles in the desired direction. The angle subtended by the front face of the front collimator was increased using a factor of 5.0 in order to avoid biasing of the evaluated tally.

However, due to this increase, a parasitic effect may occur. For example, if the objective is to calculate the neutron flux in cells corresponding to KN1, a number of neutrons may arrive directly in KN-1 cells. This may blur the influence on the flux at KN-1 cells, determined by the collar. Fortunately, in MCNP particles may be flagged when they cross specified surfaces or enter designated cells, and the contributions of these flagged particles to the tallies can be accounted.

2.1 Evaluation of the neutron scattering induced by the collar on KN1 adjacent diagnostic systems

The neutron flux in KN-1 cells caused by particles having passed through cells corresponding to: flange (cell 4), air in the middle of the flange (cell 90), collar (cell 4) and air in the middle of the collar (cell 89) were calculated. The flux was calculated also replacing the collar material with air in order to determine its influence. The increasing in the neutron flux at KN-1 cells, induced by the collar is about ~2%. In conclusion, MCNP calculations show that the supplementary neutron flux induced by the collar to the KN-1 cells is about 2% for both configurations (2.5 and 14 MeV). Therefore the scattered neutrons will have a negligible influence.

2.2 MCNP evaluation of the radiation (neutron and photon) performance of the updated configuration

The numerical simulations provided, at the detector positions, the integrated neutron and photon fluxes and also neutron and photon spectra. The shielding characteristics of the tandem collimators were defined in terms of a shielding factor, which is the ratio of the radiation fluxes in two detectors: one placed on the axis of the system and another placed behind the collimators, at a mid-radius position.

Table 1.6 – MCNP results obtained for DD discharges (2.5 MeV neutron emission)

	Previous configuration		New configuration	
Rear collimator				
n in 85	$(3.39 \pm 0.01)E-08$	$n(85/86) = 246 \pm 5$	$(7.33 \pm 0.03) E-08$	$n(85/86) = 509 \pm 12$
n in 86	$(1.38 \pm 0.07)E-10$		$1.44 \pm 0.10)E-10$	
p in 85	$(1.65 \pm 0.02)E-09$	$p(85/86) = 96 \pm 14$	$(8.22 \pm 0.34)E-10$	$p(85/86) = 31 \pm 4$
p in 86	$(1.71 \pm 0.25)E-11$		$(2.63 \pm 0.60)E-11$	
Front collimator				
n in 87	$(1.54 \pm 0.01)E-07$	$n(87/88) = 19 \pm 1$	$(3.23 \pm 0.01)E-07$	$n(87/88) = 23 \pm 1$
n in 88	$(7.94 \pm 0.05)E-09$		$(1.01 \pm 0.01)E-08$	
p in 87	$(7.39 \pm 0.05)E-09$	$p(87/88) = 5 \pm 1$	$(2.76 \pm 0.60)E-09$	$p(87/88) = 3 \pm 0.5$
p in 88	$(1.53 \pm 0.02)E-09$		$(1.08 \pm 0.04)E-09$	

Table 1.7 - MCNP results obtained for the 9 MeV parasitic gamma-ray line.

	Previous configuration		New configuration	
Rear collimator				
p in 85	$(3.03 \pm 0.01)E-08$	$p(85/86) = 464 \pm 50$	$(4.61 \pm 0.01)E-08$	$p(85/86) = 464 \pm 50$
p in 86	$(6.53 \pm 0.70)E-11$		$(5.16 \pm 0.21)E-11$	
Front collimator				
p in 87	$(9.61 \pm 0.02)E-08$	$p(87/88) = 45 \pm 5$	$(1.24 \pm 0.01)E-07$	$p(87/88) = 45 \pm 0.7$

p in 88	(2.13 ± 0.03)E-09		(1.30 ± 0.02)E-09	
----------------	-------------------	--	-------------------	--

The evaluation performed for DD discharges (2.5 MeV neutron emission) is reported in comparison with the evaluation obtained for the previous configuration. The energy distribution of the neutrons reaching the detectors was calculated in 8 energy bins. The fluxes at the location of the virtual detectors and the shielding factors are listed in Table 1.6.

For the propagation of the 9 MeV gamma-ray line the energy distribution of the photons reaching the detectors is calculated in 10 energy bins. The shielding factors are presented in Table 1.7. It can be seen from this figure that the transmission of the 9 MeV photons through the tandem collimator structure has been reduced by at least two orders of magnitude

4. Conclusion

It has been shown that the pre-collimator further improves the gamma-ray function of the tandem collimator without compromising the operation of adjacent diagnostics. According to MCNP evaluation, an increment of about 2% in neutrons flux was calculated. A satisfactory design has been put forward and formally approved. The tandem collimators were evaluated by means of MCNP calculations. The final configuration developed for deuterium discharges provides improved shielding factors of about 500 for 2.45 MeV neutrons. For neutron-capture photons induced within the collimation structure the shielding factor decreased 3 times (~30 instead of ~90). For the parasitic gamma-ray line of 9 MeV the shielding factor is ~450. The results prove that the tandem collimators are able to significantly improve the radiation field parameters at the plasma end of the diagnostics line-of-sight.

Acknowledgement

The reported work includes contributions from the following people outside the EURATOM-MEdC Association: N. Balshaw, D. Croft, T. Edlington, V. Kiptily, B. Syme (Association EURATOM-CCFE/JOC, Culham Science Centre, Abingdon, UK); P. Blanchard (Association EURATOM-CRPP-EPFL, Lausanne, Switzerland); A. Murari (Association EURATOM-ENEA, RFX, Padova, Italy).

References

- [1] G. I. Sadler *et al.*, Fusion Technol. **18**, 556 (1990).
- [2] V. G. Kiptily *et al.*, Nucl. Fusion **42**, 999 (2002).
- [3] V. G. Kiptily *et al.*, Rev.Sci, Instrum. **74**, 1753 (2003).

GAMMA RAY SPECTROMETRY

S. Olariu, A. Olariu, D. Dudu

Horia Hulubei National Institute for Physics and Nuclear Engineering, Bucharest

Overview

Gamma-ray and neutron spectra measured at the Tandem and Cyclotron accelerators of the National Institute of Physics and Nuclear Engineering, Magurele, have been analyzed in order to determine the response of a LaBr₃ detector at very intense gamma ray fluxes. Acquisition rates > 1 MHz in the gamma-ray energy range 0.1 – 3 MeV, produced at the Tandem accelerator via the reaction $^{27}\text{Al}(p,n)^{27}\text{Si}$, have been observed. The maximum acquisition rates have been > 10 MHz. Acquisition rates > 8 MHz have been observed for gamma-ray beams produced at the Cyclotron accelerator via the reaction $^9\text{Be}(\alpha,n)^{12}\text{C}$. These measurements confirm the fact that the photomultiplier tube of the LaBr₃ detector can process the transient impulses at the very high rates used in these experiments.

Detailed results

1. Response of the LaBr₃ detector to very high gamma-ray fluxes

In order to produce the high-intensity gamma-ray beams necessary for the experiments, we have used a 10 MeV proton beam incident on a thick target of Aluminum mounted on the experimental line around the MA0 analyzing magnet of the Tandem accelerator, and a 3 MeV α -particle beam incident on a thick Beryllium target at the Cyclotron accelerator. The incident proton current could be increased up to 300 nA on the target, and the α -particle current could be increased up to 5 μA on the target.

The LaBr₃ detector and the digital acquisition system have been brought to Magurele by Giuseppe Gorini, Marco Tardocchi, Massimo Nocente and Marco Silva from Milano. The response of this spectrometric system has been studied as a function of the incident gamma-ray flux whose intensity was changed by varying the distance to the target and by varying the beam current. Total counting rates in excess of 1 MHz have been measured.

For the measurements at the Tandem accelerator, the gamma-ray yield has been measured with the aid of a HPGe detector having a 50% relative efficiency and resolution of 1.9 keV at 1.33 MeV, and the neutron yield has been measured with the aid of a ^3He high resolution FNS-100 neutron spectrometer.

In order to produce the high-intensity gamma-ray beams, we have used 10 MeV proton beams incident on a thick aluminum target mounted on the MA0 experimental line of the Tandem

accelerator. The LaBr₃ detector has been placed first to a distance of 3 m from the aluminum target.

The functioning of the LaBr₃ detector has been tested with the aid of optical pulses generated by an optical pulser. The optical pulses are transmitted to the detector by an optical fiber. In order to increase the counting rate, the detector has been moved in subsequent measurements closer to the aluminum target. The electrical signals from the LaBr₃ detector have been processed with the aid of a digital acquisition system having a sampling rate of 400 MHz.

The intensity of the gamma-ray beam generated by the 10 MeV protons incident on the aluminum target has been monitored with the aid of a GeHP detector situated at a distance of 11.4 m from the target. Measurements have been conducted for beam currents of 25, 50, 75, 100, 150, 200, 250 and 300 nA.

2. Measurements at the Tandem accelerator

The gamma-ray spectra measured as a function of the beam current are shown in Fig. 1.

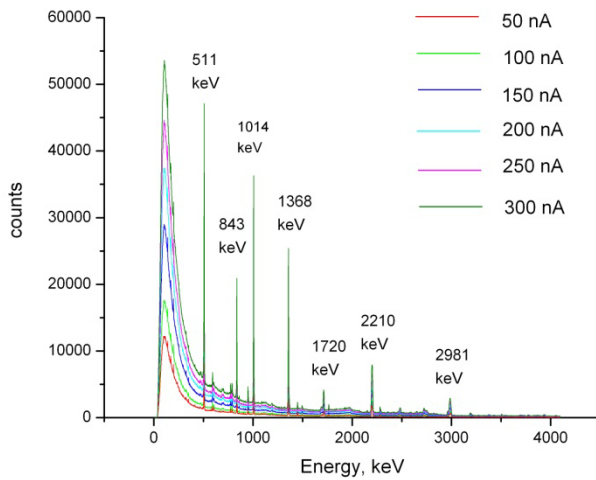


Figure. 1 - Gamma-ray spectra for a 10 MeV proton beam incident on an aluminum target as a function of the beam current, with a HPGe detector

Tests at the Tandem accelerator

Data	Corrente [nA]	Rate [KHz]	Beam	Note
01/12/09	125	1300	001	preliminary run
02/12/09	60	860	002	
02/12/09	30	500	003	
02/12/09	4	60	004	
02/12/09	0,7	40	005	
02/12/09	0,4 - 0,6	36	006	
02/12/09	250	1600	007	
02/12/09	25	1100	008	
02/12/09	50	1700	009	
02/12/09	75	1800	010	
02/12/09	75	about 8000	011	conteggio picchi
02/12/09	75	about 6000	012	Amp led 10000
02/12/09	100	8000	013	
02/12/09	120	>10000	014	
03/12/09	120	TBD	015	preampli2
03/12/09	175	TBD	016	preampli2
03/12/09	200	about 12000	017	preampli2

Summary of beam current settings

← lowest rate

← Highest Rate

Figure 2 - Proton beam currents and counting rates observed in various runs with LaBr₃ detector.

The proton beam currents and the counting rates observed in various runs are shown in Fig. 2.

The gamma-ray spectra and the widths of the 662 keV line observed at counting rates of 80 kHz and 1.3 MHz are shown in Fig. 3.

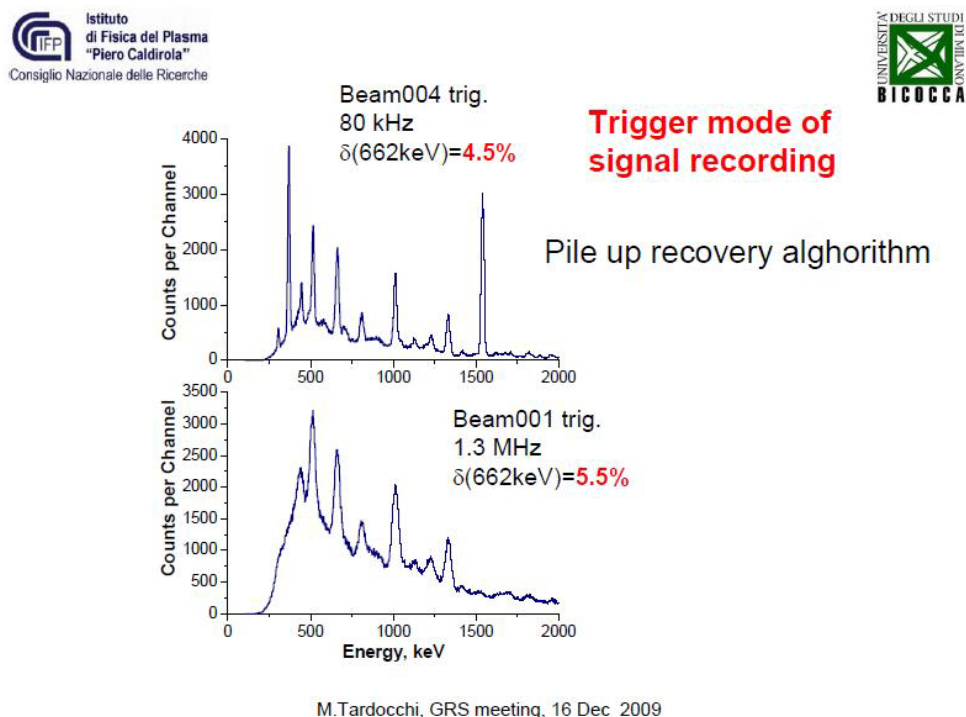


Figure 3 - The gamma-ray spectra and the widths of the 662 keV line observed at counting rates of 80 kHz and 1.3 MHz, with LaBr₃ detector.

3. Measurements at the Cyclotron accelerator

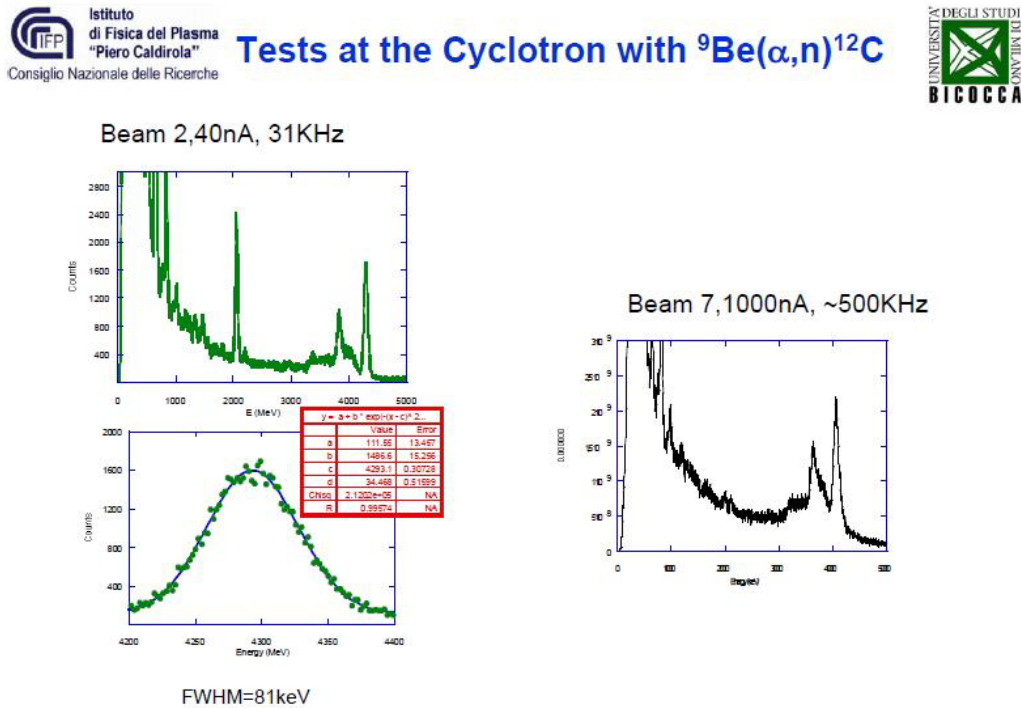
In order to study the reaction ${}^9\text{Be}(\alpha,n){}^{12}\text{C}$, the LaBr₃ detector and the digital acquisition system have been moved to the cyclotron laboratory. The energy of the α particle beam was 3 MeV, and currents up to 5 μA have been sent on the beryllium target. The LaBr₃ detector has been placed in the vicinity of the irradiation chamber containing the beryllium foil.

Spectra have been recorded for several values of the incident beam current. The α particle beam currents and the counting rates observed in various runs are shown in Fig. 4.

Corrente [nA]	Rate [Khz]	Cyclo	Note
		001	
40	31	002	
2000-3000	6000/7000	003	
5000 circa	>8MHz	004	
60	50	005	
300	131	006	
1000	423	007	
2000	>1MHz	008	
3300	>5MHz	009	

Figure 4 - The α particle beam currents and the counting rates observed in various runs.

The gamma-ray spectra for the reaction ${}^9\text{Be}(\alpha,n){}^{12}\text{C}$ observed at counting rates of 31 kHz and 0.5 MHz are shown in Fig. 5.



M.Tardocchi, GRS meeting, 16 Dec 2009

Figure 5 - Gamma-ray spectra for the reaction ${}^9\text{Be}(\alpha,n){}^{12}\text{C}$ observed at counting rates of 31 kHz and 0.5 MHz.

Finally, spectra have been recorded for a set of calibrated sources, and these spectra will make possible absolute measurements of gamma-ray counting rates using the LaBr_3 detector.

4. Conclusions

The objective of the measurements was to assess the response of the LaBr_3 detector to very high counting rates. The critical component for high rate operation is the photomultiplier tube (PMT). The tests indicate that the PMT can run at rates > 1 MHz and can cope with fast transients in rates. Gamma spectroscopy measurements (0.1-3 MeV) at rates > 1 MHz have been performed at the Tandem accelerator with the reaction ${}^{27}\text{Al}(p,n){}^{27}\text{Si}$. Highest rates achieved were > 10 MHz. Gamma spectroscopy measurements of the reaction ${}^9\text{Be}(\alpha,n){}^{12}\text{C}$ was measured at the Cyclotron accelerator. Highest rates achieved were > 8 MHz.

Acknowledgement

The reported work includes contributions from the following people outside the EURATOM-MEdC Association: G. Gorini, M. Tardocchi, M. Nocente, M. Silva (Dipartimento di Fisica "G.Occhialini", Università degli Studi di Milano - Bicocca, Milano, Italy, and Istituto di Fisica del Plasma "Piero Caldirola", CNR, Milano, Italy).

OPTIC FLOW METHODS FOR IMAGE PROCESSING OF THE DATA FROM THE VIDEO CAMERA KL-8 AT JET

T. Craciunescu, I. Tiseanu, V. Zoita

National Institute for Laser, Plasma and Radiation Physics

Overview

An optical flow method is applied to the study of several fusion plasma relevant issues, including plasma wall interactions. A multi-resolution coarse-to-fine procedure is used in order to cope with large displacements of objects between consecutive frames, characteristic of plasma images captured by JET fast visible camera. Occlusion modeling is also implemented. The method is able to provide good results for JET fast visible camera images which can be affected by saturation, discontinuous movement, reshaping of image objects, low gray-level in-depth resolution. Significant experimental cases concerning pellet injection, plasma filaments and MARFEs were analysed. The method is able to provide the real velocity for objects moving close to structures.

Publications

- [1] T. Craciunescu, A. Murari, A. Alonso, P. T. Lang, G. Kocsis, I. Tiseanu, V. Zoita. *Application of optical flow method for imaging diagnostic in JET*. Journal of Nuclear Materials, 400(2010) 205-212.
- [2] A. Murari, J. Vega, T. Craciunescu, S. Gonzalez, S. Palazzo, G. Vagliasindi, D. Mazon, M. Gelfusa, J. F. Delmond, A. de Maack, *Latest Developments in Image Processing Methods and Technologies for Magnetic Confinement Nuclear Fusion*, EFDA-JET-PR(10)03, IEEE Trans. Intell. Syst. (submitted for publication).

Detailed results

1 Introduction

A wide angle view fast visible camera (Photron APX) was recently installed in the Joint European Torus JET [1]. The camera is viewing the full poloidal cross-section of the vacuum vessel and is covering a toroidal extent of $\sim 90^\circ$. The wide angle view is appropriate for the study of pellet ablation, large scale instabilities and plasma wall interactions. Since the high confinement mode of operation (H-mode) is the standard operating regime envisaged for ITER, Edge Localised Mode instabilities (ELM) [2] are of particular importance considering the power loads they can induce on the plasma facing components. Recently it has been proven that the view of the fast visible camera is able to provide useful information about ELMs [3]. Investigations of pellet ELM triggering, as a method to mitigate the ELM-caused heat load on plasma facing components, have been also recently performed on JET by means of the fast visible camera [4]. The fast visible camera observations may support also the validation of

existing theories concerning ELM energy transport [5] and the study of filamentary structures observed during the development of the ELM instabilities [6].

Important quantitative information can be obtained by applying image processing techniques to the data provided by the fast visible camera. Specifically, the sequences of ordered images allow the estimation of motion as instantaneous image velocities or discrete image displacements, the so-called *optical flow*.

Methods

The estimation of motion information from image sequences is a recurrent problem in computer vision. In fusion the poor accessibility of the devices makes very difficult the deployment of more than one camera with the same field of view. Therefore stereoscopic methods are not applicable and the optical flow approach has been adopted. The objective of the analysis consists of finding the vector field, which describes how the image is changing with time. Under certain assumptions, this information about the optical flow can be translated into knowledge about the movements of the objects in the 3D space covered by the camera.

The basic assumption used by most algorithms is the brightness constancy: when a pixel flows from one image to another, its intensity or colour does not change. The brightness constancy assumption implies that all changes in the image are caused by the translation of brightness patterns leading to the gradient constraint equation:

$$\vec{f}_s \cdot \vec{v} + \dot{f}_t = 0 \quad (1)$$

where $f_s = (f_x, f_y)$ and f_t are the spatial and temporal gradients and v is the optical flow velocity. For small displacements, the Taylor expansion of equation (1) can be used to reformulate the optical flow constraint as:

$$f(x + u, y + v, t + 1) - f(x, y, t) = 0 \quad (2)$$

where subscripts denote partial derivatives and u and v are the two components of the optical flow. Unfortunately in practice solving equation (3) is an ill posed problem since small perturbations in the signal can create large fluctuations in its derivatives. A typical method to alleviate this drawback consists of implementing image smoothing techniques which can reduce the effect of noise and stabilize the differentiation process. The smoothing of the image sequence is typically performed prior to differentiation by convolving each frame with a Gaussian function (called K_ρ in the following). Smoothing can be extended also to the temporal dimension. However, from the mathematical point of view, even after proper smoothing is applied, the problem of finding the flow field solution of equation (2) remains ill-posed and a single equation is not sufficient to uniquely compute the two unknowns (the so-called aperture problem). The most widely used techniques to tackle with this problem are differential methods. They can be classified into local methods such as the Lucas–Kanade technique [7] and into global methods such as the Horn-Schunck approach [8]. Local and global differential methods

have complementary advantages and shortcomings. Local methods assume a small neighbourhood of constant flow. For a neighbourhood of size ρ , the optic flow (x,v) can be determined at the location (x,y,t) from a weighted least square fit by minimizing the function:

$$E_{LK}(u, v) = K_{\rho} * \left((f_x u + f_y v + f_t)^2 \right) \quad (3)$$

A sufficiently large smoothing is very successful in rendering the method robust against noise. The problem remains severe in flat regions of the emission, where the image gradient vanishes and, consequently, the aperture problem persists and the method is unable to produce dense flow fields. In order to avoid this drawback, global methods supplement the optical flow constraint with a regularizing smoothness term. The optical flow (u,v) is determined as the minimizer of the global energy functional:

$$E_{HS}(u, v) = \int_{\Omega} \left((f_x u + f_y v + f_t)^2 + \alpha (|\nabla u|^2 + |\nabla v|^2) dx dy \right) \quad (4)$$

where $\alpha > 0$ determines the amount of smoothness. Larger values for α result in a stronger penalization of large flow gradients and lead to smoother flow fields. Unfortunately global methods have been observed to be more sensitive to noise than local differential methods. Brun et al. [9] noticed the similarity between equation (5) of the Lucas-Kanade method and the first term under the integral in the formulation (6) of the Horn-Schunck method. Based on this observation they succeed to formulate a hybrid Combined Local-Global (CLG) class of methods, which bring together the robustness of local methods with the density flow fields which characterize the global approaches. These methods have been studied and optimized for the very specific case of JET images. A multi-resolution coarse-to-fine procedure was also used in order to cope with large displacements of objects between consecutive frames, characteristic of plasma images captured by JET fast visible camera. The pyramid of multi resolution images is derived from the original frame by successive down-sampling and Gaussian smoothing steps. Optical flow calculation starts at the coarse level, where the displacements are small and consequently the linearization of the grey value constancy assumption is satisfied. This estimate is then refined step by step along the pyramidal structure.

The calculated optical flow field may be affected by occlusions. Occlusions appear when two objects that are spatially separated in the 3D space might interfere with each other in the projected 2D image plane. Occlusion modeling is a difficult aspect of the optical flow. It was implemented based on the simultaneously calculation of the forward and reverse flow fields and labelling the pixels for which the two disagree. A bilateral filter, which incorporates flow from neighboring pixels that are similar in motion and appearance and that lie outside occluded regions, has also been used in order to improve boundaries.

3. Results and discussion

The final results obtained for JET images are quite encouraging. It has for example been possible to estimate the velocity of solid, cryogenic, hydrogen isotope pellets, which are

injected in Tokamaks for particle fuelling as well as for instability control (ELM triggering and mitigation). Their importance resides in the fact, among other things, that they open access to operational regimes not reachable by gas puffing. An example of the results is reported in Fig. 1, where it is shown how the optical flow estimate is very close to the nominal speed of the injected pellets.

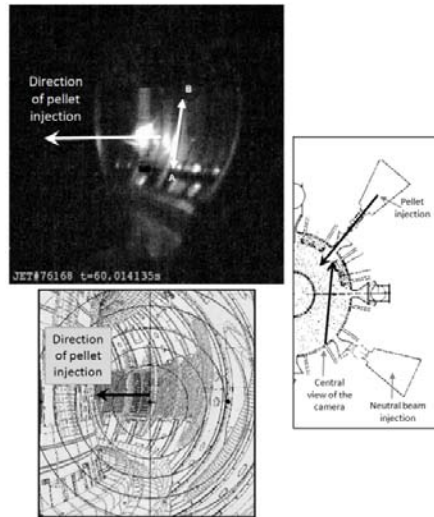


Figure 1 - Top: view of the pellet ablation cloud as seen by JET fast visible camera. Bottom: the field of view of the fast camera with an arrow indicating the pellet nominal trajectory. Right: a top view of JET vacuum vessel giving the topology of the pellet injector with respect to the field of view of the fast camera. The pellet speed estimated with the optical flow is of 215 ± 12 m/s: the nominal speed of the injected pellets is $240 \div 262$ m/s.

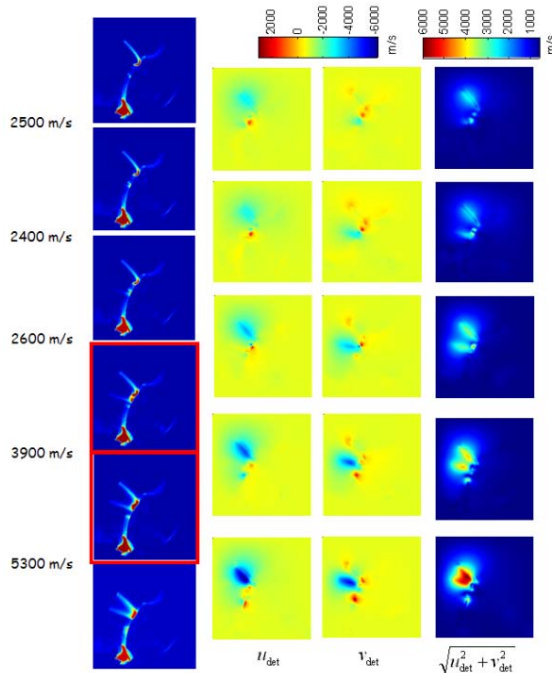


Figure 2 – MARFE image sequence (1st column) and optical flow calculation: horizontal component (2nd column), vertical component (3rd column) and modulus (4th column).

The optical flow method has been successfully used also for the evaluation of the speed of various plasma instabilities, in particular ELM filaments and MARFEs. An illustrative example is presented in Fig. 2.

It is worth mentioning that the real images provided by JET fast visible camera can be affected by discontinuous movements in the objects, low grey-level in-depth resolution and too slow acquisition rate. Therefore the basic assumptions of the optical flow model may not be always satisfied. Therefore dedicated techniques able to prevent the calculation of an inaccurate velocity have been devised. A procedure for the assessment of the uncertainties of the method has been developed and applied.

A criterion to discern between correct and wrong calculated flow fields was also introduced. The optical flow is determined using two images Im_1 , Im_2 , from a sequence of images. Using the first image and the calculated optical flow, a version $Im_2^{(rec)}$ of the second image can be reconstructed. The similarity between Im_2 and $Im_2^{(rec)}$ can be used in order to assess the

accuracy of the optical flow calculations. Therefore the error image $Im_2 - Im_2^{(rec)}$ has been used as a confidence criterion to determine the validity of the results.

The error image corresponding to the optical flow between fourth and fifth images (marked with red border in Fig. 2) is presented in Fig. 3 (top-left). In order to obtain a more complete picture about the accuracy of the calculated optical flow, three line profiles have been evaluated for the second image Im_2 and its reconstruction $Im_2^{(rec)}$ obtained from the first image I_1 and the calculated optical flow. The results are presented also in Fig. 3. The line profiles demonstrate that shapes are reconstructed accurately for all the three line profiles

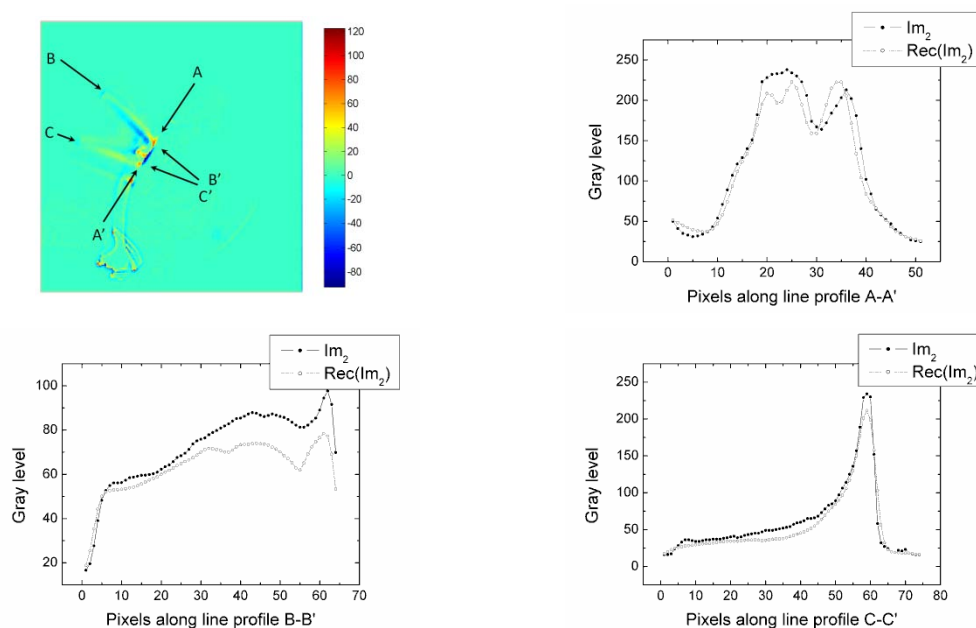


Figure 3 – Optical flow method applied to MARFEs: the error image corresponding to the optical flow calculation for the fourth and fifth images in Fig. 2 (top-left); three lines AA', BB' and CC' are defined in order to calculate line profiles and to compare the second image I_2 with its reconstruction $I_2^{(rec)}$. Line profiles along the directions AA', BB' and CC' are represented with filled circles for second image I_2 and with empty circles for the reconstruction of second image $I_2^{(rec)}$.

4. Conclusion

An algorithm based on the optical flow method, combining the advantages of local methods (robust under noise) and global techniques (which yield dense flow fields), is applied to JET fast visible camera image processing. The method incorporates a multi-resolution coarse-to-fine procedure in order to be able to work with large displacements between consecutive frames. Occlusion detection is also implemented. The method has been applied to the study of various issues relevant to the study of fusion plasmas: pellets, filaments, MARFEs. Extensively tested on synthetic images the method proved to achieve results in case of experimental images provided by the JET fast visible camera which can be affected by saturation, discontinuous movement, reshaping of image objects, low grey-level in-depth resolution. For objects moving close to known structures of the tokamak vacuum vessel, the velocity in the real 3D space has

been inferred from the 2D image analysis. The optical flow method is a unique tool able to cope with several different plasma physical phenomena and to provide useful information for modeling.

The work on this project will continue with the customization and adaptation of the optical flow method for the control of pellet extrusion speed based on the image sequences provided by a CCD camera viewing the ice at the exit of the nozzles of the extrusion cryostat. The method has to be adapted to the characteristics of the experiment. Also, in order to allow image processing of a large amount of data (more than 3000 frames for single JET pulse) an effort will be dedicated to optimization. Particular attention will have to be devoted to the extraction of useful information in real time, a very difficult task due to the extremely high computational and frame rate requirements.

Acknowledgement

The reported work includes contributions from the following people outside the EURATOM-MEdC Association: Andrea Murari (Consorzio RFX, Associazione ENEA-Euratom per la Fusione, Padova, Italy), Arturo Alonso (Laboratorio Nacional de Fusion, EURATOM-CIEMAT, Madrid, Spain), Peter Lang (Association EURATOM-IPP, Max-Planck-Institut für Plasmaphysik, Garching, Germany) and Gabor Kocsis (RMKI-KFKI EURATOM Association, Budapest, Hungary).

References

- [1] J. A. Alonso et al., 34th EPS Conference on Plasma Phys. Warsaw, 2 - 6 July 2007 ECA Vol.31F, P-2.124 (2007).
- [2] A. Kirk et al., Phys. Rev. Lett. 92(2004)245002.
- [3] J.A. Alonso et al. J. Nucl. Mater., 390-391(2009)797-800.
- [4] G. Kocsis et al. 36th EPS Conf. on Plasma Physics, Sofia, Bulgaria 2009, Europhysics Conference Abstracts, Vol. 33E, P-1.151, 2009
- [5] R Wilson et al., Phys. Rev. Lett. 92-24 (2004) 245002.
- [6] W Fundamenski et al., Plasma Phys. Control. Fusion 48 (2006) 109–156.
- [7] B. Lucas et al., Proc. Seventh International Joint Conference on Artificial Intelligence, Vancouver, Canada, 1981, pp. 674–679.
- [8] B. Horn et al, Artificial Intelligence, 17 (1981) 185–203.
- [9] A. Bruhn et al., Int. J. Comput. Vision, 61-3(2005)211-231.

TRITIUM DEPTH PROFILE MEASUREMENTS OF JET DIVERTOR TILES BY AMS

C. Stan Sion, M. Enachescu, M. Dogaru

“Horia Hulubei” National Institute for Physics and Nuclear Engineer, Bucharest

Overview

Accelerator mass spectrometry (AMS) is a high sensitive analysing method that provides complementary information to other conventional methods used to analyze or diagnose fusion experiments, but is the only method capable to determine extremely low concentrations of Tritium in different substrates. The main objective of the project in 2010 was to perform AMS experiments for T depth profile concentrations in divertor tiles from JET. The following results have been obtained: a) Tests and calibration of the new AMS depth profiling facility. T standards were used to test and calibrate the measurements at newly installed AMS experimental facility for tritium depth profiling at Horia Hulubei National Institute of Physics and Nuclear Engineering (NIPNE), Bucharest; b) Measurements of T-depth profiles carried out for the following samples: 4 samples from tiles G6D and G8A from campaigns 1998-2007; 7 samples from tiles G1A, G3A and G7A from campaigns 2004-2007.

Publications

- [1] C. Stan-Sion, M. Enachescu, O. Constantinescu and M. Dogaru, A decade of experiments and recent upgrading at the AMS facility in Buchares, Nucl. Instr. and Meth. B, Vol. 268, Issues 7-8 (2010) 863-866.

Detailed results

AMS is the most sensitive analyzing method known today and the only one capable of measuring Tritium in an efficient way. Its sensitivity is 10^{-15} for the ratio: isotope/element. That corresponds to the selection of one specified atom from a million of billions of other atoms. In fact AMS counts, one by one, every atom produced from the analysed material. To emphasize is a correlation to the global concentration in a sample material: if this concentration is small the AMS sensitivity is correspondingly very high. This makes AMS especially adequate for measuring samples when concentrations of T are low.

Moreover, AMS due to its functioning way is able to scan the depth of the material and deliver the depth profile information of the T concentration. By measuring the depth of the implanted Tritium into the bulk of pure materials (e.g. C, W, Be) it determines the energy of the incident particles and therefore, can be applied as an efficient diagnose tool for fusion experiments in

Tokamaks (ASDEX, JET). In this way, AMS characterizes the plasma confinement and stability and its perturbing interaction produced on the plasma confinement. It determines the efficiency of the divertor system to eliminate low energy particles (helium exhaust function) drifting across the separatrix and in this way maintaining the clean and detached confined plasma.

Accelerator mass spectrometry (AMS) is a high sensitive analyzing method that provides complementary information to other conventional methods used to analyze or diagnose fusion experiments, but is the only method capable to determine low concentrations of Tritium in different substrates. Measurements reported in this paper have been performed on 9 MV Van der Graaff Tandem Accelerator at the National Institute for Physics and Nuclear Engineering (NIPNE), Bucharest [1]. Sample preparation and processing of JET divertor tiles was performed by the VTT Technical Research Centre of Finland, Espoo, Finland.

2. Measurement procedure and results

2.1 Computer code for mathematical unfolding procedure:

In present research project AMS performs a depth profiling (DP) of the measured concentration. The depth scanning is done in the ion source by sputtering with accelerated ^{133}Cs beam on the sample surface. Measuring continuously the produced rare ions (tritium) one will register in the detector different beam currents corresponding to the concentration at depth of scattering. The DP requires the sputter erosion rate to be uniform on the analyzed target area. Ions sputtered from the crater slopes (Fig. 1) should not be included in the analyses because they do not reveal the true concentration. In order to correct these effects, a mathematical unfolding procedure [2] has been developed. However, optimal ion beam conditions were also investigated and established.

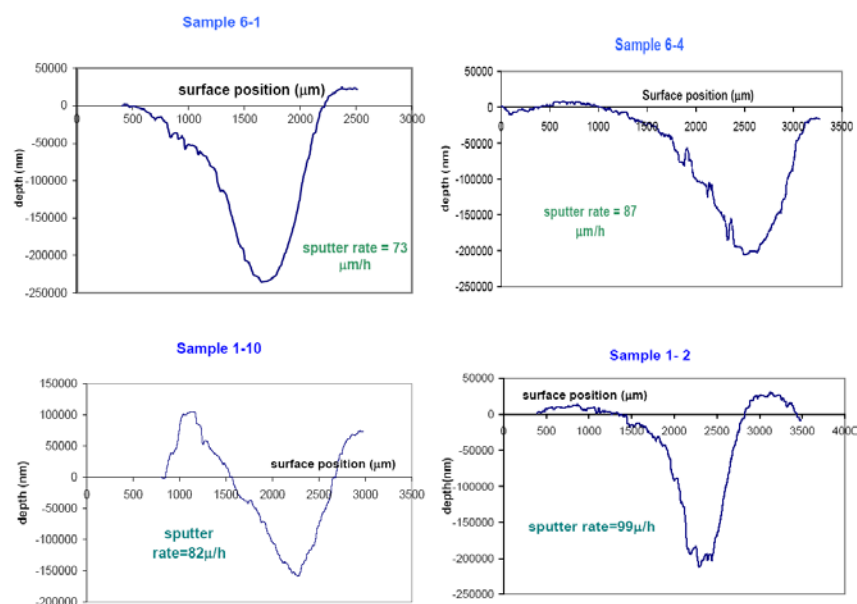


Figure 1 - Sputter craters of JET divertor samples 2BNG6D-1, 2BNG6D-4, 2IWG1A-10 and 2IWG1A-2

2.2 Experiments to test, calibrate and optimize the new AMS set up for depth profiling.

For an efficient and confident depth profiling of concentrations by AMS the parameters of the devices of the facility have to be optimized experimentally. Optimal values have to be carefully chosen for the beam currents and for the acceleration conditions.

The new prepared standard samples [3] were mounted on the target wheel and were introduced into the vacuum chamber of the ion source (two blank samples of pure Carbon were also introduced to determine the background level and the cross talk effect in the ion source). Two standard samples of low T/C concentration ratio, with T implanted in pyrolytic carbon, were introduced in the sputter ion source to calibrate the depth profile measurements.

The ^{12}C ions were chosen to form the pilot beam. However, the stripping probability of negative ions in the high voltage terminal is not the same for all possible charge stages to be attained at a certain terminal potential. A main role is on the possibility to obtain the magnetic rigidity for ^{12}C very close to the magnetic rigidity of Tritium. The differences (E_{offset}) should not exceed 0.5 MeV for the terminal voltages of the tandem accelerator. For a larger value of the difference the tuning with the pilot beam is not any more precise. The charge state 3^+ of the ^{12}C ions satisfies well this constraint. Thus, the pilot beam was chosen to be formed by $^{12}\text{C}^{3+}$ ions.

The final optimized conditions for the AMS depth profiling experiment at the FN-8MV tandem at NIPNE Bucharest are as follows:

- a) the Ion sputter source: $U_{\text{sputter}} = 6.0 \text{ kV}$, $U_{\text{extr}} = 11.0 \text{ kV}$, $U_{\text{einzel}} = 1.1 \text{ kV}$, $U_{\text{pacc}} = 55.8 \text{ kV}$,
- b) the pilot beam: $^{12}\text{C}^{3+}$, acceleration energy 32 MeV, $U_{\text{acc}} = 8 \text{ MV}$, $E_{\text{offset}} = 0.43 \text{ MeV}$,
- c) The microscopic tritium beam: $^3\text{H}^{1+}$, acceleration energy: 14.2 MeV, $U_{\text{acc}} = 7.105 \text{ MV}$.

The events in the detector are registered continuously. Assuming a continuous sputtering rate the elapsed time will be converted to depth. The calibration of the scanned depth is done off-line by optic profilometer. Spectra of the Tritium particles were recorded and depth profile spectra were also performed using the standard samples.

2.3 Results of the test measurements

For the AMS analysis samples from divertor tiles with lower T activity concentration were selected. These samples were irradiated in the following JET campaigns:

- a) 1998-2007 – 4 samples from tiles G6D and G8A.
- b) 2004-2007 – 7 samples from tiles G1A, G3A and G7A.

Fig. 2 shows the locations of the drilled samples in tiles G1B, G7A and G8B.

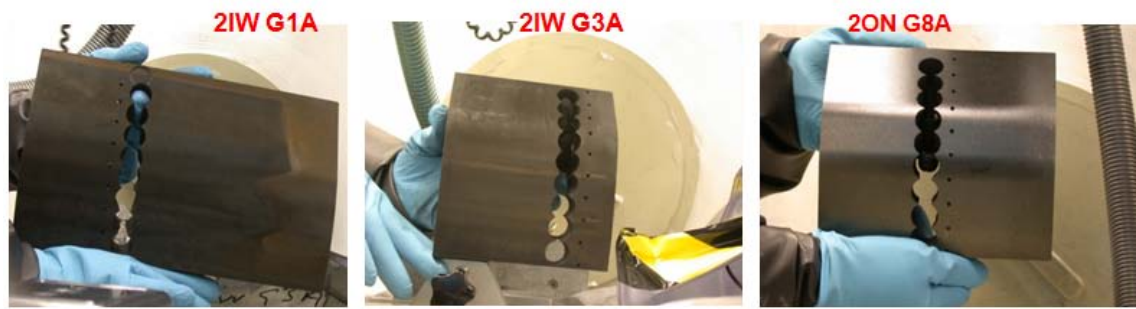


Figure 2 - Locations of samples from tiles G1A (2004-2007), G3A (2004-2007) and G8A (1998-2004)

Each sample was measured by AMS in order to determine the T concentration depth profile. During the time of an AMS-DP experiment, the sputtering beam produces a crater in the sample material. The counting rate of T atoms will depend each time on the concentration at the reached depth in the crater. The data is recorded corresponding to the elapsed time in the experiment. At the end of the experiment the sputtered sample will be measured by optical profilometry. The crater dimensions will be used to convert the time scale to depth and the rim effect correction will also be taken into account. The measured concentrations of DP are shown in Fig. 3. All data were corrected for the background value of T during the measurements. For the entire experiment, the background level was an about 10^3 lower than the smallest measured concentration. The averaged concentration of T does not exceed 10^{17} atoms/cm³. Taking into account the possible wide incidence angles of the colliding particles and the fast diffusion T in CFC, wide peaks are expected for the maximum values of the power ranges.

Integrating the DP over the measured depth one obtains the amount of T trapped per unit area (atoms/cm²). In Fig. 4, integrated values of T up to about 3 μ m depth in JET divertor tiles from 1998-2007 are presented. As can be seen from Fig.4, nearly symmetric values were found for the T concentration on the tiles No.1 and No.8. Tile No.7 has lower T concentration. In Fig. 5, integrated values of T deposition up to about 500 μ m depth of JET divertor tiles from 2004-2007 are indicated according to their locations on the divertor. The results in Fig.5 indicate strong distinction from earlier divertor sets [4], because the T retention seems to be totally different pattern from the normal deposition observed at JET (Fig 6). Usually outer divertor (tiles 7 and 8) are eroded and there is deposition at the inner divertor (tiles 1 and 3), but now T retention is more balanced.

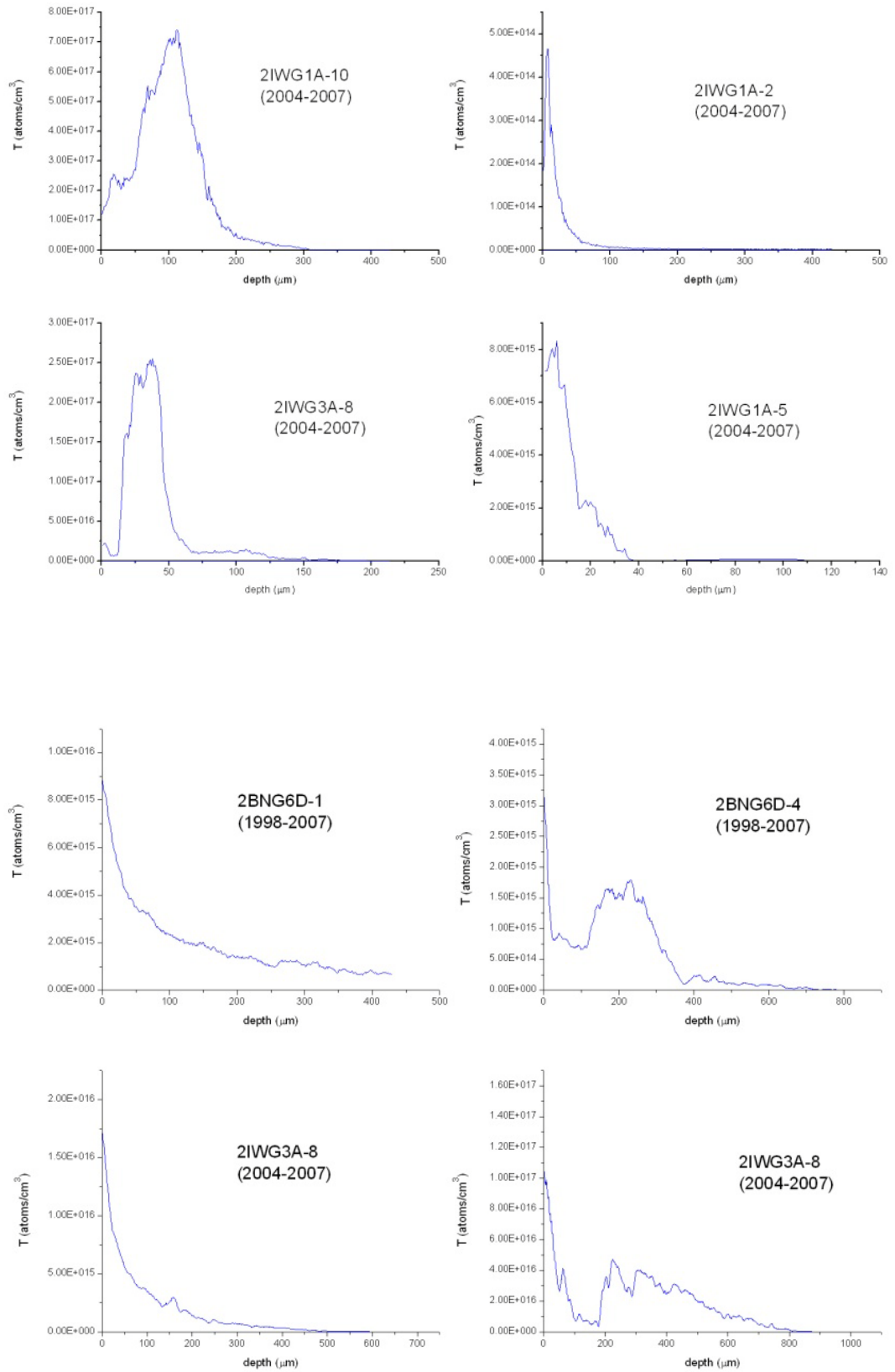


Figure 3 - Tritium depth profiles of JET divertor samples from campaigns 1998-2007 and 2004-2007 measured by AMS.

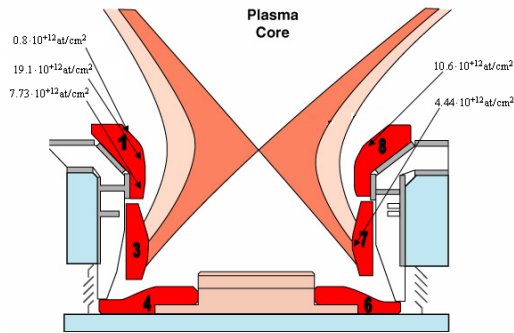


Figure 4 - AMS integrated concentration values of T in CFC tiles 22IW G1B (location 2,5 and 8), 20N G7A (location 5) and 20N G8B (location 6a) at different locations on the JET divertor 2004. The values are integrated up to the depth 3 μm .

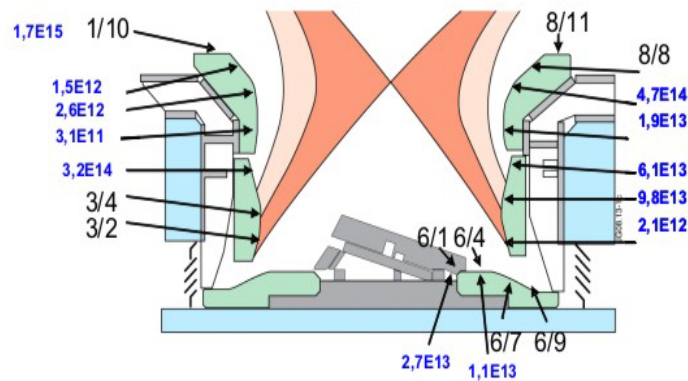


Figure 5 - AMS integrated concentration values (atoms/cm²) of T in CFC tile 2IW G1A (indicated in figure as 1/2, 1/5, 1/8 and 1/10) at different locations on the JET divertor 2004-2007; in tile 2IW G3A (indicated in figure as 3/8) at different locations on the JET divertor 2004-2007; in tile 2BN G6D (indicated in figure as 6/1 and 6/4) at different locations on the JET divertor 1998-2007; in tile 2ON G7A (indicated in figure as 7/1, 7/5 and 7/8) at different locations on the JET divertor 2004-2007; in tile 2ON G8A (indicated in figure as 8/2 and 8/6) at different locations on the JET divertor 1998-2007. Reference date for T concentrations is June 10th 2010. The values are integrated over the depth of 500 μm .



Figure 6 - Cross-sectional profile of the tile 1 from the campaign 2001-2004 [5].

3. Conclusions

Samples from campaigns 1998-2004, 1998-2007 and 2004-2007 were prepared for T-depth profile measurements by AMS technique. The depth scanning is done by sputtering with accelerated ¹³³Cs ions on the sample. Measuring continuously the produced rare ions of tritium, one will register in the detector different beam currents according to the concentration at the depth of sputtering.

The main part of this task was the upgrading work and calibration of the AMS analysing facility to correspond to the needs for T and D depth profiles in different host materials (C, W, Be). Standard samples were prepared and tested in the AMS experiments. The entire AMS analysing facility was calibrated and optimized for the measurement of light elements. From the JET divertor several tiles were analysed for the T concentration depth profile (three samples from G1B, one from tile G7A and G8B from campaigns 1998-2004; 4 samples from tiles G6D and G8A from campaigns 1998-2007; 9 samples from tiles G1A, G3A and G7A from campaigns 2004-2007). From some samples, disks with 10mm in diameter and 3mm in thickness were cut. Some samples (1998-2007, 2004-2007) were cut like narrow straps. As seen in Fig. 3, this relatively small surface area may introduce additional uncertainty in determination of the sample surface position and therefore should be avoided as much as possible in the sample preparation phase.

The results of the measurement procedure and the T depth profiles for selected samples have been presented. First preliminary results indicate differences in T distribution from earlier divertor studies [4], because the T retention seems to have different pattern (T retention is more balanced between inner and outer tiles) from the normal deposition observed earlier (outer divertor tiles 7 and 8 are eroded and there is deposition at the inner divertor tiles 1 and 3) at JET.

Acknowledgement

The reported work includes contributions from the following people outside the EURATOM-MEdC Association: M. Kiisk (University of Tartu, Institute of Physics, Estonia) and J. Likonen (VTT Technical Research Centre of Finland, Finland).

References

- [1] C. Stan-Sion, M. Enachescu, O. Constantinescu and M. Dogaru, *A decade of experiments and recent upgrading at the AMS facility in Buchares*, Nucl. Instr. and Meth. B, Vol. 268, Issues 7-8 (2010) 863-866.
- [2] M. Enachescu, V Lazarev and C Stan-Sion, *Unfolding Procedure for AMS Depth Profiling*, J. Pys. D: Appl. Phys. 39 (2006) 2876-2880.
- [3] C. Stan-Sion, M.Enachescu, I Dorobantu, R.Behrish, C.Postolache, *Tritium and Deuterium Standards for AMS Measurements*, U.P.B Sci. Bull., Series A, Vol. 66, No. 2-4, (2004) 95-101,
- [4] J.P. Coad, N. Bekris, J.D. Elder, S.K. Erents, D.E. Hole, K.D. Lawson, G.F. Matthews, R.-D. Penzhorn, P.C.Stangeby, *Erosion/deposition issues at JET*, Journal of Nucl. Materials 290-293 (2001) 224-230.
- [5] J. Likonen, P. Coad, A. Widdowson, *JET task JW6-FT-3.27*, JET TF FT monitoring meeting, November 27th, (2006).

***COLLECTIVE TRAINING OF YOUNG ENGINEERS AND
SCIENTISTS***

RESEARCH ACTIVITY IN ICIT RAMNICU VALCEA IN THE FRAME OF “TRI-TOFFY” EFDA NETWORK TRAINING

I.Spiridon, S. Brad, G. Ana, M. Vijulie, A. Lazar

National Research and Development Institute for Cryogenics and Isotopic Technologies, Rm Valcea

Overview

The “Tritium Technology for Fusion Fuel Cycle” (“TRY-TOFFY”) EFDA training network programm support the EU activities for recruiting skilled professional staff required in the Deuterium-Tritium Fuel Cycle area for ITER. ICIT Ramnicu Valcea together with EUATOM-MEdC is one of the parties involved in this network, sustaining training and research activities in fusion technology. This paper presents the activities in TRY-TOFFY training network, focusing on the research activity and experience gain by the ICIT Ramnicu Valcea trainee in the last periode of his training (2010).

Publications

- [1] I. Spiridon, S. Brad, I. Ștefănescu, *Experimental H₂ and D₂ extraction rig with active charcoal packing*, The 16th National Conference with International Participation “PROGRESS IN CRYOGENICS AND ISOTOPES SEPARATION”, 13-15 Oct. 2010, Călimanesti, Romania

1. Results and discussion

Participation to calibration of quadrupole mass spectrometer

Cryogenic Pilot Plant of ICIT Rm. Valcea is an experimental plant for separating tritium and deuterium from tritiated heavy water by LPCE-CD method (Liquid Phase Catalytic Exchange – Cryogenic Distillation).

One of the key tasks in characterizing the separation performance of hydrogen isotopes by cryogenic distillation is the ability to measure with high accuracy the concentrations of molecular species of hydrogen isotopes. Mass spectrometry (MS) is an analytical technique that measures the mass-to-charge ratio of charged particles. It is used for determining masses of particles, elemental composition of a sample or molecule, and for elucidating the chemical structures of molecules, such as peptides and other chemical compounds. The MS principle consists of ionizing chemical compounds to generate charged molecules or molecule fragments and measurement of their mass-to-charge ratios. The technique has both qualitative and quantitative uses. These include identifying unknown molecular compounds, determining the

isotopic composition of elements in a molecule, and determining the structure of a compound by observing its fragmentation. Other uses include quantifying the amount of a compound in a sample or studying the fundamentals of gas phase ion chemistry (the chemistry of ions and neutrals in a vacuum). In future experimental campaigns in the cryogenic pilot plant for tritium and deuterium separation a GSD 320 quadrupole mass spectrometer will be used to determine the concentration profiles of hydrogen isotopes species along a cryogenic distillation column (Fig. 1).

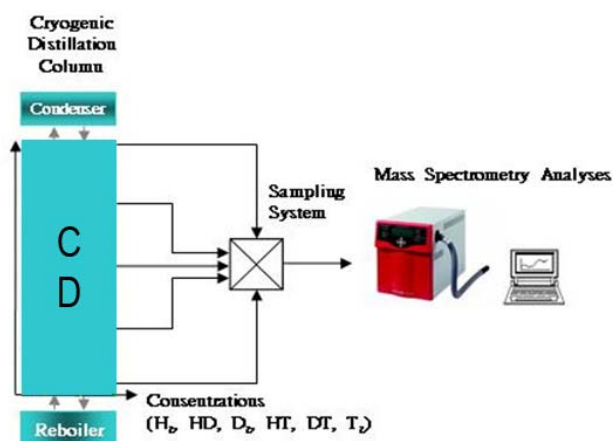


Figure 1 – Possible measurement system with GSD 320

This major issues of mass spectrometric analysis of hydrogen isotopes mixtures are the isobaric interferences due to ionic species that are produced inside the ion source by dissociation of molecules or by reactions between ions and neutral molecules. The mass spectrometric performed analysis of the gas mixtures of hydrogen isotopic species H_2 , HD and D_2 have involved the measuring of the mass-2, -3 and -4 ion currents signals generated by H_2^+ , HD^+ and D_2^+ ions, but these currents are affected by isobaric interferences.

The GSD 320 mass spectrometer, that we have, has a lower resolving power, than required for the separation between these close masses. So that, algorithms for determining these interferences and for correcting the main mass ion currents are necessary. A first approach of this issue was made by using mixtures of hydrogen & argon, deuterium & argon, and hydrogen & deuterium, at a constant pressure at the inlet of mass spectrometer (and, consequently, at a constant pressure inside the analytic of the mass spectrometer). A 3D design of an experimental rig was required to understand better the set-up for the calibration experiment for the GSD 320.

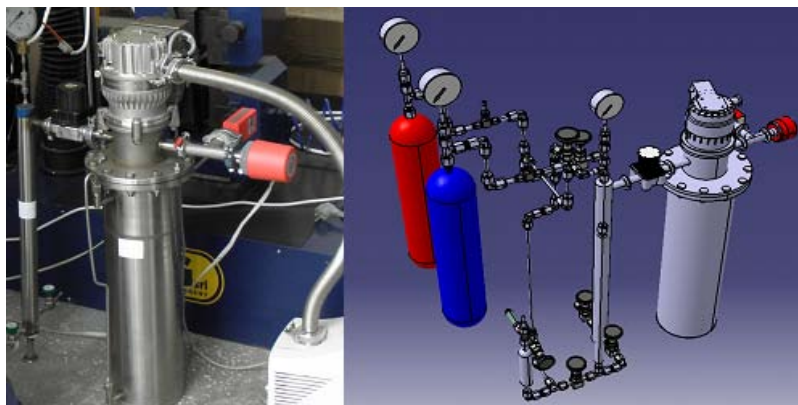


Figure 2 – Constructed experimental rig after 3D design proposal

The quadrupole mass spectrometer had no system for controlling the total pressure inside the analytic chamber and this could be kept at a constant value, only by trying to maintain, all the time, a constant pressure at the inlet of mass spectrometer. Having in this way a issue regarding the difficulty in sampling of the gas, from several points on the cryogenic separation column, at the same (and constant) pressure, another approach that consists of determining the isobaric interferences at variable pressure was a necessity. That has been solved with the experimental rig constructed based on the proposed 3D model (Fig. 2).

Designing of tritium extraction system based of active charcoal packing

Using CATIA V5, a proposed 3D model of tritium extraction rig, with active charcoal, was designed. The research was focused on the activated charcoal characteristics and physical properties for a mixture of H_2-D_2 . Tests have been made with the activated charcoal as main probe for minimum absorption ratio determination on the constructed rig after the 3D proposed model (Fig. 3). Construction of the extraction rig was also based on documentation about tritium compartment in active charcoal from cryopumps in ITER and cryotrapping properties in activate charcoal.

For the experiments, a mixture of H_2-D_2 gas was used and absorbed at different temperature between 85 – 77 K, into an absorbent mass of activate charcoal, with apparent density of 450 g/l and specific surface of 1115 m^2/g . The total mass of the used charcoal was of 130 g.

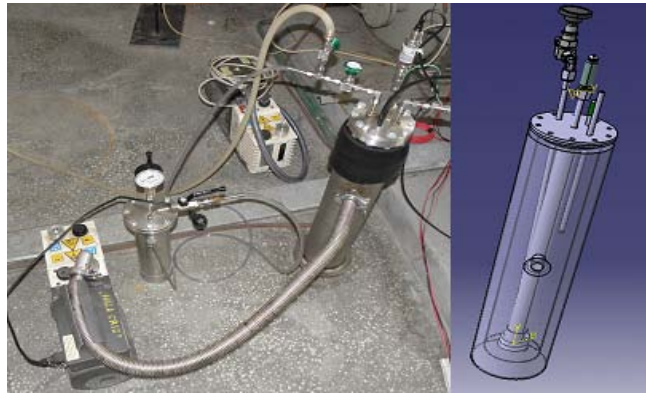


Figure 3 – Constructed experimental test rig after 3D design proposal

Knowing the mass and the apparent density the total charcoal probe volume of pores was determined and compared then with the volume of the container that holds the activate charcoal. Inputs of H_2 - D_2 were made in three determined quantities (batches), with variable pressure of: 5 bars pressure the first input, 4 bars the second one and the last one with a pressure of 3.5 bars. The vessel used to hold the gas mixture inputs had a volume of 1400 cm^3 . For each input a temperature of absorption was selected, having for the 5 bars input a temperature of 83.15 K, for the 4 bars input a temperature of 78.65 K and for the final input of 3.5 a temperature of 77 K. Some observations were made regarding that absorption time has increased directly with the decrease of temperature. The density of the used gas mixture was change at different input temperature, in the charcoal absorber, result a big variation in absorption time and absorbed quantity of H_2 - D_2 . After studying experimental data base of thermodynamic proprieties of the H_2 at different pressures and temperatures, different values for each input of gas mixture in the absorber were chossen. Practically the first two H_2 - D_2 inputs were totally absorbed and only the third one was partially absorbed meaning that the activated charcoal total volume and vessel volume of charcoal filling were fully occupied. The final result concluded with different absorption levels for each input of H_2 - D_2 , regarding the temperature, pressure and time used for the input, the first batch giving a maximum absorption factor of 128.46 %, the second one a absorption factor of 65% and the last one with a minimum absorption rate of 47.30%. These values assure a minimum guaranteed absorption rate of 80.25% of the activated charcoal probe.

Study of equipment associated with low-temperature systems used in cryogenic facilities

ICIT Ramnicu Valcea extends the research capacity in the field of tritium and deuterium extraction and storage with the purpose of decontaminate the tritiated heavy water resulted from CANDU reactors. This, allow, to recover high quantity of tritium, which could be used for fusion applications. The “CRYO-HY” structural funds project implemented at ICIT Ramnicu Valcea will have a great impact factor over all the technology development in the cryogenic research domain in the European Union. The purpose of a 14.5 million euro technology and construction investment is to develop the biggest European low-temperatures laboratory for cryogenic fluids and also to increase the processing power of the actual

“*Experimental Pilot Plant for Deuterium and Tritium Separation*”, also called Tritium Removal Facility (TRF) available at ICIT Ramnicu Valcea for the ITER future demands. Using the knowledge accumulated in the “TRY-TOFFY” training regarding the cryogenic distillation systems functionality and equipment assembly, experience through direct work involvement in activities regarding the upgrading of the refrigeration unit in this structural funds project “CRYO-HY” at ICIT Ramnicu Valcea was obtained. The new refrigerating system that will be acquisitioned is based on the cryogenic helium cycle with a power of 1000 W at 20 K, and is designed to provide various operating modes of cryogenic distillation at different flows (Fig. 4). Helium gas provided by the refrigerator feeds the condensers of the distillation columns, having the main role of condensing the vapors which run in counterflow with the liquid in the columns for cryogenic distillation

The new refrigeration system, based on Helium cycle will be installed in the existing Hydrogen separation experimental pilot building and the related compressor will be positioned in a special designed light-room with natural ventilation. The proposed investment will triple the refrigeration power of the cryogenic distillation facility, which will allow for development of experiments in conditions that are close to those in the future fusion reactors. One of the most important equipment used in refrigeration unit configuration beside the liquefactor, that has a major impact over the optimized functionality of the refrigeration system is the compressor.

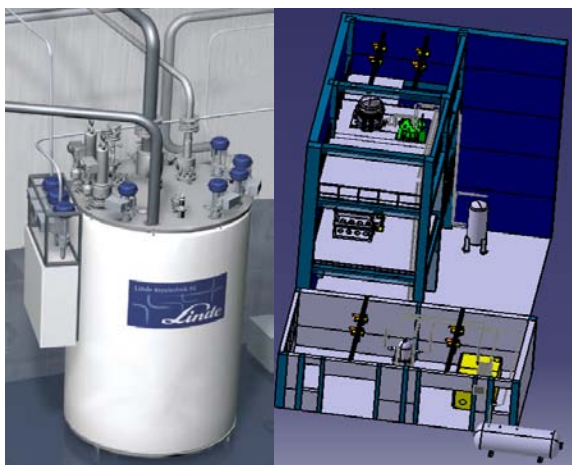


Figure 4 –3D designs for the Linde unit and proposed TRF upgrade configuration

Compression accounts for most of the energy requirements in refrigeration and liquefaction of gases in cryogenics facilities. Identifying this equipment importance a study on types of compressor used in equipment associated with low-level temperatures was necessary. In the new refrigeration unit configuration, the compressors used will be screw compressors, because of the high quality of compression and low energy and maintenance cost. A rotary screw compressors use two helical screws, known as rotors, to compress the gas. Because of special demands of quality compression and purity of the gas dry running rotary screw compressor will be used. In an oil-free compressor, the air is compressed entirely through the action of the screws, without the assistance of an oil seal. They usually have lower maximum

discharge pressure capability as a result. However, multi-stage oil-free compressors, where the air is compressed by several sets of screws, can achieve pressures of over 150 psig, and output volume of over 2000 cubic feet (56.634 cubic meters) per minute (measured at 60 °C and atmospheric pressure). However, this does not exclude the need for filtration as hydrocarbons and other contaminants ingested from the ambient air must also be removed prior to the point-of-use. The process of compression is follows this path:

- gas enters at the suction side and moves through the threads as the screws rotate
- clearances between the threads decrease and compress the gas
- the gas exits at the end of the screws compressed

The effectiveness of this mechanism is dependent on precisely fitting clearances between the helical rotors and the chamber for sealing of the compression cavities. The rotary screw compressor has low leakage levels and low parasitic losses comparative with other types of compressors (example roots-type compressor). The work involvement in the “CRYO-HY” project was an opportunity to better understanding of the functionality and assembly importance of equipments used in cryogenic facilities, improving and verifying in this way the actual knowledge gain in the “TRY-TOFFY” training.

4. Conclusion

The experience gain trough work involvement and participation in experimental campaigns in ICIT Ramnicu Valcea in short time is one of the aspects that the TRI-TOFFY training network encourages. Having the opportunity to be directly involved in the experiment, to compare results and also to combine computer aided design (CADs) programs like CATIA V5 for developing and simulating installations it is a real challenge and also an enormous scientific experience gain completed also by direct work involvement in projects like “CRYO-HY”.

References

- [1] B.N. Khare, M. Meyyappan, J. Kralj, P.Wilhite, M. Sisay, H. Imanaka, J. Koehne, C.W. Baushchlicher, *Appl. Phys. Lett.*81, 5237–5239 (2002).
- [2] P.Ruffieux, O. Groning, M. Biemann, P. Mauron, L. Schlapbach, P. Groning, *Phys. Rev. B* 66 (2002), Art. no. 245416.
- [3] O. Gulseren, T. Yildirim, S. Ciraci, *Phys. Rev. Lett.* 8711 (2001), Art. no. 116802.
- [4] AL. Polihroniade, *Absortia-Adsorbtiia*, Editura Tehnica Bucuresti, 13-60, (1967).

